

DISSERTATION ZUR ERLANGUNG DES DOKTORGRADES DER
TECHNISCHEN FAKULTÄT DER
ALBERT-LUDWIGS-UNIVERSITÄT FREIBURG IM BREISGAU

MICROSCOPY WITH SELF-RECONSTRUCTING BEAMS

FLORIAN OLIVIER FAHRBACH



Albert-Ludwigs-Universität
Technische Fakultät
Institut für Mikrosystemtechnik

DEKAN:

Prof. Dr. Yiannos Manoli

REFERENTEN:

Prof. Dr. Alexander Rohrbach

Prof. Dr. Karsten Buse

TAG DER VERTEIDIGUNG:

16. Januar 2013

ABSTRACT

Light microscopy readily allows the investigation of small details with a size of only few hundred nanometers. However, the investigation deep inside optically inhomogeneous samples is rendered difficult due to scattering that decreases image contrast and signal strength. This problem affects light-sheet microscopy as well, where the sample is illuminated from the side by a thin sheet of light and the image is detected orthogonally. Here, it is shown that the light-sheet microscope is very well suited for quantitative analysis of the propagation of light-beams in turbid media. A spatial light modulator in the illumination path allows flexible, holographic shaping of various beams. Bessel beams were of special interest since these self-reconstructing beams were known regain their initial beam profile behind an isolated obstruction. Here it could be shown for the first time, that these beams are also self-reconstructing in strongly scattering samples as they are more robust to phase perturbations and thereby increase image quality by reducing artifacts. Moreover, because they are able to penetrate deeper into the sample than conventionally used Gaussian beams they allow to visualize more details within larger depth. To further increase image quality and information content, a new detection method was developed where images are acquired line-wise at the position of the illumination beam as it is scanned across the sample. Using newly developed sectioned Bessel beams, the contrast could be further increased and optical sectioning could be decoupled from the illumination beam's depth of field and thus the size of the field of view. Furthermore, two-photon fluorescence excitation with Bessel beams in scattering media revealed a significant increase in penetration depth and image contrast. Especially in combination with confocal-line detection details deep within strongly scattering media can be visualized in a better way enabling new insights into large specimens like tumor cell cluster, fish and fly embryos that are of high interest to modern biomedical research.

ZUSAMMENFASSUNG

Lichtmikroskopische Methoden erlauben die Erforschung von strukturellen Details mit einer Größe von Bruchteilen eines Mikrometers. Allerdings können Bildkontrast und Signalstärke durch die Streuung des Lichts stark nachlassen. Dadurch werden Untersuchungen tief in streuenden Objekten maßgeblich erschwert. Dieses Problem betrifft auch die Lichtscheibenmikroskopie, in der jeweils nur eine dünne Schicht des Objektes seitlich beleuchtet wird und das Bild in dazu orthogonaler Richtung mit einer Kamera detektiert wird. Aufgrund der hohen Geschwindigkeit und effizienten Nutzung von Licht ist das Lichtscheibenmikroskop ideal für die Abbildung dreidimensionaler biologischer Proben. Es eignet sich aber auch zur quantitativen Untersuchung der Ausbreitung von Lichtstrahlen in streuenden Medien. Zu diesem Zweck wurde ein spatialer Lichtmodulator in den Beleuchtungsarm integriert, der es erlaubt verschiedene Strahlen holographisch zu formen. Dabei waren Bessel-Strahlen von besonderem Interesse. In der vorliegenden Arbeit konnte zum ersten Mal gezeigt werden, dass diese Strahlen auch in stark streuenden Medien ihr ursprüngliches Strahl-Profil beibehalten. In einem Lichtscheibenmikroskop führt diese Selbst-rekonstruktion zu einer erhöhten Bildqualität durch stark reduzierte Artefakte. Darüber hinaus konnten durch die höhere Eindringtiefe kleine Details weit innerhalb großer, streuender Objekte sichtbar gemacht werden, die für konventionelle Beleuchtung mit Gauss'schen Strahlen nicht sichtbar sind. Um die Bildqualität in streuenden Medien weiter zu erhöhen wurde eine neuartige Detektionsmethode entwickelt, bei der das Objekt zeilenweise an der Position des Bessel-Strahls aufgenommen wird. Dadurch ergeben sich neue Freiheitsgrade für die Beleuchtung und in Verbindung mit neu entwickelten segmentierten Bessel-Strahlen konnte so erstmals die Auflösung von der Tiefenschärfe des Beleuchtungsstrahls und damit der Größe des Bildfeldes entkoppelt werden. Außerdem konnte durch die Zwei-Photonen-Fluoreszenzanregung mit Bessel-Strahlen eine weitere Steigerung von Eindringtiefe, Auflösung und Kontrast erreicht werden. Die Ergebnisse der vorliegenden Arbeit erlauben es, neue Erkenntnisse zum Beispiel über Objekte wie Krebszellcluster oder Embryonen, die für die moderne biomedizinische Forschung von großer Bedeutung sind, zu gewinnen.

PUBLICATIONS

The following publications feature concepts & results from this thesis:

F.O. Fahrbach, P. Simon, and A. Rohrbach, *Microscopy with self-reconstructing beams*, *Nature Photon.* **4**, 4780-4785 (2010)

F.O. Fahrbach and A. Rohrbach, *A line-scanned light-sheet microscope with phase-shaped self-reconstructing beams*, *Opt. Express* **18**, 24229-24244 (2010)

F.O. Fahrbach and A. Rohrbach, *Propagation stability of self-reconstructing Bessel beams enables contrast-enhanced imaging in thick media*, *Nature Commun.* **3**, 632 (2012)

Further publications are submitted:

F.O. Fahrbach, V. Gurchenkov, K. Alessandri, P. Nassoy, and A. Rohrbach, *Light-sheet microscopy in thick media using scanned Bessel beams and two-photon fluorescence excitation*

F.O. Fahrbach, V. Gurchenkov, K. Alessandri, P. Nassoy, and A. Rohrbach, *Decoupling optical sectioning from the size of the field of view in light-sheet microscopy by using sectioned Bessel beams*

This document was typeset using the typographical look-and-feel `classicthesis` developed by André Miede. The style was inspired by Robert Bringhurst's seminal book on typography "*The Elements of Typographic Style*". `classicthesis` is available for both \LaTeX and \LyX :

<http://code.google.com/p/classicthesis/>

Hermann Zapf's *Palatino* and *Euler* type faces (Type 1 PostScript fonts *URW Palladio L* and *FPL*) are used. The "typewriter" text is typeset in *Bera Mono*, originally developed by Bitstream, Inc. as "Bitstream Vera". (Type 1 PostScript fonts were made available by Malte Rosenau and Ulrich Dirr.)

ACKNOWLEDGEMENTS

First, I thank *Alexander Rohrbach* for introducing me to the fascinating world of modern optics. Throughout the last years, his enthusiasm has been a constant motivation. I appreciate his creativity and persistence. I knew he would listen to and care about whatever was on my mind.

I would like *Prof. Dr. Karsten Buse* for being a referee for this thesis.

When mechanical parts had to be costume-made in short time with great precision, I could always rely on *M. Stoll, F. Großmann* and the team of the mechanical workshop at the institute of physics.

Thanks to *Roland Nitschke* for lending the Coherent Chameleon laser and many gadgets.

Many biologists have provided samples to test the performance of the microscope. Thank you, *Björn Wendik, Enrica Charbonnier & Georgios Pyrowlakis* for *Drosophila*, *Meta Rath, Alida Filipi* for Zebrafish.

Lars Friedrich started to write MicPy and many colleagues (*Ben, PvO*) have made contributions that I was happy to use.

It was a pleasure to meet *Vasily Gurchenkov* on multiple conferences. I thank him, *Kevin Alessandri* and *Pierre Nassoy* for providing the magnificent spheroidal cell clusters.

As part of his diploma thesis *Philipp Simon* helped me a lot by building electronics and programming software for which I am very grateful. I also enjoyed our football matches.

Over the years I shared the office with great people: *Michael, Lars, Cris, Beni, Andi* have made going to work fun every day. With *Ben, Felix, PvO, Markus, Matze, Felix, Dominic, Marc, Julian, Martin* and *Hoda* they have contributed to an exceptional, joyful, relaxed but (tightly) focused atmosphere at the lab and helped to reconstruct my motivation after some perturbations I encountered.

I am especially grateful to *Lars Friedrich* for many discussions on topics that range from the Abbe criterion to Zernike polynomials and *Cristian Gohn-Kreuz* for joining the MISERB-task force in the group.

I enjoyed discussions about music, photography and life in general with *Anne Rottler*.

Uli Jentschura's encouragement and motivation as a tutor during a difficult period of my studies were of paramount importance to me.

My uncle *Eberhard* gave me an important advice at the right time - this thesis would maybe not exist without him.

My parents, *Anne & Uli* gave me all the freedom but have always supported me in every possible aspect.

Alice and *Lionel* are the best reason in the world to leave the lab and come home in the evening.

CONTENTS

1	INTRODUCTION	1
1.1	Summary & Outline	2
1.2	Scientific Background	5
1.2.1	Microscope Utility Parameters	5
1.2.2	Light-Sheet Fluorescence Microscopy	11
1.2.3	Self-Reconstructing Beams	13
1.3	Concept of the Investigations	15
2	THE LIGHT-SHEET MICROSCOPE	17
2.1	Description of the Image Formation	17
2.2	Definition of Image Quality Parameters	19
2.2.1	The System-Point-Spread-Function	19
2.2.2	Resolution	22
2.2.3	Optical Sectioning	23
2.2.4	Signal-to-background	24
2.2.5	Image Artifacts	25
2.3	Description of the Setup	28
2.3.1	Optical Components	29
2.3.2	Sample Mounting and Positioning Components	33
2.3.3	Software	35
2.4	Discussion	35
3	ILLUMINATION BEAMS	39
3.1	Conventional beams	39
3.1.1	Focused Flat-Top Beams	39
3.1.2	Gaussian Beams	41
3.1.3	Elliptical Beams	42
3.2	Self-Reconstructing Beams	43
3.2.1	Bessel Beams	43
3.2.2	Sectioned Bessel Beams	45
3.3	Radial Distribution of Beam Power	45
3.3.1	Comparison using Numerical Data	46
3.3.2	Comparison using Analytical Approximations	47
3.4	Holographic Generation of Illumination Beams	49
3.4.1	Holographic Beam Shaping	49
3.4.2	Spatial Separation of the SLM's Diffraction Pattern	50
3.4.3	Beam Shaping and Axial Positioning	51
3.4.4	Alignment and Orientation	54
3.4.5	Low-Pass-Filtering of the Amplitude Mask Against Axial Oscillations of the Beam's Irradiance	56
3.5	Coherent Imaging of Illumination Beams	59
4	BEAM PROPAGATION THROUGH SCATTERING MEDIA	61
4.1	Measures for Beam Propagation Stability	61
4.1.1	Directional Stability	61
4.1.2	Image Contrast from Directional Stability	62
4.2	Simulation of Beam Propagation through Scattering Media	63
4.3	Light-sheet Microscopy Images of Beam Propagation in Scattering Media	66

4.3.1	Two Large Spheres	66	
4.3.2	A Cluster of Small Spheres	69	
4.3.3	Human Skin	71	
4.4	Discussion	73	
5	LIGHT-SHEET MICROSCOPY WITH SCANNED SELF-RECONSTRUCTING BEAMS	77	
5.1	Numerical Comparison of Light-Sheet Properties	77	
5.1.1	Axial Resolution of Line-Scanning Light-Sheet Microscopes	77	77
5.1.2	Optical Sectioning	78	
5.2	Two Beads	80	
5.3	A Barrier of Spheres	82	
5.4	A Clusters of Spheres	84	
5.5	Drosophila Embryos	89	
5.6	Discussion	90	
6	LIGHT SHEET MICROSCOPY WITH CONFOCAL-LINE DETECTION		95
6.1	The Principle of Confocal-Line Detection	95	
6.2	Description of Image Formation	96	
6.3	Axial Resolution and Optical Sectioning Performance	99	
6.3.1	Resolution	99	
6.3.2	Optical Sectioning	100	
6.4	Confocal-Line Detection with a Conventional Light-Sheet Microscope	102	
6.4.1	Beam Multiplexing	102	
6.4.2	Calibration	103	
6.5	Performance Analysis using Images of Strongly Scattering Beads	104	
6.5.1	Determination of Resolution and Signal-to-background	107	
6.6	Imaging Performance in Drosophila Egg-Chambers	109	
6.7	Quantitative Contrast Analysis in Images of Multicellular Spheroids	111	
6.7.1	Image Decomposition	112	
6.7.2	Image Contrast Dependency on the Confocal Line Width	112	
6.7.3	Image Contrast Comparison	113	
6.8	Improved Optical Sectioning by Sectioned Bessel Beams	117	
6.8.1	The Optimum Section Angle	117	
6.8.2	Analysis of Optical Sectioning Dependency on the Depth of Field	118	
6.8.3	Analysis of the Quality of Images of Tumor Multicellular Spheroids	119	
6.9	Discussion	121	
6.9.1	Speed	122	
6.9.2	Sample Exposure to Light	123	
6.9.3	Confocal-line detection vs. Structured Illumination	126	
7	TWO-PHOTON FLUORESCENCE EXCITATION		131
7.1	Motivation	131	
7.2	Principle and Background	132	
7.2.1	Two-photon Absorption and Fluorescence Emission	132	
7.2.2	Fluorescence Signal in Scattering Media	133	
7.2.3	Dimensions of the Two-Photon Bessel Beams	134	
7.2.4	Dependence of the Fluorescence on the Beam's Depth-of-Field	136	

7.2.5	Optical Sectioning	136
7.2.6	Importance of Precise Alignment of the Illumination Beam	138
7.3	Simulation of the Imaging Performance	140
7.4	Experimental Setup	143
7.5	Beam Images Measured in Homogeneous Fluorescence	146
7.6	Resolution and Contrast Measured Using Scattering Fluorescent Spheres	146
7.7	Imaging Performance Measured in Multicellular Spheroids	148
7.7.1	Analysis of Image Artifacts	149
7.7.2	Contrast Improvement by Confocal-line Detection	151
7.7.3	Measurement of Penetration Depth	151
7.8	Discussion	152
8	SUMMARY, CONCLUSION & OUTLOOK	157
8.1	Summary & Conclusion	157
8.2	Final Discussion and Outlook	159
8.2.1	Penetration & Image Artifacts	162
8.2.2	Confocal-Line Detection: Outlook	163
8.2.3	Two-Photon Excitation by Bessel beams: Outlook	165
A	COMPARISON OF LINE WISE DETECTION AGAINST PLANE-WISE DETECTION	167
B	THE BEAM-PROPAGATION METHOD	169
B.1	Theoretical Background	169
B.2	Estimation of the Errors arising from Approximations	170
B.3	Errors arising from negligence of backward scattering	171

INTRODUCTION

To understand structure and function of living matter, biologists often rely on imaging methods. Many investigations are based on conventional microscopy techniques and therefore have to use thin samples that are mounted on coverslips. By this means, samples are easily accessible to light from two sides. However, the natural environment for biological processes is not two-dimensional [Pampaloni et al., 2007] and the impact of a non-natural environment on the results obtained can be critical. The behavior and interaction of cells in living samples, e.g. developing embryos, plant roots, the brain, or tumors happen in a three-dimensional setting. The importance of this aspect has only been realized lately - the third dimension was even termed biology's *new* dimension [Abbott, 2003]. However, the observation of processes deep inside extended three-dimensional samples is challenging: To reach these regions, illumination and detection light have to travel through the sample which is generally hazy and turbid due to an inhomogeneous refractive index distribution. Images obtained using conventional methods are of limited use as the amount of details discernible is strongly reduced at larger depths within the samples. A major goal of microscopy is therefore, to develop techniques that allow to overcome this limitation and to gain high-quality images of extended samples in their natural environment.

A technique that is particularly useful to achieve this goal is light-sheet microscopy, where only a thin slice within a large object can be illuminated by a sheet of light. The main purpose of the light-sheet microscope is the investigation of large biological samples. It is very interesting to biologists due to the high speed and efficient use of illumination light. The low light dose enables long-term observation of the development of embryos without causing damage. Furthermore, the technique enables imaging objects that only allow staining with very susceptible fluorophores such as brain tissue. However, image quality in light-sheet microscopes is strongly reduced in thick, scattering samples. Therefore, the main goal of this thesis was an improvement of the light-sheet microscope for such samples.

In a more abstract treatment, microscopy can be seen as a tool that uses light to gain knowledge about the structure of the sample. Focused light waves are employed to locally deposit energy in a sample. The elastically and inelastically scattered light is then collected to infer the position of the scatterer. In media where light is scattered only once, there is a well-defined relationship between the detected light and its sources within the sample. In the case of inelastic scattering the source is a fluorophore that absorbs illumination light and emits light at a longer wavelength. Precise knowledge about the distribution of sources within an object is possible because the propagation of light in homogeneous media is well understood. It can be described mathematically by the wave equation with great accuracy, as it is analytically solvable for homogeneous media.

The situation is much more challenging for media that interact with the light. This interaction of a medium with electromagnetic waves is described by its refractive index. The refractive index influences the wave by absorption,

reflection and retardation. In inhomogeneous media, the local variations in the interaction between light and matter quickly generate a complicated distribution of the light. Additionally, for coherent laser light which is used for tightly focused illumination, the interference of scattered and unscattered light leads to a seemingly chaotic redistribution of the energy. In principle, an additional term can be added to the wave equation to include the refractive index. However, in general no analytical solution can be found for inhomogeneous media. Therefore, strong limitations arise to the predictability of the energy distribution of waves in media with strong small-scale changes in the refractive index distribution. These effects render the acquisition of structural information about media, e.g. for imaging, a very hard task.

Waves are used for many different applications and the aforementioned problem affects many of these. For example, ultrasound waves, that obey the same mathematical laws, are used for tomographic biomedical imaging or non-destructive material inspection. Moreover, telecommunications, where waves are used for signal transmission, or remote sensing could greatly benefit from improved performance in inhomogeneous media like atmospheric turbulence. Therefore, one of the goals of this thesis which consists in a better understanding of the propagation of coherent electromagnetic waves, i.e. beams, inside scattering media is a challenging task with clear potential for important applications far beyond the scope of microscopy.

It is especially interesting to investigate the interaction of waves with matter at the scale of the wavelength, where diffraction effects arise. A light-sheet microscope is the ideal tool to study the propagation of electromagnetic beams in scattering media, because the beam can be observed sideways along its propagation through the sample.

1.1 SUMMARY & OUTLINE

In the following, the structure of this thesis is outlined. Chapter 2 describes the experimental setup together with important background. For this thesis a light-sheet microscope with a slight alteration was built: A spatial light modulator (SLM) was integrated in the illumination beam path. This device is able to spatially control the shape of the coherent illumination beam by applying computer generated holograms. Details on the illumination beams and the holographic generation are given in chapter 3. The combination of an SLM and a light-sheet microscope represents an instrument with unique features. First, it allows to control the light field incident on a scattering medium. Furthermore it enables to observe the evolution of the light beam during the propagation through the sample. The experiments presented here investigate a special class of beams, the so-called self-reconstructing beams. The most prominent self-reconstructing beam, the Bessel beam, was previously reported to be able to regain its initial profile behind a perturbation that partially scatters or even blocks the beam. Measurements and simulations described in Chapter 4 investigate the directional propagation stability, i.e. the ability to maintain the initial power along the propagation axis in the presence of perturbation. It was found that Bessel beams are superior to conventional Gaussian laser beams in various scattering media. Chapter 5 presents the investigations carried out to study if this property can be used to increase the image quality in comparison to illumination by Gaussian beams. The results shown demonstrate that Bessel beams illuminate samples

more homogeneously up to larger depths within the sample. At the same time a lower relative strength of artifacts arises from scattering of the illumination beam.

In contrast to Gaussian beams with a monotonously decaying radial irradiance, Bessel beams feature a thinner main peak that is surrounded by a ring system. The Bessel beam carries a significant amount of its power in these rings. When it is scanned across the field of view during image acquisition these rings are smeared out effectively creating a thick light-sheet. This sheet illuminates planes below and above the focal plane of the detection lens. Due to the resulting inferior optical sectioning the recorded images exhibit lower contrast. Chapter 6 presents the confocal-line detection scheme that was developed in the context of this thesis in order to solve this problem. By recording the images line-wise at the position of the illumination beam's central peak the method makes use of the directional stability of the Bessel beam and delivers images with high contrast and resolution up to large depths within scattering media. It is also possible to improve contrast further by the use of a special variant of the Bessel beam - the Sectioned Bessel beam (Section 6.8). This propagation-invariant beam also exhibits directional propagation stability and, most importantly, offers optical sectioning that is independent of the size of the field of view along the beam's propagation axis. No other beam investigated so far can offer this advantage.

Finally, two-photon fluorescence excitation (TPE) by Bessel beams in a light-sheet microscope was studied and the results are presented in Chapter 7. The advantages offered by TPE include the suppression of fluorescence excitation by the Bessel beam's ring system. Moreover, because each of the two photons contributes half the energy needed to excite the fluorophore, light at the double wavelength can be used where small particles scatter less strongly. This dependency was expected to result in a stronger robustness of the illumination against scattering. However, simulation results show that TPE with Gaussian beams is very sensitive to scattering, while TPE with Bessel beams offers best contrast and lowest strength of artifacts (Section 7.3). The penetration depth into the sample can be increased only slightly, but experiments on scattering fluorescent spheres (Section 7.6) as well as cell clusters (Section 7.7) show that optical sectioning and image contrast can be strongly increased by TPE with Bessel beams.

1.2 SCIENTIFIC BACKGROUND

The following chapter outlines the scientific background for the work presented in this thesis. The goal of this section is to introduce the reader to important concepts. Many of the mentioned aspects will be described more formally and detailed later. First of all, in order to be able to build a better microscope, it is important to know exactly which parameters influence the performance of a microscope and how. These parameters are introduced in Section 1.2.1. Second, the principles of light-sheet based microscopy are presented in Section 1.2.2. Even though light-sheet microscopy represents a very powerful tool, it also has some major optical limitations such as the strong visibility of artifacts arising from scattering and absorption which are also briefly described. One goal of this thesis was to improve these deficits by employing sample illumination with self-reconstructing beams. These are introduced in Section 1.2.3. The chapter closes by Section 1.3 that outlines the basic concept of the experiments performed for this thesis.

1.2.1 *Microscope Utility Parameters*

In the following, different parameters are presented that account for the usefulness of an imaging system. The aspects are divided into two categories:

1. Optical properties that directly affect the image quality like resolution and contrast (§ 1.2.1.1).
2. Non-optical aspects such as the image acquisition speed or sample mounting (§ 1.2.1.2).

Note that there is no unique set of parameters and the one presented here was chosen in a way as to attempt a broad coverage of the range of relevant properties. While a strong emphasis is put on the microscopical investigation of biological samples, most of the aspects are relevant beyond this scope to imaging in general, e.g. optical techniques for material inspection or even non-optical techniques like ultrasound tomography.

1.2.1.1 *Optical Image Quality Parameters*

For scientific use, the quality of an image is based on its information content. The ideal image is an exact copy of the object or a chemical or structural subset. The ideal imaging system generates such a digital three-dimensional copy in a computer where further analysis and post-processing can be performed. Optical properties that define the usefulness of a microscope by increasing the information content of the images are resolution, the optical sectioning capability, the strength of artifacts, the penetration depth and image contrast (see Figure 1.1 for an illustration). The following outline is meant to give an overview. Therefore, no mathematical formalism is given at this point, but can be found in later chapters using the given references.

In order to understand the following explanations, the concept of the point-spread function (PSF) of a microscope (or imaging system) is of great importance. In short, the PSF describes the three-dimensional image of a single point. Each point in the object is represented by the PSF in the image. Mathematically, the image is given by the convolution of the object with the point-spread function.

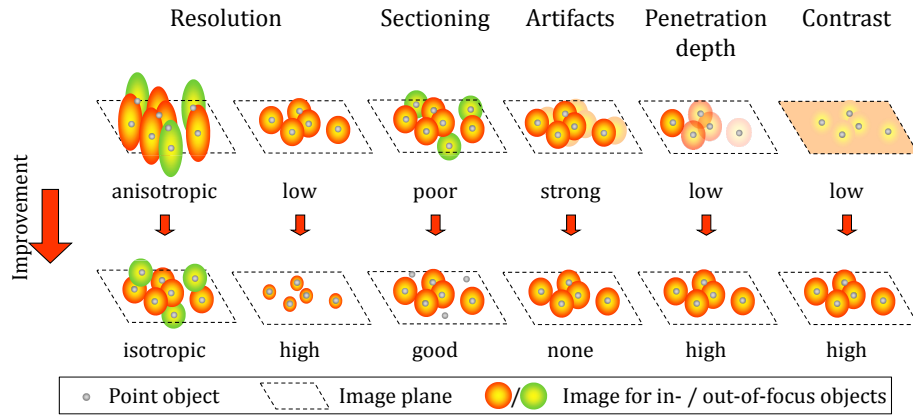


Figure 1.1: Illustration of fundamental image quality parameters.

The distribution of point objects is shown by small gray-shaded circles. The focal plane is indicated by a dashed rectangle. The three-dimensional image of a point, the PSF, is shown in orange for in-focus objects and in green for out-of-focus objects. The top row schematically illustrates the typical situation for standard microscopy techniques, whereas the bottom row shows the desired improvement.

Resolution: Higher resolution enables identification of smaller structures.

An imaging system with a higher resolution yields images that resemble the object more closely. High spatial resolution is necessary to resolve small details or to separate agglomerates. Fine object structures in close proximity to each other can only be separated in an image if the resolution is sufficient. In general, resolution along the optical axis is always inferior to lateral resolution. When imaging three-dimensional samples, an increase in axial resolution to achieve isotropic resolution is of special interest. Figure 1.1 illustrates the difference between low anisotropic and high isotropic resolution.

Ernst Abbe derived the most widespread definition of resolution as the minimum distance that is necessary between two point objects so that they can be identified separately. This measure is proportional to the size of the PSF, which can therefore also be used as measure for the resolution of an imaging system (see § 2.2.2). As the three-dimensional image of a point source is given by the PSF, resolution can be determined experimentally by imaging point sources, i.e. particles much smaller than the resolution. From a system theoretical point of view the microscope can be seen as a low-pass filter with a transfer function that suppresses the transmission of high-frequency components of the object's spatial spectrum.

It is important to separate the term *resolution* from the term *localization*. Favorable circumstances, e.g. a very sparse object distribution or knowledge about the object shape may allow a localization precision that is much higher than the resolution. For example, it is possible to localize single point objects with a precision of only few nanometers. To achieve this goal, the center of the image of the point object can be evaluated. Localization techniques usually work with a large number of images of a weakly fluorescing sample. For each image only the photons emitted by few fluorophores are detected, thereby allowing a precise localization.

Light microscopy techniques that offer resolution that surpasses the resolution limit imposed by diffraction are called super-resolution techniques. Examples for far-field super-resolution techniques are stimulated emission depletion

microscopy (STED) [Hell and Wichmann, 1994] and structured illumination microscopy (SIM) [Gustafsson, 2000, 2005]. The most prominent localization techniques are called photo-activation localization microscopy (PALM) [Hess et al., 2006, Betzig et al., 2006] and stochastic optical reconstruction microscopy (STORM) [Zhuang, 2009]. These techniques achieve a lateral localization precision in the range of 20 nm.

Sectioning: Better sectioning provides images from thinner planes and thereby better signal-to-background ratio.

When imaging three-dimensional samples, the sharp image of objects in the focal plane is superposed by blurred images of out-of-focus planes, because a single lens cannot discriminate against (fore- or) background. Better sectioning leads to images with better contrast due to lower background so that structures are more clearly discernible. The goal of good sectioning is to extract the image of a thin plane from a three-dimensional object, as illustrated in Figure 1.1. Sectioning can be achieved mechanically by slicing the object into very thin pieces that are imaged separately. This method cannot be used for live-imaging or the study of the development of samples over time. In contrast, optical sectioning techniques extract images with reduced background from intact three-dimensional objects thus enabling non-destructive imaging [Conchello and Lichtman, 2005].

Described in more quantitative terms, the optical sectioning (OS) capability is a measure for the relative amount of signal contribution from each plane. The optical sectioning performance can be determined using the fluorescence sea method [Brakenhoff et al., 2005, Vicidomini et al., 2007, Schrader et al., 1998]. Thereby, the amount of signal at a single detector point that is detected from individual planes is measured by recording the full signal of a thin fluorescent layer that is moved along the detection optical axis. Mathematically speaking, the image of a point, the PSF, is integrated over its cross-section for each axial layer (see § 2.2.3). The concept of sectioning is closely related to axial resolution and both measures can be derived from the point-spread function. However, OS represents a more suitable measure than resolution to describe the amount of background to images of single two-dimensional planes in a three-dimensional object.

The most common technique that achieves optical sectioning by discriminating against fluorescence on the detection side is confocal microscopy. In contrast, it is also possible to excite fluorescence almost exclusively in a small volume around the focal plane by two-photon microscopy [Denk et al., 1990]. Both methods rely on a point-scanning approach, where the object is imaged point-by-point. Another wide-field method, structured illumination, removes background from out-of-focus planes in a post-processing step [Neil et al., 1997].

Artifacts: Images with less artifacts more closely resemble the imaged sample.

An artifact is defined as a structure formed by artificial means which is not naturally present in the matter being observed. It is an error in representation which is introduced by the involved technique. In the case of microscopy, the ideal image represents a map of the object with a proportionality between the density of the (fluorophore) structure and the recorded signal. Deviations from this proportionality are termed artifacts or ghost images [Rohrbach, 2009]. In extreme cases an artifact dominates the image of a sample detail so that it cannot

be identified at all, or objects are seen with a different shape and/or at a different position. In microscopy images of strongly scattering media artifacts arise from inhomogeneous illumination or detection, which is caused by distortions in the light field by scattering and/or absorbing parts in the object. An example for an artifact is shown in Figure 1.1. It is therefore necessary to overcome these distortions by suitable illumination and detection techniques. The extraction of ghost and ideal images from real images is described in detail in Section 2.2.5.

Penetration depth: A higher penetration depth enables selective illumination of details deeper within the sample.

Ideally, resolution and sectioning are independent of the position in the sample. However, due to scattering and absorption of light by the sample, the image quality is degraded when the coherent illumination beam or the incoherent fluorescence have to travel long distances through the sample. Spreading of the illumination beam causes weaker irradiance of the fluorophores, but over a larger volume (see Figure 1.1, where the illumination coming from the left is attenuated along the propagation through the sample). A measure for beam penetration is given in Section 4.1.1. On the detection side, the scattering blurs the image. The sample perturbs the beam thereby increasing its dimensions. The aberrated illumination and detection point-spread functions are more extended which leads to a lower signal strength and resolution for positions deeper inside samples. Therefore, so-called adaptive optics methods have been developed to correct for the specimen induced aberrations [Girkin et al., 2009, Schwertner et al., 2004, Booth et al., 2002].

A system's penetration depth can be measured by evaluation of the signal in dependence of the distance to the surface (§ 4.3.3) or the directional propagation stability of the illumination beam (§ 4.1.1).

Some optical techniques that allow to image especially deep into samples rely on the rejection of scattered light. The pinhole in a confocal microscope works in such a way. Nonlinear microscopy techniques strongly suppress fluorescence excitation by scattered light as long as it is weak in amplitude in comparison to the focus. Optical techniques that are well-suited for strongly scattering media include optical coherence tomography [Huang et al., 1991] and optical projection tomography [Sharpe et al., 2002]. Large and strongly scattering samples are currently mainly investigated using non-optical techniques like ultrasound imaging and magnetic resonance tomography. These techniques offer higher penetration but lower overall resolution than optical systems [Ntziachristos, 2010]. Most importantly, they do not offer the flexibility that is obtained by marking with fluorescent dyes and especially proteins. This issue is discussed in more detail below in the paragraph on chemically specific imaging.

Contrast: Images that show higher contrast show structures more clearly and are more suitable for automated analysis.

Contrast, the ratio between the signal and the background, is the most important image property because it determines the overall information content of an image. It is influenced by and influences all the above mentioned criteria. In fact, background can be seen as an artifact introduced by the deficient imaging system. Low resolution, weak optical sectioning, artifacts and noise all give rise to background. For example a higher resolution and better optical sectioning lead

to lower background and better contrast. Ideal images contain no background (see Figure 1.1) as it is not present in the object being observed.

Contrast is directly linked to the bandwidth of the signal magnitudes in an image. For example, contrast can be measured globally by a normalized difference of maximum to minimum signal strength. But this method is very susceptible to outliers. A more robust measure is the width of the signal histogram as utilized by Keller et al. [2010]. An even more refined method is to analyze the spatial spectrum of the images and extract the relative signal strength in a frequency range that is expected to contain the relevant information (§ 2.2.4). In general, it can be assumed, that the high-frequency contributions to the spectrum arise from fine structures in the image, which must lie within the focal depth of the detection lens. The method will be used throughout this thesis. It is especially sensible when the structure is unknown or exhibits a repetitive periodic pattern [Truong et al., 2011], i.e. when all information is contained within a limited frequency bandwidth. It is important to note that high spatial high-frequency artifacts are counted as *image information* for all presented measures of contrast. A solution to this problem is presented in Section 2.2.5

1.2.1.2 General Parameters

Chemically specific labeling: Fluorescent markers allow to study the spatio-temporal distribution of chemical substances.

The usefulness of an image is not exclusively determined by the amount of information but also by the possibility to solely extract a desired subset of information. This subset might be a spatially or chemically selected part of the object's components, i.e. the cell walls or the nuclei of an organism. Using fluorescent markers to specifically label a component of the sample allows to observe only this part of the object. The thereby achieved reduction of image content greatly facilitates the image analysis, because the image features a reduced amount of structures. Moreover, it is possible to visualize the distribution of single molecules that are much smaller than the resolution limit of any microscope by attaching specific fluorescent markers to it. Other optical techniques such a optical coherence tomography or phase-contrast techniques, are susceptible to local variations in the refractive index but do not directly allow chemically specific imaging.

Light-sheet microscopy is a fluorescence microscopy technique and therefore benefits from the possibility of chemically specific marking by fluorescent dyes and proteins.

Sample exposure to light: The efficient use of light is important because light causes damage to biological samples and fluorescent markers.

It is important to limit the light dose that a sample is exposed to. On the one hand, the illumination of samples for microscopy may cause damage. Light may be absorbed by non-fluorescent molecules that relax to the ground state by exchanging energy with their environment by collisions, effectively heating it. More importantly, light might trigger toxic reactions in the sample by creating free radicals. Plant cells are especially susceptible [Foyer et al., 1994]. The apoptosis (cell death) in a rat Brain due to photo-toxic effects was investigated by [Jou et al., 2002].

On the other hand, fluorescent markers in the sample are themselves susceptible to strong illumination. The molecule may not relax from the excited state to the ground state, but to a so-called dark state which is meta-stable, i.e. it takes a long time until the eventual relaxation to the ground state. Over this time, the molecule does not emit fluorescence. This effect is termed *bleaching*. Absorption of another photon might lead to a reconfiguration of the molecule so that it might even act toxic [Song et al., 1995]. It was found that photo-toxic processes depend on the oxygen concentration and can therefore be suppressed to a certain degree [Bernas et al., 2004]. However, for long-term imaging of live specimens under natural conditions the efficient use of light by the microscope is indispensable.

By illuminating mainly a thin volume around the plane within the object that is imaged, light-sheet microscopy makes very efficient use of illumination light and allows to reduce the sample exposure to light.

Sample mounting: A natural environment is necessary for three-dimensional in-vivo imaging

An important aspect of an imaging system is the way that the sample is mounted and the environment it is kept in. On the one hand, it should be practical, i.e. simple and not time-consuming. On the other hand, especially when imaging the behavior of living samples, the environmental conditions should be as natural as possible. Non-physiological sample mounting may lead to a different development of organisms. Recently, in fields like cancer research or cell culture a strong influence of the environment on the sample was proven. This insight has led to a paradigm shift away from cover-slip based two-dimensional biology to three-dimensional observation in physiological environment [Pampaloni et al., 2007]. However necessary and helpful, the step towards the third dimension [Keller et al., 2006] implies a loss in sample accessibility. First, samples are kept in their natural environment during observation which may affect image quality, e.g. in the case of turbid culture medium. Second, in order to obtain images of single planes within the extended sample, ways to *optically* section it have to be employed. Third, illumination and detection light have to travel longer distances through the sample. Contrast and resolution are degraded due to the interaction of the light with the sample that may consist of hundreds of single cells and may contain strongly scattering structures as for example collagen fibers. These inhomogeneities in optical density or refractive index absorb, deflect and spread the light. Therefore, physiological sample mounting has to go along with more robust imaging methods such as light-sheet microscopy with self-reconstructing beams.

Light-sheet microscopy is not based on the use of cover-slides. The sample can be mounted in a three-dimensional gel matrix, which exerts only low pressure on the sample [Kaufmann et al., 2012]. Nutrients and other chemical substances can diffuse through the gel so that the sample can be kept alive over extended periods of time.

Image acquisition speed: A higher image acquisition speed allows the observation of faster processes.

Many imaging techniques achieve an improvement in image quality only at the cost of acquisition speed, thereby severely limiting the method's suitability to

observe dynamical processes in living organisms. In the worst case, when the acquisition time is in the order of tens of minutes it is necessary to look at fixed samples. There are at least two benefits arising from a faster microscope: A high imaging speed allows the acquisition of high-resolution images of living samples, that are undergoing constant change. A slow imaging system would create artifacts due to that change. Moreover, important information about a (biological) system can be obtained by observing its temporal behavior. In principle, the speed of an imaging system is limited by the time necessary to collect a sufficient number of photons from each fluorophore to obtain a sufficient signal-to-background ratio. The speed of a system should be measured by the amount of points that can be resolved in a certain amount of time. A possible measure therefore would be the space-bandwidth product [Lohmann et al., 1996] normalized to the image acquisition time.

In contrast to point-scanning techniques, light-sheet microscopy acquires entire image planes at once using modern CCD and sCMOS cameras with high light efficiencies. It is therefore currently the fastest three-dimensional light microscopy technique.

1.2.2 *Light-Sheet Fluorescence Microscopy*

Light-sheet fluorescence microscopy (LSFM) is an imaging technique that is especially useful for high-speed high-content imaging. It offers images with high information content due to the greatly improved optical sectioning which provides high contrast. LSFM illuminates only the part of the object, which is in the plane of focus of the detection objective. It therefore works more light efficient than other techniques, especially confocal microscopy, which illuminates the whole sample for each plane that is imaged. In LSFM, objects are imaged plane-wise, but not point-wise as in confocal microscopy. For this reason, exceptionally high image acquisition speeds are possible especially for large samples. Additionally, in a LSFM the samples can be mounted under various close-to-physiological conditions.

In a light-sheet microscope, illumination light penetrates the sample from the side and, being focused to a thin light-sheet, illuminates only a thin volume around the focal plane of a detection lens. Three-dimensional image stacks can be obtained by subsequently taking images of adjacent planes within the sample. Therefore, the translation of the sample along the detection axis is necessary. The idea of perpendicular illumination and detection was first presented more than one hundred years ago to measure the size of colloidal particles [Siedentopf and Zsigmondy, 1903]. While the principle was first rediscovered by Voie et al. [1993] to investigate the structure of the inner ear, the full potential of the technique as a fluorescence microscope for modern biological investigations was only realized later by Huisken et al. [2004]. At first the light-sheet was produced using a cylindrical lens [Voie et al., 1993, Fuchs et al., 2002, Dodt et al., 2007]. Later, a laterally scanned beam [Keller et al., 2008] focused by an objective lens was employed that offers higher image quality and improved flexibility. The sample is usually mounted in a cylinder of transparent agarose gel, but there are various other possibilities [Reynaud et al., 2008]. LSFM has been successfully used especially in modern developmental biology [Huisken and Stainier, 2009], in neurology [Holekamp et al., 2008] and especially for the observation of highly dynamic (living) samples [Planchon et al., 2011, Truong et al., 2011, Arrenberg.

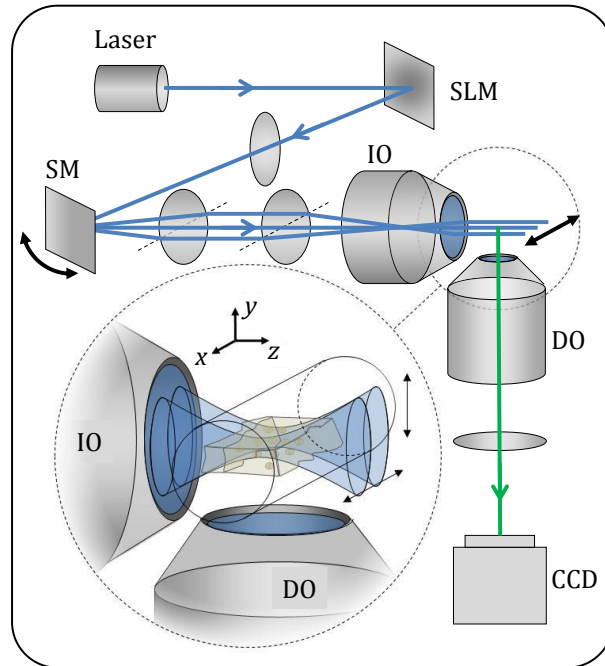


Figure 1.2: Schematic of a light-sheet microscope setup.

A laser beam is focused into the sample volume by an illumination objective (IO). The scan mirrors (SM) enable a beam tilt in the back focal plane of the IO, leading to a lateral scan of the beam in the x -direction. In the time average, a light-sheet is generated that illuminates only the part of the object in the focal plane of the detection objective (DO). Fluorescence light is detected in the orthogonal y -direction and imaged onto a CCD camera. To obtain a three-dimensional image stack, the object can be moved along the y -direction. For this thesis, a spatial light modulator (SLM) is included that is imaged into the focal plane of the IO and allows to holographically shape the illumination beam.

[et al., 2010](#)]. It is also well-suited to observe exceptionally large samples, for example entire brains [[Dodt et al., 2007](#)].

However, LSFM also suffers from some restrictions. Thinner light-sheets resulting in higher axial resolution, can only be achieved by stronger focusing of the illumination beam which at the same time reduces the depth of field of the illumination beam [[Buytaert and Dirckx, 2007](#)]. The spreading of the beam along the propagation direction (Fig 1.3a) leads to inferior axial resolution and contrast. Thus, the axial resolution and optical sectioning in LSFM depend on the sample size for conventional illumination by diffraction-limited foci.

When the illumination light propagates through a medium with refractive index inhomogeneities it is deflected and scattered. The resulting redistribution of light momentum and energy in the imaged plane causes prominent dark and bright stripes. These specimen-induced aberrations onto the coherent illumination beam become especially pronounced in plane scanning systems due to coherent field superposition. Hence, the light-sheet homogeneity is deteriorated and the image quality degraded. Image artifacts created by scattered illumination light can be regarded as a ghost-image superposed with the ideal image [[Rohrbach, 2009](#)]. Furthermore, scattering of illumination light out of the focal plane (see Fig. 1.3b) leads to decreased signal-to-background, since

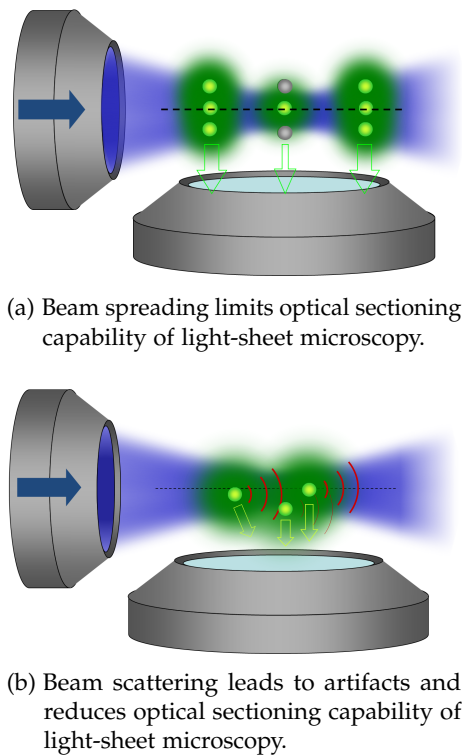


Figure 1.3: Illustration of limitations of light-sheet based microscopy.

The blue illumination beam propagates through the sample represented by small spheres. The focal plane of the detection lens is marked by a dashed line. Green fluorescence of the particles that lie in the focal plane should be excited, whereas the particles lying below and on top should remain dark. Figure a illustrates the problem that the beam excites exclusively the object in the focal plane solely at the position of the beam waist. The spreading of the illumination beams causes out-of-focus objects to be excited for larger distances along the illumination beams axis. In Figure b, the object in the center lies below the focal plane and should therefore not be illuminated. However, the light scattered by the first object scatters the illumination beam so that the central object is illuminated.

the irradiance of objects in the focal plane is decreased and more out-off-focus objects are illuminated.

Approaches to remove background blur and to increase image contrast include structured illumination by [Keller et al., 2010, Breuninger et al., 2007] and variations thereof by [Kalchmair et al., 2010, Mertz and Kim, 2011]. Larger objects can be observed with higher quality for two-sided illumination [Dodt et al., 2007, Huisken and Stainier, 2007]. The visibility of the stripe-shaped artifacts can be reduced by blurring them using illumination by a light-sheet that is quickly tilted around the detection axis during the image acquisition time [Huisken and Stainier, 2007].

1.2.3 Self-Reconstructing Beams

Beams that regain their initial transverse irradiance profile behind a perturbation were termed self-reconstructing beams. The perturbation of the beam's field can be caused by an obstacle that scatters (locally shifts the phase) or absorbs (locally reduces the amplitude) of the light. The most prominent self-reconstructing beam is the Bessel beam. Bessel beams are also non-diffracting in free space

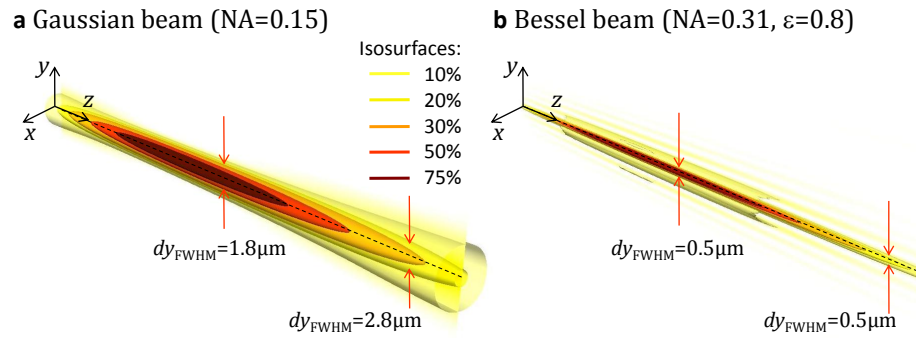


Figure 1.4: Iso-surface plot of a Gaussian and a Bessel beam.

The figure shows iso-surfaces from 10% to 75% of the beam's peak irradiance for (a) a Gaussian beam ($NA = 0.15$) and (b) a Bessel beam ($NA = 0.31$, $\epsilon = 0.8$). The beam parameters were chosen in order to achieve equal depth of field of $dz \approx 50\mu\text{m}$ for both beam types.

[Durnin et al., 1987]. The angular spectrum of non-diffracting beams is so narrow that the plane waves forming the beam do not run significantly out of phase along the propagation direction. This effect leads to a change of the transverse profile of beams with a broad angular spectrum, as e.g. Gaussian beams that spread significantly while propagating in free space. Because the transverse profile of non-diffracting beams does not change along the propagation axis they are also referred to as propagation-invariant beams.

Beams with a radial irradiance profile that can be described by Bessel functions were first described by Kelly [1960]. The central lobe of a so-called Bessel beam is much narrower than the waist of a Gaussian beam with equal depth of field (Fig. 1.4). However, this lobe is surrounded by a system of equidistant rings. While the amplitude of the field in the rings decays quickly for larger radii, the energy content within the rings does not. Therefore, the rings contain a large proportion of the beam's total energy.

Bessel beams can be created by coherent illumination of annular apertures [Sheppard and Wilson, 1979] or axicons [Lit and Tremblay, 1973, Welford, 1960], i.e. transmitting or reflecting optical elements with a conical shape [McLeod, 1954, Fujiwara, 1962]. Bessel beams can also be generated by computer holograms using spatial light modulators [Vasara et al., 1989, Davis et al., 1993], i.e. devices that allow to spatially control phase and amplitude of the incident light.

Annular apertures and (binary Fresnel) axicons have been used in linear [Sheppard and Wilson, 1979, Gu and Sheppard, 1991, 1992] and nonlinear [Botcherby et al., 2006, Hell et al., 1995] confocal microscope setups to enhance the depth of field to accelerate imaging of 3D samples at the cost of a reduction of the axial resolution [Botcherby et al., 2008]. Furthermore, an annular aperture placed in the illumination path of a confocal microscope improves image contrast for a structure located behind a scattering layer [Gu et al., 1996].

Simple experiments demonstrated how a Bessel beam is able to recover its initial intensity profile behind an obstruction [Bouchal et al., 1998, Bouchal, 2002]. However, the obstacle was constituted by a single, isolated absorbing disk, much smaller than the beam's cross-section [Anguiano-Morales et al., 2007b]. These experiments were repeated with similar results for other non-diffracting continuous wave and pulsed beams by Anguiano-Morales et al. [2007a] and Dubietis et al. [2004], Chong et al. [2010], respectively. The self-reconstruction ability was exploited when the optical forces exerted by a Bessel beam were

used to simultaneously manipulate several particles in different planes along the propagation axis and behind a layer of particles [Garcés-Chávez et al., 2002]. This groundbreaking study demonstrated the potential of self-reconstructing beams for future applications in nano- or biotechnology. However, the interaction of the beam with the medium and the profile of the perturbed beam were neither visualized nor analyzed in detail. The beam profile behind an extended turbid medium was shown for a vortex beam [Tao and Yuan, 2004] and an airy beam [Broky et al., 2008], i.e. a propagation-invariant beam that is created by a cubic phase mask [Bradburn et al., 1997]. The behavior of self-reconstructing beams in more complex or even biological material has not been explored yet.

1.3 CONCEPT OF THE INVESTIGATIONS

Some fundamental concepts of the investigations for this thesis are briefly outlined in the following.

1. Quantitative analysis and reduction in data:

In all cases, the analysis was performed as quantitative as possible. The goal was to analyze the property of interest and describe it quantitatively with a minimum of figures. For example, the optimum would be to describe an essential image property such as the strength of artifacts in an image by only one number. Of course, more figures are needed to analyze dependencies. For example an interesting property is the strength of artifacts in dependence of the propagation distance of the illumination beam through the sample.

2. Use of well-defined samples:

The use of well-defined samples with known scattering properties is the foundation of many measurements performed in this thesis. First, small spheres allow the experimental measurement of the point-spread function of the microscope at their respective positions. Second, using artificial phantoms composed of spheres allows to exert a great amount of control over the properties of the sample. The overall scattering strength can be tuned by the volume density of the spheres in the medium. The scattering properties like the anisotropy can be steered by the diameter of the spheres. Scatterers can be either silica (Si) and polystyrene (PS) spheres. Silica spheres have a refractive index of $n \approx 1.41$ which is close to that of some features in biological tissue. The refractive index of PS spheres is much higher ($n \approx 1.59$) making PS-spheres stronger scatterers than Si-spheres of the same size. PS spheres are advantageous because they can be stained with fluorescent dye. The use of artificial samples offers another advantage: In many cases, the distribution of the spheres and hence of the refractive index of the sample is easily extractable from the images and allows the comparison of experimental results to theory and numerical simulations.

3. Direct comparison of different imaging methods on the same sample:

The different illumination and detection techniques that are directly compared using the same sample, i.e. equal refractive index distributions $n(\mathbf{r}) = n_0 + \delta n(\mathbf{r})$. The precondition for a meaningful and significant comparison of different illumination and detection techniques is that only one parameter is varied and all other parameters are fixed. For example,

all comparisons between different illumination beams are performed for an equal depth of field. Also, all images are made with beam powers that deliver comparable strength of the (fluorescence) signal to make equal use of the dynamic range of the camera. At the same time it was always made sure that aspects like the sequence in which the sample was imaged with different beams did not significantly influence the measurement, e.g. by bleaching of the sample fluorescence or drift.

4. Staining:

One of the most important contributions to image quality is sample staining. In the context of this thesis, staining was used to visualize and analyze different aspects.

The following two types of staining were used for different experiments. On the one hand, by using unstained objects in a stained medium it is possible to visualize their effect on the illumination beams. A homogeneously stained sample allows to precisely detect the profile of a static illumination beam or inhomogeneities in the light-sheet induced by the sample. This analysis is not possible in most biological samples where the marking is sparse, irregular and unknown.

On the other hand, small stained probes allow the measurement of the microscopes point-spread function (PSF). Knowledge of the PSF allows to infer many important properties of the microscope like resolution and optical sectioning. The following chapter covers this topic in more detail.

5. Computer simulations:

As complement to the measurements performed, computer simulations were used for two main aspects. First, for preliminary tests like the usefulness of the confocal-line detection method. Second, to investigate situations that could not be addressed otherwise. For example in a simulation it is possible to account for the effect of scattering on the image quality of the same object distribution simply by changing the refractive index, which would be impossible or very impracticable in an experiment.

In this chapter, which is divided in two parts, the light-sheet microscope is presented. The first part describes the microscope's image formation process (§ 2.1) and its image quality parameters like resolution, optical sectioning (§ 2.2) using mathematical formalism. Important terms used through this thesis are explained as e.g. the system point-spread function. A quantitative measure for image artifacts is also introduced (§ 2.2.5). The second part (§ 2.3) presents the experimental setup and its optomechanical components. The chapter closes by a discussion of the advantages and disadvantages as well as particular the strengths and weaknesses of the microscopy setup that was built to perform the experiments presented in this thesis (§ 2.4).

2.1 DESCRIPTION OF THE IMAGE FORMATION

Incoherent imaging of an object represented by the fluorophore distribution $c(x, y, z)$ can be described by

$$p(\mathbf{r}) = (h_{\text{ill}}(\mathbf{r} - \mathbf{r}_{0,\text{ill}}) \cdot c(\mathbf{r})) * h_{\text{det}}(\mathbf{r}) \quad (2.1)$$

where $*$ denotes a convolution, $h_{\text{ill}}(x, y, z)$ is the point-spread-function (PSF) describing the irradiance of the illumination beam, $h_{\text{det}}(x, y, z)$ is the detection objective's PSF. An illustration is shown in Figure 2.1.

The illumination PSF is displaced by $\mathbf{r}_{0,\text{ill}}$ relative to the origin of the coordinate system, where the object $c(\mathbf{r})$ is centered. In the following, it will be assumed that $r_{0,\text{ill}} = 0$. Equation 2.1 describes the image formation: the fluorophores are imaged with a relative weight determined by the illumination. It is therefore helpful to define the illuminated fluorophore distribution

$$c_{\text{ill}}(\mathbf{r}) = h_{\text{ill}}(\mathbf{r}) \cdot c(\mathbf{r}) \quad (2.2)$$

as it constitutes the object that is effectively imaged. The convolution with h_{det} yields a 3D image

$$p(\mathbf{r}) = c_{\text{ill}}(\mathbf{r}) * h_{\text{det}}(\mathbf{r}) \quad (2.3)$$

of *all* illuminated fluorophores. Note that whereas h_{ill} represents an irradiance in units W/m^2 , h_{det} is unit-less and describes the three-dimensional detection probability distribution, i.e. the spatial distribution of the origin of light that is detected at a single point in the image plane.

In wide-field imaging, a sensor (typically a CCD or sCMOS) records a 2D-image

$$p(x, y = y_i, z) = (c_{\text{ill}}(x, y, z) * h_{\text{det}}(x, y, z))|_{y=y_i} \quad (2.4)$$

of a xz -plane at an axial position $y = y_i$ that corresponds to the sensor's y -location. The 3D-image is obtained by subsequent imaging of all planes y_i . Wide-

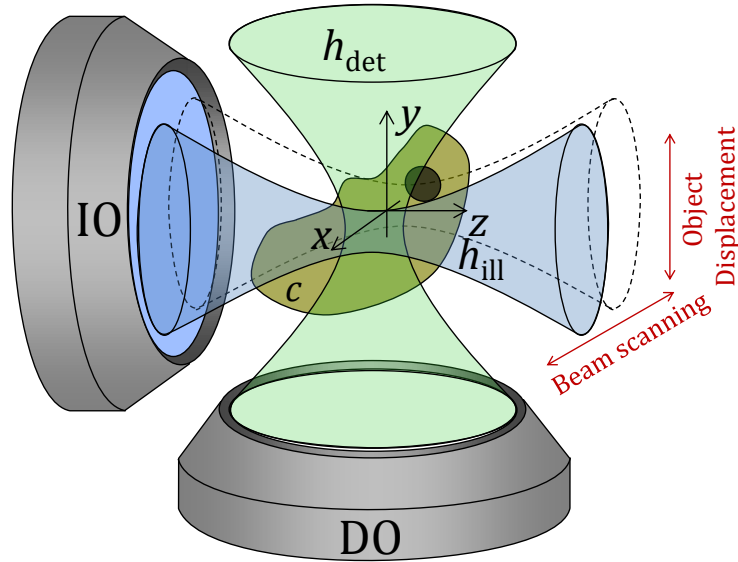


Figure 2.1: Sketch of the light-sheet microscope.

The illumination objective (IO) launches the illumination beam with irradiance $h_{\text{ill}}(x, y, z)$ from the left. The beam can be scanned along the x -axis, to excite the fluorophore distribution c of the sample only within a thin slice around the focal plane of a the detection objective lens (DO) with point-spread function given by $h_{\text{det}}(x, y, z)$. Images of the entire sample can be acquired by moving it along the y -axis.

field imaging offers no possibility to discriminate against parts of $c_{\text{ill}}(x, y, z)$ along the detection axis. The lack of *sectioning* poses several problems: First, all objects within the depth of focus are imaged. It is therefore impossible to obtain information on their y -location. Second, those parts of $c_{\text{ill}}(\mathbf{r})$ that are not in the plane of focus are blurred proportionally to the distance of the plane of focus $|y - y_{0,\text{det}}|$ and NA of the detection lens NA_{det} .

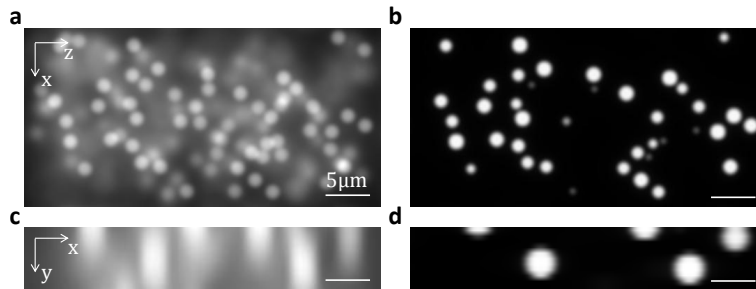


Figure 2.2: Images of fluorescent spheres for an epi-fluorescence and a light-sheet microscope.

The left column (a,c) shows the epi-fluorescence image that results from $h_{\text{ill}}(\mathbf{r}) = \text{const}$. The lack of optical sectioning results in a strong background and poor contrast. In the xy -slice (b) one can clearly see the poor confinement along the detection y -axis. In the case where the sample is illuminated by a thin homogeneous sheet of light $h_{\text{ill}}(\mathbf{r}) = \delta^{(3)}(y)$, as shown on the right side (b,d), the situation is strongly improved. The resolution is isotropic as can be seen from circular images of the spheres in the yz -image (d).

However, when the sample is illuminated only in an infinitely thin layer, the illuminated object distribution becomes

$$\begin{aligned} c_{\text{ill}}(\mathbf{r}) &= \delta^{(3)}(\mathbf{y} - \mathbf{y}_i) \cdot c(\mathbf{r}) \\ &= c(x, y_i, z) \end{aligned} \quad (2.5)$$

where $\delta^{(3)}$ is the three-dimensional delta-distribution. The resulting images can be described by

$$p_{\text{OS}}(x, y = y_i, z) = c_{\text{ill}}(x, y_i, z) * h_{\text{det}}(x, z), \quad (2.6)$$

where the convolution is only carried out in the xz -plane. In this case, the lack of discrimination on the detection side is no longer relevant.

The slicing of the object by optical means, leaving the object intact, is termed *optical sectioning* (OS). One possible realization of optical sectioning is to illuminate the sample from the side. Technically, a light-sheet in the xz -plane is obtained by illuminating the sample orthogonally to the detection optical y -axis, which can be achieved by a system with an optical axis lying the xz -plane. In this work, the illumination axis will be referred to as the z -axis. Figure 2.2 illustrates the effect of optical sectioning by showing image slices for bright-field imaging (no optical sectioning) and for illumination by a thin light-sheet (ideal optical sectioning).

In the ideal case the illuminated slice c_{ill} is infinitely thin and not affected by the sample. However, in reality, the thickness is limited by diffraction of the illumination beam that leads to a trade-off between the light-sheet's extensions along the detection and illumination axis. Moreover, it is scattered and absorbed by the sample. These effects were sketched in Figure 1.3. The ideal illumination must therefore not only exhibit a small extent along the detection optical axis but ideally robust to perturbation by the sample. Possible illumination schemes will be discussed in the following chapter where special emphasis will be put on the holographic generation of illumination beams.

2.2 DEFINITION OF IMAGE QUALITY PARAMETERS

As outline above, the strength of the light-sheet microscope lies in the plane-wise illumination of the sample. To quantify the gain achieved thereby, two main factors, namely axial resolution and optical sectioning capability are of special interest. Both can be assessed using the System-PSF h_{sys} . In the following, the System-PSF will be presented and its suitability for assessing light-sheet microscopes will be demonstrated. Then, the terms resolution and optical sectioning are explained using the system-PSF. The section closes by the introduction of measures for two other image quality parameters: the signal-to-background ratio and the strength of artifacts.

2.2.1 The System-Point-Spread-Function

In a point-scanning system, the illumination and detection objective remain fixed relative to each while the object is scanned relative to the detection and illumination point-spread functions h_{det} and h_{ill} , respectively. In a confocal microscope a detector behind a pinhole that is placed at a position corresponding

to $\mathbf{r}_{0,\text{det}}$ records the image intensity point-by-point for the illumination centered at $\mathbf{r}_{0,\text{ill}}$ with $\mathbf{r}_{0,\text{ill}} = \mathbf{r}_{0,\text{det}}$. The final image is then given by

$$p(\mathbf{r}) = (h_{\text{ill}}(\mathbf{r} - \mathbf{r}_{0,\text{ill}}) \cdot h_{\text{det}}(\mathbf{r} - \mathbf{r}_{0,\text{det}})) * c(\mathbf{r}) \quad (2.7)$$

where it is convenient to define a point-spread-function of the system

$$h_{\text{sys}}(\mathbf{r}; \mathbf{r}_{0,\text{ill}}, \mathbf{r}_{0,\text{det}}) = h_{\text{ill}}(\mathbf{r} - \mathbf{r}_{0,\text{ill}}) \cdot h_{\text{det}}(\mathbf{r} - \mathbf{r}_{0,\text{det}}). \quad (2.8)$$

In principle, h_{sys} corresponds to the image taken with a conventional microscope when $c(\mathbf{r}) = \delta^{(3)}(\mathbf{r})$. The system-point-spread-function is equal for each point of the image if the offset between illumination and detection is held constant: $\mathbf{r}_{0,\text{ill}} - \mathbf{r}_{0,\text{det}} = \text{const}$. For simplicity, the offsets $\mathbf{r}_{0,\text{ill}}$ and $\mathbf{r}_{0,\text{det}}$ of the illumination and detection point-spread function, respectively, will be set to zero for most of the further analysis. The only exception is Section 7.2.6, where the property of $\mathbf{r}_{0,\text{ill}}$ and $\mathbf{r}_{0,\text{det}}$ to account for misalignments of the system is used. Also, interesting applications may arise from well-defined offsets $\mathbf{r}_{0,\text{ill}} - \mathbf{r}_{0,\text{det}}$ between illumination and detection.

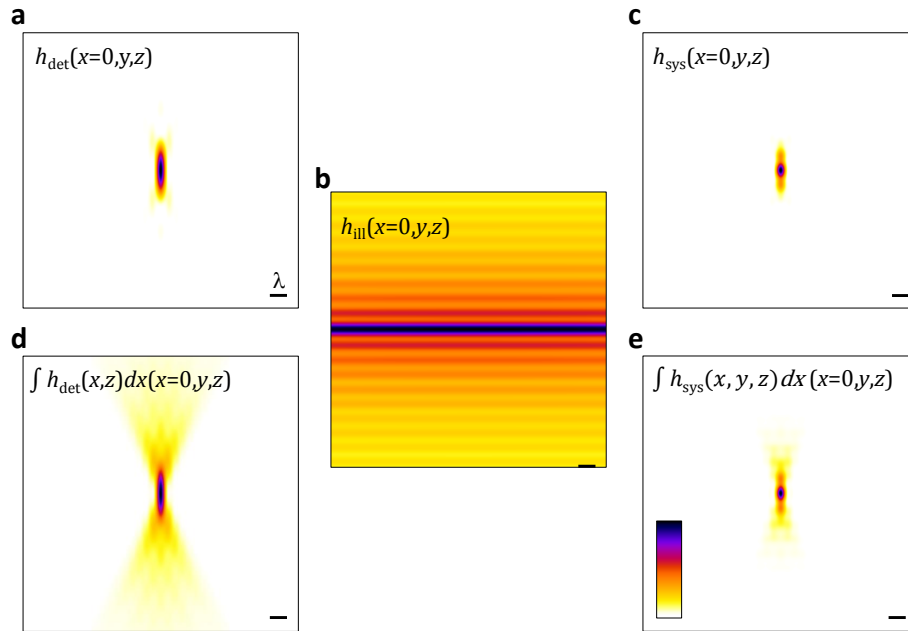


Figure 2.3: The point-spread function of a light-sheet microscope with scanned Bessel beam illumination.

The system point-spread-function (PSF) is the product of the detection PSF h_{det} (a, d) and the illumination PSF h_{ill} (b). Slices through $x = 0$ are shown in the top row (a, c), projections along the x -axis in the bottom row (d, e). The profile of the scanned illumination beam $h_{\text{ill}}(y, z)$ is independent of x . The length of the scale bar corresponds to the wavelength λ .

$h_{\text{sys}}(\mathbf{r})$ depends on the illumination as well as the detection. An illustration is shown in Fig. 2.3. Therefore, it fully describes the optical properties of the imaging system (for a point-detector) and in contrast to eqn 2.1 one can directly use it to assess the optical properties of the system as e.g. resolution and optical sectioning capabilities. Because of these advantages it would be very helpful if it could also be used to assess the (wide-field) light-sheet microscope. In fact, this is possible. This fact can be understood if each pixel of the camera corresponding to position $(x_{0,\text{det}}, z_{0,\text{det}})$ in a plane $y_{0,\text{det}}$ is seen to work as the

pinhole of a confocal point-scanning microscope. Eqn 2.1 and eqn 2.7 yield the same value for a single point of the detector, the image of the confocal spot $\mathbf{r} = (0, 0, 0)$, regardless of the shape of h_{ill} and h_{det} . The statement

$$p_{\text{WF}}(0, 0, 0) = p_{\text{PS}}(0, 0, 0) \quad (2.9)$$

holds due to

$$\begin{aligned} p_{\text{WF}}(\mathbf{r}) &= (h_{\text{ill}}(\mathbf{r}) \cdot c(\mathbf{r})) * h_{\text{det}}(\mathbf{r}) \quad (2.10) \\ &= \iiint h_{\text{ill}}(\mathbf{r}') \cdot c(\mathbf{r}') \cdot h_{\text{det}}(\mathbf{r} - \mathbf{r}') d\mathbf{r}' \end{aligned}$$

$$p_{\text{WF}}(0, 0, 0) = \iiint h_{\text{ill}}(\mathbf{r}') \cdot c(\mathbf{r}') \cdot h_{\text{det}}(-\mathbf{r}') d\mathbf{r}' \quad (2.11)$$

and

$$\begin{aligned} p_{\text{PS}}(\mathbf{r}) &= (h_{\text{ill}}(\mathbf{r}) \cdot h_{\text{det}}(\mathbf{r})) * c(\mathbf{r}) \quad (2.12) \\ &= \iiint h_{\text{ill}}(\mathbf{r}') \cdot h_{\text{det}}(\mathbf{r}') \cdot c(\mathbf{r} - \mathbf{r}') d\mathbf{r}' \end{aligned}$$

$$p_{\text{PS}}(0, 0, 0) = \iiint h_{\text{ill}}(\mathbf{r}') \cdot h_{\text{det}}(\mathbf{r}') \cdot c(-\mathbf{r}') d\mathbf{r}'. \quad (2.13)$$

The system point-spread-function can therefore also be used to assess the light-sheet microscope as done by [Engelbrecht and Stelzer \[2006\]](#). This conclusion can be easily derived. The wide-field image of a single plane is given by

$$\begin{aligned} p_{\text{WF}}(x, 0, z) &= \iiint h_{\text{ill}}(\mathbf{r}') \cdot c(\mathbf{r}') \cdot h_{\text{det}}(\mathbf{r} - \mathbf{r}') d\mathbf{r}' \delta^{(3)}(\mathbf{y}) d\mathbf{y} \\ &= \iiint h_{\text{ill}}(x', y', z') \cdot c(x', y', z') \\ &\quad \cdot h_{\text{det}}(x - x', -y', z - z') d\mathbf{r}' \quad (2.14) \end{aligned}$$

Using the commutative property of the convolution and $\mathbf{r}'' = \mathbf{r} - \mathbf{r}'$ the point-scanning image reads

$$p_{\text{PS}}(\mathbf{r}) = \iiint c(\mathbf{r}'') \cdot h_{\text{ill}}(\mathbf{r} - \mathbf{r}'') \cdot h_{\text{det}}(\mathbf{r} - \mathbf{r}'') d\mathbf{r}'' \quad (2.15)$$

Note that the negative factor arising from $d\mathbf{r}'/d\mathbf{r}'' = -1$ is compensated by reversal of the infinite integration ranges. The point-scanned image of a plane can be written as

$$\begin{aligned} p_{\text{PS}}(x, 0, z) &= \iiint h_{\text{ill}}(\mathbf{r}') \cdot h_{\text{det}}(\mathbf{r}') \cdot c(\mathbf{r} - \mathbf{r}') d\mathbf{r}' \delta^{(3)}(\mathbf{y}) d\mathbf{y} \\ &= \iiint h_{\text{ill}}(\mathbf{r} - \mathbf{r}'') \cdot h_{\text{det}}(\mathbf{r} - \mathbf{r}'') \cdot c(\mathbf{r}'') d\mathbf{r}'' \delta^{(3)}(\mathbf{y}) d\mathbf{y} \\ &= \iiint h_{\text{ill}}(x - x'', -y'', z - z'') \cdot c(x'', y'', z'') \\ &\quad \cdot h_{\text{det}}(x - x'', -y'', z - z'') d\mathbf{r}'' \quad (2.16) \end{aligned}$$

It follows that $p_{\text{WS}}(x, 0, z) = p_{\text{PS}}(x, 0, z)$ if the requirement that h_{ill} is independent of x and z is fulfilled and $h_{\text{ill}}(x, y, z) = h_{\text{ill}}(x, -y, z)$. Note that this is the case for ideal light-sheets, for homogeneous illumination and for infinitely thin plane illumination. The special case of $p_{\text{WS}}(0, 0, z) = p_{\text{PS}}(0, 0, z)$ is illustrated in Fig. 2.4 for sample illumination by a static Bessel beam, which is propagation invariant

along the propagation axis. Therefore, the system-point-spread-function is independent from the z -coordinate. This finding is important for the confocal-line detection technique that will be presented in detail in Section 6.

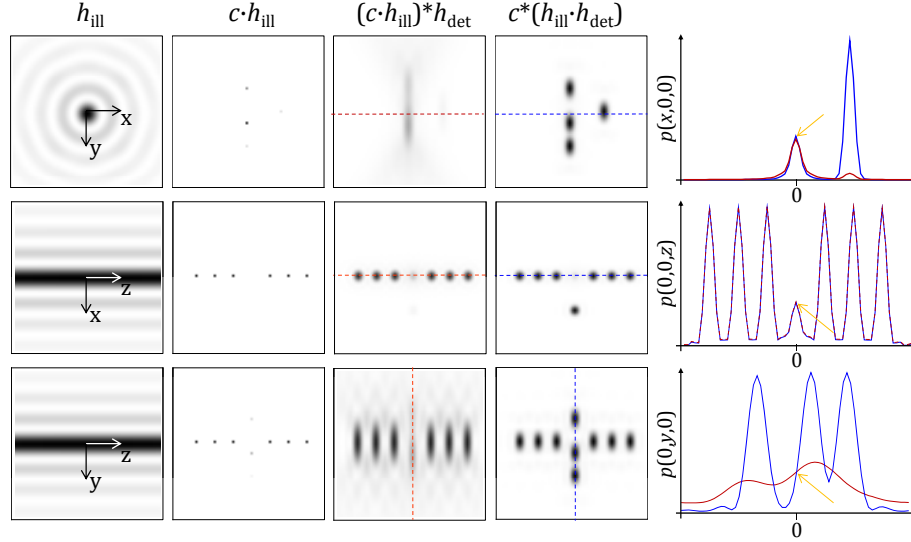


Figure 2.4: Comparison of the image formation for wide-field and confocal point detection.

The figure shows slices through the illumination h_{ill} in the left column. The illuminated object distribution $c \cdot h_{\text{ill}}$ is shown to the right. The next column shows the image obtained using the general image formation formula $(c \cdot h_{\text{ill}}) * h_{\text{det}}$, next to the result for confocal point scanning using $c * (h_{\text{ill}} \cdot h_{\text{det}})$. The right-most column shows line-profiles along the x , y , and z -axis, respectively as indicated by dashed lines of the same color in the corresponding images to the left. It can be seen that the two image formation descriptions yield the same result in the origin. Moreover, due to the invariance of h_{ill} along z , the results are also equal on the z -axis, i.e. for $x = y = 0$.

Note that in a light-sheet microscope a slightly different h_{sys} results for different positions along the illumination axis. While the detection PSF h_{det} is ideally independent of the position in the sample $(x_{0,\text{det}}, z_{0,\text{det}})$, the illumination beam h_{ill} changes along the illumination z -axis due to diffraction. For an ideal light-sheet (that is independent from z), the illumination PSF is independent of x & z , too.

2.2.2 Resolution

As briefly outlined in Section 1.2.1, resolution is a measure for the system's ability to transfer high spatial frequencies, i.e. to image small structures in vicinity to each other separately. More precisely, it is common to define resolution as the smallest distance between two points that allows them to be distinguished. The image of a point is determined by the system point-spread-function h_{sys} (§2.2.1). The values used in this work to characterize resolution are the $1/e$ -widths of the PSF, Δx and Δz laterally and Δy along the detection axis. The perpendicular arrangement of detection and illumination axis leaves the lateral resolution of the microscope unchanged in the case of conventional light-sheet microscopy. However, the axial resolution is strongly influenced and is determined by the illumination beam as well as the detection objective lens. The FWHM values

of the PSF can be determined from experimental and numerical data with high accuracy and robustness to background. The resolution can be extracted from the images of point-like objects by fitting the functions

$$h_{\text{sys}}(x, 0, z) \approx \exp \left\{ - (x^2 + z^2) / \Delta r^2 \right\} \quad (2.17)$$

$$h_{\text{sys}}(0, y, 0) \approx \exp \left\{ -y^2 / \Delta y^2 \right\} \quad (2.18)$$

where $\Delta r^2 = \Delta x^2 + \Delta y^2$ to lateral and axial profiles. This measure for resolution according to the *Rayleigh criterion* is well suited to assess a system's performance in sparse media like filaments, as it yields values for the typical size of objects that can be resolved. However, it does not account for the potentially large out-of-focus contributions to $h_{\text{sys}}(x, y, z)$ for $x, y, z \neq 0$, i.e. background. Also, the width of a profile might be a misleading measure for resolution if it is not monotonously decaying, but features side-lobes. For such profiles, e.g. those resulting for Bessel beam illumination in light-sheet microscopy, the approximation by a Gaussian function does not hold. In these cases the width of the profile can be measured directly, but one has to carefully consider the validity of the result, i.e. if the non-monotonous decay of the profile affects the separability of two adjacent points. This issue will be further discussed in the respective sections.

2.2.3 Optical Sectioning

The optical sectioning performance concerns the detection of background. Especially when imaging extended three-dimensional samples it is important to be able to discriminate against out-of-focus contributions. Otherwise the sharp image of the focal plane is overlaid by blurred images of out-of-focus layers. Resolution, as discussed in the previous section, is not the adequate measure to assess the ability of an imaging system to obtain background-free images of large samples. It is more appropriate to analyze which y -planes contribute to the total fluorescence signal detected at a single point. The integral

$$F(y) = \iint h_{\text{sys}}(x, y, z) dx dz. \quad (2.19)$$

gives the amount of signal detected from the plane y . $F_{\text{tot}} = \int F(y) dy$ is the total signal. It is useful to define

$$G(y) = \frac{1}{F_{\text{tot}}} \int_0^y F(y') dy' \quad (2.20)$$

which gives the contribution to the detected signal that arises from the volume in-between the focal plane ($y = 0$) and plane y . An illustration is shown in Figure 2.5.

For better optical sectioning (OS) capabilities of the imaging system $F(y)$ becomes narrower and $G(y)$ steeper. Ideally, $F(y)$ is only non-zero for the focal plane ($y = 0$). $F_{\text{int}}(y)$ is then given by $G(y) = \Theta(y) - 1/2$ where $\Theta(y)$ is the Heaviside step function.

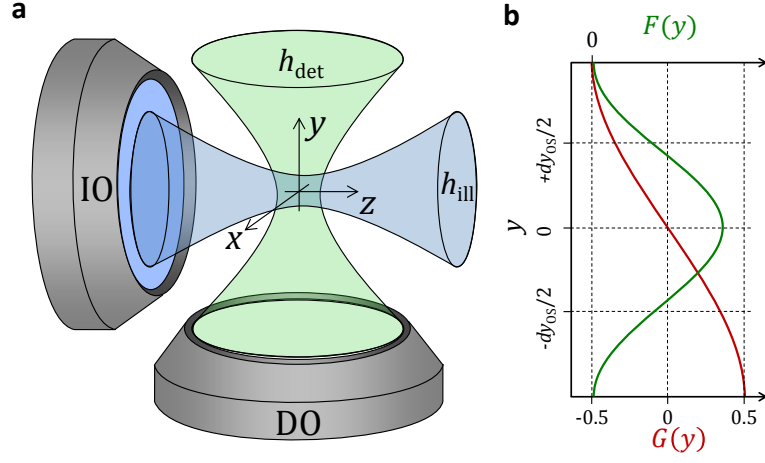


Figure 2.5: Illustration of optical sectioning.

a) The system point-spread function $h_{\text{sys}}(\mathbf{r}) = h_{\text{ill}}(\mathbf{r}) \cdot h_{\text{det}}(\mathbf{r})$ is integrated along the x and the z axis to give the total contribution $F(y)$ of the y -planes to the total detected fluorescence signal. b) The graph shows an example of $F(y)$ and the integral along y , $G(y)$, for a Gaussian illumination beam (see also eqn. 2.19 and 2.20).

In the context of this thesis, optical sectioning means the thickness dy_{OS} of the layer out of which $1 - 1/e = 63\%$ of the total signal F_{tot} is detected. dy_{OS} is defined by

$$G(dy_{\text{OS}}/2) - G(-dy_{\text{OS}}/2) = 63\%. \quad (2.21)$$

If $F(y)$ is symmetrical with respect to $y = 0$, this equation simplifies to $G(dy_{\text{OS}}/2) = 31.5\%$. Note that

$$G(dy_{\text{OS}}/2) - G(-dy_{\text{OS}}/2) = \int_{-dy_{\text{OS}}/2}^{dy_{\text{OS}}/2} F(y) dy / F_{\text{tot}}. \quad (2.22)$$

In contrast to $F(y)$, the measure $G(y)$ yields reliable results even when h_{sys} is non-monotonously decaying along the y -axis, as is the case for illumination by Bessel beams, for example.

2.2.4 Signal-to-background

Image contrast and optical sectioning can be measured indirectly by performing a spatial frequency analysis. The spatial spectrum of the image is given by the Fourier Transform of the image $\tilde{p}(k_x, k_y, y) = \mathcal{FT}_{x,y} \{p(x, y, z)\}$. The image of objects in the focal plane is sharp. Objects in the focal plane therefore contribute high-frequency components to the spatial frequency spectrum of an image. In contrast, structures of the same size contribute low spatial frequency components if they are not situated in the focal plane. Therefore, the low-frequency content of the image

$$\text{LSF}(y) = \iint_{k_x^2 + k_y^2 \leq k_F^2} \tilde{p}(k_x, k_y, y) dk_x dk_y \quad (2.23)$$

mainly originates from background. The relevant information from the focal plane resides in the high frequency part of the spectrum

$$\text{HSF}(y) = \iint_{k_x^2 + k_y^2 > k_F^2} \tilde{p}(k_x, k_y, y) dk_x dk_y. \quad (2.24)$$

By computing

$$\text{SBR}(y) = \text{HSF}(y) / \text{LSF}(y) \quad (2.25)$$

one obtains a measure for the signal-to-background ratio of the image.

Absolute values are of course highly dependent on the sample and the choice of the corner frequency k_F . The effect of k_F can be validated by visually checking the high- and the low-pass filtered images. Low-frequency features within the sample falsely contribute to the background in this measure. However, there are two reasons why this does not affect the validity of the measure when images of the same object are compared. First, in the optimum case, the staining is very sparse and therefore necessarily in the high-frequency range. Second, when images of the same object are directly compared, the contribution of low frequencies in the image that arise from real structural information has to be equal. In this case the SBR measure is offset. This behavior has been taken into account when the quotient of the SBR-values of two images is taken.

The spatial-frequency analysis method is simple and flexible and the relative results strongly support the visual impression to a well-trained observer. A similar measure has also been used to assess relevant image information, i.e. the signal within a relevant spatial frequency range, especially along the detection optical axis [Truong et al., 2011]. However, there exist drawbacks to the method. One is the inability to account for artifacts - if they are strongly localized they may contribute to *good* HSF. Another limitation of this measure is that the relation between high and low spatial frequencies does not account for lower overall signal strength. Dark regions of the image have only small impact on the SBR as HSF and LSF contributions are mainly determined by the bright parts of the image. If images are compared that are not equally bright, the SBR may be unreliable. This problem is especially pronounced for confocal-line detection light-sheet microscopy images where background is suppressed already by the detection process. Therefore, this problem will be discussed in detail in Section 6.7.3.

2.2.5 Image Artifacts

The aim of this section is to show that the contribution of the artifacts to the total image contrast can be measured separately and used to quantify the strength of image artifacts. Therefore, it is necessary to extract the scattered intensity, i.e. the ghost image and the ideal image from real image of a scattering medium. The contrast of the images is then measured by computation of the standard deviation of the normalized image intensity values.

2.2.5.1 Extraction of Artifacts from Real Images

As mentioned above, in a light-sheet microscope ideal illumination consists in a homogeneous plane of light. However, in reality, illumination is a result of

the superposition of the field of the ideal unscattered illumination beam and the field of the light scattered by the object. The real irradiance is therefore

$$\begin{aligned}
 h_{\text{ill}}(\mathbf{r}) &= |E_{\text{tot}}(\mathbf{r})|^2 \\
 &= |E_{\text{holo}}(\mathbf{r}) + E_{\text{sca}}(\mathbf{r})|^2 \\
 &= |E_{\text{holo}}(\mathbf{r})|^2 + |E_{\text{sca}}(\mathbf{r})|^2 + 2\text{Re}\{E_{\text{holo}}^*(\mathbf{r}) \cdot E_{\text{sca}}(\mathbf{r})\} \\
 &= h_{\text{holo}}(\mathbf{r}) + h_{\text{sca}}(\mathbf{r})
 \end{aligned} \tag{2.26}$$

where E_{holo} and E_{sca} are the unscattered and scattered field, respectively, and

$$h_{\text{holo}} = |E_{\text{holo}}(\mathbf{r})|^2 \tag{2.27}$$

and

$$h_{\text{sca}}(\mathbf{r}) = |E_{\text{sca}}(\mathbf{r})|^2 + 2\text{Re}\{E_{\text{holo}}^*(\mathbf{r}) \cdot E_{\text{sca}}(\mathbf{r})\} \tag{2.28}$$

the corresponding irradiances (see also [Rohrbach, 2009, Fahrbach et al., 2010]). Both excite the fluorophore distribution $c(\mathbf{r})$ yielding a real 3D image that can

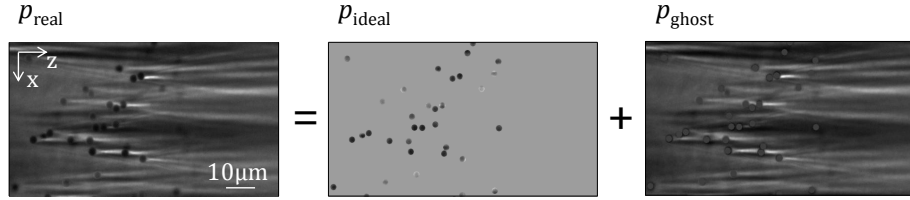


Figure 2.6: Image decomposition: Example

The real image shows a cluster of non-fluorescing spheres in a fluorescent environment that is illuminated along z by a Gaussian beam that is scanned in x -direction. It is decomposed into an ideal image that contains only the image of the spheres on a homogeneous background. The ghost image is the deviation of the real image from the homogeneous background. It exhibits strongly visible stripes that arise from the scattering of the illumination beam by the spheres.

be decomposed according to

$$\begin{aligned}
 p_{\text{real}}(\mathbf{r}) &= [(h_{\text{holo}}(\mathbf{r}) + h_{\text{sca}}(\mathbf{r})) \cdot c(\mathbf{r})] * h_{\text{det}}(\mathbf{r}) \\
 &= p_{\text{ideal}}(\mathbf{r}) + p_{\text{ghost}}(\mathbf{r})
 \end{aligned} \tag{2.29}$$

where the ideal image

$$p_{\text{ideal}} = [h_{\text{holo}}(\mathbf{r}) \cdot c(\mathbf{r})] * h_{\text{det}}(\mathbf{r}) \tag{2.30}$$

results from unscattered illumination. It is superposed by the ghost image

$$p_{\text{ghost}} = [h_{\text{sca}}(\mathbf{r}) \cdot c(\mathbf{r})] * h_{\text{det}}(\mathbf{r}) \tag{2.31}$$

created by scattered illumination (eqn 2.28). An example is shown in Figure 2.6. The ghost image describes the artifacts in the image that arise from the interaction of the illumination light with the sample. Note that it can also become negative due to the interference term.

For a known fluorescence distribution $c(\mathbf{r})$, e.g. in experiments with a distribution of spheres that can be inferred from the images or in computer simulations, the decomposition can be easily performed.

2.2.5.2 Measure for the Strength of Artifacts

Object and background should exhibit a large difference in signal strength. The ideal image should exhibit a large standard deviation of the image intensity values. In contrast, variations in the image intensity due to artifacts should be small. Therefore, the standard deviation of the ghost image should be as small as possible. The separation of the real image into an ideal and a ghost image (eqn 2.29) enables to analyze the contrast within these images separately. It will be shown in the following, that the lateral standard deviation of the image is given by

$$\hat{s}(z) = \sqrt{\hat{s}_{\text{ideal}}(z)^2 + \hat{s}_{\text{ghost}}(z)^2}. \quad (2.32)$$

Moreover, using the separation into ideal and ghost image contrast, one can quantify the quality of an image by the ratio

$$Q = \frac{\int \hat{s}_{\text{ideal}}(z) dz}{\int \hat{s}_{\text{ghost}}(z) dz} \quad (2.33)$$

that gives the relative strength of artifacts in contrast to the ideal image contrast, similar to [Rohrbach, 2009].

Scattering of the illumination beam mainly leads to a redistribution of the energy in the image plane that is manifested by stripes parallel to the beam propagation z -axis. These can be assessed by the normalized lateral standard deviation of the image intensity

$$\begin{aligned} \hat{s}(z) &= \frac{s(z)}{\bar{p}_{\text{real}}(z)} \\ &= \frac{1}{\bar{p}_{\text{real}}(z)} \sqrt{\frac{1}{n_x - 1} \sum_{i=1}^{n_x} (\bar{p}_{\text{real}}(z) - p_{\text{real}}(x_i, z))^2} \end{aligned} \quad (2.34)$$

where the counter $i = 0 \dots n_x$ denotes the lateral pixel number, and $\bar{p}(z)$ is the mean value of $p(x, z)$ along x . For simplicity, the normalized variance will be evaluated from here on. Inserting eqn 2.29 and sorting the product terms yields

$$\begin{aligned} \hat{s}(z)^2 &= \hat{s}_{\text{ideal}}(z)^2 + \hat{s}_{\text{ghost}}(z)^2 \\ &\quad - \left(\frac{2n_x}{n_x - 1} - 4 \right) (\bar{p}_{\text{ideal}}(z) \cdot \bar{p}_{\text{ghost}}(z)) \\ &\quad + \frac{2}{n_x - 1} \sum_{i=1}^{n_x} p_{\text{ideal}}(x_i, z) \cdot p_{\text{ghost}}(x_i, z) \end{aligned} \quad (2.35)$$

For large images, where $n_x \gg 1$ holds, it is valid to approximate

$$\frac{1}{n_x - 1} \sum_{i=1}^{n_x} p(x_i, z) \approx \frac{1}{n_x} \sum_{i=1}^{n_x} p(x_i, z) = \bar{p}(z) \quad (2.36)$$

and

$$\frac{2n_x}{n_x - 1} - 4 \approx 2. \quad (2.37)$$

To obtain eqn 2.32, the last terms of eqn 2.35 have to vanish so that

$$\begin{aligned} & -2 (\bar{p}_{\text{ideal}}(z) \cdot \bar{p}_{\text{ghost}}(z)) \\ & + \frac{2}{n_x - 1} \sum_{i=1}^{n_x} p_{\text{ideal}}(x_i, z) \cdot p_{\text{ghost}}(x_i, z) \approx 0 \end{aligned} \quad (2.38)$$

Since $\bar{p}_{\text{ideal}}(z) \approx 1$ holds for sparse object distributions, the first term can be approximated as

$$-2 (\bar{p}_{\text{ideal}}(z) \cdot \bar{p}_{\text{ghost}}(z)) \approx -2\bar{p}_{\text{ghost}}(z) \quad (2.39)$$

For the second term of eqn 2.38 one can assume that all summands $p_{\text{ideal}}(x_i, z) \neq 1$ result in $p_{\text{ghost}}(x_i, z) = 0$ if there is no ghost image intensity at the locations of the objects. The image intensity is then entirely attributed to the object. Therefore

$$\frac{2}{n_x - 1} \sum_{i=1}^{n_x} p_{\text{ideal}}(x_i, z) \cdot p_{\text{ghost}}(x_i, z) = \sum_{i=1}^{n_x} p_{\text{ghost}}(x_i, z) \quad (2.40)$$

$$\stackrel{n_x \gg 1}{\approx} 2\bar{p}_{\text{ghost}}(z), \quad (2.41)$$

which confirms the requirements of eqn 2.38 so that eqn 2.32 is valid. Experimental results that confirm the assumptions made here are shown in Figure 5.9.

2.3 DESCRIPTION OF THE SETUP

In the following sections, the experimental setup, shown in Figure 2.7, is described. The following paragraph gives an overview over the setup with references to subsections that contain more detailed information.

The right angle between illumination and detection optical paths makes light-sheet microscopy setups very different from most conventional microscopes. Therefore, most light-sheet microscopes are built as stand-alone devices from the start. However, for this thesis it was chosen to build a flexible add-on module to a conventional inverted microscope in order to be able to make use of its mechanical stability and the components like bright-field and epi-fluorescence illumination, sample positioning devices and detection optics. The add-on module for light-sheet illumination consists of two parts: The illumination optics and a device for sample mounting and positioning.

The illumination optics are presented in detail in section 2.3.1. A multi-line laser unit is used as light source (§ 2.3.1.1). The unique feature of the light-sheet microscope presented here is a holographic beam shaping device, i.e. a spatial light modulator (SLM) that allows sample illumination with custom phase-shaped beams (§ 2.3.1.2). To correct for intensity fluctuations of the illumination beam a feedback loop was implemented (§ 2.3.1.3). The illumination beam path is designed to enable illumination of the large sample requiring a large depth of field of the illumination beam. Therefore, the SLM must be imaged into the sample volume with an adequate magnification. Moreover, a

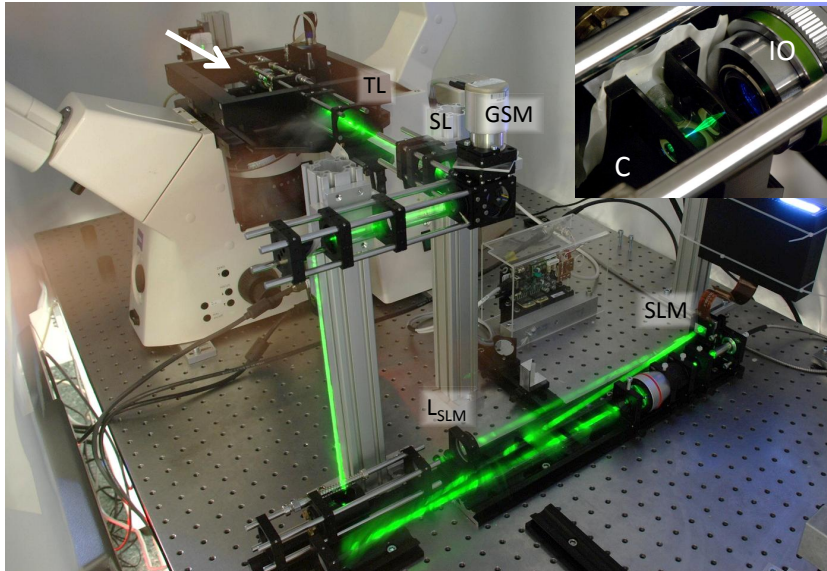


Figure 2.7: Photo of the setup.

The green laser beam is visualized on its way from the fiber through the beam expander onto the SLM and 4 lenses (L_{SLM} , SL, TL, IO), into the sample chamber (C). The viewpoint for the inset is indicated by an arrow.

telecentric lens system and a galvanometric scanning mirror are included so that light-sheets can be created by sweeping the beam in the focus plane of the DO (§ 2.3.1.4). The detection optical components are those of the inverted microscope. As a consequence of the perpendicular arrangement of detection and illumination optical axis the choice of high-NA detection lenses is strongly restricted. Therefore the setup features a long working distance illumination objective that puts only one restriction to the detection lens, i.e. to have a radius that is smaller than the working distance of the illumination lens (§ 2.3.1.5).

The perpendicular illumination also necessitates new techniques especially for sample mounting and positioning vis-à-vis to a common microscope that are presented in section 2.3.2. Of the many different possibilities to mount an object, the most established approach is to embed the object in a transparent gel cylinder (§ 2.3.2.1) that is mounted on a stage to control its position and angular orientation (§ 2.3.2.3).

The microscope and image acquisition is controlled by a PC using custom software written in Python (§ 2.3.3).

2.3.1 Optical Components

A sketch of the optics is shown in Fig. 2.8. The optical part of the add-on module consists of three parts: the light source (§ 2.3.1.1), the beam shaping optics (§ 2.3.1.2) and the sample illumination optics (§ 2.3.1.4). These are presented in detail below.

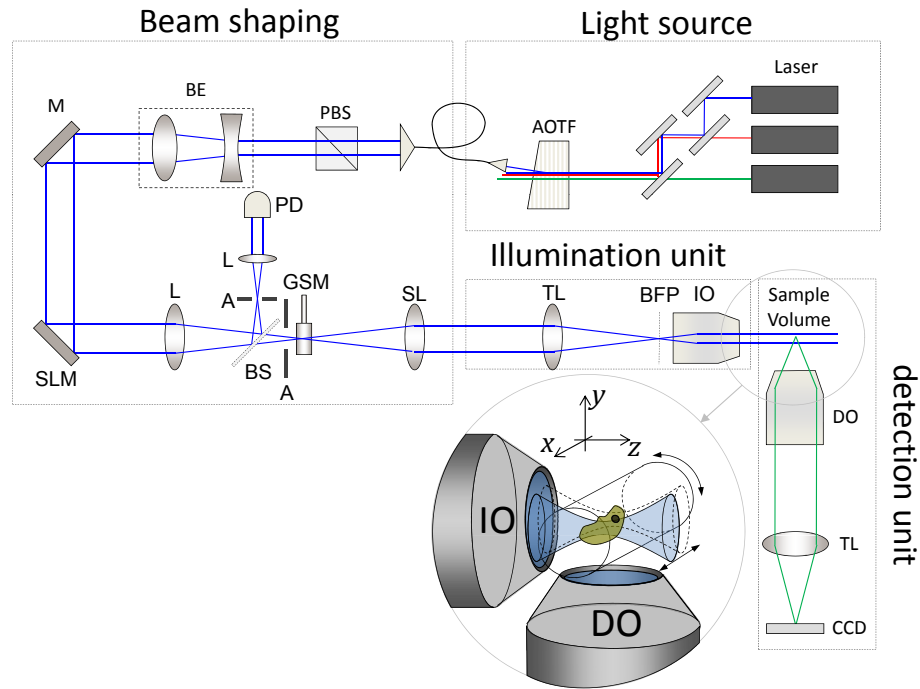


Figure 2.8: Sketch of the light-sheet illumination add-on.

Light from the light-source is polarized by a polarizing beam splitter (PBS), transmitted through a beam expander (BE) and guided onto the spatial light modulator (SLM) by a mirror (M). A lens (L) images the far-field diffraction pattern onto a galvanometric scanning mirror (GSM). A telecentric 4f-lens system made of a scan lens (SL) and the tube lens (TL) of the illumination objective lens (IO) translates the tilt angle of the mirror into a tilt angle of the beam in the back-focal plane (BFP) of the IO, which leads to a lateral beam displacement (along y) in the sample volume. The fluorescence excited by the illumination beam is collected by a detection lens (DO) and imaged onto a camera (CCD) by a tube lens (TL). In order to stabilize the laser power a small part of the illumination beam is deflected by a pellicle beam splitter and measured by a photo-diode (PD). Apertures (A) are used to block higher diffraction orders of the SLMs diffraction pattern.

2.3.1.1 Light Source

As light source a laser unit (Laser module LSM 510 - Release 3.2, Zeiss) is used. It consists of three gas lasers that are mounted on a massive block of marble. An Argon-Ion laser operates at $\lambda = 488\text{nm}$ with an output power of $P = 2.7\text{mW}$ and two Helium-Neon-Lasers provide light at 542nm and 633nm at output powers of $P = 1\text{mW}$ and $P = 10.4\text{mW}$, respectively. An acousto-optic tunable filter (AOTF) is used for selection of the laser and fast modulation of the beam power. A single-mode fiber transfers the light of the AOTF's first order to the beam-shaping unit situated on an optical table along with the microscope. The transmission efficiency is $T_{\text{AOTF+Fiber}} \approx 60\%$. Losses result from the diffraction efficiency of the AOTF and coupling efficiency into the single-mode fiber. The spatial light modulator (SLM) is polarization sensitive. Therefore a polarizing beam splitter (PBS) is integrated for a better definition of the beam's polarization. The PBS also regulates polarization modulation induced by mechanical vibrations of the fiber as it transforms polarization modulation into intensity variations that can be compensated for by a feedback loop (§ 2.3.1.3). A beam expander increases the beam diameter to fully illuminate the SLM. It is best to illuminate the SLM homogeneously, for example to be able to generate Bessel beams with long

depths of field. A modular beam expander allowing magnifications of 3x, 5x, 8x (bm.x VIS-YAG, Linos) is used, that enables adaptation of the beam expansion to the specific requirements. These include the illumination beam's type and the power and depth of field that are required. To switch between the laser lines, three digital output channels are used. Together with a custom-made electronic switch the signal of one analog output channel is used to steer the power of all three available laser lines.

2.3.1.2 *Beam Shaping Optics*

A spatial light modulator (LC-R 2500 or PLUTO NIR II, Holoeye) is used to shape the illumination beam. This diffractive device allows precise spatial manipulation of the phase and amplitude of the incident light - hence the term *holographic beam shaping*. By modulation of both phase and amplitude of the field incident on the SLM, an illumination beam with intensity profile $h_{\text{holo}}(r) = |E_{\text{holo}}(r)|^2$ is formed. The holographic generation of illumination beams is described in detail in chapter 3.

2.3.1.3 *Laser Power Stabilization*

Intensity fluctuations of the illumination light are detrimental since the scanning of the beam in the image plane translates any temporal modulation into a spatial modulation. Stripes become visible at high scanning frequencies, where the beam displacement during an intensity fluctuation period is larger than the lateral beam size. The modulation of the diffraction efficiency of the SLM [Lizana et al., 2008] results in an intensity modulation that has a complex shape with a hologram-dependent amplitude of up to 30% at a frequency of 70Hz and a much higher cut-off frequency. This amplitude modulation by the SLM can be reduced by adapting the polarization of the incoming light [Hanes et al., 2009]. This method causes a decrease in the diffraction efficiency of the device and thereby reduces the amount of laser light available for sample illumination. Recently, it was also proposed to cool the SLM in order to increase the viscosity of the liquid crystal and reduce the fluctuations by [García-Márquez et al., 2012]. The disadvantage of this method is a significant time lag when the hologram is changed.

An experimental setup that allows to correct for the amplitude modulation by an electronic feedback circuit was tested. One advantage of this solution is that it is capable of eliminating other possible instabilities as well as e.g. a drift in the output power of the laser. The system is shown as a part of the beam shaping module in Fig. 2.8 and works as follows: The power of the illumination beam is measured by a reference photo-diode (PDR-S, TEM). A pellicle beam splitter PEL (BP108, Thorlabs) is placed in front of the scanning mirror (GSM) and reflects a small part (~8%) of the incident light. This light is spatially filtered by an aperture to block higher orders and focused onto the photodiode with a lens. This signal is stabilized by steering the diffraction efficiency of the AOTF using a feedback loop (NoiseEater 2.1, TEM, Germany). The system was tested by acquiring images of a beam that was scanned across the field of view in a homogeneously fluorescent solution. Moreover, the power was measured independently with a photo-diode. Both experiments indicated a sufficient stabilization of the laser power for exposure times of up to 10ms. However, image acquisition rates that would have required the laser power stabilization could not be performed in the

context of this thesis. The laser power was generally too low to produce high enough fluorescence signal in biological samples. Therefore, the feedback loop was removed after proof-of-principle measurements.

2.3.1.4 Sample Illumination Optics

The hologram is imaged into the sample volume by four lenses. The first lens (L_{SLM}) images the SLM's far-field diffraction pattern onto a galvanometric scan mirror (M2, GSI), which is used to scan the illumination beam laterally in the focal plane of the detection objective lens (DO) to illuminate the full field of view. Therefore, the tilt angle $\pm\beta$ of the galvanometric scanning mirror (GSM) is translated into a lateral displacement δx of the illumination beam in the sample volume by the illumination objective lens (LD Achromplan 20x/0.40 Corr, Zeiss) and an intermediate telecentric lens system. The system consists of the scan lens (SL) and the tube lens (TL) and therefore has a magnification $M_{\text{TS}} = f_{\text{TL}}/f_{\text{SL}}$. The dependence of the beam displacement on the (small) mirror tilt angle is

$$\delta x \approx \frac{f_{\text{IO}}}{M_{\text{TS}}} \cdot 2\beta. \quad (2.42)$$

As the deflection angles $\pm 2\beta$ provided by the GSM tilted by $\pm\beta$ are relatively small it is unnecessary to use an expensive scanning lens. Instead, a Laser-Monochromat (Linos) with $f_{\text{SL}} = 120\text{mm}$ that offers improved off-axis performance was chosen. The tube-lens with $f_{\text{TL}} = 164.7\text{mm}$, (Zeiss) was replaced by an achromatic lens ($f_{\text{TL}} = 120\text{mm}$, Linos). The tube lens and the illumination objective lens are integrated in a kinematic mount which is placed on the stage of the microscope. It is thus easily removable to facilitate access and can be repositioned with high accuracy. The position of the kinetic mount can be adjusted by a manual linear stage (M-SDS25, Newport) in x -direction to center the illumination beam in the field of view of the detection objective.

2.3.1.5 Detection Optics

A standard inverted microscope (Axiovert 200M, Zeiss) with suitable detection objective lenses (Achromplan 63x/0.95 W, 40x/0.8 W or 20x/0.5 W, Zeiss) is used for detection. The features that it provides include an emission filter wheel. The filter set includes a filter for Cy3 and Alexa568 (composed of a dichroic mirror with cut-off-wavelength $\lambda_c = 590\text{nm}$ and an emission bandpass filter with central wavelength $\lambda_{bp} = 605\text{nm}$ and a width of $d\lambda_{bp} = 70\text{nm}$) and one for GFP, eGFP and Alexa488 ($\lambda_c = 490\text{nm}$, $d\lambda_{bp} = 525\text{nm}$, $d\lambda_{bp} = 50\text{nm}$).

The images are recorded using a monochrome CCD-Camera (AxioCam mRm, Zeiss) with a sensor (Sony ICX-285) that consists of 1388×1040 pixels with a size of $(6.45\mu\text{m})^2$. The camera was usually connected to the microscope using an adapter with a magnification of $M = 0.63$ to enlarge the field-of-view. For this sensor and adapter, the sizes of the corresponding fields of view for the three DOs are listed in Table 1. The Nyquist-criterion requires that the discretization δx by the pixels of the camera sensor is smaller than half the resolution of the DO Δx , i.e. $\delta x < \Delta x/2$. Looking at the values for Δx and δx in Table 1, one can see that this condition was not met. This situation was no problem, because the absolute values of the lateral resolution were never measured. Moreover, scattering media that were the prime sample for the investigations degrade the resolution so that theoretical values are generally

Objective	63x/0.95	40x/0.8	20x/0.5
Field of view	226x169 μm^2	355x266 μm^2	710x532 μm^2
lat. resolution Δx	0.27 μm	0.33 μm	0.52 μm
ax. resolution Δy	0.33 μm	1.63 μm	4.4 μm
Discretization δx	0.162 μm	0.25 μm	0.50 μm

Table 1: Image parameters for different detection objective lenses.

exceeded. However, by employing a larger sensor that delivers equivalent FOVs without the 0.63x-adapter this issue could be resolved.

2.3.2 Sample Mounting and Positioning Components

It is common practice in microscopy to mount samples on object slides made of glass. It is possible to do so in light-sheet microscopy, but the slide should be placed under an angle of $\approx 45^\circ$ relative to both illumination and detection axis [Planchon et al., 2011, Wu et al., 2011]. One must be careful to avoid artifacts in the image by reflections of the illumination beam that are collected by the detection lens. Moreover, slides do not allow to use the full potential of light-sheet microscopy. Alternative sample mounting techniques have therefore been developed [Reynaud et al., 2008]. It has proven to be most advantageous to mount the sample freely in a gel cylinder that can be moved and rotated, thereby allowing multi-view reconstruction [Verveer et al., 2007]. Also, precise control over the environment is possible, e.g. for tissue culture [Pampaloni et al., 2007]. Therefore, this approach was also adopted for the setup presented in this thesis.

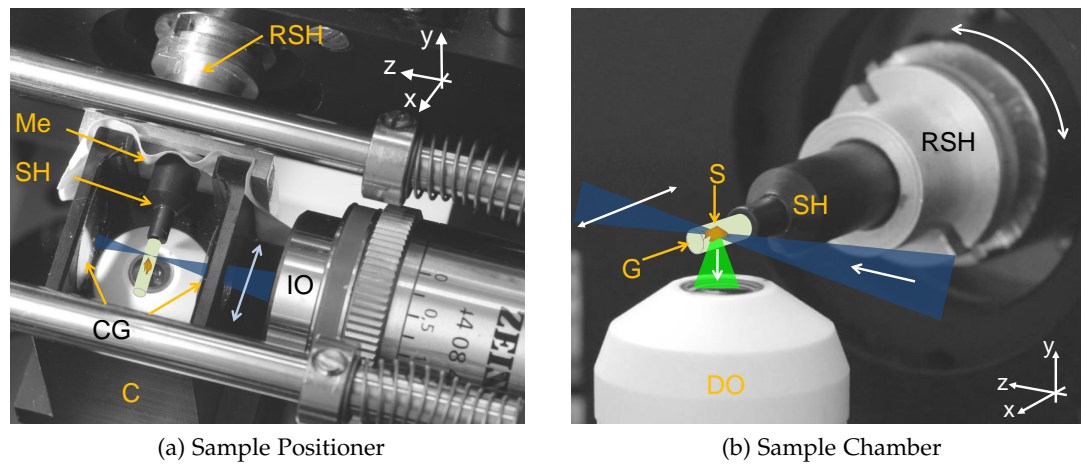


Figure 2.9: Sample mounting and positioning in the sample chamber. The sample (S) is mounted in a gel cylinder (G). The rotating sample holder (RSH) allows positioning and rotation of the sample. The light-sheet is focused by the illumination objective (IO). Fluorescence is detected by the detection objective (DO). A membrane (Me) and cover glasses (CG) are used to seal the chamber (C) that is filled with the immersion medium.

2.3.2.1 Sample Mounting in Agarose Gel Cylinders

Samples are mounted in agarose gel cylinders [Huiskens et al., 2004, Greger et al., 2007]. The axis of the gel cylinder must lie perpendicular to the plane spanned

by illumination and detection optical axis. The use of an upright microscope imposes the restriction that the detection optical axis is vertical. Therefore, the gel cylinder has to be mounted horizontally (Fig. 2.9a). Usually, gel cylinders with diameters $>1.2\text{mm}$ and Agarose concentrations $>1\%$ are used to ensure sufficient mechanical stability: The gel cylinder should not bend due to gravity and hold the object in the desired position over extended periods of time without deforming.

To prepare the agarose gel it is first heated to liquify. Then, the sample is added and the gel together with the sample is sucked into a glass capillary using a syringe. The gel solidifies while cooling down to room temperature. The capillary is introduced into a holder (SH in Fig. 2.9a) and the gel cylinder is pushed out of the capillary. While the capillary fits loosely into the holder so that it can be removed easily, the nozzle of holder tightly grips the agarose and serves as an interface to the positioning and rotating device (RSH in Fig. 2.9a). As measurements are performed in an immersion medium, e.g. water, a chamber holding the liquid has to be used (Fig. 2.9b). The chamber is made of bio-compatible, black Delrin and features sealed openings for both the water dipping detection objective lens and the sample holder.

2.3.2.2 *Sample Chamber*

The sample chamber is shown in Fig. 2.3.2.2. A long working-distance air immersion objective (IO) lens is used for illumination through a hole in the chamber that is sealed by a cover-glass (CG). Spherical aberrations of the illumination beam are introduced by the refractive index mismatch. These depend on the distance that the light propagates through the water-filled chamber. The chamber is thus designed in a way that this distance is reduced to a minimum, which is determined by mechanical restrictions such as objective lens dimensions and space needed for sample positioning. Samples are introduced sideways through a third opening that has to be sealed by a flexible membrane (Me) that allows positioning of the sample. A piece of a latex glove with a small cut through which samples are introduced is sufficient.

2.3.2.3 *Sample Positioning*

The capillary mount is fixed in a combined positioner-rotator-unit (PRU in Fig. 2.9b). The PRU is mounted on the microscope stage allowing the manual lateral (horizontal) displacement of the sample in the image xy -plane. The sample can be moved along the detection optical y -axis in discrete using a piezo positioner (NanoSX400, PiezoJena). Coarse adjustment is possible by a manual translation stage. A rotary support (RSH, custom modification based on DMT40, OWIS) allows the orientation of the gel cylinder along its symmetry axis. This degree of freedom can be useful when imaging non-symmetric objects, e.g. a piece of human skin. The rotation speed was customized to increase rotation speed to about $1/3$ turn per second. The motor is steered via a controller (Motion Controller V2.5 MCDC 3006S, Faulhaber) that is connected to the RS-232 serial port of the PC.

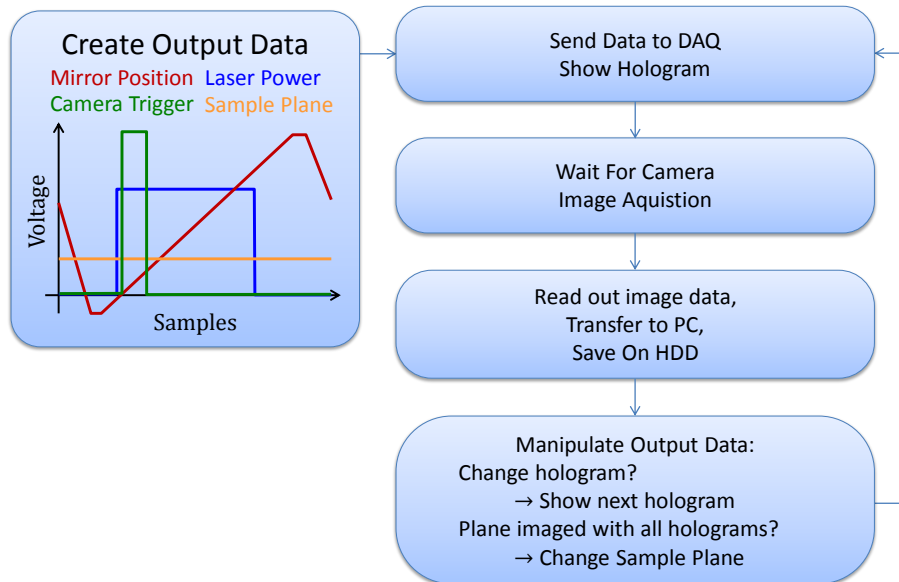


Figure 2.10: Scheme of the image acquisition process.

At first, the data to steer laser power, scan mirror, object position and the camera is generated with parameters set by the user. Then, the loop is started to acquire the image data.

2.3.3 Software

All devices are connected to the PC using an interface card (NI-6299, National Instruments). In order to control the image acquisition of the microscopy, custom software was written in Python. The basic framework, MicPy, was developed by Lars Friedrich and upgraded by members of the lab to control a photonic force microscope. The software is based on a loop that continuously executes the functions that are referenced in a list. The basic entries in the list perform the image acquisition from the camera and display the images on the computer screen. Arbitrary additional functions can be added to the list. For example, the images can be post-processed or streamed onto the hard disk. For the acquisition of light-sheet microscopy images, the list was modified to steer the mirror and the laser power synchronously to the image acquisition by the camera. The complete list is visualized by Fig. 2.10.

2.4 DISCUSSION

Advantages and disadvantages of the setup: The choice to realize the light-sheet microscope as an add-on module to an inverted microscope has shown both advantages and disadvantages. On the one hand, it was beneficial to be able to rely on the variety of features offered by the microscope like epi-fluorescence or bright-field imaging, but also the sample positioning device. Moreover, the microscope features a refined detection optics layout with a motorized filter wheel and binoculars but also adequate mechanical stability. On the other hand, some major draw-backs of this approach became obvious such as the limited flexibility, the comparatively large dimensions of the inverted microscope and the large distance of the illumination plane from the top of the optical table. Most importantly, due to horizontal orientation of the detection focal plane, the gel cylinders had also to be mounted horizontally. To ensure sufficient

mechanical stability of the gel cylinders, it was necessary to use much higher agarose gel concentrations than for vertical orientation resulting in restricted optical transparency. Moreover, the gel was less suited for live imaging due to the larger forces exerted on the sample. This problem can probably be strongly reduced by using transparent tubes with the refractive index of water to stabilize the gel cylinder [Kaufmann et al., 2012].

Limitations to image acquisition speed: For practical applications, the high image acquisition speed is one of the key advantages of a light-sheet microscope. However, the scope of the investigations was put on a detailed comparison of different imaging modalities. In order to achieve this goal, the emphasis was put on optical performance of the microscope. Fast image acquisition in biological samples was impossible with this microscope but for the proof-of-principle investigations carried out in the context of this thesis the speed was sufficient.

The two main reasons for the low imaging speed were the low total power delivered by the laser unit and the low efficiency of the optical illumination beam path that was aimed at high flexibility rather than high efficiency. High-speed imaging with linear fluorescence excitation by Gaussian beams requires $\approx 10\text{mW}$ of power in the back focal plane of the illumination lens. For Bessel beams, 3 to 10 times more power is needed to generate equal signals from the main lobe due to the ring system. The fiber coupled laser unit delivers only about 3 to 10 mW depending on the wavelength used. The efficiency of the illumination beam path is less than 20%, mainly due to low coupling-efficiency of the fiber, the over-illumination of the SLM and the SLM's low diffraction efficiency. Therefore, only less than 2mW of power was available for sample illumination.

Due to the hardware-restricted imaging speed, the software architecture was not optimized to provide maximum speed, but to provide a high flexibility. As illustrated by Fig. 2.10, the computer controls the whole image acquisition process. The camera has to wait for the trigger signal sent by the computer which limits the speed to roughly 10fps. This speed was not achieved due to the limited fluorescence signal produced by the low laser power available. If the camera was run in continuous acquisition mode the image acquisition speed could have been increased to approximately 30fps. However, when the camera continuously acquires images it cannot be triggered externally anymore. Therefore it has to take control of the scanning mirror, the laser power, etc. instead of the computer. This major change to the system will drastically reduce its flexibility. At the point when all other hardware limits are overcome this time-consuming step will nevertheless be necessary.

Outlook - possible experiments with an optimized setup: With a faster system, live-imaging would have been an interesting option to study the long-term imaging performance of the microscope, especially in the context of photo-toxic effects. Therefore, a stable and motorized sample mount would be required. Most hindering to long term observation was the missing motorization of the sample mount. A piezo-stage allowed precise adjustment of the sample along the detection optical axis, but only over a very limited range of $320\mu\text{m}$, which is not enough for samples like zebrafish embryos or tumor multicellular spheroids. Moreover, it was not sufficient to correct for sample drift during long-term measurements. For positioning along x and z , the manual stage of the microscope had to be used with the following drawbacks: First, it made automated drift correction impossible and second, the smooth manual stage itself introduced drift which could not be corrected. Moreover, the small path of the piezo-mount

and the manual xy -stage didn't allow for automatic positioning of the sample in the field of view after rotation of the gel-cylinder making multi-view imaging an extremely tedious imprecise procedure that requires strong interaction by the user.

This chapter presents and discusses beams that are used for illumination in light-sheet microscopy. The first two sections give an overview over different conventional and self-reconstructing beams and gives mathematical descriptions. Subsequently, in Section 3.3 all beams are compared based on a criterion that is of special relevance for the use as illumination beams in light-sheet microscopy: the radial power distribution. Section 3.4 extensively describes the generation (or shaping) of beams using a pixelated phase shaping device, i.e. a spatial light modulator (SLM). The chapter concludes with experimental results of coherently imaged illumination beams (§ 3.5).

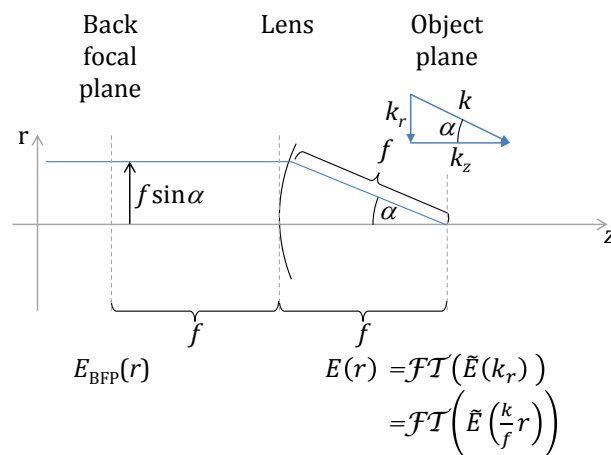


Figure 3.1: Illustration of the variables used for the description of light focused by a lens.

3.1 CONVENTIONAL BEAMS

In this thesis, the term *conventional* is used to group beams that spread while propagating through homogeneous space. The beams introduced in this chapter have been used in light-sheet microscopy before (Voie et al. [1993], Huisken et al. [2004], Buytaert and Dirckx [2007], Dodt et al. [2007], Keller et al. [2008]) and constitute the benchmark against which new illumination techniques must persist. In light-sheet microscopy, the illumination beams exhibit a large depth of field so that the beams can be described using the paraxial approximation, $\alpha \approx \sin \alpha \approx \tan \alpha$, where $\alpha = \arcsin(\text{NA}/n)$ with $\text{NA}/n < 0.4$. A sketch that illustrates the variables used is shown in Fig. 3.1.

3.1.1 Focused Flat-Top Beams

The light-sheet can be produced by scanning a (circularly symmetrical) beam across the focal plane of the detection objective lens (DO) during the acquisition time of the camera. Most simply, a focused flat-top beam can be used, which can

be created by illumination of a circular aperture in the back-focal plane of the illumination lens (compare Fig. 3.1). An example is shown in Fig. 3.2.

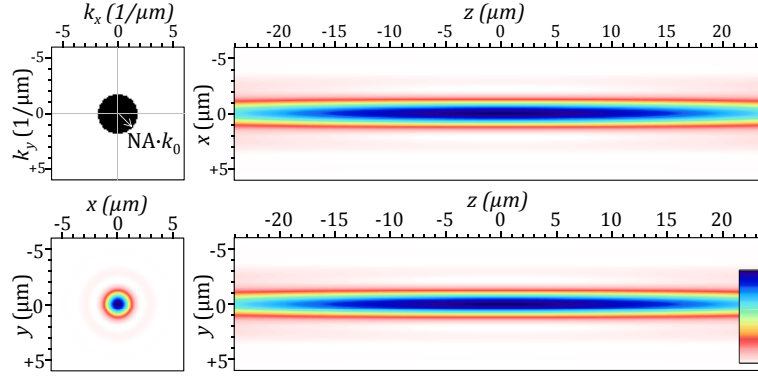


Figure 3.2: Simulated irradiance of a focused flat-top beam (NA = 0.12).

Illustration of the spectrum in the object plane $\tilde{I}(k_x, k_y)$ and slices through the three-dimensional irradiance $I(x, y, z)$ of a focused flat-top beam.

A focused flat-top beam is created by focusing a beam with a homogeneous irradiance $I_0 = |E_0|^2$ within a circular, sharp-edged area with radius b . The flat-top illumination in the BFP can be described by

$$E_{\text{BFP}}(r) = E_0 \cdot \text{circ}(r/b). \quad (3.1)$$

This field distribution produces a beam with the angular spectrum

$$\tilde{E}(k_r) = \tilde{E}_0 \cdot \text{circ}(k_r/k_b). \quad (3.2)$$

in the focal plane of the lens. Note that $k_b = k_0 \text{NA} \approx 2\pi b / \lambda_0 f$ because a field distribution with radius b in the back-focal plane of a lens with focal length f corresponds to focusing with $\text{NA} = n \cdot \sin \alpha = n \cdot b / f$ (see Figure 3.1). Hankel-Transformation of eq. 3.2 yields the irradiance in the focal plane of the lens

$$I(r) = I_0 \cdot \left(\frac{J_1(k_b r)}{k_b r} \right)^2 \quad (3.3)$$

where $I_0 = (\tilde{E}_0 / \lambda_0 f)^2$. The FWHM-beam diameter can be inferred from $J_1(x)/x = 0.5/\sqrt{2}$ for $x = 1.62 = k_b \cdot \Delta r / 2$ to be

$$\Delta r = 0.52 \cdot \frac{\lambda_0}{\text{NA}} \approx 0.52 \cdot \frac{\lambda_0 \cdot f}{b}, \quad (3.4)$$

where the approximation is valid for $\text{NA}/n \lesssim 0.4$ or lenses obeying the sine-condition (see Fig 3.1). Note that $J_1(x)/x \xrightarrow{x \rightarrow 0} 0.5$.

The depth of field (DOF) of beams with an angular spectrum described by eqn 3.2 can be estimated using the width of the spectrum's projection on the k_z -axis, defined by $k_z = \sqrt{k_0^2 - k_r^2}$ via the Ewald sphere [McCutchen, 1964]. The axial irradiance is

$$I(z) \propto (\text{sinc}(\Delta k_z \cdot z/2))^2 \quad (3.5)$$

with $\Delta k_z = k - \sqrt{k^2 - k_b^2} = k_0 n \cdot (1 - \cos \alpha)$. The FWHM depth of focus

$$\Delta z = \frac{0.88\lambda_0}{n(1 - \cos \alpha)} \approx \frac{0.88\lambda_0}{n - n\sqrt{1 - (b/f)^2}} \quad (3.6)$$

follows with $\text{sinc}(x/2) = 1/\sqrt{2}$ for $x = 2 \cdot 1.39 = \Delta k_z \cdot dz/2$.

Focused flat-top beams are very simple to use as only the diameter of the aperture has to be varied in order to adapt the beam's depth-of-field to the sample size. However, side-lobes in the radial intensity profile result from the hard-edged aperture. These may potentially reduce image contrast in a light-sheet microscope. However, the main lobe is much thinner than for Gaussian beam with equal depth of field.

3.1.2 Gaussian Beams

In contrast to focused flat-top beams, the radial profile of a Gaussian beam decays smoothly (see Figure 3.3 for an example).

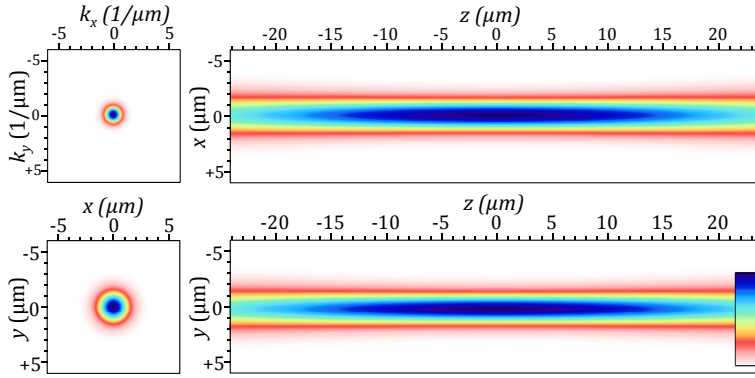


Figure 3.3: Simulated irradiance of a Gaussian beam (NA = 0.083).

Illustration of the spectrum in the object plane $\tilde{I}(k_x, k_y)$ and slices through the three-dimensional irradiance $I(x, y, z)$ of a Gaussian beam.

The most important property of a Gaussian beam is that its transverse profile follows a Gaussian function independently from the position along the z -axis. The Gaussian beam is a solution to the paraxial Helmholtz equation and the exact mathematical description is:

$$E(r, z) = E_0 \cdot \frac{dr}{2R(z)} \cdot \exp \left\{ - (r/R(z))^2 \right\} \cdot \exp \left\{ -ik \frac{r^2}{2\rho(z)} \right\} \cdot \exp \{ i(\zeta(z) - kz) \} \quad (3.7)$$

where $R(z)$ is the $1/e$ -radius of the beam, $\rho(z)$ is the curvature of the phase front, $\zeta(z)$ describes the Guoy Phase shift [Saleh and Teich, 2007, Born and Wolf, 1999]. The above field yields an irradiance

$$I(r, z) = I_0 \cdot \frac{dr^2}{4R(z)^2} \cdot \exp \left\{ -2r^2/R(z)^2 \right\} \quad (3.8)$$

with a Gaussian cross section. The beam's $1/e$ -radius at the position of the waist is $R(0) = \lambda/\pi\alpha$ which corresponds approximately to the value of the FWHM diameter

$$\Delta r \approx \frac{1.2\lambda}{\pi\alpha}. \quad (3.9)$$

The beam diameter at the position of the focus is primarily determined by the focusing angle $\alpha = \arcsin(\text{NA}/n)$ for a given wavelength λ . According to [Saleh and Teich, 2007] the FWHM depth of field is given by

$$\Delta z = \frac{2}{\pi} \frac{\lambda}{\alpha^2} \approx 1.7\pi \frac{\Delta r^2}{\lambda}. \quad (3.10)$$

Due to the paraxial approximation, Gaussian beams do only accurately describe weakly focused light ($\text{NA}/n < 0.4$). This condition is met in general for light-sheet illumination beams, where Δz is two to three orders of magnitudes larger than the wavelength. Because of the quadratic interdependency of Δz on the beam diameter Δr the thickness of the light-sheet is determined by the required depth of field.

3.1.3 Elliptical Beams

The first light-sheet microscopes featured a static light-sheet, which was created by focusing an expanded beam with a cylindrical lens [Voie et al., 1993, Fuchs et al., 2002, Huisken et al., 2004, Dodt et al., 2007]. However this approach does not enable high axial resolution because high-quality cylindrical lenses with a high NA are not readily available. As a compromise for moderate axial resolution, custom-made achromatic cylindrical lenses can be used [Buytaert and Dirckx, 2007]. The design of the illumination beam path was improved by introducing a microscope objective lens that focuses a field distribution created by a cylindrical lens [Huisken and Stainier, 2007]. A rectangular mask located in the back-focal plane of the illumination objective lens produces the field distribution

$$E_{\text{BFP}}(x, y) = E_0 \cdot \text{rect}(x/b_x) \cdot \text{rect}(y/b_y) \quad (3.11)$$

where b_x and b_y are the dimensions of the slit mask is used to adjust the spectrum in the front focal plane to be

$$\tilde{E}(k_x, k_y) = \tilde{E}_0 \cdot \text{rect}(a k_x/b_x) \cdot \text{rect}(a k_y/b_y) \quad (3.12)$$

with $a = \lambda_0 f$ and $\tilde{E}_0 = a E_0$. A 2D-Fourier transformation of the spectrum yields the irradiance

$$I(x, y) = \text{sinc}(x \cdot b_x/2)^2 \cdot \text{sinc}(y \cdot b_y/2)^2. \quad (3.13)$$

It can be seen that the lateral width (along the x -axis) of the light-sheet can be controlled by adapting the parameter $1/b_x$. The thickness (along the detection y -axis) is governed by $1/b_y$. Slit stops offer a simple way to steer properties of the light-sheet and are therefore employed in several above mentioned setups. However as in the case of flat-top beams, the sharp edges give rise to side-lobes. A light-sheet with a Gaussian beam profile can be created by adjusting the

beam dimensions using appropriate cylindrical lenses that create a strongly asymmetrical Gaussian beam with

$$I(x, y) = \exp \left\{ - (2x/\Delta x)^2 \right\} \cdot \exp \left\{ - (2y/\Delta y)^2 \right\}. \quad (3.14)$$

with an elliptical cross-section [Ritter et al., 2008]. However, flexibility is then lost unless a complex cylindrical zoom lens [Ritter et al., 2011] is integrated. The depth of field is equivalent to the respective circularly symmetric beams. Note that in contrast to a light-sheet produced by a scanned beam, the static light-sheet has a high degree of spatial coherence. Artifacts arising from scattering can therefore be increased due to interference effects (eqn 2.26).

3.2 SELF-RECONSTRUCTING BEAMS

Self-reconstructing beams feature two properties that conventional beams do not possess. First, they are propagation-invariant in homogeneous space, i.e. they do not spread over a comparatively long distance along the propagation axis [Durnin et al., 1987]. This property is linked to the very small width of their angular spectrum. Second, they have shown to be self-reconstructing behind isolated obstacles, i.e. regain their initial beam profile [Bouchal et al., 1998]. The beams presented in this chapter have not been used in light-sheet microscopy before.

3.2.1 Bessel Beams

The angular spectrum of an ideal zero-order Bessel beam focused with $\text{NA} = n \cdot \sin \alpha$ is infinitely thin and can be written as

$$\tilde{E}(k_r) \propto \delta(k_r - k_0 \text{NA}), \quad (3.15)$$

where k_0 is the wave-vector in vacuum and k_r its radial component. Hankel-Transformation of eq. 3.15 yields the irradiance as a function of the radius r is

$$I(r) \propto |J_0(k_r r)|^2, \quad (3.16)$$

where J_0 is the Bessel function of the 0th order. In this idealized case $I(r)$ does not depend on the propagation distance z , which can be attributed to the lack of diffraction in free space. Due to the infinitely thin angular spectrum of the beam there is no angular dispersion and therefore no diffraction in free space. Bessel beams were therefore termed non-diffracting beams [Durnin et al., 1987].

For the ideal Bessel beam, both the carried amount of energy and the propagation invariant distance are infinite. However, there are realistic approximations to the ideal Bessel beam. The angular spectrum of the Bessel beam can be approximated by a ring (Fig. 3.4 for an example) with homogeneous irradiance:

$$\tilde{E}(k_r) = \tilde{E}_0 \cdot (\Theta(k_0 \text{NA} - k_r) - \Theta(\sqrt{\epsilon} k_0 \text{NA} - k_r)) \quad (3.17)$$

where $\Theta(x)$ denotes the Heaviside step function. $\epsilon < 1$ is the ring width parameter. If the Bessel beam is created by an annular mask in the back-focal plane of a lens, $\sqrt{\epsilon}$ is the ratio of the inner ($r_{\text{in}} = a k_{\text{in}} = a \sqrt{\epsilon} k_0 \text{NA}$) and outer

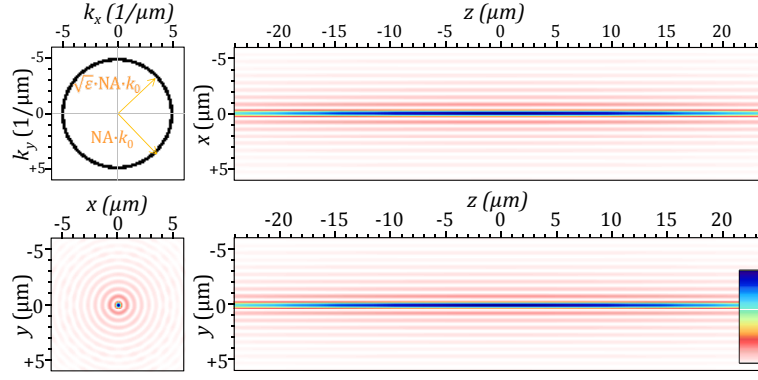


Figure 3.4: Simulated irradiance of a Bessel beam ($NA = 0.4, \epsilon = 0.94$).

Illustration of the spectrum in the object plane $\tilde{I}(k_x, k_y)$ and slices through the three-dimensional irradiance $I(x, y, z)$ of a Bessel beam.

$r_{\text{out}} = ak_{\text{out}} = ak_0NA$ radius of the annulus, where $a = \lambda_0 f$ is a proportionality factor with the unit m^2 that links the angular spectrum with the focal length of the lens. Note that $\epsilon = 0$ corresponds to a flat-top beam. The irradiance profile

$$I(r) = I_0 (a \cdot k_0 \cdot NA)^2 \cdot \frac{(J_1(k_0NAr) - \sqrt{\epsilon}J_1(\sqrt{\epsilon}k_0NAr))^2}{r^2}. \quad (3.18)$$

is obtained from eqn 3.17 by a Hankel-Transformation (\mathcal{HT}). The depth of field (DOF) of beams with an angular spectrum described by eq. 3.17 can be estimated using the width of the spectrum's projection on the k_z -axis [McCutchen, 1964].

Using $k_z = \sqrt{k_0^2 - k_r^2}$ defined by the Ewald sphere the width is

$$\Delta k_z = k_0 \left(\sqrt{n^2 - \epsilon NA^2} - \sqrt{n^2 - NA^2} \right). \quad (3.19)$$

Note that the exact shape of the angular spectrum depends on the apodization of the illumination objective. The depth of field (DOF) $\Delta z = q/\Delta k_z$ depends on the exact shape of $\tilde{E}(k_z)$ and the acceptable intensity drop-off. Assuming a rectangular shape of $\tilde{E}(k_z)$, the FWHM-length Δz is obtained with $q = 5.56$ and the $1/e$ -DOF $\Delta z_{1/e}$ for a value of $q = 6.57$ so that $\Delta z_{1/e} = 1.18 \cdot \Delta z$. The focal depth

$$\Delta z = \frac{0.88\lambda_0}{\left(\sqrt{n^2 - \epsilon NA^2} - \sqrt{n^2 - NA^2} \right)} \quad (3.20)$$

can be approximated to

$$\Delta z \approx \frac{1.76 n \lambda_0}{NA^2(1 - \epsilon)} \quad (3.21)$$

with a precision of more than 96% for $NA < 0.4$ and more than 89% for $NA < 0.6$ for the typical value of $n = 1.33$ that corresponds to water. Note that, in contrast to Gaussian beams, where the beam's diameter and depth of field which are both fully determined by the NA, there are two free parameters for the Bessel beam, the NA and ϵ that allow to steer both diameter and depth-of-field independently. An increase in the NA together with a matching decrease in ϵ to hold $\Delta z_{1/e}$ constant due to $NA^2 \cdot (1 - \epsilon) = \text{const}$. Alternatively, the NA can be reduced

when the ring parameter ϵ is increased. The influence of the choice of NA and ϵ on the relative amount of power in the main lobe of the Bessel beam are discussed in detail in Section 3.3.

3.2.2 Sectioned Bessel Beams

Other than Bessel beams with a ring-shaped angular spectrum, the sectioned Bessel beams consists of two opposed sections of the ring. The spectrum exhibits a mirror symmetry in the $k_x k_y$ -plane with respect to an axis defined by its angle φ_0 against the k_x -axis. An example is shown in Fig. 3.5.

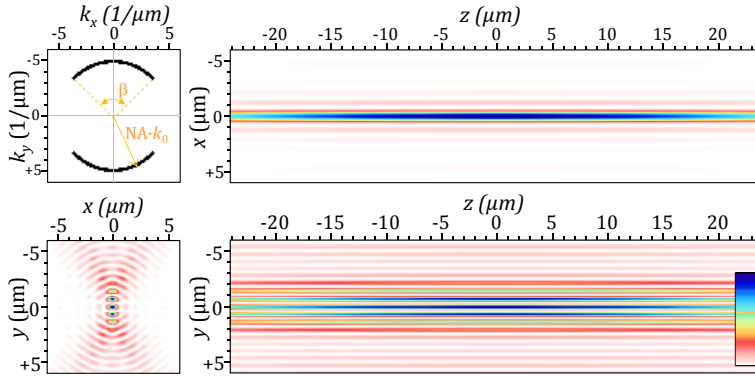


Figure 3.5: Simulated irradiance of a sectioned Bessel beam.

Illustration of the spectrum in the object plane $\tilde{I}(k_x, k_y)$ and slices through the three-dimensional irradiance $I(x, y, z)$ of a sectioned Bessel beam (NA = 0.4, $\epsilon = 0.94$, $\beta = 88^\circ$).

The spectrum can be mathematically described by

$$\begin{aligned} \tilde{E}(k_r, \varphi) = \tilde{E}_0 \cdot & (\Theta(k_0 \text{NA} - k_r) - \Theta(\sqrt{\epsilon} k_0 \text{NA} - k_r)) \\ & \cdot \Theta(|\text{mod}(\varphi - \varphi_0 + \beta/2, \pi)| - \beta) \end{aligned} \quad (3.22)$$

where β is the angular width and φ_0 the polar position of the segment. Due to the broken polar symmetry, there is no simple analytical solution for the field distribution of sectioned Bessel beams. In principle, when diffraction effects are neglected the resulting beam is similar to a Bessel-beam where two opposed segments are cut out. However, while the extension of the main lobe along the φ_0 -axis is approximately equal to that of a conventional Bessel beam it is more extended along the perpendicular axis. But the ring structure is strongly suppressed along this axis. The important implications that arise from this property will be presented in Section 6.8. These beams are similar to zero-order Mathieu beams (Gutiérrez-Vega et al. [2000, 2001, 2003]). This class of self-reconstructing beams is represented by solutions to the Helmholtz-equation in elliptical cylindrical coordinates.

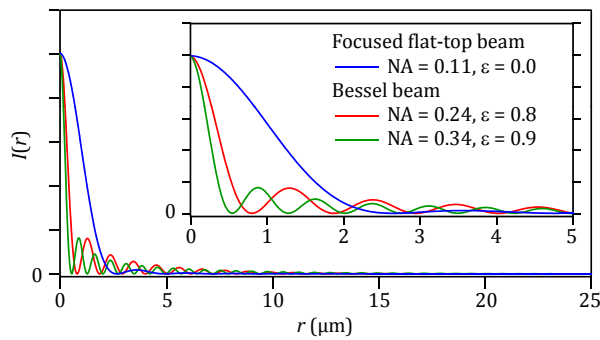
3.3 RADIAL DISTRIBUTION OF BEAM POWER

Bessel beams and focused flat-top beams feature an entirely different radial distribution of the power. For an equal depth of field, the Bessel beam features a much thinner main lobe than the focused flat-top beam but also carries significantly more power in an extended ring system. The ring system is negligible

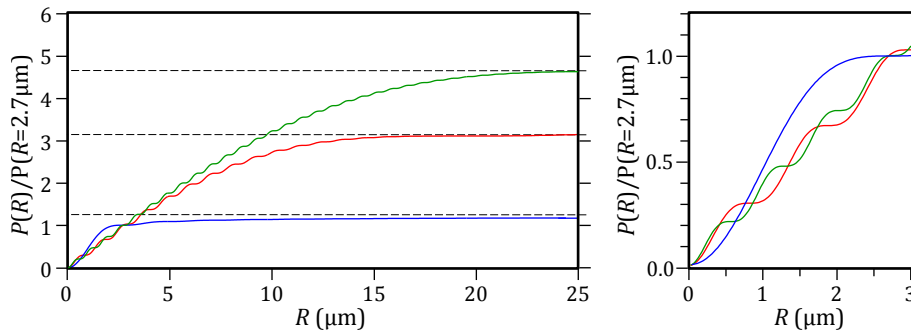
for the focused flat-top beam. In the first part of this section, numerical data is used to compare the radial distribution of power of one focused flat-top beam and two Bessel beams with equal DOFs. In the second part, approximations are used to derive an analytical mathematical description of the relative power in the main lobe of Bessel beams depending on the parameters NA and ϵ .

3.3.1 Comparison using Numerical Data

The radial irradiance of one focused flat-top beam and two Bessel beams with equal depths of field (DOF) are compared in this section. Bessel beams with a DOF of $\Delta z = 100\mu\text{m}$ are obtained by NA = 0.24 and $\epsilon = 0.8$ or by NA = 0.34 with $\epsilon = 0.9$. The corresponding focused flat-top beam is generated with NA = 0.11. Plots of the radial irradiance $I(r)$ according to eqn 3.18 are shown in Figure 3.6a. It can be seen that the Bessel beam's ring system covers a large



(a) Radial irradiance for a focused flat-top beam and two Bessel beams with equal depth of field. The beams are normalized to equal on-axis irradiance $I(r = 0)$ for better comparability.



(b) Radial Power $P(R)$ of focused flat-top beam and two Bessel beams. The beams are normalized so that they carry equal power in the area of the Airy disc (radius $r = 2.7\mu\text{m}$) of the focused flat-top beam.

Figure 3.6: Radial irradiance and power for a focused flat-top beam and two Bessel beams with equal depth of field.

transverse area. The irradiance of the rings is much smaller than that of the main lobe. However, the power P carried in the rings is almost of the same order. The beam's power P up to radius R is

$$P(R) = 2\pi \int_0^R I(r)rdr. \quad (3.23)$$

The graph in Figure 3.6b shows that a large fraction of the Bessel beam's power resides in the ring system. For equivalent powers in the area of the Airy disc

of the conventional illumination beam, the Bessel beam carries approximately 3 times more total energy for $\text{NA} = 0.24$, $\epsilon = 0.8$ and to 5 times more energy for $\text{NA} = 0.34$, $\epsilon = 0.9$. The Bessel beam's ring system is essential for the long depth of field, but for imaging applications (not only but especially perpendicular to the Bessel beam axis), it leads to inferior optical sectioning and decreased contrast. This issue will be discussed in more detail below.

Apart from that, Bessel beams are produced at higher NAs than conventional beams for equivalent DOFs, resulting in a narrower central lobe (see enlargement in the right part of Fig. 3.6b). In principle it should therefore be possible to achieve better resolution in light-sheet microscopy provided that a method is employed that removes or suppresses the rings. Another important difference between conventional beams (Gaussian or focused flat-top) and Bessel beams lies in the fact that in contrast to conventional beams where the beam diameter increases by a factor of $\sqrt{2}$ over the FWHM-depth of field (Fig. 1.4), for Bessel beams the size of the thin central lobe is maintained over the whole depth of field.

3.3.2 Comparison using Analytical Approximations

To obtain a mathematical description of the relative power in the main lobe, analytical expressions for the total power P_0 and the power in the main lobe P_m have to be derived.

First, the total power is obtained in the Fourier-plane by integration of eq. 3.17 over the radius r and the polar angle φ .

$$P_0 = I_0 \cdot A_{\text{ring}} = a^2 \cdot I_0 \cdot \pi \cdot (1 - \epsilon) \cdot (k_0 \cdot \text{NA})^2 \quad (3.24)$$

is obtained for homogeneous illumination of the ring with irradiance I_0 where $\tilde{I}_0 = a^2 \cdot I_0$ is taken into account. Note that using equation 3.23 does not yield an analytical solution for the total power in the beam because the integral over $I(r) \cdot r$ does not converge for $R \rightarrow \infty$.

Second, an analytical expression of the power in the main lobe

$$P_m = 2\pi \int_0^{r_0} I(r) \cdot r \, dr \quad (3.25)$$

is needed. This equation requires an expression for the radius of the main lobe, i.e. the position of the first minimum r_0 , and for the irradiance of main lobe $I_{\text{main}}(r)$. The position of the first minimum of eqn 3.18 is approximated by

$$r_0 \approx 0.76 \cdot \frac{\lambda_0}{(1 + \sqrt{\epsilon}) \text{NA}} = 4.77/k_0 (1 + \sqrt{\epsilon}) \text{NA} \quad (3.26)$$

$$\stackrel{\epsilon > 0.6}{\approx} 0.4 \cdot \frac{\lambda_0}{\text{NA}} \quad (3.27)$$

For small values of $r/r_0 < 3$ and $\epsilon > 0.2$ the beam's radial shape can be described by

$$I_{\text{main}}(r) = I(0) \cdot \left(J_0 \left(\frac{(1 + \sqrt{\epsilon})}{2} k_0 \text{NA} r \right) \right)^2. \quad (3.28)$$

with the on-axis irradiance $I(0)$. Using the approximation $J_1(x) \approx x/2$ that is valid for $x \ll 1$ in equation 3.18 one finds

$$\begin{aligned} I(r=0) &= a^2 \cdot I_0 \cdot (k_0 \cdot NA)^4 \cdot (1 - \epsilon)^2 / 4. \\ &\approx \frac{A_{\text{ring}}}{4\pi^2 a^2} \cdot P_0 \end{aligned} \quad (3.29)$$

The value depends only very weakly (<10%) on the ring width ϵ for $\epsilon > 0.6$ allowing the approximation in the second line. The power in the main lobe is

$$\begin{aligned} P_m = \pi \cdot I(0) \cdot r_0^2 \cdot \left(J_0 \left((1 + \sqrt{\epsilon}) k_0 NA r_0 / 2 \right)^2 \right. \\ \left. + J_1 \left((1 + \sqrt{\epsilon}) k_0 NA r_0 / 2 \right)^2 \right). \end{aligned} \quad (3.30)$$

With r_0 from eqn 3.26 and by using $J_0(2.39)^2 + J_1(2.39)^2 \approx 0.273$ one obtains

$$P_m \approx 0.857 \cdot I(0) \cdot r_0^2. \quad (3.31)$$

With equations 3.29 and 3.24 the relative power in the central lobe of the beam can be written as

$$P_m / P_0 = 1.56 \cdot (1 - \epsilon) / (1 + \sqrt{\epsilon}). \quad (3.32)$$

This result is in agreement with values obtained by numerical integration within 15% for $\epsilon \approx 0.2$. The deviation is less than 1% for larger values of ϵ . Note that for $\epsilon = 0$ only $\approx 85\%$ of the power lies in the main lobe and this result is not reflected by the above formula due to the approximation made in eqn 3.28. The relation between P_m and P_0 is shown in Figure 3.7. Taylor expansion around $\epsilon = 1$ up to the second order yields

$$P_m / P_0 \approx 0.58 - 0.78\epsilon + 0.19\epsilon^2. \quad (3.33)$$

which is a good approximation to within 20% for $\epsilon > 0.3$ and within 10% in the range $\epsilon > 0.5$. However, this approximation yields values closer to the numerical data (Fig. 3.7). Also, the linear approximation

$$P_m / P_0 \stackrel{\epsilon > 0.6}{\approx} 0.4 \cdot (1 - \epsilon), \quad (3.34)$$

which fits well for $\epsilon > 0.6$ is useful. Light-sheet microscopy requires beams with long depths of field which is usually created at $\epsilon \approx 0.7 \dots 0.95$.

The choice of the numerical aperture directly affects the relative amount of power in the main lobe for a fixed depth of field which scales with NA^{-2} . This result follows directly from solving eqn 3.21 for ϵ and inserting the term into eqn 3.34. The relative power in the main lobe is given by

$$P_m = \frac{5.3 \cdot n}{k_0 \cdot NA^2 \cdot dz_{1/e}} \cdot P_0. \quad (3.35)$$

Using equation 3.24, one finds that when creating a Bessel beam by homogeneous illumination of an annular mask the total power of the beam

$$P_0 = \frac{13.14 \pi a^2 n k_0 I_0}{dz_{1/e}}. \quad (3.36)$$

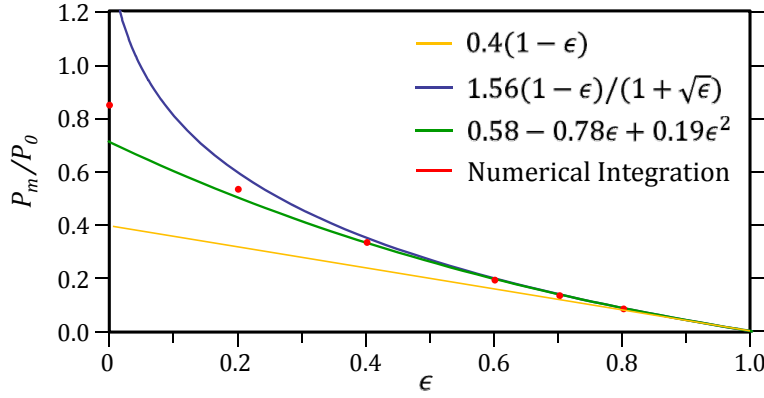


Figure 3.7: The relative power in the Bessel beam's main lobe.

The blue line shows the analytical approximation derived in equation 3.32. The green line is a second order Taylor series approximation around $\epsilon = 1$ as shown in equation 3.33. The red dots are obtained from numerical integration $\int_{\text{main}} I(r) r dr / P_0$. The numerical integration is more precise for small values of ϵ , whereas the power is underestimated for large ϵ . Numerical errors of up to 10% arise from the product $I(r) \cdot r$ when $I(r)$ is small for large radii r , i.e. when $\epsilon \rightarrow 1$ leads to a strong ring system.

is independent of the NA and ring width parameter ϵ but scales inversely with the focal depth of the beam. The use of annular apertures therefore leads to very inefficient use of the available laser power for large depths of field $dz_{1/e}$. In this thesis illumination beams are not generated by the use of annular apertures in a Fourier-plane but by phase shaping with a conical phase, i.e. a phase axicon, in a conjugate plane. The power within the beam scales quadratically with the depth of field (see § 3.4, especially § 3.4.3).

3.4 HOLOGRAPHIC GENERATION OF ILLUMINATION BEAMS

To be able to compare the different illumination beams presented above, a holographic beam shaping device is used. The spatial light modulator (SLM) is able to manipulate the phase and amplitude of the incident beam with high spatial resolution. However, special care has to be taken to minimize artifacts. In the following chapter, details on holographic beam shaping using an SLM will be given. Subsequently, the holograms for the beams introduced in the preceding chapter are presented. The section will be concluded by remarks on how the device can be used for beam alignment, which is a critical issue in high-resolution light-sheet microscopy.

3.4.1 Holographic Beam Shaping

A hologram $H(x, y)$ generated with an SLM can shape an incoming beam with field $E_{\text{in}}(x, y)$ to obtain

$$E(x, y) = E_{\text{in}}(x, y) \cdot H(x, y). \quad (3.37)$$

The hologram has the general form

$$H(x, y) = t(x, y) \cdot e^{i\delta\phi(x, y)} \quad (3.38)$$

where $t(x, y)$ denotes the amplitude modulation and $\phi(x, y)$ the phase modulation. For phase-only SLMs $t(x, y) = \text{const.}$ holds. A small amplitude modulation $t_{\delta\phi}(x, y)$ in the dependence of the phase modulation that occurs in practice is neglected at this point. Gradual amplitude modulation is not directly possible. However, a method to achieve amplitude modulation with phase-only SLMs is presented below (eqn 3.54 in § 3.4.5). Fourier transformation of the modulated field (eqn 3.37) yields the ideal irradiance in the far-field or the focal plane of a lens:

$$I_{\text{ideal}}(a \cdot k_x, a \cdot k_y) = |\mathcal{FT} \{H(x, y) \cdot E_{\text{in}}(x, y)\}|^2, \quad (3.39)$$

where $a \propto \lambda \cdot f \cdot M$ is a scaling factor which is proportional to the wavelength λ , the illumination objective's focal length f and the magnification M of the optical system used to image the SLM into the sample volume.

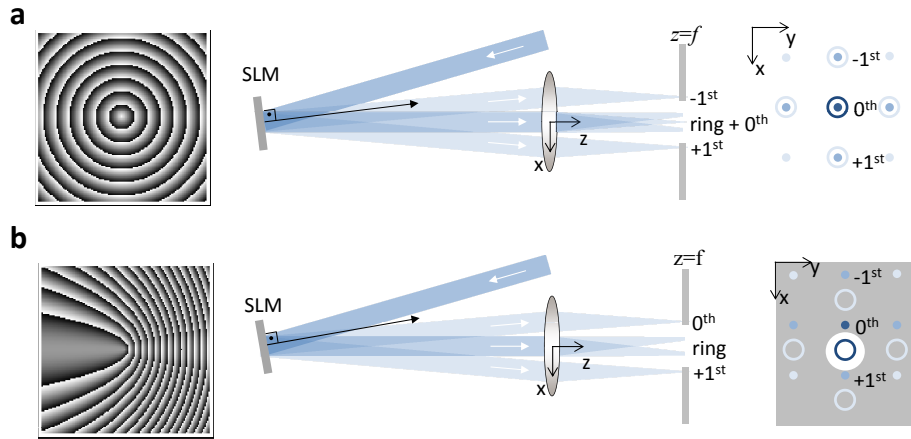


Figure 3.8: Illustration of the spatial separation of the hologram's far-field-diffraction. An SLM creates a superposition of the far-field diffraction pattern of the hologram and of the periodic structure of the pixelated device. For a regular phase axicon hologram (a, left) the SLM generates a ring-shaped irradiance in the far-field (a, center) around a strong zeroth order and higher orders. By applying a phase grating to the hologram (b, left) the ring is shifted with respect to the zeroth and order which can be blocked by an aperture (gray) together with higher orders .

3.4.2 Spatial Separation of the SLM's Diffraction Pattern

The SLM has a pixelated display with a non-unity fill-factor (93% for the Holoeye LC-R2500, 87% for the Holoeye PLUTO, 95% for Hamamatsu X10468 Series), meaning that there are gaps between the active pixels. The SLM therefore acts as a two-dimensional rectangular grating. Its field reflection coefficient is described by $t_{\text{pix}}(x, y)$. A field incident on the SLM is additionally modulated by the periodic function $t_{\text{pix}}(x, y)$, such that the total diffracted irradiance

$$I_{\text{total}}(x, y) = |\mathcal{FT} \{t_{\text{pix}}(x, y) \cdot E_{\text{in}}(x, y)\}|^2 * I_{\text{ideal}}(a k_x, a k_y) \quad (3.40)$$

features sidebands or higher diffraction orders and a prominent zero-frequency contribution. These have to be eliminated because they create additional background in light-sheet microscopy. There exist a number of propositions to do so [Maurer et al., 2008]. Figure 3.8a shows an example of $I_{\text{total}}(k_x, k_y)$ for a

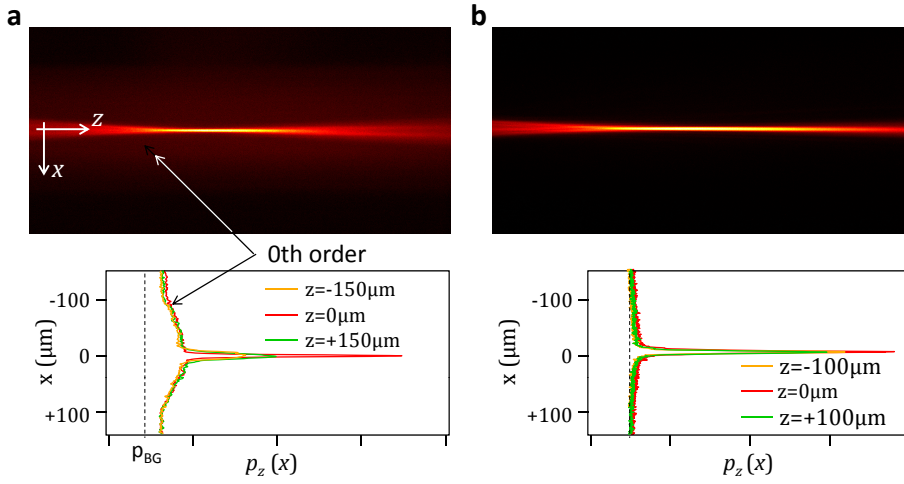


Figure 3.9: Image of a holographically shaped illumination beam in fluorescence with and without zeroth order.

Fluorescence excited by the zeroth diffraction order of the spatial light modulator creates background over a large area around the beam (a). By adding a grating to the beam shaping hologram, the zeroth and higher orders can be blocked in the back-focal plane of the detection lens with a circular aperture. The reduction in background is demonstrated in (b).

hologram creating a ring-shaped irradiance in the far field. Higher diffraction orders $n \neq +1$ created by the SLM's reflectivity can be easily eliminated by a circular stop centered around the 0th diffraction order. But the central spot is difficult to block, especially for symmetric phase holograms like phase axicons that result in a distribution of $I_{ideal}(x, y)$ around the spot (Fig. 3.8a).

An effective method to circumvent this problem is to introduce an asymmetry into the hologram. A blazed grating $\phi_{bg}(x, y) = x \cdot \gamma$ is added to the hologram yielding the intensity distribution

$$I_{total}(x, y) = |\mathcal{FT} \{t_{pix}(x, y)\} * \mathcal{FT} \{h(x, y) \cdot e^{i\phi_{bg}(x, y)} \cdot E_{in}(x, y)\}|^2 \quad (3.41)$$

The optimal slope $\gamma = 2\pi/p_{bg}$ shifts $I_{ideal}(k_x, k_y)$ to the center between the 0th and the +1st (lateral) order, so that there is no overlap with the central spot of the 0th diffraction order. If the SLM is positioned under an angle such that $I_{ideal}(k_x, k_y)$ lies centrally on the optical axis a circular stop (shown in gray in Fig. 3.8b) can be used to block all higher orders as well as the central spot of the 0th order. The experimentally acquired image of a Gaussian beam in fluorescence, with and without the zeroth order is shown in Figure 3.9.

3.4.3 Beam Shaping and Axial Positioning

The exact adjustment of the illumination beam in light-sheet based microscopy is crucial to the image quality. In this section details on the shaping and positioning of illumination beams with an SLM are presented. As can be seen in Figure 2.8, the SLM is imaged by 4 lenses in an $8f$ -configuration into the sample volume. In this section, the scan lens (SL) and the tube lens (TL) are omitted as they are only necessary to include the scanning mirror and contribute a magnification $M = f_{TL}/f_{SL}$. The situation is sketched in Figure 3.10. The SLM is positioned at

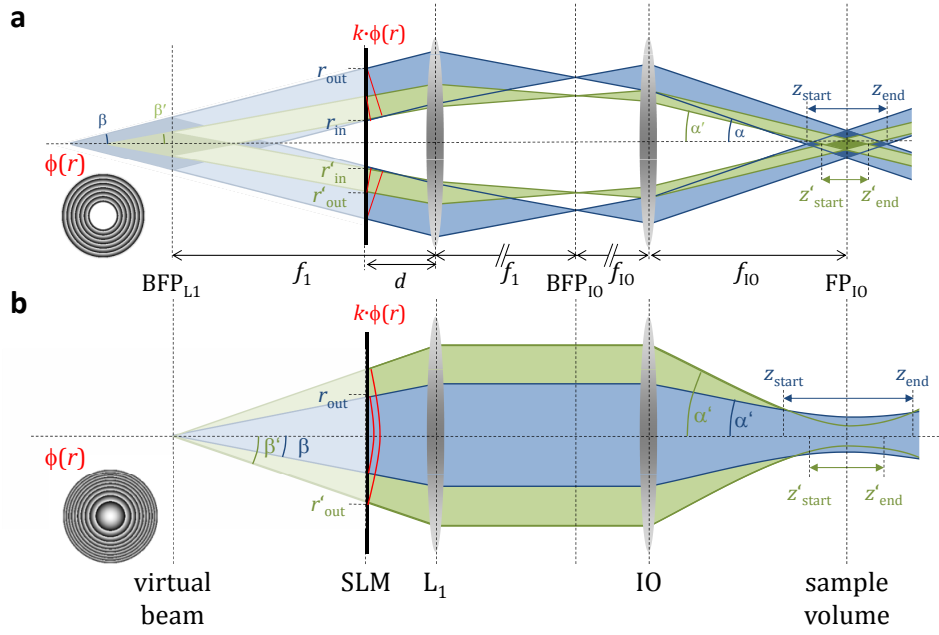


Figure 3.10: Holographic control of the depth of field of Gaussian and Bessel beams.

The virtual beam created by an SLM located at a distance $d < f_1$ to the lens L_1 is imaged into the sample volume by a $4f$ -system consisting of the lens L_1 and the illumination objective lens IO. The phase delay caused by the hologram $\phi(r)$ is shown in red. Beams with shorter and longer depth of field are shown in green and blue, respectively. The position and the depth of field $dz = |z_{\text{start}} - z_{\text{end}}|$ of the Bessel illumination beam (a) can be adjusting over the inner and outer radius of the annular amplitude mask r_{in} and r_{out} . The depth of field of the Gaussian beam (b) depends only on the outer radius r_{out} .

a distance d to the lens L_1 that is smaller than its focal length f_1 . A hologram is applied so that the virtual image of a beam is reproduced in the sample volume by the $4f$ -system consisting of two lenses: lens L_1 and the illumination objective (IO). Thereby, the optical path is shortened. Additionally, the afocal position of the SLM offers an elegant possibility to use the SLM for the generation of Bessel beams and Gaussian beams at the same axial position within the sample volume.

Each hologram consists of three parts, as depicted in Figure 3.11. After adding a phase grating to the hologram phase $\delta\phi(x, y)$ to block parasitic orders of the SLM (3.4.2), an aperture function $t(x, y)$ is multiplied to steer the position and size of the beam. Section 3.4.5 contains details on the optimum shape of the aperture function.

In the following, holograms for the generation of Bessel beams, Gaussian beams and light-sheets as shown in Figures 3.12 will be presented. Following eqn 3.38 the hologram for the generation of a Bessel beam is given by

$$\delta\phi(x, y) = -k_r \cdot r \quad (3.42)$$

$$t(x, y) = \Theta(r - r_{\text{out}}) \cdot \Theta(r_{\text{in}} - r) \quad (3.43)$$

where $r = \sqrt{x^2 + y^2}$ is the radial distance from the optical axis (and the SLM center) and $k_r = 2\pi/p$ is the slope of the phase axicon. The amplitude modulation is given by an annular aperture with inner and outer radius defined by r_{in} and r_{out} , respectively. The phase of the Bessel beam has a conical shape. The beam can be decomposed in plane waves that propagate with an angle

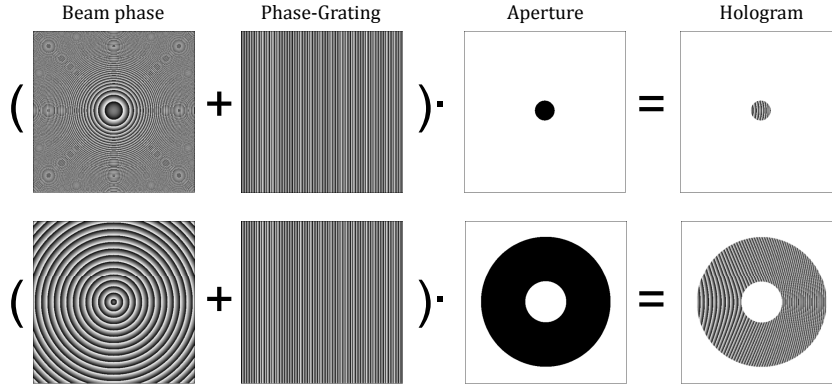


Figure 3.11: The composition of holograms for beam shaping.

The hologram for holographic shaping of beams with well-defined focal depth by application of an aperture is demonstrated for a Gaussian beam (top row) and a Bessel beam (bottom row).

$\beta = \arctan(\lambda/p) = \arcsin(k_r/k_0)$ relative to the optical axis. In the object plane, the Bessel beam is formed by the interference of plane waves with their wave-vector lying on the surface of a cone with angle $\alpha = \beta/M$, where $M = f_{IO}/L_1 \cdot f_{TL}/f_{SL}$ is the magnification of the telecentric lens system. The illumination beam's NA is determined by $NA = n \cdot \sin \alpha = n \cdot \sin(k_r/k/M)$. The dimensions of the diamond-shaped area of interference where the Bessel beam is formed, i.e. the central lobe with the surrounding ring system, can be estimated by geometrical considerations, yielding length dz and radius dr

$$dz = -M^2 \cdot \frac{r_{\text{out}} - r_{\text{in}}}{\tan \beta} \quad (3.44)$$

$$dr = M \cdot (r_{\text{out}} - r_{\text{in}}) \quad (3.45)$$

An example is shown in Fig. 3.10a. For Bessel beams, there are two parameters to tune the depth of field: the radii r_{in} and r_{out} of the aperture and slope of the phase k_r . The radii of the annular aperture can also be used to manipulate the position the Bessel beam. The exact lateral and axial beam profile (the beam's depth of field dz) is dependent on the beam's intensity profile at the SLM $E_{\text{in}}(x, y)$ and the amplitude hologram $t(x, y)$ applied to the SLM. Using eqs 3.44 and 3.45 it is evident that for a given beam length dz the radius $dr = -M \cdot \Delta z / \tan \beta$ increases for a steeper slope $k_r = k_0 \cdot \sin \beta$ of the phase hologram, which corresponds to focusing by a higher NA. Therefore a Bessel beam created by a higher NA carries more energy in the ring system for an equivalent depth of field, as shown in Figure 3.6b.

For comparison, a focused Gaussian beam can be generated by the quadratic approximation to a spherical hologram phase given by

$$\delta\phi(x, y) = -k_0 \cdot r^2 / (2\rho) \quad (3.46)$$

$$t(x, y) = \exp(-r^2 / r_{\text{max}}^2). \quad (3.47)$$

ρ is the radius of the spherical wavefront, which is determined by eqn 3.7. If the distance between the SLM and the back focal plane of lens L_1 is much larger than the beam's depth of field the approximation $\rho \approx f_1 - d$ can be used. The radius r_{max} of the hologram's transmission determines the NA of the illumination beam

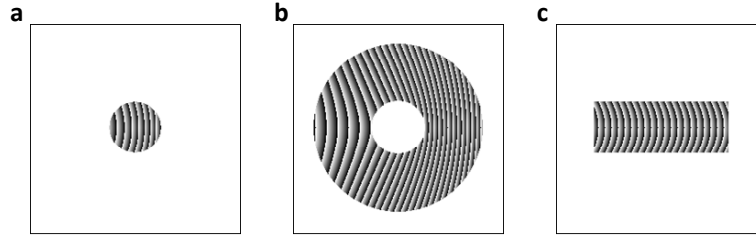


Figure 3.12: Exemplary phase holograms $\delta\phi(x, y)$ for the generation of Gaussian beams (a), Bessel beams (b) and elliptical beams (c) are shown as gray scale images where a phase-shift of $\delta\phi = 0$ is indicated in white and $\delta\phi = 2\pi$ in black.

to which it is linearly proportional. An illustration is shown in Figure 3.10b. Axial positioning is possible by changing the lens phase radius ρ .

The creation of a light-sheet is possible by using a cylindrical lens with a slit aperture according to

$$\delta\phi(x, y) = -k \cdot x^2 / (2\rho) \quad (3.48)$$

$$t(x, y) = \Theta(|x| - w_x/2) \cdot \Theta(|y| - w_x/2). \quad (3.49)$$

In analogy to spherical holograms it is possible to adapt the DOF by changing the aperture width of the cylindrical lens w_x . Positioning along the optical axis is possible via ρ . The width of the light-sheet can be tuned inversely by the width of the lens w_y .

3.4.4 Alignment and Orientation

In light-sheet microscopy the image quality strongly depends on the exact orientation of the light-sheet in the focal-plane of the detection objective lens. The areas illuminated by a misaligned beam suffer from suboptimal contrast. An alignment procedure must therefore guarantee that the axis of the illumination lies perfectly within the plane of focus of the detection objective lens. The beam must neither be tilted nor offset against the focal plane of the DO.

The angular alignment precision of $\tan\vartheta = \delta y / dz$, where ϑ is the tilt angle, is required if a change of the beam position along the detection optical axis of less than δy across the field of view dz is desired.

A Gaussian beam with a depth of field of $dz = 300\mu\text{m}$ exhibits a relatively large width of $dr = 4.2\mu\text{m}$. Gaussian beams with a larger depth of field dz necessarily also feature a larger waist size dr . The requirement on the alignment precision $\delta y < dr$ is approximately independent of the field of view and comparatively weak. For perfect alignment, the requirements are much stronger for Bessel beams because these show a pronounced peak with a diameter in the order of a wavelength over the whole depth of field. The width of the main lobe of a Bessel beam is given by $dr \approx 0.52\lambda / \text{NA}$ and therefore independent the depth-of-field, which depends on the parameter ε for a given NA. A Bessel beam with of a depth of field of $dz = 300\mu\text{m}$ features $dr \approx 0.5\mu\text{m}$ so that it requires $\vartheta < 0.19$ deg. The system is therefore susceptible to mechanical instabilities and thermal drift.

In conclusion, especially for large fields of view the potentially high axial resolution offered by the profile of the Bessel beam also demands precise control over the tilt angle of the beam against the focal plane of the detection objective lens. Manual alignment of the setup is tedious and requires high-precision

optomechanical components. An alternative consists in using the SLM for alignment. As can be seen from eqn 3.39 the position of the beam is determined by the position of the hologram on the spatial light modulator. The orientation (i.e. the tilt angle against the optical axis) is a parameter that is of special importance to illumination beams in light-sheet microscopy because of their large depth of field. Using the blazed grating it is possible to fine-tune the tilt-angle of the illumination beam (Fig. 3.13).

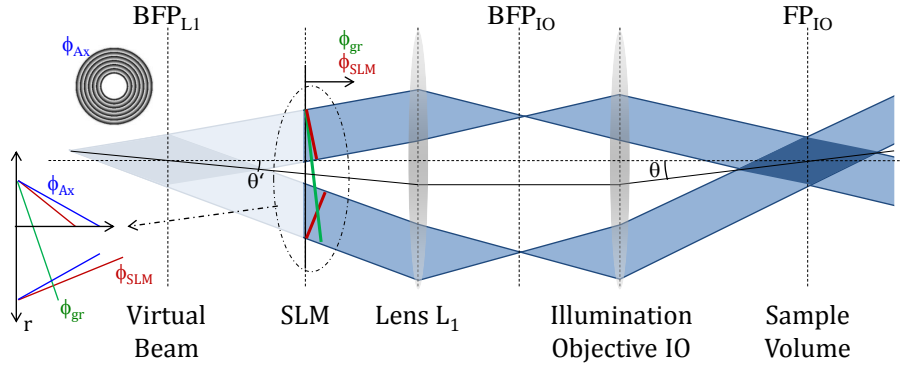


Figure 3.13: Holographic control over the beam orientation.

Addition of a phase grating leads to a tilt of the beam against the optical axis in the sample volume. This effect can be used to precisely align the beam with respect to the optical axis even for oblique illumination of the SLM.

The beam can be moved without being tilted when the hologram is moved on the SLM. The minimum step size

$$s_{x,y} = M \cdot \delta_{SLM}$$

is determined by the pixel pitch of the SLM δ_{SLM} and the magnification of the illumination optics $M = M_{TS} \cdot f_{IO} / f_{L1}$. Typical values are $\delta = 18\mu\text{m}$ and $M = 1/70$ for the Holoeye LC-R2500 or $\delta = 8\mu\text{m}$ and $M \approx 1/40$ for the Holoeye PLUTO so that $s_{x,y} \approx 200 - 250\text{nm}$ which is sufficient because the focal depth of the detection lenses is more than twice as large.

Correction of the tilt angle

$$\vartheta_{x,y} \approx \frac{\lambda}{p_{x,y}} \frac{1}{M}$$

is possible with higher precision and can be achieved by adding a phase grating with 2π -period $p_{x,y}$ to the beam shaping hologram. Tilts within the plane of focus can be corrected by a grating in x -direction and those against the DO's focal plane by a grating in y -direction. Note that the tilt angle in the object volume is increased by the optical system along the illumination path, which consists of two $4f$ -systems with $M \ll 1$ as described above. There is no practical lower limit to the correction as p can be chosen almost infinitely large. It is limited only by the discretization of the phase-shifting capability of the SLM which is $2\pi/256$.

The computer-controlled SLM offers the possibility of automatic alignment. Therefore, a suitable measure for the beam misalignment must be available so that a feedback loop can be used to iteratively correct the hologram. Practical experience has shown that it is most suitable to align the beams in homogenous

fluorescent solution and to insert the sample only afterward. To minimize the tilt angle within the image plane θ_x the peak positions of the (low-pass filtered) lateral intensity profile on both sides of the field of view (i.e. $p(x)$ for small z and large z , respectively) are evaluated. The beam can be aligned by iteratively minimizing the difference in the x -coordinate of the beam positions in the front and the back of the image. The correction of misalignment in y -direction is more complicated. In order to shift the beam into the focal plane, or to correct the tilt against the focal plane several images have to be taken for one tilt angle of the illumination beam θ_y with respect to the object plane. It is assumed that the beam is in the focal plane when the fluorescence signal collected at the position of the main lobe is highest. An iterative procedure based on the repetition of the following steps has proven to be the most robust method to align and position the beam along the detection optical y -axis:

1. Record an image stack for a series of holograms shifted by $y_i = i \cdot s_y$ along the y -axis
2. Find the hologram indices i_{\max} and j_{\max} for which maximum intensity in the front $p(x, y_i, z \approx 0)$ and back $p(x, y_j, z \approx z_{\min})$ is obtained.
3. If $i_{\max} \neq j_{\max}$: Adjust tilt angle θ_y and repeat steps 1-3.

Finally, it is important to note, that alignment using the SLM is suited best for small corrections of the manually pre-adjusted illumination beam.

3.4.5 Low-Pass-Filtering of the Amplitude Mask Against Axial Oscillations of the Beam's Irradiance

Hard clipping apertures $t(x, y)$ result in oscillations of the irradiance $\tilde{I}(k_x, k_y) = |\tilde{E}(k_x, k_y)|^2$ in the BFP, i.e. in pronounced side lobes of the illumination beam, which are detrimental to the image quality. But more importantly, they cause undulations in the axial beam intensity (Fig. 3.14). To solve this problem low-pass filtered smooth apertures can be used which are introduced in this section. A special method is presented to achieve the required amplitude modulation on a phase-only SLM.

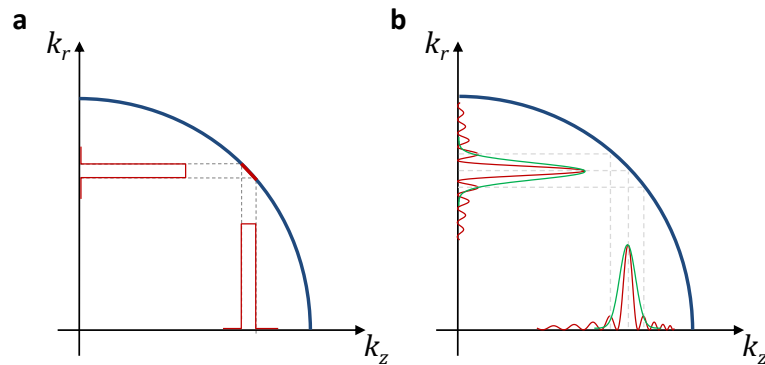


Figure 3.14: Schematic explanation of the effect of low-pass filtering against axial oscillations of the on-axis beam irradiance.

The axial spectrum $\tilde{E}(k_z)$ depends on the lateral spectrum $\tilde{E}(k_r)$ via $k_z^2 = k^2 - k_r^2$. The ideal spectra are shown in (a) in red. $\tilde{E}(k_r)$ created by hard circular apertures is shown in (b) in red. The side lobes are translated into the axial spectrum $\tilde{E}(k_z)$. A low-pass filter (green) can be applied to suppress the side lobes.

The lateral field in the BFP, the spectrum $\tilde{E}(k_x, k_y)$ is a convolution of the spectra of the phase hologram and the amplitude aperture function, respectively and can be written as

$$\begin{aligned}\tilde{E}(k_x, k_y) &= FT \left\{ e^{i\phi(x,y)} \cdot t(x, y) \right\} \\ &= FT \left\{ e^{i\phi(x,y)} \right\} * \tilde{t}(k_x, k_y).\end{aligned}\quad (3.50)$$

When the amplitude function $t(x, y)$ is a circular aperture, then the spectrum \tilde{E} is the Fourier-Transform of the phase-only hologram convolved, i.e. smoothed, with an Airy pattern. In the case of an axicon phase-hologram, the convolution of the Airy pattern with the ring-shaped spectrum creates auxiliary concentric rings (see Figure 3.14). As each ring (k_r -component) produces a Bessel beam with a different k_z -component of the wave-vector, these run out of phase along the propagation axis and produce a (periodic) intensity variation. One can also explain this result with the Talbot-Effect: For periodic spectra the convolution results in periodic side-lobes in the angular spectrum that translate into a periodic axial modulation of the beam. This effect is undesirable for illumination purposes and it can be reduced by applying a smoother aperture on the SLM, i.e. by applying a Gaussian low-pass-filter to the aperture function so that the spectrum does not exhibit side lobes. The low-pass filtered hologram

$$t_{LP}(x, y) = t(x, y) * e^{-(r/r_{LP})^2} \quad (3.51)$$

yields a spectrum

$$\tilde{E}(k_x, k_y) = \mathcal{FT} \left\{ e^{i\phi(x,y)} \right\} * \left(\tilde{t}(k_x, k_y) \cdot e^{-(k_r \cdot r_{LP}/2)^2} \right). \quad (3.52)$$

For example, in the case of a circular aperture $t(r) = \Theta(r - r_{\max})$ the spectrum is given by

$$\begin{aligned}\tilde{E}(k_r) &= \mathcal{FT} \left\{ e^{i\phi(x,y)} \cdot \left(\Theta(r - r_{\max}) * e^{-(r/r_{LP})^2} \right) \right\} \\ &\propto \mathcal{FT} \left\{ e^{i\phi(x,y)} \right\} * \left(\frac{J_1(k_r r_{\max})}{k_r r_{\max}} \cdot e^{-(k_r \cdot r_{LP}/2)^2} \right)\end{aligned}\quad (3.53)$$

The rings of the Airy disc $J_1(k_r \cdot r_{\max})/k_r r_{\max}$ resulting from the sharp aperture are suppressed strongly enough by the Gaussian function to avoid on-axis intensity oscillations of the beam for $r_{LP} < r_{\max} \cdot 3.83/5$ - as the first root of the Bessel-Function lies at $J_1(k_r r_{\max}) = 3.83$. For small r_{LP} the low-pass filter is equivalent to a Gaussian illumination of the hologram. By applying a low-pass filter with a very low r_{LP} it is possible to generate Gaussian beams using the hologram described in eqs 3.46 & 3.47.

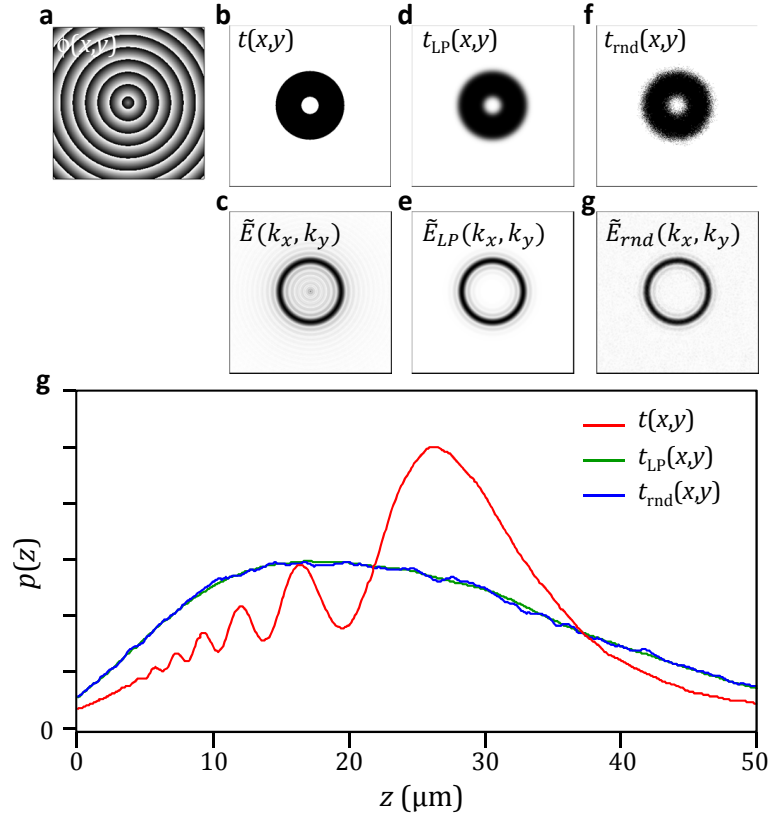


Figure 3.15: Reduction of axial undulations of the on-axis irradiance of a Bessel beam by low-pass filtering of the hologram aperture.

Bessel beams are generated by phase-axicons $\phi(x, y)$ (a) with ring aperture masks $t(x, y)$. The suppression of additional rings in the spectrum (c) of the hard-clipped ring aperture (b) is achieved by low-pass filtering the aperture, shown in (d,e). A random pixel mask (f) can be used to achieve comparable results on phase-only modulators (f). The aperture $t(x, y)$ leads to strong oscillations and an asymmetry of $p(z)$ shown in (g), that is removed for masks $t_{LP}(x, y)$ and $t_{rnd}(x, y)$.

The application of low-pass-filtered apertures requires amplitude modulation by the beam shaping device, in this case an SLM. Similar to most currently available SLMs, the devices (LC-R2500, Pluto by Holoeye, Berlin) used for MISERB do not allow independent field and amplitude modulation. For that reason, a random pixel mask technique similar to [Roichman and Grier, 2006] was applied. The amplitude modulation

$$t_{rnd}(x, y) = \Theta(\text{rnd} - t(x, y)) \quad (3.54)$$

is used where rnd is a random number in the interval $(0,1)$ and $t_{LP}(x, y)$ is the amplitude pattern normalized to 1. In this case the amplitude is modulated by the number of pixels that apply a phase shift to the beam. An example is shown in Figure 3.15f. The resulting axial profile 3.15g is approximately equal to the one obtained for direct amplitude modulation with t_{LP} .

The random pixel distribution technique will be less efficient if only few pixels of the SLMs are used, or, it leads to a strong background of undiffracted light if $t(x, y) < 1$ over large areas. In this case an SLM-based alternative would be to use another SLM for amplitude shaping [Jesacher et al., 2008]. However, losses are to be expected from the non-unity reflection of the SLM, the polarization rotation coupled to the phase manipulation, and the highly increased free-space

propagation distance of the large-diameter beam. An alternative method consists of the grouping of pixels to allow complex field modulation [Agour et al., 2009, van Putten et al., 2008] at the cost of a reduced effective resolution of the SLM.

3.5 COHERENT IMAGING OF ILLUMINATION BEAMS

The holographically shaped beams can be coherently imaged onto the camera sensor by placing a small mirror under an angle of 45° in the sample chamber so that the illumination beam is reflected into the detection objective lens. The transverse irradiance profile of the illumination beam can be measured for several positions along the propagation axis by moving the mirror along the z -axis or y -axis using the precise sample positioning device as presented in Section 2.3.2.3. The coherent imaging process is independent from the PSF of the detection objective (DO), as long as $NA_{\text{det}} > NA_{\text{ill}}$ due to the coherent imaging process. Profiles are shown in Figure 3.16. The Bessel-beam exhibits a thin main lobe with a very narrow FWHM-width of $0.6\mu\text{m}$ over a propagation distance of $dz \approx 130\mu\text{m}$. Distinct rings are visible surrounding the Bessel beam's peak and even though their amplitude is very small, they carry a considerable amount of energy. In contrast, a conventional beam with a considerably shorter depth of field of roughly $40\mu\text{m}$ has a larger waist size of $1.4\mu\text{m}$.

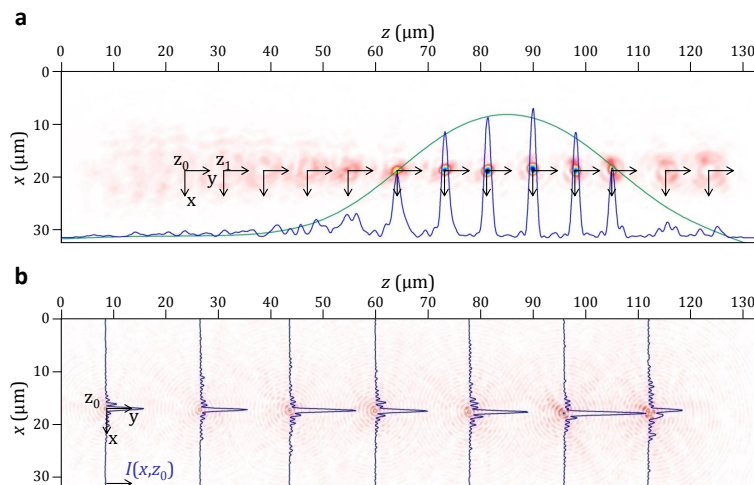


Figure 3.16: Coherent imaging of illumination beams.

Direct measurement of the irradiance cross-section $I(x, y)$ of a Gaussian beam (a) and a Bessel beam (b) with a mirror placed in the confocal volume. The graph shows the sum of the xy -cross-sections that were recorded at equally spaced z -positions.

BEAM PROPAGATION THROUGH SCATTERING MEDIA

In this chapter, the propagation of static beams through scattering media is investigated both by numerical simulation and by recording the beam profile in a light-sheet microscope.

4.1 MEASURES FOR BEAM PROPAGATION STABILITY

An important property of self-reconstructing beams that propagate through scattering media is the directional propagation stability. A measure for this property can be used to answer the following question:

Does the beam follow its initial direction even in the presence of phase perturbations?

Or, put in a more quantitative way:

How large is the proportion of the beam's power within a small area around the beam's axis even in the presence of strong scattering?

In the following section a measure for directional propagation stability is introduced. It is based on the amount of power that a beam carries over a small region around its optical axis. Good images with homogeneous illumination require that this power is independent on the perturbation of the beam. The position-dependence of the on-axis power of the illumination beam that arises from scattering is one source of artifacts in an image. Its strength can be measured by the standard deviation of the position dependent on-axis power (see section 4.1.2).

4.1.1 Directional Stability

A stable beam keeps a large proportion of the power in a small area around the propagation axis in contrast to beams that are scattered or deflected by obstacles. Therefore, directional propagation stability is measured by the radial distribution of the beam's irradiance, i.e. the power that the beam carries up to a certain radius around its propagation axis:

$$P(z; R) = \int_{x^2+y^2 < R^2} I(x, y, z) dx dy. \quad (4.1)$$

The meaning of this formula is illustrated by Figure 4.1.

It is sensible to normalize the power of the beam propagating through a scattering sample P_{scat} to the power of the corresponding ideal beam in homogeneous space P_{ideal} . Thereby, one obtains

$$Q(z; R) = \frac{P_{\text{scat}}(z; R)}{P_{\text{ideal}}(z; R)}. \quad (4.2)$$

which is robust against beam spreading due to diffraction in homogeneous space. Moreover, $Q(z; R)$ is comparable for beams which differ in irradiance and total power. $Q(z; R)$ gives the relative power that a beam is able to maintain within a

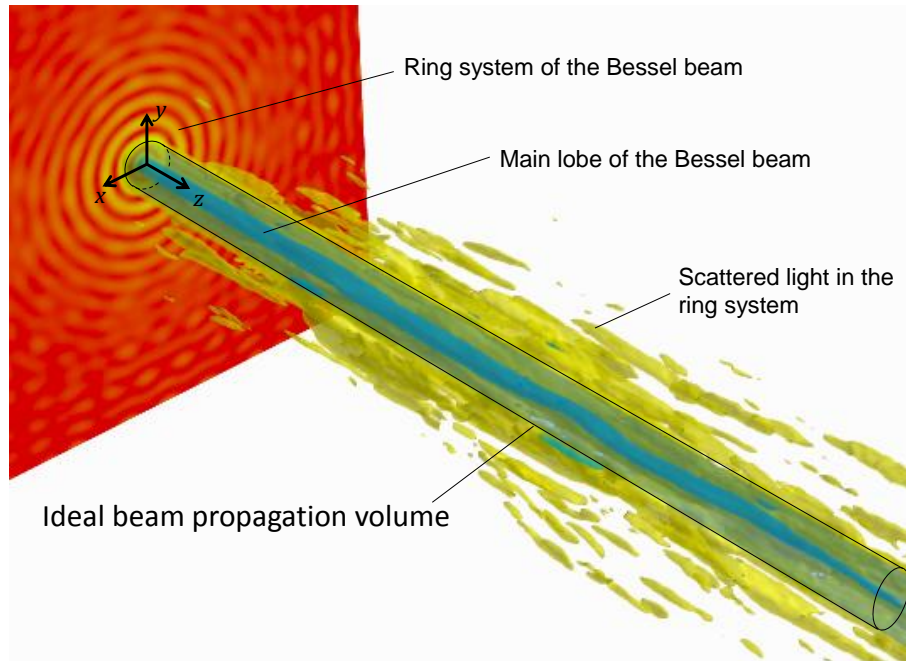


Figure 4.1: Illustration of directional propagation stability.

The figure shows a 3D surface plot of the intensity distribution of a Bessel beam propagating through a cluster of spheres. The data was generated by a computer simulation employing the beam propagation method (BPM) - see Appendix for details. The beam cross-section on the left shows the initial intensity with main lobe and ring system. The intensity of the main lobe (in blue) hardly deviates from a straight line along the propagation in z -direction due to beam self-healing. Scattering is well visible in the ring system (yellow). While the ring system (in yellow) contributes background, the cylindrical outline (black) indicates the optimum detection volume.

small radius R around its axis in the presence of perturbations. The normalized average deviation of the perturbed beam

$$\bar{Q} = \frac{1}{\Delta z} \int_{\Delta z} Q(z) dz \quad (4.3)$$

measures the total deviation from the ideal beam.

Note that $Q(z)$ and especially \bar{Q} offer a significant reduction in data. By computing \bar{Q} only a single value can be used to assess the beam's propagation stability. If this value is used instead of a volume that contains the beam's three-dimensional irradiance $I(r)$, for example in a volume with $256 \times 256 \times 512$ voxels, a reduction of $> 10^7 : 1$ is possible which greatly simplifies data storage and analysis.

4.1.2 Image Contrast from Directional Stability

Using the beam's normalized on-axis power $Q(z)$, it is possible to measure the inhomogeneity of the illumination. If one looks at values of $Q_{i,j}(z)$ for a variety of positions $\mathbf{d}_i = (x_i, y_i)$ in several refractive index distributions $n_j(\mathbf{r})$, it is interesting to compute the normalized standard deviation $\hat{s}(z)$ of the difference

between the on-axis power of the unperturbed beam, $Q_{\text{ideal}}(z)$, and the perturbed beam, $Q_{\text{scat}}(z)$ as a function of the propagation distance z . The expression reads

$$\begin{aligned}\hat{s}(z) &= s(z)/\bar{P}_{\text{ideal}}(z) \\ &= \sqrt{\frac{1}{m_i m_j} \sum_{i,j} (Q_{i,j}(z) - \bar{Q}(z))^2}\end{aligned}\quad (4.4)$$

where m_i and m_j are the number of beam positions \mathbf{d}_i and refractive index volumes n_j , respectively. Note that \bar{P}_{ideal} is independent from i, j so that $\sum_{i,j} \bar{P}_{\text{ideal}}(z) = \sum_{i,j} P_{\text{ideal},i,j}(z)$.

One particular advantage of this measure is that it covers an aspect important to microscopy: the predictability of the beam intensity at a certain location in the sample. The larger the standard deviation, the stronger is the dependency of the illumination on the position of the beam relative to the scatterers and the worse is the homogeneity of the illumination.

This measure can be readily applied to the analysis of light-sheet microscopy images. The beam propagates in the focal plane of the detection lens. The lateral position of the beam axis in the plane relative to a scatterer is b . The line-image $p_{\text{ill}}(b, z)$ along the propagation axis can be described by $p_{\text{ill}}(b, z) = h_{\text{ill}}(x - b, y, z) * h_{\text{det}}(x, y, z)|_{x=b, y=0}$. The normalized standard deviation $\hat{s}(z)$ or the variance $\hat{s}(z)^2$ is

$$\hat{s}(z)^2 = \frac{1}{p_{\text{ideal}}(z)^2} \cdot \frac{1}{B^2} \int_B (p_{\text{ideal}}(z) - p_{\text{ill}}(b, z))^2 db. \quad (4.5)$$

Beams with small values of $\hat{s}(z)$ also exhibit small relative changes in on-axis beam power which may arise from beam deflection or scattering by one or several particles. Analogous to the radius R in eqn 4.1, the on-axis power of the beam can be computed from profiles

$$p_w(b, z) = \frac{1}{w} \int_{-w/2}^{w/2} h_{\text{ill}}(x - b, y, z) * h_{\text{det}}(x, y, z)|_{x=b+x'} dx', \quad (4.6)$$

where the irradiance of the beam along z is averaged over a region of width w . Using p_w makes the measure more robust and practical but less sensitive to the beam power directly on the beam axis. It is sensible to choose the width w to be at least 2 times the beam waist $\Delta x \approx 1.22\lambda/\text{NA}_{\text{ill}}$, i.e. $w > 2\Delta x$. The normalized lateral standard deviation

$$\hat{s}(z) = \frac{1}{\bar{p}_{\text{ideal}}(z)} \cdot \frac{1}{B} \cdot \sqrt{\int_B (\bar{p}_w(z) - p_w(x, z))^2 db} \quad (4.7)$$

where $\bar{p}_w(z)$ is the average axial signal over all positions, i.e. the image width B , can therefore be used as a measure for the light-sheet's inhomogeneity.

4.2 SIMULATION OF BEAM PROPAGATION THROUGH SCATTERING MEDIA

At first, the propagation of coherent beams through scattering samples is investigated numerically. The scattering medium is represented by a distribution of silica spheres with refractive index of $n_{\text{scat}} = 1.41$ in water $n_{\text{med}} = 1.33$ with equal radii. The standard Gaussian beam focused by $\text{NA} = 0.08$ is compared

to two Bessel beams: one with a low-NA ($NA = 0.2$, $\varepsilon = 0.74$) and one with a high-NA ($NA = 0.4$, $\varepsilon = 0.94$). Additionally, a sectioned Bessel beam (see Section 3.2.2) with a high NA ($NA = 0.4$, $\varepsilon = 0.94$) and an azimuthal width of the section of $\beta = 88^\circ$ was analyzed.

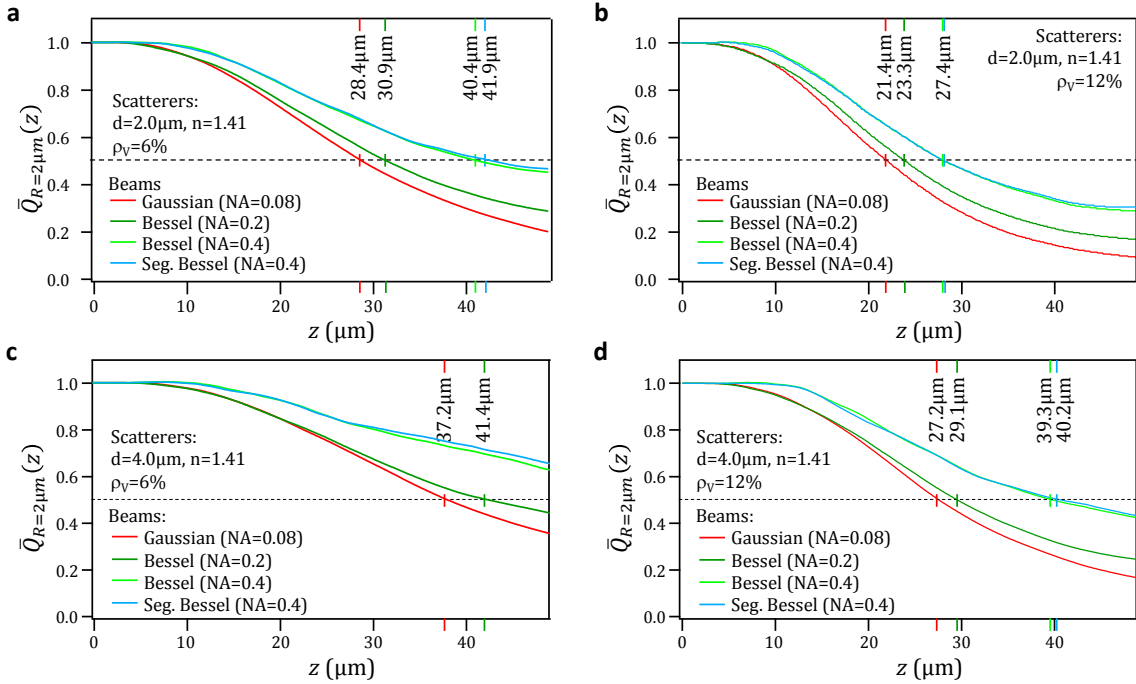


Figure 4.2: Average on-axis power for different illumination beams propagating through scattering media. The graphs show the normalized on-axis power $\bar{Q}(z; R = 2\mu\text{m})$ for different beams. The scattering medium consists of randomly distributed spheres with a difference in refractive index of $\delta n = 0.08$ with respect to the surrounding volume. The diameter of the spheres is $d = 2.0\mu\text{m}$ in (a), (b) and $d = 4.0\mu\text{m}$ in (c), (d). The volume concentration is $\rho_V = 6\%$ in (a), (c) and $\rho_V = 12\%$ in (b), (d). $\bar{Q}(z; R = 2\mu\text{m})$ is the the beam power measured over a circular cross-section with a radius of $R = 2\mu\text{m}$. The average is taken over 9 different lateral positions (x_i, y_i) in 15 different distributions of scattering spheres.

The directional stability is measured by computing the stability ratio $Q(z)$, i.e. the power carried by the beam within a defined radius R around the beam axis as described in 4.1.1. To obtain representative results, the beams were propagated at different positions $\mathbf{d}_i = (x_i, y_i)$ for several refractive index distributions $n_j(x, y, z)$. The stability ratio $\bar{Q}(z)$ was then computed as the average over all beam positions in all samples. Different parameters of the scattering sample, i.e. volume concentrations ($\rho = 6\%$, $\rho = 12\%$) and size ($d = 2\mu\text{m}$, $d = 4\mu\text{m}$) were evaluated. Typical results are shown in Figure 4.2. It can be seen that $\bar{Q}_{R=2\mu\text{m}}(z)$ is essentially equal for the Gaussian beam and the low-NA Bessel beam. For both beams the values of $\bar{Q}(z)$ for large z are inferior to those for the high-NA Bessel beam and surprisingly also the sectioned high-NA Bessel beam. This result means, that the power of the beam within a radius R around the propagation axis is higher for (sectioned) Bessel beams if the NA of the beam is high. The penetration depth is higher for larger spheres for all illumination beams. These obstacles scatter more light in forward direction, i.e. they remove less light from the beams. This result qualitatively agrees with a rough estimate using the reduced scattering coefficient $\mu'_{\text{scat}} = (1 - g)\mu_{\text{scat}}$ where g is the size-dependent scattering anisotropy factor.

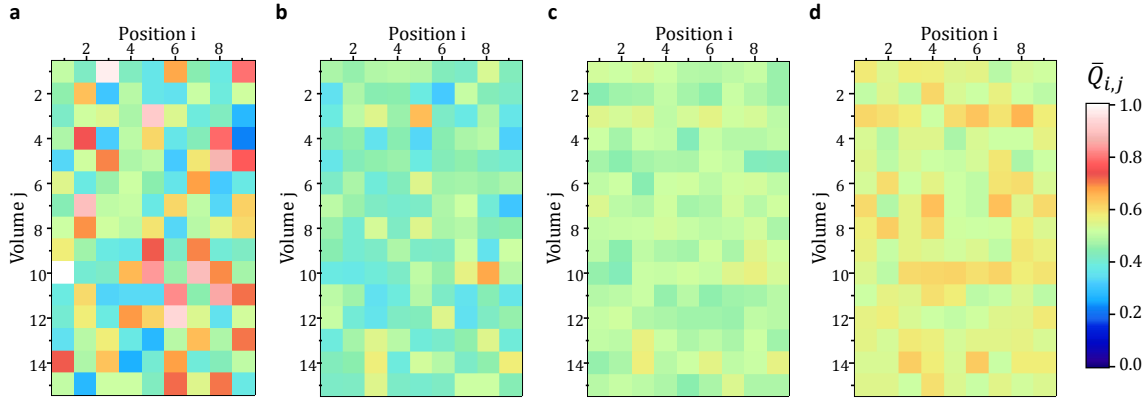


Figure 4.3: Average normalized on-axis power for beams propagating through distributions of scattering spheres at different beam positions.

The average on-axis power $\bar{Q}_{i,j}$ for beams that propagate through a scattering media made of scattering spheres ($d = 2\mu\text{m}$, $\delta n = 0.08$, $\rho_V = 6\%$) is shown for different beam positions i and different random position configurations of the spheres j . The color codes the on-axis power average along the propagation distance through the scattering spheres for a Gaussian beam with $\text{NA}=0.08$ (a), a Bessel beam with a low $\text{NA}=0.2$ (b), a Bessel beam with a high $\text{NA}=0.4$ (c) and a sectioned high-NA Bessel beam with the same NA (d). The variation in the values $\bar{Q}_{i,j}$ is strongest for the Gaussian beam and weakest for the high-NA Bessel beam and sectioned Bessel beam.

The data obtained was analyzed in more detail. The average power ratio along the simulated volume $\bar{Q}_{i,j} = 1/\Delta z \int_{\Delta z} \bar{Q}_{i,j}(z) dz$ in dependence of the beam position i (lateral axis) and the volume j (vertical axis) is shown in Figure 4.3. $\bar{Q}_{i,j}$ is coded by the color. While white represents $\bar{Q}_{i,j} \approx 1$, meaning that the power is approximately equal in the scattered and unscattered case, green and blue spots indicate weak irradiance and a low power of the beam in the area around the propagation axis. Note that Figure 4.2 shows that the on-axis power decreases monotonously, which is a prerequisite for the conclusions drawn from the values of $\bar{Q}_{i,j}$. A large difference between the results for a Gaussian beam and the various Bessel beams can be observed. The variance of the values $\bar{Q}_{i,j}$ is high for the Gaussian beam (Fig 4.3a) while it is small for the high-NA Bessel beam (4.3d). This indicates the stronger susceptibility of the Gaussian beam to local perturbations. The low-NA Bessel beam shows stronger variance than the Gaussian beam but significantly more than the high-NA Bessel beam. The sectioned Bessel beam surprisingly shows very moderate variations.

It is interesting to look at the intensity distribution of the beams for two extreme situations, i.e. position $i = 1$ in volume $j = 10$ where $\bar{Q}_{i,j}$ is exceptionally high for the Gaussian beam and position $i = 9$ in volume $j = 4$ where $\bar{Q}_{i,j}$ for the Gaussian beam is very low. In the first case, the Gaussian beam propagates through a region practically without spheres and therefore remains almost unperturbed, whereas in the second case the Gaussian beam directly hits an obstacle and is strongly perturbed and deflected from its initial propagation axis. In contrast, the high-NA Bessel beam 4.3 exhibits a very weak perturbation in both cases that mainly affects the ring system. Most importantly, the main lobe is neither deflected nor strongly distorted.

It can be seen in Figure 4.4 that for $i = 1$ & $j = 4$, i.e. an average value of $\bar{Q}_{i,j}$, the central peak of both beams is quite well maintained of the whole distance. The main lobe of the Bessel beam is much more confined and is well separated from the ring system, whereas the Gaussian beam is blurred over a larger area.

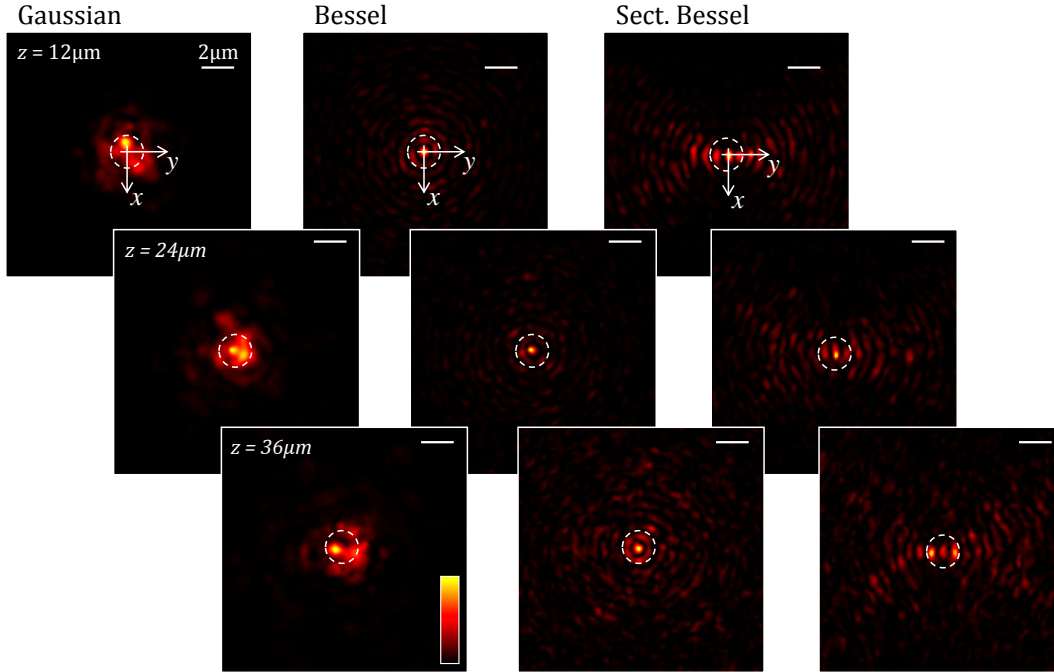


Figure 4.4: Irradiance cross-sections of a Gaussian (a) and a Bessel beam (b) propagating through a scattering medium that consists of spheres with $d = 1\mu\text{m}$, $n = 1.41$ at a volume concentration of $\rho = 6\%$. A slice $I(x = 0, y, z)$ is shown alongside transverse cross-sections $I(x, y, z = z_i)$ for three propagation distances $z_0 = 12\mu\text{m}$, $z_1 = 24\mu\text{m}$, $z_2 = 36\mu\text{m}$.

From these simulation results the following conclusions can be drawn. Gaussian beams show penetration depth and directional propagation stability that is inferior to high-NA Bessel beams, but not to low-NA Bessel beams. Surprisingly, high-NA sectioned Bessel beams are equally robust as Bessel beams with the same NA. Moreover, whereas Gaussian beams are sensitive to local perturbations. This is possibly due to the larger cross-section of the Bessel beams: more scatterers affect the beam, but the impact of each single scatterer is much lower. A potential application for sectioned Bessel beams is presented in Section 6.8.

4.3 LIGHT-SHEET MICROSCOPY IMAGES OF BEAM PROPAGATION IN SCATTERING MEDIA

In this section, the propagation of static beams through various samples will be investigated using a light-sheet microscope. The section is structured in a way that the complexity of the refractive index distribution under investigation increases from a few isolated objects that are aligned to extended clusters of many objects with a random distribution.

4.3.1 Two Large Spheres

The first sample under investigation consists of two large silica spheres (radius $a = 4\mu\text{m}$) that are positioned behind each other in a distance of $L = 19\mu\text{m}$ on the illumination z -axis in the focal plane ($y = 0$) of the detection objective lens. The non-fluorescent spheres are embedded in a fluorescent medium. The Gaussian and Bessel beam, positioned in the image plane, are moved in discrete steps of

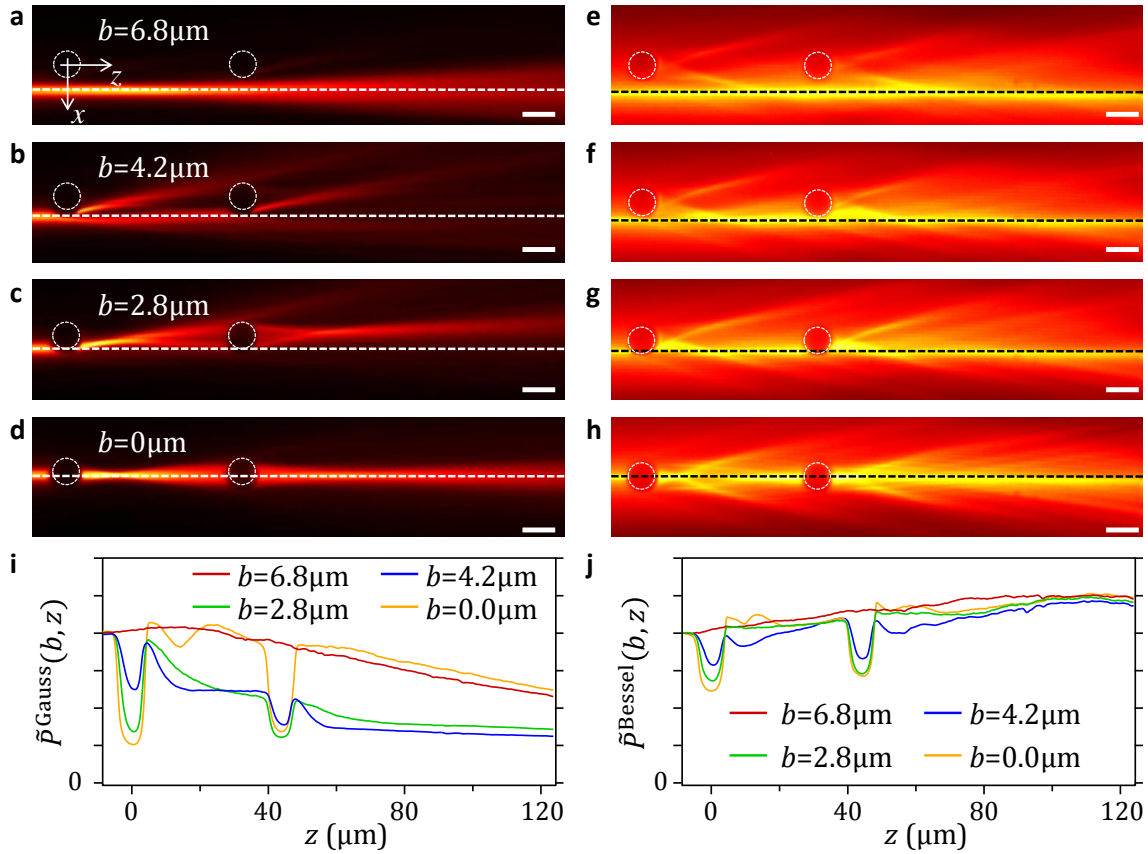


Figure 4.5: Images of Gaussian and Bessel beams propagating at different distances to two large spheres. The images show fluorescence excited by a Gaussian beam (a–d) and a Bessel beam (e–h) at distances b between spheres and the beam axis. The non-fluorescing spheres (diameter $2a = 8\mu\text{m}$) are outlined by white circles. The beam positions are indicated by dashed lines in the images. The on-axis line-profiles of the beams are shown below for the Gaussian beam (i) and the Bessel beam (j). All images have the same dynamic range. The size of the scale bar is $10\mu\text{m}$.

$\delta b = 1.4\mu\text{m}$ towards the sample axis from an initial distance of $b_0 = 6.8\mu\text{m}$. For each beam position i , an image $p_i(x, z)$ of the fluorescence excited by the beam is recorded. For selected positions images are shown in Figure 4.5.

The integral over the image values within a thin stripe of width $w = 2x_m = 4\mu\text{m}$ at lateral position b , $p_w(b, z)$ as defined by eq. 4.6, is proportional to the beam's on-axis power $h_{\text{III}}(b, z)$. An offset is included in $p_w(b, z)$ that is caused by the detection of background fluorescence from out-of-focus planes. Normalization to the unperturbed beam yields $\tilde{p}_w(b, z)$, which is shown in Figure 4.5i and j for the Gaussian and the Bessel beam, respectively.

For a distance $b = 6.8\mu\text{m}$ the Gaussian beam is not affected by the spheres. The corresponding measure for the on-axis power $\tilde{p}_{w=4\mu\text{m}}^{\text{Gauss}}(b = 6.8\mu\text{m}, z)$ of the unperturbed beam is shown in red in Figure 4.5e. For smaller distances of $b = 4.2\mu\text{m}$ and $b = 2.8\mu\text{m}$ shown in 4.5b and c, respectively, the Gaussian beam impinges on the edge of the first sphere and is thereby strongly deflected. This perturbation results in a steep drop of $\tilde{p}_w^{\text{Gauss}}(b = b_0 - i \cdot \delta b, z)$ for $i = 3$ shown in blue and $i = 4$ shown in green, respectively. When the Gaussian beam hits the sphere centrally it is not deflected but only slightly focused (see Figure d and $\tilde{p}_w^{\text{Gauss}}(b = 0\mu\text{m}, z)$ shown in orange in Figure 4.5e.

The Bessel beam shows a completely different behavior. Due to its larger cross-section, the beam is also partly affected at a large distance $b = 6.8\mu\text{m}$. However,

the beam is otherwise unaffected, especially, not deflected. The scattered light forms a V-shaped region of higher signal behind the spheres. The on-axis power $\tilde{p}_w^{\text{Bessel}}(b, z)$ (Figure 4.5j) shows only a slight dependence on the relative distance between beam axis and scatterers b .

The normalized standard deviation of the on-axis illumination power, shown in Figure 4.6, also strongly differs for both beams. The values of $\hat{s}(z)$ are close to zero for the Bessel beam over the full z -range, except the regions occupied by the spheres, indicating the independence of the beams on-axis power from the perturbation by the spheres. For the Gaussian beam, $\hat{s}(z)$ strongly increases behind the first obstacle, even more behind the second sphere and only decreases for larger values of z . The standard deviation that is obtained at the position of the spheres can be regarded as a measure for object contrast offered by the illumination. The contrast due to scattering, $\hat{s}(z \approx 80\mu\text{m})$, reaches approximately 60% of the object contrast for the Gaussian beam.

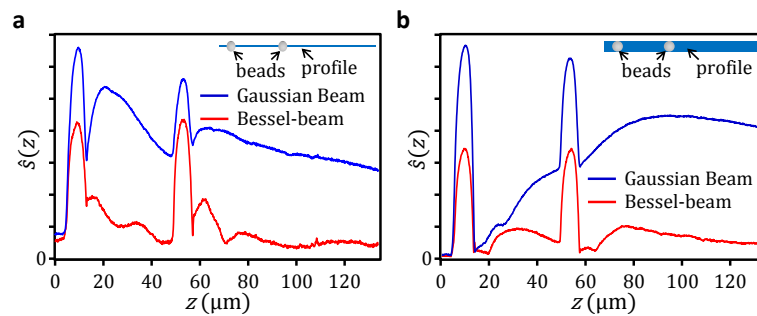


Figure 4.6: Normalized standard deviations of the on-axis beam power.

The normalized standard deviations $\hat{s}(z)$ of the on-axis beam power for beam positions b in the range $b = 0\mu\text{m} \dots 6.8\mu\text{m}$. The analysis was performed for two different widths of the axial profile $2x_m = w = 0.8\mu\text{m}$ and $w = 8\mu\text{m}$.

For this experiment, the object contrast for the Gaussian and the Bessel beam cannot be compared because the focal depth of the beams is not matched. The amount of background is proportional to the beam's depth of field, which is much larger in the case of the Bessel beam. Accordingly, the drop in signal $p_w(b = 0\mu\text{m}, z)$ and the standard deviation at the position of the non-fluorescent sphere is weaker for the Bessel beam. It is important to note that this difference is not the cause for the fundamentally different propagation behavior in the presence of scattering obstacles.

Additionally, a simulation of the beam propagation for $b = a$ was carried out which corresponds to the experimental situation shown in Figures 4.5b and f. Iso-surface plots of the simulated irradiance of the Gaussian beam and the Bessel beam are shown in the top row of Figure 4.7. Irradiance cross-sections in front of and behind the scatterers are shown below. The Gaussian beam is divided into two parts by the edge of the first sphere. The irradiance is strongly reduced behind the second sphere, so that even the iso-surface for the weakest irradiance $I = 50\% \cdot I(x, y, z = 0)$ vanishes. The transverse profile behind the scatterers is strongly distorted (Fig. 4.7d). The line profiles $I_{\text{Gauss}}(x, y = 0)$ and $I_{\text{Gauss}}(x = 0, y)$, shown as insets, reveal that the beam is widely spread at $z = +z_0$. In contrast, the Bessel beam's central lobe impinges precisely on the edge of both the 1st and the 2nd sphere without noticeable change in propagation direction. The Bessel beam's transverse profile at $z = +z_0$ is, besides

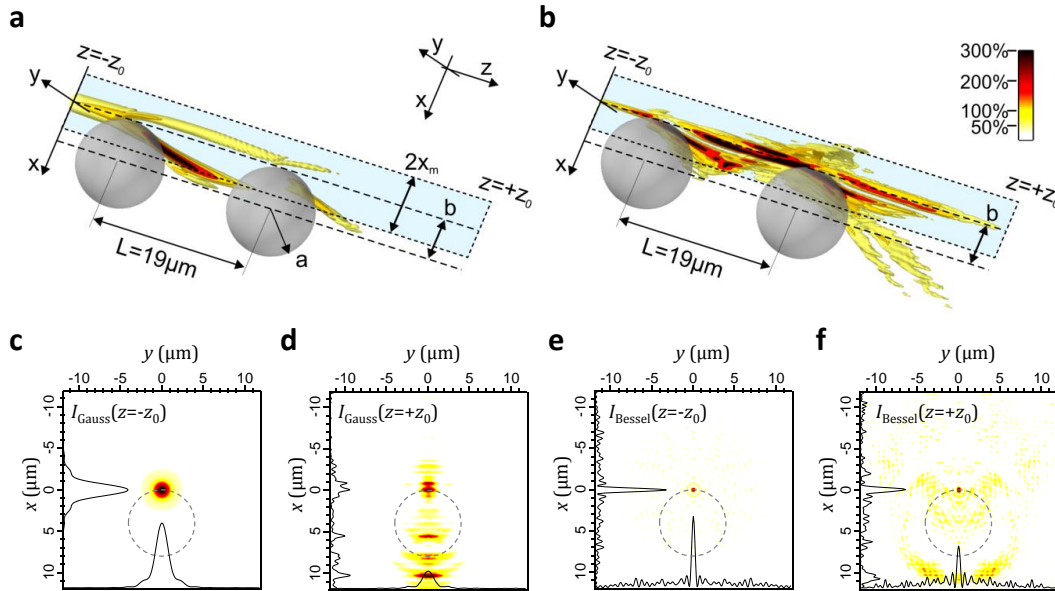


Figure 4.7: Simulation of the irradiance of Gaussian and Bessel beams scattered by two spheres. The spheres with radius $a = 4\mu\text{m}$ and $n = 1.41$ are displaced along the x -axis by a distance $b = a$ from the beam axis. Iso-surfaces of the irradiance for values corresponding to 50%, 100%, 200% and 300% of $I_{\text{max}}(0,0,z = -z_0)$ are shown for a Gaussian beam (a) and a Bessel beam (b). The area shaded in light blue indicates the width w over which the beam irradiance is averaged to obtain $p()$ in Fig 4.5. Cross-sections $I(x,y,z = -z_0)$ before and $I(x,y,z = z_0)$ behind the two spheres are shown in (c) and (d) for the Gaussian beam as well as (e) and (f) for the Bessel beam, respectively. Line-scans through the beam center quantify the beam width and irradiance. The parameters are $\text{NA}_{\text{ill}} = 0.15$ for the Gaussian beam (a, c, d) and $\text{NA} = 0.3$, $\epsilon = 0.8$ for the Bessel beam (b, e, f).

a lower peak irradiance, almost identical to the one at $z = -z_0$ with a distinct localization of intensity at $x = y = 0$.

In summary, experiments and simulations illustrate the far superior performance of the Bessel beam in the presence of two large scattering spheres in an otherwise homogeneous medium. These results were also published [Fahrbach et al., 2010]. The next step is the investigation of beam propagation and self-reconstruction inside scattering media.

4.3.2 A Cluster of Small Spheres

This section presents an investigation of the propagation of Gaussian and Bessel beams into an extended scattering medium (see also [Fahrbach et al., 2010]). The experiment was performed using a cluster of silica spheres ($d = 2\mu\text{m}$, $n = 1.41$) in an otherwise homogenous fluorescent agarose gel cylinder. In contrast to the situation in the previous section, the scattering medium extended over several hundred micrometers so that the beams are affected over a large part of their cross-section.

First, an image of each beam $p_0(x,z)$ was recorded in a plane that was entirely free of scatterers (Fig. 4.8a and c). The sample was subsequently displaced in steps of $\Delta y = 1\mu\text{m}$ along the detection optical axis and an image $p_i(x,z)$ was recorded for each position. A fluorescence image $p_{\text{inh}}(x,z)$ of the scattered beam was recorded in a region with a high concentration of spheres. The image of the Gaussian beam (Fig. 4.8b) clearly shows the spreading due to the perturbation.

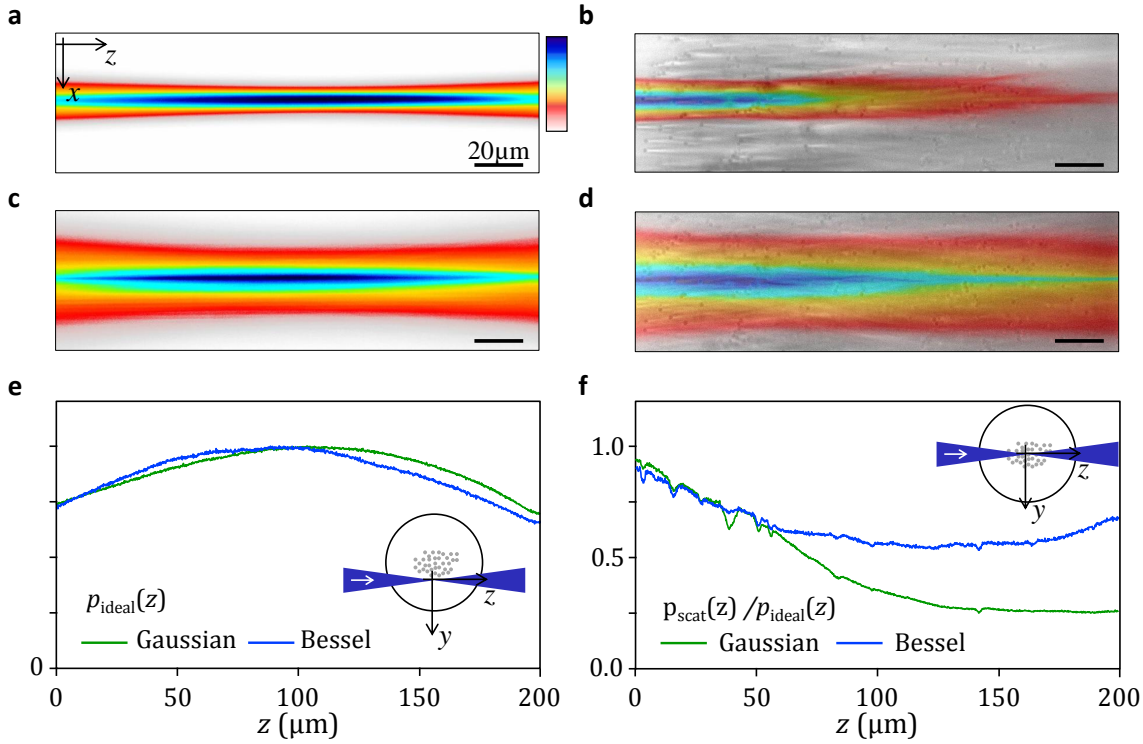


Figure 4.8: Measurement of beam propagation through a scattering medium.

Images of unperturbed static Gaussian and Bessel beam are shown in Figure a and b, respectively. Corresponding images of the fluorescence $p_{\text{scat}}(x, z)$ excited by the beams propagating through a cluster of spheres are shown in c, d. The beams propagate along the z -axis from the left to the right. The static beams are shown in false colors. To show the distribution of silica spheres ($d = 2\mu\text{m}$), a gray-scale image of the sample, taken by scanning the beams across the sample, is overlaid in b, d. The normalized axial intensity line-scans $p_{\text{ideal}}(z)$ with width $w = 10\mu\text{m}$ are shown in e. The relative axial image intensity of the perturbed beam $p_{\text{scat}}(z)/p_{\text{ideal}}(z)$ is shown in f. The position of the beam relative to the cluster is indicated by small insets in e, f.

The beam's focus is almost entirely destroyed in a distance of $z \approx 100\mu\text{m}$. The Bessel beam is much less affected by scattering and a pronounced maximum along the propagation optical axis is maintained even in a depth of $200\mu\text{m}$ inside the scattering medium (Fig. 4.8d)

Axial line-profiles with a width of $w = 10\mu\text{m}$ show that both beams feature an equivalent depth of focus in a homogeneous volume (Fig. 4.8e). The profile of the beam in the inhomogeneous medium relative to that of the unperturbed beam $p_{\text{inh}}/p_{\text{hom}}$ is shown in Figure 4.8f. It can be seen, that the intensity of the Gaussian beam drops to 25% of its initial intensity from $z = 150\mu\text{m}$ on. In contrast, the intensity drops only to 60% for the Bessel beam. It is noteworthy that the Gaussian and Bessel beam show very similar behavior over the first $50\mu\text{m}$. The normalized profile of the Bessel beam shows an increase over the last tens of microns. This effect is partly due to the decreasing $p_{\text{hom}}(x, z)$, by which the profile is normalized, but also indicates a strong self-reconstruction ability even deep inside scattering media. The slopes of the curves are independent from the lateral width of the intensity profile.

4.3.3 Human Skin

To demonstrate the performance on a biomedical object, a piece of fresh human skin with a size of several hundreds of microns was imaged by Philipp Simon [Fahrbach et al., 2010]. Skin features several layers. The refractive index distribution within the layers of the skin is highly inhomogeneous and causes strong perturbation of the beam. The sample is mounted in a way that the laser beam propagates first through the outermost layer, the stratum corneum, and then through the epidermis. The auto-fluorescence of skin yielded only very small signal strengths. Therefore, fluorescing eosin solution was added which can be excited by both the green ($\lambda = 543\text{nm}$) and blue ($\lambda = 488\text{nm}$) laser that were available. The eosin diffused into the skin thereby staining it. However, the diffusion and adhesion worked differently well for the layers so that the fluorophore concentration $c(r)$ could only be assumed to be homogeneous within a layer, but not across the different layers. Images $p_i(x, z)$ of the illumination beam $h_{\text{ill}}(x, z, b_i)$ propagating into the sample at two positions are shown in Figure 4.9.

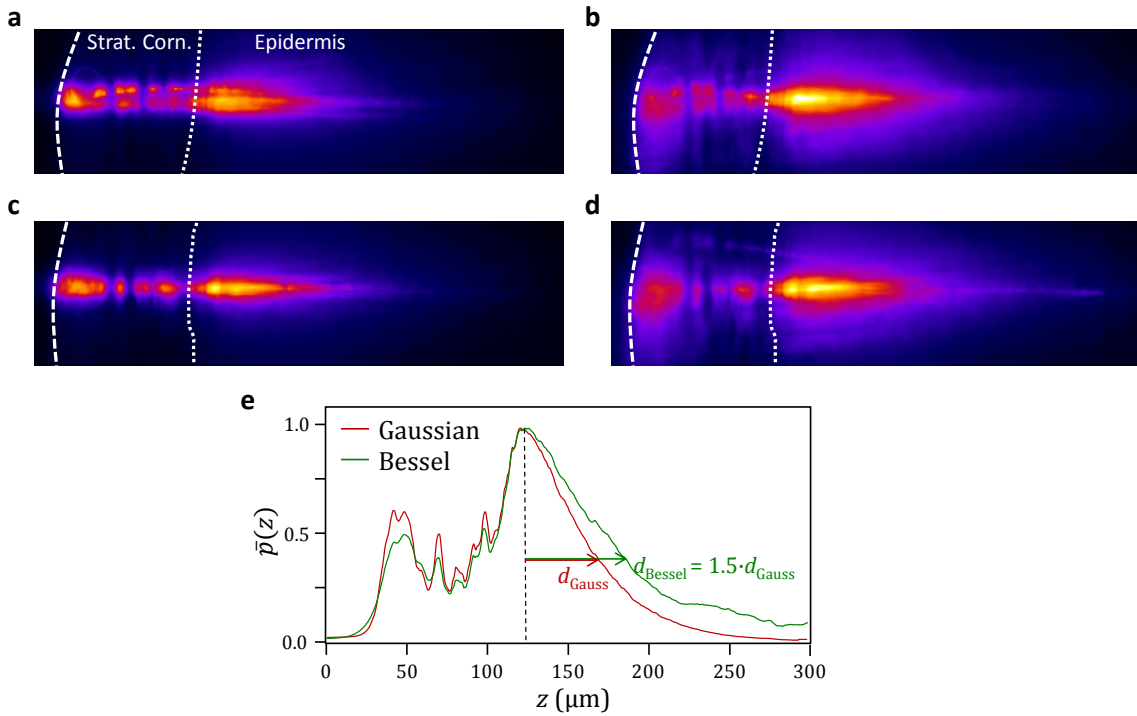


Figure 4.9: Propagation of Gaussian and Bessel beams into human skin.

A Gaussian (a, c) and a Bessel beam (b, d) of equal depth of field propagate into a piece of fluorescently stained human skin. The images show beams at the same lateral position $b = 43.2\mu\text{m}$ (a,b) and $b = 62.3\mu\text{m}$ (b,c). The on-axis beam power $\bar{p}(z)$ averaged over 210 positions in the sample is shown in e.

An image $p_i(x, z)$ of the beam propagating into the sample was taken at 210 positions. The on-axis power $p(z) = 1/w \int_{b-w/2}^{b+w/2} p_i(x, z) dx$ over a width $w = 0.83\mu\text{m}$ was extracted and averaged over all positions to obtain $\bar{p}(z)$. The penetration capability is obtained by a fit of an exponentially decaying function

$$p_{\text{fit}}(z) = p_0 \exp \left\{ - (z/d)^2 \right\} \quad (4.8)$$

to images of the beam profile along z in the region of the epidermis ($z = 138...225\mu\text{m}$). The penetration depth parameters determined in this manner are $d_{\text{Gauss}} = 50\mu\text{m}$ and $d_{\text{Bessel}} = 77\mu\text{m}$. This result indicates an average increase in penetration depth d by 55% for Bessel beams over Gaussian beams (Fig. 4.9e).

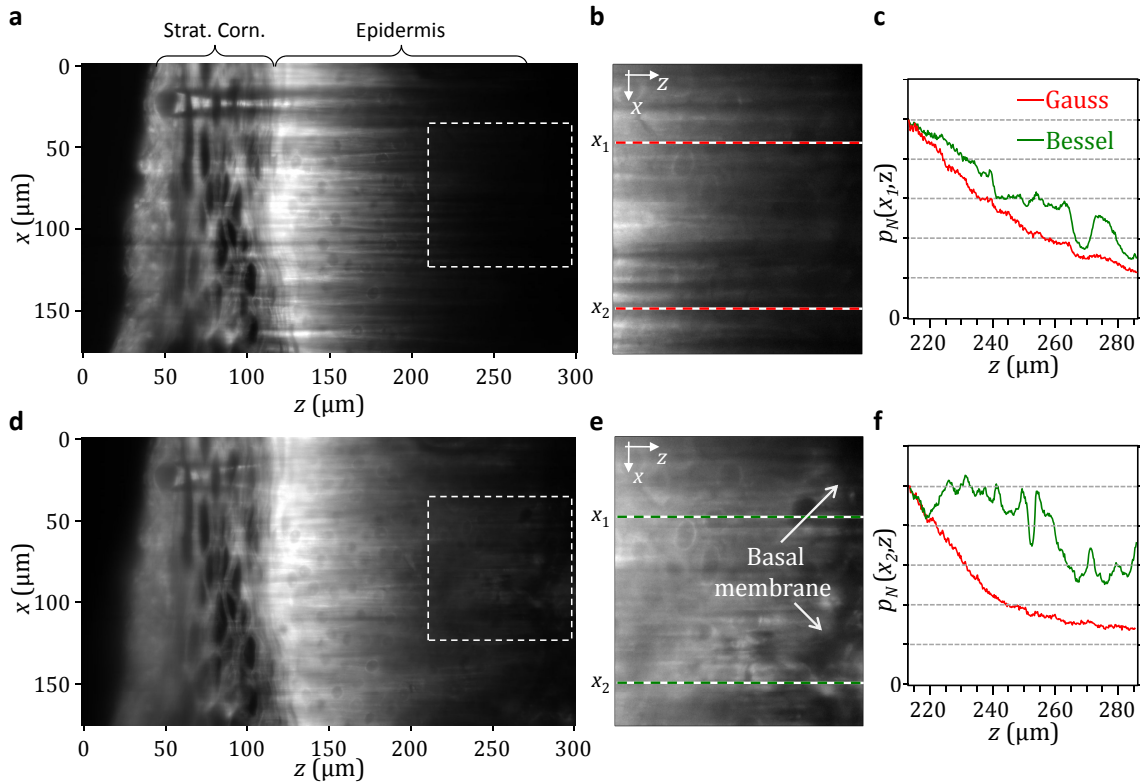


Figure 4.10: Maximum selection images of human skin.

Fluorescence excitation in human skin is shown for a conventional beam (a-c) and a self-reconstructing Bessel beam (d-f). The beams illuminate the skin from the left to the right. The part of the epidermis close to the Basal membrane, is shown in (b) and (e), magnified and separately auto-scaled. The positions are indicated by dashed lines in (a), (d). Single cells are revealed only for Bessel beam illumination (e). Line profiles $p(x_i, z)$ in (c) and (f) reveal the higher contrast provided by Bessel beam illumination. The profiles are normalized to $p(x_i, z = 210\mu\text{m})$. The positions of x_1 and x_2 are marked by dashed lines in (b, e).

This effect has important practical implications. Figure 4.10a, d show images assembled from the beam maxima. The image Fig 4.10b, e show separately auto-scaled details for large penetration depths of the illumination beams $z \approx 205...285\mu\text{m}$, where the higher information content for Bessel beam illumination is apparent: Single cells can be discerned and even the Basal membrane (Figure 4.10e) can be identified. The normalized line-scans shown in Figure 4.10c, f confirm this visual impression. Whereas the Gaussian beam illumination results in monotonously decaying profiles, the illumination by self-reconstructing Bessel beams results in profiles that reveals high-contrast small-scale details.

4.4 DISCUSSION

In this chapter, the propagation of static beams inside scattering media was investigated numerically and experimentally using a light-sheet microscope to observe the fluorescence excited by the beams from the side.

The **definition and use of appropriate measures to quantify beam properties of interest** was of special interest. So far, many important investigations on beam self-reconstruction were not performed in a quantitative way [Bouchal et al., 1998, Garcés-Chávez et al., 2002, Anguiano-Morales et al., 2007a, Broky et al., 2008]. One aspect lay in a large reduction of data volume to enable good comparability. Especially, a direct connection to the properties that link the behavior of the beam to the resulting image quality had to be established. In contrast to [Ersoy et al.], the quantitative analysis was performed in a way to be able to assess the directional stability of the beam (see Section 4.1). By measuring the beam power within a small area around the beam propagation axis, one can directly quantify many important parameters that are of great interest to microscopy: the penetration depth into inhomogeneous media and the influence of the beam position relative to the distribution of scatterers. These are important in a number of other fields as e.g. telecommunication or atmospheric physics [Baykal, 2005]. Beams that show superior directional propagation stability are beneficial to light-sheet microscopy in two ways: increased penetration depth and reduced artifacts. First, an increase in penetration depth, i.e. higher value of $Q(z)$ at large depths z , allows the observation of details deeper within scattering samples. Second, a weaker dependence of the on-axis power on the position of the beam in the medium leads to a more homogeneous illumination of scattering samples. Moreover, confocal-line detection light-sheet microscopy, that is presented in Chapter 6 strongly benefits from beams that show directional propagation stability.

Experimental investigation of beam self-reconstruction: First, an experiment was carried out where the beams are scattered by two spheres with a diameter that is in the order of the cross-section of the Gaussian beam. The experimental data shown in section 4.3.1 is a direct consequence of the self-reconstruction ability of the Bessel beam. The Gaussian beam is affected very strongly because it effectively *sees* a surface strongly inclined against its propagation axis. Consequently, it is deflected. The Bessel beam exhibits two properties that make up its self-reconstruction ability. First, its cross-section is much larger than the spheres so that only a small part of the total power is scattered by the spheres. Secondly, the energy in the beam is transported radially from the rings to the central lobe and then again through the ring system. This effect was also termed *conical dynamics* [Anguiano-Morales et al., 2007b]. The large spheres are mainly forward scattering. For the Bessel beam that is built up of plane waves traveling under an angle $\alpha = \arcsin(\text{NA}/n)$ to the optical axis the scattered field is therefore concentrated on a cone with an opening angle of α behind the scatterers. In images of the beam's cross-section taken by the light-sheet microscope the resulting scattered intensity distribution can be seen as a v-shaped artifact with an angle of $\pm\alpha$. Note that the "v" is also apparent in images (Figure 4.5) where the distance between the beam's propagation axis and the spheres is large and the Gaussian beam is therefore unaffected. However, this off-axis perturbation has only a small effect on the on-axis power as can be seen in the axial beam profiles. Overall, these spheres which have similar size and refractive

index as biological cells are not able to greatly affect the propagation direction or the on-axis power of the Bessel beam. For this thesis this effect was, in contrast to previous studies, quantitatively investigated by computing the standard deviation of $P(z)$ for different distances of the spheres to the beam axis (see section 4.3.1).

Another experiment was performed that shows the beam profile *inside* a scattering medium (§4.8). A comparable measurement has not yet been performed. So far, self-reconstruction was shown by measuring the lateral beam cross-section behind an obstruction with coaxial (anti-parallel) optics [Bouchal et al., 1998, Bouchal, 2002]. Here, due to the perpendicular arrangement of illumination and detection setup the entire beam is visualized and the increasing perturbation of the beam along the propagation axis due to the scattering by the spheres is visualized. A profile of the perturbed beam's axial power is quantitatively compared to that of the unperturbed beam.

Comparison to previous studies on beam self-reconstruction: Few experiments and simulations on the self-reconstruction of beams in inhomogeneous media have been performed so far. They have been mainly restricted to single localized absorbing obstructions. An exception is the work by [Garcés-Chávez et al., 2002] who demonstrated stable optical trapping behind a layer of scattering spheres. However, also in that publication, it was stated that no reconstruction can be expected if the whole cross-section of the beam is blocked and it is not clear how large the fraction of the beam affected by scattering samples was in cases where trapping was achieved. Because the beam profile was not measured it cannot be excluded that trapping was achieved in local maxima of a speckle-like pattern. The numerical studies on the propagation of (higher order) Bessel beams that have been carried out so far dealt with an isolated absorbing object [Bouchal et al., 1998, Bouchal, 2002, MacDonald et al., 1996] with a size comparable to that of the beam's main lobe. In most cases no direct and quantitative comparison between Bessel beams and conventional beams, as e.g. Gaussian beams was performed. To conclude, so far self-reconstruction of Bessel beams has always been investigated for scattering samples that only affect a sub-region of the beam's cross-section. The self-reconstruction was observed in a region that lay behind the so-called self-reconstruction length, where the beam is formed by its parts that were not affected by the upstream obstruction.

Another beam belonging to the class of self-reconstructing beams is the Airy beam [Dowski and Cathey, 1995]. However, this beam, whose self-reconstruction ability has been investigated both numerically and experimentally [Broky et al., 2008, Ersoy et al.], features a main lobe that does not stay on-axis while propagating but moves on a curved trajectory. Due to this property the beams have also been claimed to *accelerate*, even though this effect is simply the result of a change in lateral position of the constructive interference of the plane waves that form the beam. Even though the beam shares the fascinating capability of self-reconstruction, due to its shape it seems not sensible to include Airy beams into a study on light-sheet based microscopy.

Identification of parameters that influence the self-reconstruction ability using simulation data: In section 4.1.1, directional propagation stability was used to evaluate simulation data of coherent beam propagation in scattering media with two different sizes and densities of the scattering spheres. Most importantly, the random distributions extended over the whole cross-section of the beam. This situation has not been investigated so far. It was found that

the robustness of the Bessel beam depends on its NA. The similar performance of the conventional and the sectioned Bessel beam further indicates that the self-reconstruction ability depends on the radial component of the wave-vectors. If the performance was dependent on the cross-section, the conventional beam with the higher NA would show a better performance than the sectioned Bessel beam. For $\beta = 88^\circ$, the sectioned Bessel beam exhibits a cross section that is only half as large as that of the conventional Bessel beam. It seems that while the conventional Bessel beam is affected by more scatterers, the relative weight of each is smaller than in the case of the sectioned Bessel beam. Therefore, in a medium where the scatterers are homogeneously distributed, the relative perturbation of the phase of the Bessel beam and the sectioned Bessel beam are similar.

Sectioned Bessel beams are similar to Mathieu beams with the advantage of a smaller extent of the central lobes along the detection optical axis. Despite the fact that Mathieu beams have been investigated for a long time, no study on their propagation performance in strongly scattering media has been reported so far. Therefore, the results shown here and later in Section 6.8, where a possible application of sectioned Bessel beams is presented, are the first investigation of this class of beams and the first indication that Mathieu beams might show self-reconstruction ability that is similar to Bessel beams.

Simulations were performed using the beam propagation method (BPM) [Feit et al., 1976]. At first, one question has to be answered: **Is it valid to use the beam propagation method?** Despite the obvious advantages like speed, relative simplicity and acceptable precision the method is not widely employed to investigate scattering but the field distribution in optical waveguides or micro-lenses [Feit and Fleck Jr., 1978, Brenner and Singer, 1993]. Other methods that are used to simulate the propagation of light through scattering media as e.g. Monte-Carlo simulations are not suited to account for the beam's phase and therefore of limited usability for the study of beam propagation and the beam's directional stability. The finite-difference time domain (FDTD) method is able to rigorously compute a solution according to the Maxwell equations. FDTD simulations have been successfully employed to simulate the concentration of light by the nuclear architecture of rod photo-receptors in the eye Solovei et al. [2009]. The method is potentially more accurate, but computationally very demanding making it not practically usable to investigate the large volumes that are relevant to the study of beam self-reconstruction in extended scattering media.

The beam propagation method can only correctly account for small changes in refractive index and is based on the paraxial approximation. For this thesis, simulations feature spheres with a refractive index close to that of biological material ($n = 1.41$) in a medium with the refractive index of water ($n = 1.33$). Therefore, the change in refractive index $\Delta n = 0.08$ is small. Moreover, beams with a low $NA < 0.4$ through samples that are mainly forward scattering were investigated. Therefore, only multiple scattering leads to a significant power of the plane wave components at large angles relative to the propagation axis. In the presented data, the relative amount of light affected is small. The simulated volume is not much longer than the mean-free scattering length. The qualitative comparison of the shape of the beam scattered by a large sphere shown in Section 4.3.1 shows a good agreement between theory and experiment. By adding a

small imaginary refractive index the loss of light due to back-scattering can be incorporated.

Comparison to adaptive optics approaches: Altogether the simulations and experiments shown in this chapter indicate that Bessel beams are well suited to direct light into a scattering medium in a controlled way. Recently, a lot of studies have tried to exploit the deterministic nature of the scattering process by adaptive optics. Starting from a perturbed beam these methods employ a feedback loop that measures the power in the beam's focus and iteratively increases it by adapting the spectrum of the incoming beam. These techniques are especially powerful in focusing light onto a spot through a scattering medium [Vellekoop and Mosk, 2007]. It was even achieved to transmit a whole image [Popoff et al., 2010, Vellekoop and Aegerter, 2010] through a turbulent medium. The results are impressive but the method is time-consuming and needs a reference probe that enables the measurement of the power in the focus. Adaptive optics have also been used in point-scanning microscopy [Booth et al., 1998, Booth and Wilson, 2000, Booth et al., 2002, Ji et al., 2010] and optical trapping [Čižmár et al., 2010]. An interesting approach that allows not only to measure the point-wise irradiance but also the phase distortion is the use of the coherent emission of the second-harmonic generated by a probe as presented by [Hsieh et al., 2010]. Mostly, correction is very slow as it must be performed separately for each focus position because it is intrinsically dependent on the local perturbation by the sample. Algorithms used for ptychographic imaging [Rodenburg et al., 2007] that allow to reconstruct the phase delay of an object make use of the overlap for adjacent spots. While this approach might be able to increase speed, the algorithm is not yet designed to deal with thick strongly scattering samples, but treats the sample as a single plane. In conclusion, the Bessel beam's strong robustness against scattering suggests that it might be a better candidate for adaptive optics approaches and enable a faster correction that is less dependent on the surrounding medium.

Summary: Numerical and experimental results shown in this section demonstrate the resilience of Bessel beams to relatively large objects like silica spheres that mainly scatter in forward direction. Biological samples also comprise isotropically scattering fractions which can hardly be separated from the larger particles. Based on the results presented here, addressing the question how self-reconstruction works in the presence of (more) isotropic scattering appears obvious and should be addressed in more detail.

However, in the context of the work presented here, the next step is to investigate if the self-reconstruction ability of the Bessel beam can be exploited to enhance the image quality in light-sheet based microscopy.

LIGHT-SHEET MICROSCOPY WITH SCANNED SELF-RECONSTRUCTING BEAMS

This chapter presents investigations of the image quality produced by illumination with different light-sheets. The light-sheets are generated by scanning a coherent beam in the object plane during the exposure time of the full-frame camera. The first section presents a comparison of the axial resolution and optical sectioning obtained for different illumination beams using simulated data (§ 5.1). In the following, the light-sheet quality is evaluated using unstained samples in a stained environment, as outlined in the concept (§ 1.3). The samples and the analysis are of growing complexity, starting with two large glass spheres (§ 5.2) followed by a barrier of spheres (§ 5.3) and finally, a cluster of spheres (§ 5.4). As an example for the application to a biological sample - images of a drosophila fly are shown and analyzed (§ 5.5). A discussion of the findings closes the chapter (§ 5.6).

5.1 NUMERICAL COMPARISON OF LIGHT-SHEET PROPERTIES

In standard line-scanned light-sheet microscopy the beam is moved with speed $v_x = x_m/T$ along the x -axis, across the field of view with width x_m during the exposure time T of the camera. For the time-dependent displacement $\mathbf{b}(t) = (v_x \cdot t, 0, 0)$ of the illumination beam $h_{\text{SB}}(\mathbf{r} - \mathbf{b}(t))$ the effective irradiance of the light-sheet is

$$h_{\text{scan}}(\mathbf{r}) = \frac{1}{T} \int_0^T h_{\text{SB}}(\mathbf{r} - \mathbf{b}(t)) dt. \quad (5.1)$$

This expression is qualitatively equivalent to the projection of the power distribution of the beam along the scan direction $h_{\text{proj}}(\mathbf{r}) = 1/x_m \int_{x_m} h_{\text{SB}}(\mathbf{r} - \mathbf{b}_x) db_x$ with $\mathbf{b}_x = (b_x, 0, 0)$. In both cases no border effects are taken into account.

In the following, resolution and optical sectioning that can be achieved with light-sheets generated by Gaussian and Bessel beams are assessed by using the system point-spread function $h_{\text{sys}}(\mathbf{r}) = h_{\text{ill}}(\mathbf{r}) \cdot h_{\text{det}}(\mathbf{r})$, where $h_{\text{ill}}(\mathbf{r})$ is the illumination point-spread function and $h_{\text{det}}(\mathbf{r})$ the detection point-spread function. Note that whereas h_{ill} has units W/m^2 , the three-dimensional detection probability distribution h_{det} is unit-less (see §2.1). Using the measure introduced in section 2.2.2, it is possible to assess the performance offered by different illumination. In this chapter, the analysis will be conducted using numerical data obtained from simulations with the propagator approach (see Appendix B).

5.1.1 Axial Resolution of Line-Scanning Light-Sheet Microscopes

Resolution, as introduced in Section 2.2.2 is a measure for the minimum distance at which two point sources can be perceived as two separated objects. It can be obtained from the $1/e$ -width of the profile along the detection axis through the system-PSF $h_{\text{sys}}(0, y, 0)$. A slice through the detection PSF $h_{\text{det}}(0, y, z)$ is shown

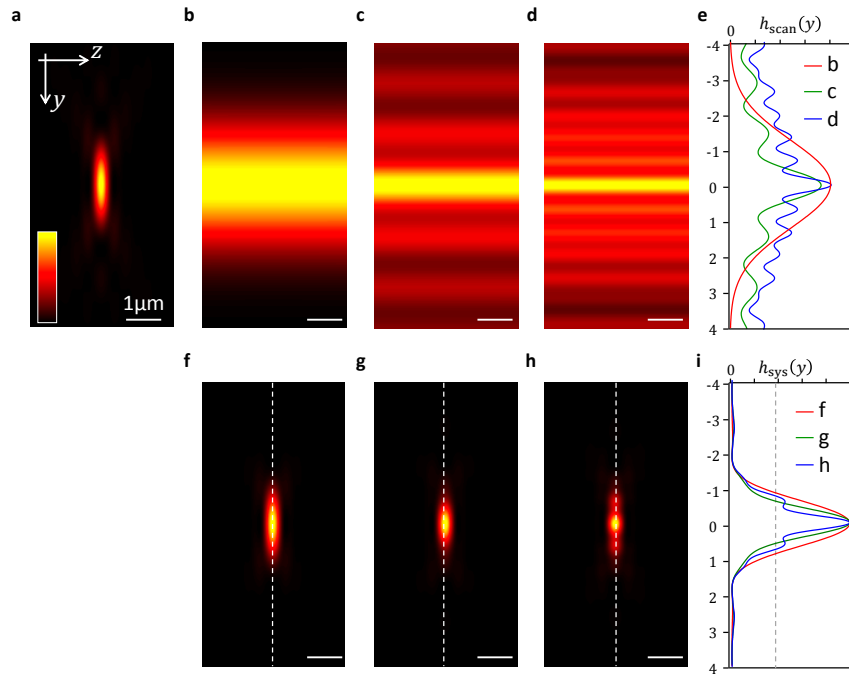


Figure 5.1: Axial Resolution for different scanned illumination beams:

The figure shows slices ($x = 0$) through the detection point-spread function for $\text{NA}=0.95$ (a), the irradiance $h_{\text{scan}}(0, y, z)$ of three illumination light-sheets (b-d) and the corresponding image of a point, i.e. the system PSF $h_{\text{sys}}(0, y, z)$ (f-h). The light-sheet is generated by a Gaussian beam (b,f), a low-NA Bessel beam with $\text{NA}=0.2$ (c, g) and a high-NA Bessel beam with $\text{NA}=0.4$ (d, h). Axial profiles ($x = y = 0$) through the light-sheets are shown in (d). The axial resolution can be deduced by measuring the $1/e$ -width (indicated by gray dashed line) of $h_{\text{sys}}(0, y, 0)$ shown in (i). All beams exhibit equal depth of field.

in Figure 5.1a alongside cross-sections $h_{\text{scan}}(0, y, z)$ for three light-sheets with equal depth of field along z (Fig. 5.1b-d). The line-profiles shown in Figure 5.1e reveal that the projection due to the beam scanning (eq. 5.1) blurs the ring system of the Bessel beams and effectively broadens the light-sheet by a considerable amount. In the row below, slices through the image of a point source $h_{\text{sys}}(0, y, z)$ are shown for illumination by the three light-sheets. It can be seen from Figure 5.1i that the resolution, corresponding to the $1/e$ width of the profile $h_{\text{sys}}(0, y, 0)$, is very similar for all modes because it is dominated by the detection PSF.

5.1.2 Optical Sectioning

Optical sectioning measures the thickness the light-sheet. More precisely, it quantifies the range along the detection axis out of which signal is detected. It was introduced in detail in Section 2.2.3. Numerical results are shown in Figure 5.2 for the same three light-sheets as in the previous section. However, here, projections of the detection PSF and the system PSF along the x -axis are shown in Figures 5.2a and f-h, respectively. The fluorescence detected from the different xz -layers, $F(y)$ is proportional to the irradiance of the light-sheet $h_{\text{scan}}(y)$. The integral of $F(y)$ along y , $G(y)$ (eq. 2.20) is shown in Figure 5.2i. There, one can see that while the scanned Gaussian beam offers best optical sectioning (a step slope around $x = 0$), the scanned Bessel beams lead to inferior

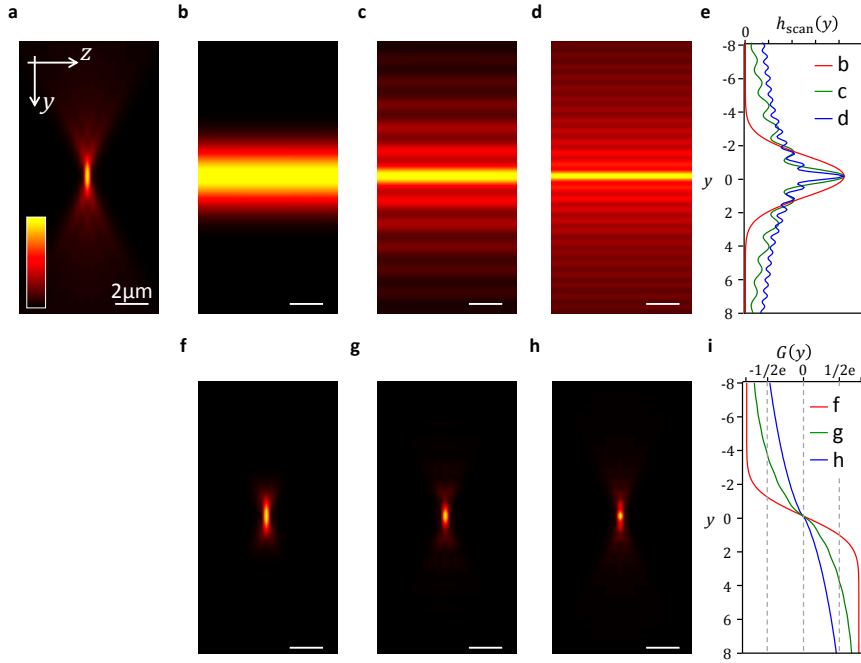


Figure 5.2: Optical sectioning for different scanned illumination beams:

The projection of the detection point-spread function for a numerical aperture of $NA_{\text{det}} = 0.95$ is shown in a. Cross-sections through light-sheets generated by a Gaussian beam, and a Bessel beam with a low NA and a high NA are shown in b-d. The projection of the image of a point (h_{sys}). The slope of the curves indicates the relative amount of signal detected from the specific plane. A flatter curve indicates weaker optical sectioning.

performance especially for the high NA. A lower relative amount of the collected signal originates in the vicinity of the focal plane of the detection objective lens and therefore the signal-to-background ratio is lower for illumination by scanned Bessel beams.

Note that while $h_{\text{sys}}(y, z)$ shown in Figures 5.2f, g, h is affected by NA_{det} , F_{int} in 5.2i is not. This fact can be understood by looking at

$$\begin{aligned} F(y) &= \iint h_{\text{sys}}(x, y, z) dx dz \\ &= \iint h_{\text{ill}}(x, y, z) \cdot h_{\text{det}}(x, y, z) dx dz. \end{aligned} \quad (5.2)$$

For illumination by a light-sheet one can assume h_{ill} to be invariant along the scan axis (x) and along the illumination optical axis (z) over the whole field of view. Therefore

$$F(y) = h_{\text{ill}}(y) \iint h_{\text{det}}(x, y, z) dx dz.$$

holds. Due to energy conservation the power of the beam along the detection optical axis is constant: $\iint h_{\text{det}}(x, y, z) dx dz = \text{const}$ so that

$$F(y) \propto h_{\text{ill}}(y). \quad (5.3)$$

As a consequence, the optical sectioning for scanned illumination beams is solely given by the shape of the illumination beam $h_{\text{ill}}(y)$.

5.2 TWO BEADS

A good example for the effect of illumination light scattering by individual cells is represented by two silica spheres ($d = 8\mu\text{m}$, $n = 1.41$), which, in the measurement shown in Figure 5.3, are positioned along the illumination optical axis at a distance of $70\mu\text{m}$. The situation is similar to that shown in Section 4.3.1 except for a larger distance between the spheres. Three illumination beams with equal depth of field are used. A static light-sheet formed by a cylindrical lens, a laterally scanned Gaussian beam with $\text{NA} \approx 0.06$ and a laterally scanned Bessel beam with $\text{NA} \approx 0.18$, $\varepsilon \approx 0.88$. A normalized axial profile $p_N(z) = p_{\text{scat}}(z)/p_{\text{ideal}}(z)$ is shown in Figure 5.3d. The width of the profile $w = 16\mu\text{m}$ accounts for the v-shaped scattering artifacts behind the spheres in the case of the Bessel beam illumination as well as the thin foci in the other illumination modes. The normalization profile $p_{\text{ideal}}(z)$ is recorded in another y -plane without spheres. The optimum light-sheet would lead to a constant value of $p_N(z) = 1$ except at the positions of the spheres. Overall, a higher value of p_N is apparent behind the spheres for all illumination modes. The deviations are strongest for illumination by a static light-sheet where the second sphere is hardly visible due to the strong shadow-like scattering artifact originating at the first sphere. While scattering of the Gaussian beam primarily leads to a very localized increase in signal by the focusing of the sphere, the normalized profile reveals a significant drop in signal meaning that $p_N(z) < 1$ behind the foci. For a light-sheet generated by a scanned Bessel beam the line profile $p_N(z)$ is almost constant. The increase due to scattering by the spheres is very small and the profile regains its initial value shortly behind each of the two scatterers.

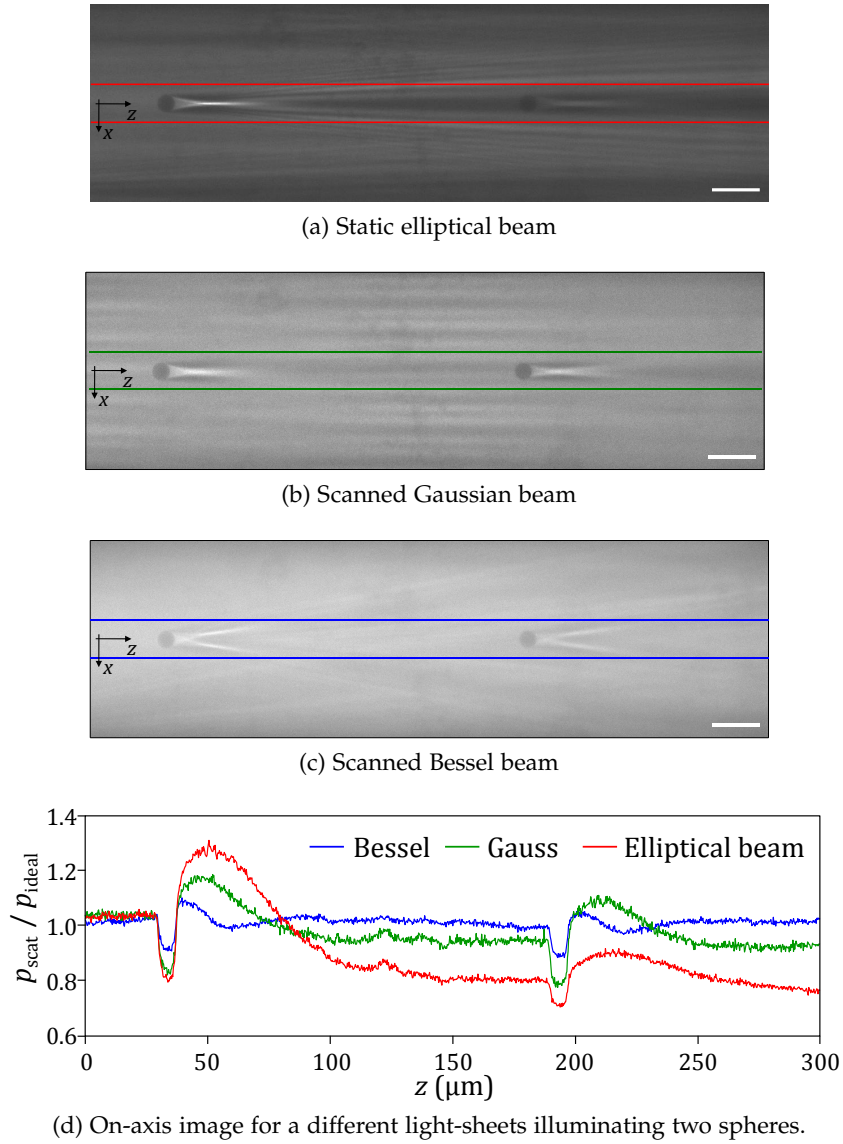


Figure 5.3: Light-sheet microscopy of two non-fluorescent spheres.

A sample consisting of two silica spheres ($d = 8\mu\text{m}$) located on the illumination optical z -axis is imaged by a light-sheet microscope for three different illumination modes: A static light sheet formed by a static elliptical beam (a), a scanned Gaussian beam (b) and a scanned Bessel beam (c). The normalized intensity profile $p_{\text{scat}}(z)/p_{\text{ideal}}(z)$ is shown in (d). $p_{\text{scat}}(z)$ is obtained from the region that is marked by the lines in the corresponding color in the images above.

5.3 A BARRIER OF SPHERES

The effect on the light-sheet homogeneity when illumination beams have to propagate through a scattering environment is investigated in this section. Figure 5.4 shows the image of a light-sheet for scanned Gaussian and Bessel illumination beams. The beams propagate along the z -axis and have to penetrate through a localized barrier consisting of randomly distributed silica spheres. The spheres can be seen on the left side of the images. The refractive index and fluorescent dye concentration to the right side of the spheres are constant so that solely the fluorescence signal is proportional to the irradiance of the light-sheet. The comparison of two regions is especially noteworthy. The positions α are good examples for an artifact created by constructive interference of scattered light, whereas at positions β destructive interference leads to shadowing of the illumination light by the aggregation of spheres. Remarkably, Bessel beam illumination is able to reduce both effects. Apparently, the v-shaped distribution of light scattered by the spheres leads to a weaker localization of the artifacts.

A lateral profile $I(x, z = 10\mu\text{m})$ through the images shown in Figure 5.4c reveals that the deviations for illumination by a Gaussian beam are much more pronounced. The higher value of the normalized standard deviation $\hat{s}(z)$ shown in Figure 5.4d also indicates the strong inhomogeneity of the light-sheet (§ 2.2.5). Behind the scatterers, the value of $\hat{s}(z)$ is about two times larger for the Gaussian beam than for the Bessel beam.

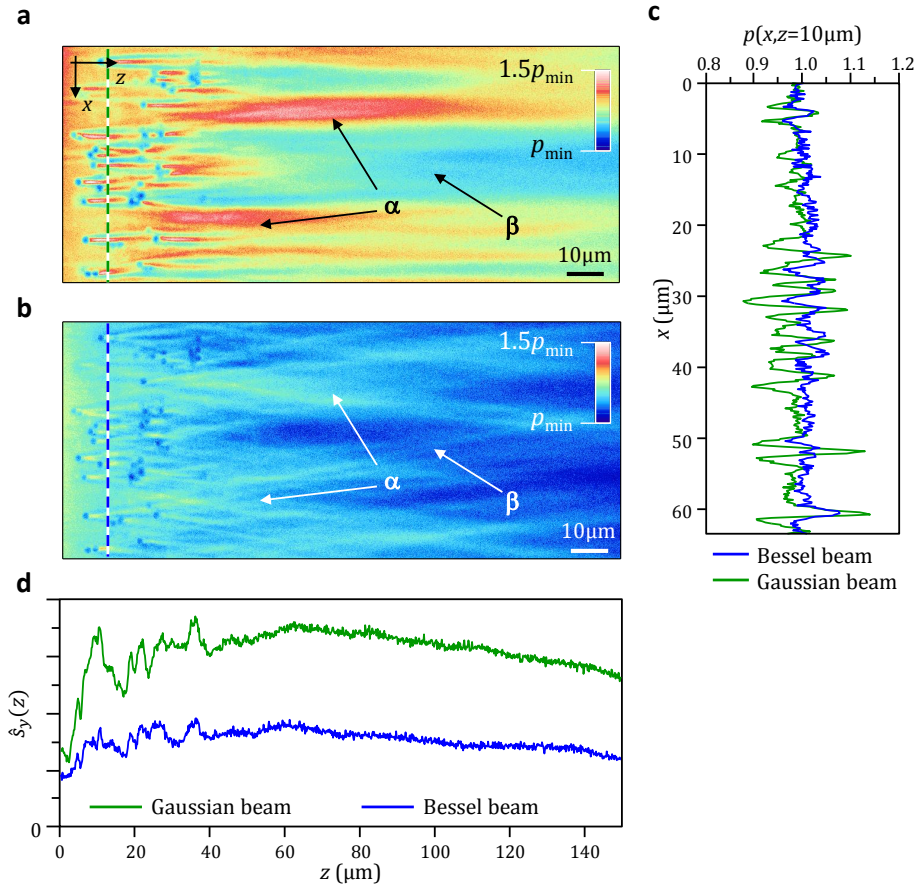


Figure 5.4: Light-sheet microscopy behind a cluster of non-fluorescing spheres.

Imaging of a cluster of silica spheres. Images of a cluster of silica spheres ($d = 2\mu\text{m}$) are illuminated by a scanned Gaussian beam (a), a scanned Bessel beam. Normalized lateral intensity profiles at the position indicated by the dashed line in (a) and (b) is shown in (c). The normalized lateral standard deviation of the image intensity $\hat{s}_x(z)$ as a function of propagation distance z , shown in d, is higher for the Gaussian beam. The color-scale of the images is chosen in a way to cover the range from the minimum image signal p_{\min} to $1.5p_{\min}$.

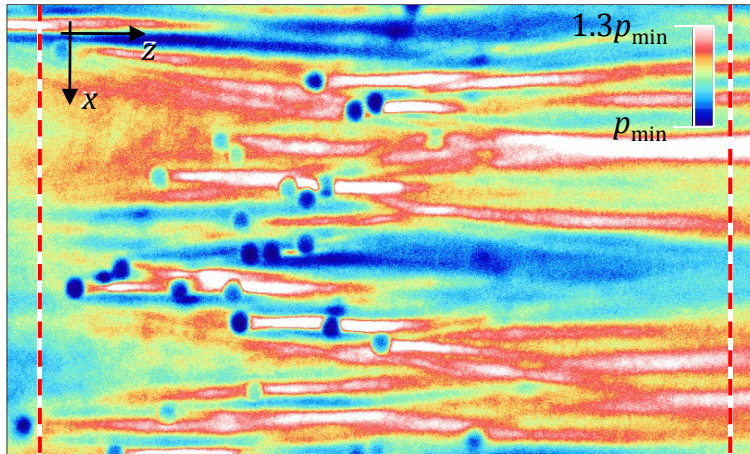
5.4 A CLUSTERS OF SPHERES

The sample under investigation in this section is a cluster of silica sphere. A large number of spheres ($d = 2\mu\text{m}$) is randomly distributed in a volume with a diameter of approximately $100\mu\text{m}$. In contrast to the previous section, the emphasis here lies on the evaluation of the image quality within the cluster. Therefore, a more sophisticated method had to be developed to be able to separate the contrast arising from the sample, i.e. the image, from the artifacts, i.e. the ghost image. The analysis is performed for an image obtained for illumination by an elliptical beam generated with a holographic cylindrical lens in addition to scanned Gaussian and Bessel beams. The fluorescence images $p(x, z)$ were acquired by scanning the Gaussian and Bessel beam across the sample during the camera's acquisition time. The elliptical beam covers the whole width of the field of view and therefore needs not to be moved during image acquisition. A first glance at the images shown using the same dynamic range in all images (Figure 5.5) gives the following impression:

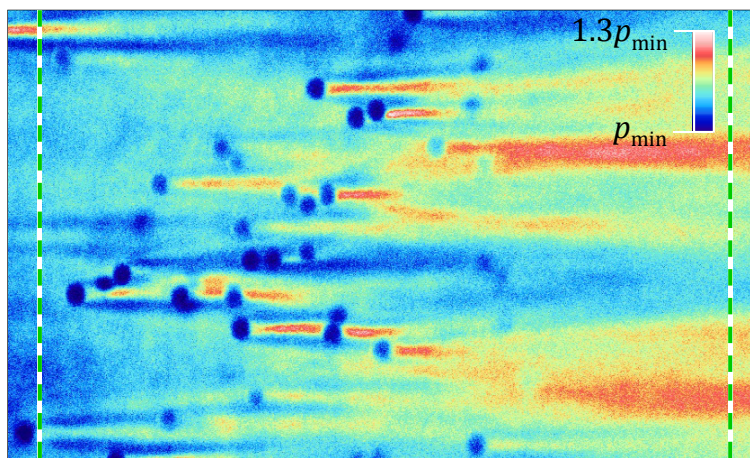
- The static light-sheet (formed by an elliptical beam) as it is used in a conventional light-sheet microscope [Voie et al., 1993, Huisken et al., 2004, Fuchs et al., 2002, Dodt et al., 2007, Holekamp et al., 2008] produces strong artifacts in the form of bright stripes resulting from diffracted and focused light (Figure 5.5a). The distribution of the illumination light is affected by the interference of the scattered and unscattered light $E_{\text{holo}} \cdot E_{\text{scat}}$ (compare eq. 2.26).
- The scanned Gaussian beam [Keller et al., 2008] yields an improved image quality. The intensity of the stripes is greatly reduced and the spheres are shown with a good contrast (Figure 5.5b). Due to small spatial coherence of the light-sheet, the distribution of the illumination light interference of scattered and unscattered light is strongly suppressed. The irradiance of the illumination is simply given by $h_{\text{ill}}(\mathbf{r}) = |E_{\text{tot}}(\mathbf{r})|^2 = |E_{\text{holo}}(\mathbf{r})|^2 + |E_{\text{sca}}(\mathbf{r})|^2$.
- The self-reconstructing Bessel beam leads to images that are only very weakly affected by artifacts. Note that the shape of the artifacts is also entirely different, consisting of a v-shaped region of increased intensity behind the spheres. However, the object contrast is also lower than for the other types of illumination (Figure 5.5). As for the scanned Gaussian beam, the spatial coherence is very small and the interference term $E_{\text{holo}} \cdot E_{\text{scat}}$ in eqn 2.26 can be neglected.

These results are analyzed more quantitatively in the following. Figure 5.6 shows lateral profiles at two axial z -positions: in front of ($z = z_1$) and behind ($z = z_2$) the cluster of spheres. The lateral profile $p(x, z_1)$ is relatively flat for all three illumination types. The variations in the profile behind the cluster are very pronounced for the static light-sheet, smoother for the scanned Gaussian beam and nearly flat for the Bessel beam. The normalized lateral standard deviation $\hat{s}(x, z = z_1)$ computed with eq 2.34 is 1.9 times larger for illumination by the Gaussian beams than that for the Bessel beam. For the light-sheet, $\hat{s}(x, z = z_1)$ is even 3.3 times larger.

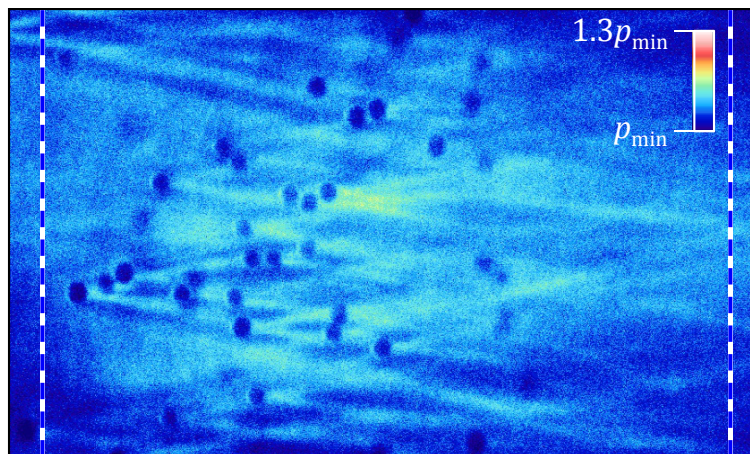
To further analyze the image quality, the magnitude of the artifacts is quantified by computing the ghost image contrast. This property is measured by the lateral standard deviation of the ghost image $\hat{s}_{\text{ghost}}(z)$ which is shown in Figure



(a) Static elliptical beam



(b) Scanned Gaussian beam



(c) Bessel beam

Figure 5.5: Comparison of light-sheet microscopy images of a cluster of spheres for different illumination beams.

The cluster of glass spheres ($d = 2\mu\text{m}$, $n = 1.41$) in fluorescent agarose gel ($n = 1.31$) is illuminated by a static elliptical beam (a), a scanned Gaussian beam (b) and a scanned Bessel beam (c) to yield images $p(x, z)$. The beams propagate along the z -axis from the left to the right.

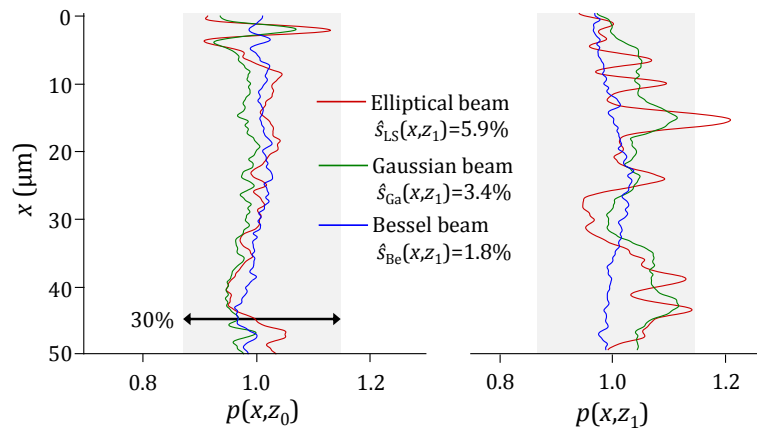


Figure 5.6: Transverse intensity profiles of the images shown in Figure 5.5.

The profile at $z_0 = 5\mu\text{m}$ is taken in front of the spheres for the unperturbed light-sheets and the profile at $z_1 = 70\mu\text{m}$ is measured at the back of the cluster. The positions are indicated by dashed lines in Figure 5.5. \hat{s} denotes the mean fluctuation of the profile. The gray-shaded areas indicate the magnitude of the dynamic range of $30\% \cdot p_{\text{min}}$ that is used for the images in Figure 5.5 and equal for all illumination beams.

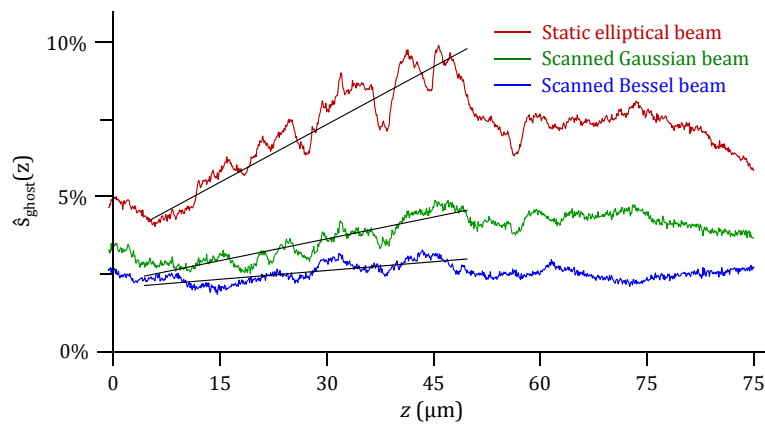


Figure 5.7: Contrast of the ghost image of a cluster of spheres for different illumination beams.

The graph shows the ghost image contrast corresponding to the real images shown in Figure 5.5 in dependence of the propagation distance z into the cluster. Line-fits illustrate the strongest increase in ghost image contrast for illumination by a static elliptical beam. Scanned Gaussian show lower ghost image contrast while Scanned Bessel beams lead only to marginal increase in ghost image contrast over the range of the scattering cluster of spheres.

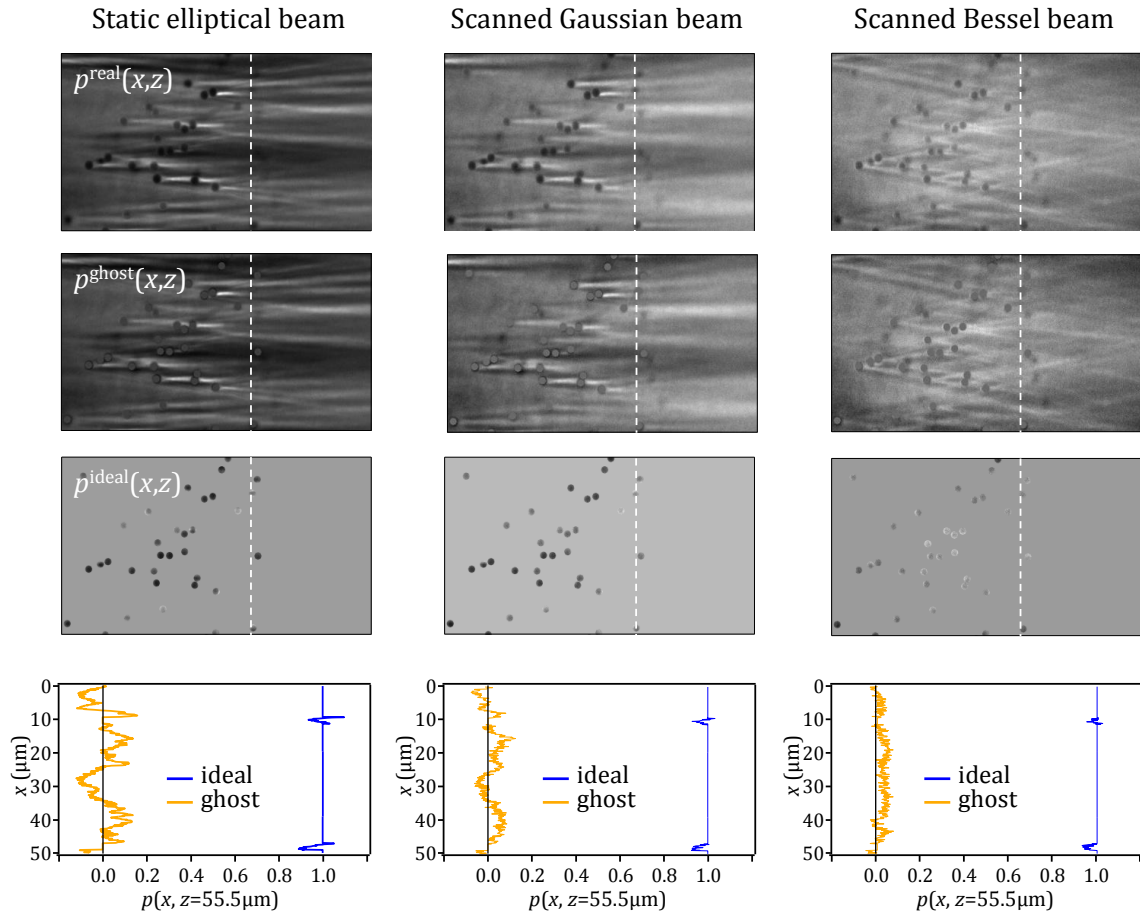


Figure 5.8: Comparison of real, ideal and ghost images for different illumination beams. The real images (upper row) can be separated into ghost images (2nd row) and ideal images (3rd row) due to a priori information about the shape and position of the objects. Line-profiles in the lower row show the signal along the lines marked by the vertical dashed lines in the images above. Thereby the contrast of the real image can be compared to that of the ideal and the ghost image.

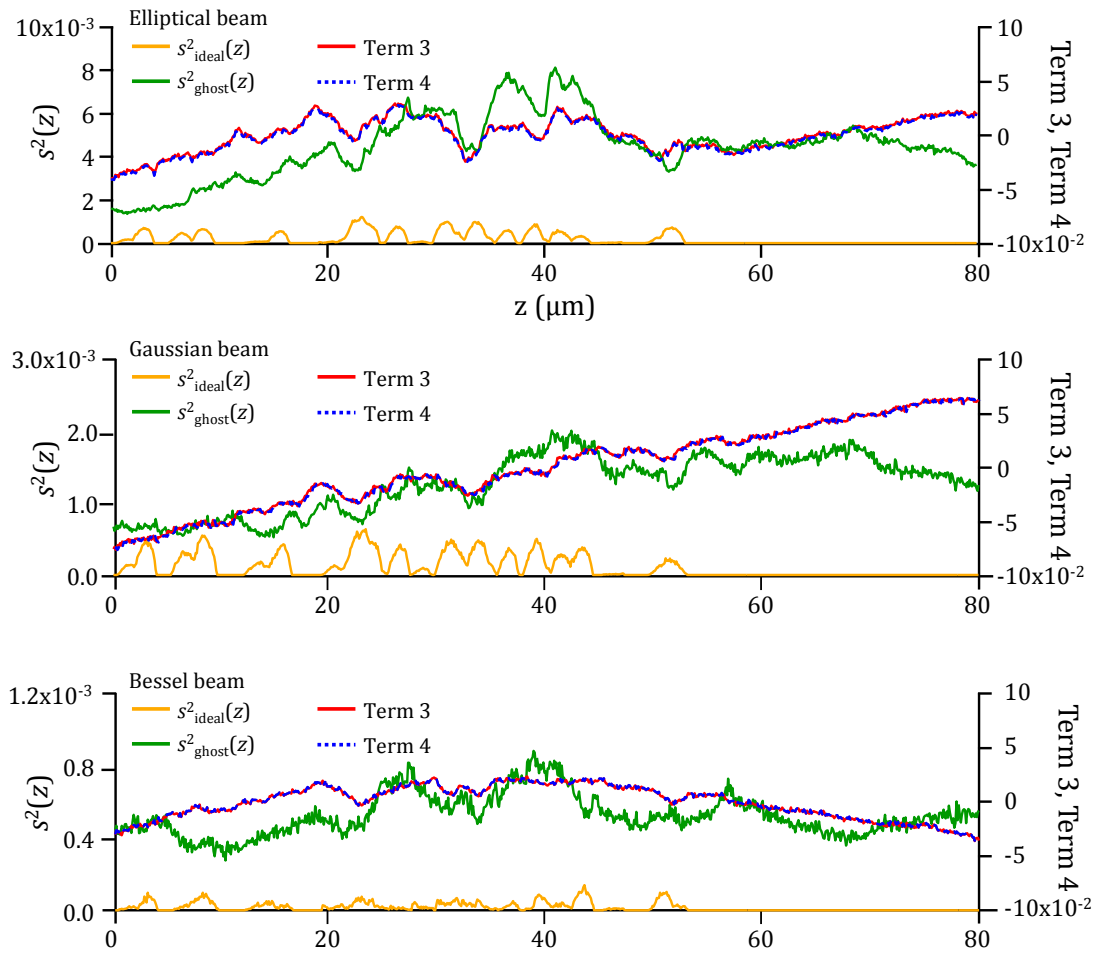


Figure 5.9: Decomposition of the image contrast for different illumination beams.

The contrast of the real image is decomposed into four terms according to eqn 2.35: the ideal contrast s_{ideal}^2 , the ghost image contrast s_{ghost}^2 and two other terms. If the difference of the Terms 3 and 4 vanishes (eqn 2.38), the total image contrast is completely determined by ideal and ghost image contrast (eqn 2.35). The figure shows that this assumption holds for all three illumination beams.

5.7 together with an averaged slope $\partial/\partial z \hat{s}_{\text{ghost}}(z)$. For Bessel beam illumination $\hat{s}_{\text{ghost}}(z)$ is smallest. To compute $\hat{s}_{\text{ghost}}(z)$ the real image $p^{\text{real}}(x, z)$ is separated into two contributions. First, an ideal image $p^{\text{ideal}}(x, z)$ of the spheres on a constant background. Second, a ghost image $p^{\text{ghost}}(x, z)$ that contains only the artifacts, i.e. the deviations from a constant light-sheet which can be positive and negative. Because the spheres are non-fluorescent in a fluorescent environment, p^{ideal} is 1 everywhere except at the position of the spheres where it is smaller. The decomposed images are shown in Figure 5.8. Lateral profiles $p^{\text{ideal}}(x)$ and $p^{\text{ghost}}(x)$ for $z = 55.5\mu\text{m}$ are shown below. From these, the standard deviations are extracted and normalized to the average value $\bar{p}^{\text{real}}(x)$ to obtain the ideal image contrast $\hat{s}_{\text{ideal}}(z)$ and the ghost image contrast $\hat{s}_{\text{real}}(z)$. It was shown mathematically their sum accounts for the total image contrast, i.e. that $\hat{s}(z) \approx \hat{s}_{\text{ideal}}(z) + \hat{s}_{\text{ghost}}(z)$ is valid, when the difference of Term 3 and 4 in eq. 2.35 vanishes. It can be seen that Term 3 and 4 are equal in Figure 5.9 which shows the four terms of eq. 2.35 for all three illumination modes. Note that the small non-fluorescent spheres in the fluorescent environment the ideal image contrast is very small. Around the spheres the image would ideally exhibit a constant value $p_{\text{ghost}}(x, z) = p(x, z) - p_{\text{ideal}}(x, y) = 0$. However, the light-sheet is inhomogeneous due to scattering.

5.5 DROSOPHILA EMBRYOS

A drosophila embryo stained with Sytox serves as an example for a biological specimen. The recorded data consists of a stack of 34 images spaced by $2\mu\text{m}$ along the detection optical y -axis. Figure 5.10 shows images of a maximum-value projection along the detection axis for illumination by a Gaussian beam and a Bessel beam. Magnifications of a small sub-region are shown alongside. To reach this region, the illumination beams have to propagate a considerable distance through the strongly scattering embryo. It is apparent from the line-scans shown in Figure 5.10 that the decay of the recorded fluorescence for deeper penetration into the sample is clearly less pronounced for illumination by a Bessel beam. However, it is also apparent that Gaussian beam illumination does provide higher contrast in the left part of the image where scattering of the beam by the sample hardly affects the beam shape and the image quality. For samples that show a high density of fluorophores over a large volume, as in this case, the Bessel beam's ring system excites a lot of background fluorescence which reduces the image contrast thereby concealing a potential gain in illumination quality by an improved homogeneity of the light-sheet.

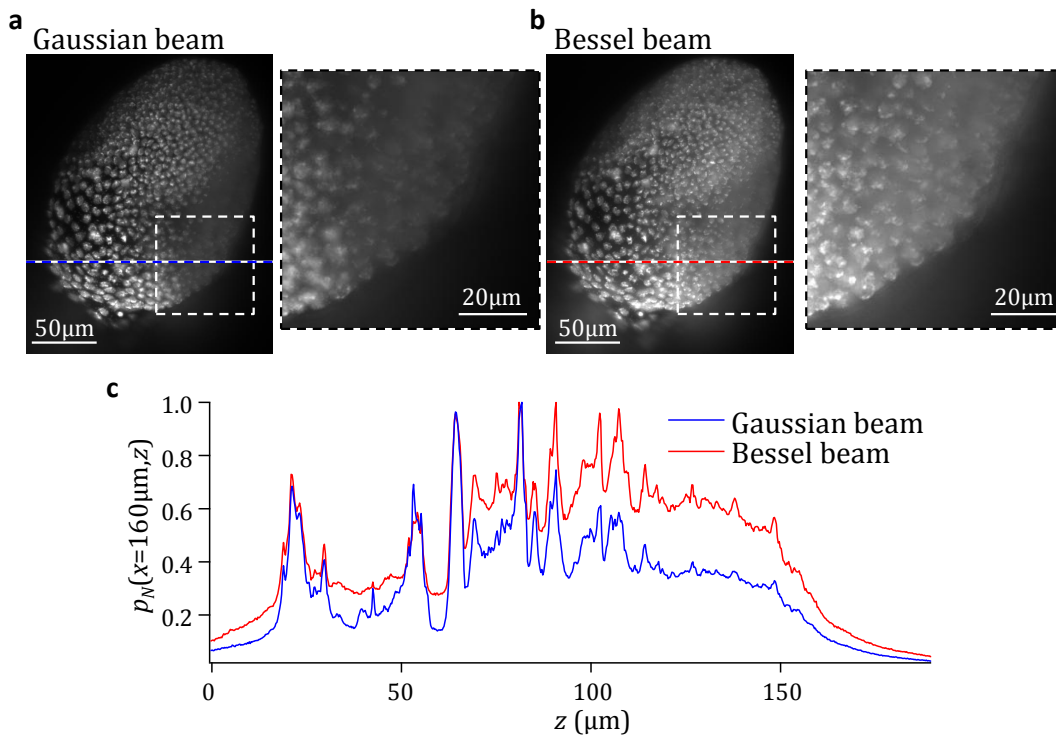


Figure 5.10: Light-sheet microscopy images of a drosophila.

The embryo is illuminated from the left. The maximum projection along the detection y -axis of a stack of 34 images is shown for illumination by a scanned Gaussian (a) and Bessel beam (b). In the enlargement of the region ($75\mu\text{m} \times 75\mu\text{m}$) marked by a dashed square that is shown alongside the better signal at high penetration depth of the illumination beam is clearly visible. A normalized line profile (width $8\mu\text{m}$) at the position marked by the dotted line shown below (c) is further evidence of the higher signal at large depths within the sample that is generated by the Bessel beam.

5.6 DISCUSSION

Conventional light-sheet microscopy images feature stripe-like artifacts behind strongly scattering objects as well as a decrease in signal and contrast along the direction of illumination. In this chapter these effects are investigated in a quantitative manner. To reduce the problem caused by scattering self-reconstructing Bessel beams are used for illumination. Samples of growing complexity were imaged using a line-scanning light-sheet microscope with holographically shaped illumination beams. Each sample was illuminated by different beams in order to be able to accurately attribute the differences in the images to the illumination. A strong emphasis of the investigations lay on the visualization and quantification of the quality of the light-sheet by using samples that were homogeneously stained with fluorescein (compare §1.3).

Quantitative comparison of image quality: In order to be able to quantitatively evaluate the image quality a new method was developed. The method is unique in its capability to assess the strength of image artifacts. It is based on the decomposition of the image into a real image that contains the unperturbed image of the object and a ghost image that contains all artifacts. In practice, the ghost image is obtained as the difference between the real image that is recorded and the ideal image that is expected when the object distribution is known. The knowledge of the sample is thereby the only prerequisite of the method. Details are given in Section 2.2.5. In the present case the sample consisted of spheres

with known diameter and therefore the ideal image could easily be inferred. The strength of the ghost image contrast (Fig. 5.7) could therefore be measured separately from that of the real image. The results clearly show that the ghost image is smallest for the scanned Bessel beam. This finding is in agreement with the Bessel beam's superior directional propagation stability that was found in the previous chapter and that was linked to the ghost image contrast by eq. 4.7. Furthermore, the experimental results thereby confirm the simulations Rohrbach [2009].

Artifacts and homogeneity of light-sheets for different illumination types:

A sample consisting of two large spheres in a row and a cluster of smaller spheres were imaged for illumination by a static elliptical beam as well as scanned Gaussian and Bessel beams. This study is the first and so far only direct comparison of the effect of illumination by static elliptic and scanned circularly symmetric beams. The image analysis clearly indicates that static light-sheets are significantly more susceptible to scattering and show more pronounced artifacts. The difference is accredited to the high degree of spatial coherence. In the line-scanning mode the beam at the different positions incoherently superposes to form the final image. The intensity of the perturbed beam at every position is added up and artifacts appear more smoothly. However for static light-sheet illumination, the light scattered at different positions is able to interfere due to the determined phase (see eq. 2.26). As discussed in Section 5.4, the coherent superposition gives rise to stronger artifacts, i.e. regions of localized constructive and destructive interference.

Sample illumination by self-reconstructing Bessel beams has shown to strongly reduce the strength of artifacts. On the one hand, the Bessel beam is less susceptible to local perturbations as was demonstrated in the experiments presented in the last chapter. On the other hand, the scattering artifact of an isolated scatterer is also qualitatively different from that of a conventional (Gaussian) beam. The forward-scattered light is not concentrated on a small region directly behind the scatterer. The wave-vectors of the plane waves constituting a Bessel beam lie on the surface of a cone. Forward scattering leads only to a small deviation and broadening of the angular spectrum. The scattered power is therefore distributed over a larger conical volume which intersects with the image plane forming an image artifact that is a v-shaped region of increased signal strength. These artifacts of Bessel beams perturbed by forward scattering obstacles can be clearly observed in Figures 5.3, 5.4 & 5.5. Note that the assumption of mainly forward-scattering obstructions is reasonable as the constituents of neural tissues, for example, feature anisotropy factors of $g \approx 0.9$ at a wavelength of $\lambda = 0.5\mu\text{m}$ [Yaroslavsky et al., 2002]. Moreover, the dark regions that arise from the redistribution of the Gaussian beam's energy, i.e. into a focus behind a sphere are much less pronounced for Bessel beams due to their self-reconstruction ability. However, while the strength of artifacts can be reduced by using Bessel beams, the image contrast is strongly decreased.

Resolution and Optical Sectioning: To obtain values for the resolution and optical sectioning performance that can theoretically be achieved numerical simulations were performed (§ 5.1). These reveal two seemingly contradictory results: While the thickness of the light-sheet created by scanned Bessel beams is larger than that by Gaussian beams, the theoretical value for the axial resolution provided by Bessel beam illumination is better. The non-monotonous decrease of the radial profile of the Bessel beam is responsible for this effect. The extent of

the image of a point source along the detection y -axis, $h_{\text{sys}}(y) = h_{\text{ill}}(y) \cdot h_{\text{det}}(y)$, which is used to measure the resolution, is dominated by the narrow main lobe of the Bessel beam while the ring system is suppressed by the decline of the detection probability $h_{\text{det}}(y)$. However the optical sectioning performance depends on the integral over the cross-section $\iint h_{\text{det}}(\mathbf{r}) dx dz$ that is independent of y due to energy conservation. In other words, the detection lens cannot discriminate against out-of-focus light and for linear excitation of a homogeneously distributed dye the amount of fluorescence detected from each plane is proportional to the irradiance of the light-sheet. The overall thickness of a light-sheet created by Bessel beams is larger and therefore the image contrast is lower. It is important to note that quantitative comparison of signal to background revealed that for Bessel beams with optimum depth of field the decrease in artifacts is larger than the loss in contrast of the the real image, i.e. the spheres [Rohrbach, 2009].

Application to biological samples: Finally, as an example for a biological sample a drosophila embryo was imaged. The results (Fig. 5.10) indicate that the robustness to scattering leads to better penetration into the sample. The image detail and the profile through the sample along the illumination direction clearly show that a larger signal is detected at the back side of the sample and more details are visible. However, the overall image contrast is inferior due to the thickness of the Bessel-beam light-sheet. To benefit from the superior image quality that Bessel-beam illumination in light-sheet microscopy may offer, this problem has to be solved. Several methods to increase optical sectioning exist already. The next chapter presents a new technique that was developed in the context of this thesis which achieves the goal of greatly improved image contrast by using the special propagation stability property of the Bessel beam.

Possible application to the study of the dynamics of complex granular materials: In the context of this thesis, clusters of small silica spheres are used as well-defined samples to assess the quality of the microscope. However, similar samples where non-fluorescent spheres are immersed in fluorescent solution can also be used to investigate the dynamics of densely packed granular materials. Therefore, the positions of the individual spheres are measured with a setup very similar to a light-sheet microscope [Dijksman et al., 2012]. So far, the technique is limited by the penetration of the laser light-sheet into the sample and major efforts are undertaken to reduce scattering by employing immersion liquids with matching refractive indices. However, these are in general very expensive. Based on the results presented in this thesis, the illumination by Bessel beams is a promising approach to overcome the limitations. Moreover, for the simple detection of the positions of the spheres the lower contrast should be a minor problem.

An important aspect of microscopy is the **photo-damage and photo-bleaching caused by the illumination beam**. Static illumination acts differently on the overall sample and especially the fluorophores. For static light-sheet illumination the whole field of view is illuminated during the exposure time of the camera. Therefore, a much lower irradiance of the illumination beam can be employed to collect the same amount of fluorescence photons during the same acquisition time as for a scanned illumination beam. However, the dependence of photo-toxicity on irradiance has not yet been quantitatively investigated yet especially in the context of light-sheet microscopy. Scanned illumination beams may offer transient molecular dark states the possibility to relax between two molecular

absorption events and thereby decrease bleaching effects [Donnert et al., 2007]. The same could be achieved by a pulsed static light-sheet, but no quantitative analysis on this domain has been performed yet.

Alternative methods for the removal of artifacts: It was suggested to remove artifacts computationally in a post-processing step [Lee et al., 2009, Leischner et al., 2010]. This step is time-consuming and not very robust. As can be seen in Figures 5.3 and 5.5 the perturbation of the light-sheet is complex in shape and is caused by objects that may not be clearly visible in the image because they are located in different planes. Moreover, the methods presented so far are hardly applicable to sparsely stained samples. A very practical method to remove the striped artifacts is to tilt the light-sheet in the image plane [Huisken and Stainier, 2007]. This technique leads to an incoherent superposition of the stripes directed in different directions behind the scatterer and effectively blurs the artifacts so that they are no longer visible. One could imagine to combine this method with the line-scanning approach, i.e. to scan a beam across the field-of-view that is continuously tilted with a very high frequency. However, this technique does only address the detrimental effect of the stripes on the image quality. Other, even more important problems that arise from scattering like an increase in the thickness of the light-sheet or the limited penetration depth are not solved.

Another approach to reduce the effect of artifacts and overcome the limited penetration depth of the light-sheet into the sample is to illuminate the sample from opposite directions [Dodt et al., 2007, Huisken and Stainier, 2007] or acquire images at several angles of the sample and to subsequently merge the images [Swoger et al., 2007, Tomer et al., 2012, Krzic et al., 2012]. However, the precise fusion of the images taken from different directions is challenging because of drift and the need for the precise knowledge of the position of the rotation axis in the images. While important progress has been made in the meantime [Temerinac-Ott et al., 2012], multi-view image fusion is still limited to samples that are smaller than two times the penetration depth of the light-sheet. The registration of the different images works reliable and robust for arbitrary samples only when small fluorescent spheres are embedded in the gel around the sample. Therefore, the recorded image has to be much larger than the sample so that the image acquisition speed is reduced or a smaller magnification has to be used.

In **conclusion**, Bessel beams are more robust than conventional illumination beams. This effect leads to weaker artifacts in light-sheet microscopy images. The problem to be solved is the decrease in contrast that is caused by the beams ring system. This issue will be addressed in the following chapters.

LIGHT SHEET MICROSCOPY WITH CONFOCAL-LINE DETECTION

After a short introduction into the principle of confocal-line detection (§ 6.1), a theoretical description of the image formation in a light-sheet microscope with confocal-line detection is given (§ 6.2). Simulation results were used to evaluate, the potential improvement in axial resolution and optical sectioning performance of the method (§ 6.3). Section 6.4 explains how confocal-line detection can be performed with a conventional light-sheet microscope without changes to the hardware. The performance of the method can experimentally quantified using scattering fluorescent spheres (§ 6.5). Images of biological samples, like drosophila egg-chambers (§ 6.6) and tumor multicellular spheroids (§ 6.7) are shown and analyzed in detail. Finally, it was found that confocal-line detection in combination with illumination by sectioned Bessel beams provides the best combination of image contrast and penetration depth (§ 6.8). The chapter closes by an in-depth discussion of these findings (§ 6.9).

6.1 THE PRINCIPLE OF CONFOCAL-LINE DETECTION

In line-scanned light-sheet microscopy with wide-field detection (DSL / MIS-ERB) the beam is moved by $\mathbf{b}_x = (v_x \cdot t, 0, 0)$ across the field of view during the exposure time of the camera. Therefore, the effective light-sheet is equivalent to the projection of the irradiance of the static beam $h_{\text{SB}}(\mathbf{r})$ along the scan direction (see eqn 5.1) and independent of x . For Bessel beam illumination, the resulting light-sheet irradiance $h_{\text{scan}}(\mathbf{r})$ is broadened considerably along y due to the contributions of the rings of the Bessel-beam (see $h_{\text{scan}}(y, z)$ in Figure 6.1a). The non-monotonous radial decay of the Bessel beam's radial irradiance profile means that the scanning substantially increases the effective thickness of the light-sheet making it much larger than the beam's central peak, as can be seen by comparing $h_{\text{scan}}(y)$ to $h_{\text{SB}}(y)$ for the Bessel beam in Figure 6.1. The thick light-sheet illuminates objects around the focal plane of the detection objective (DO). Their blurred image generates background which leads to a loss in image contrast.

Confocal-line detection consists in recording the image only at the position of the static illumination beam. To record a full image, the beam is scanned in discrete steps across the sample. By using confocal-line detection it is possible to discriminate against the fluorescence excited by the ring system of the Bessel beam which otherwise reduces the image contrast. The sketch shown in Figure 6.1b illustrates the principle. Cross-sections through the effective irradiance of the sample for illumination by Gaussian and Bessel beams are displayed below. The axial profiles for scanned illumination, $h_{\text{scan}}(y)$, and static illumination, $h_{\text{SB}}(y)$ reveal that the profile is much thinner for static illumination than when the beam is scanned.

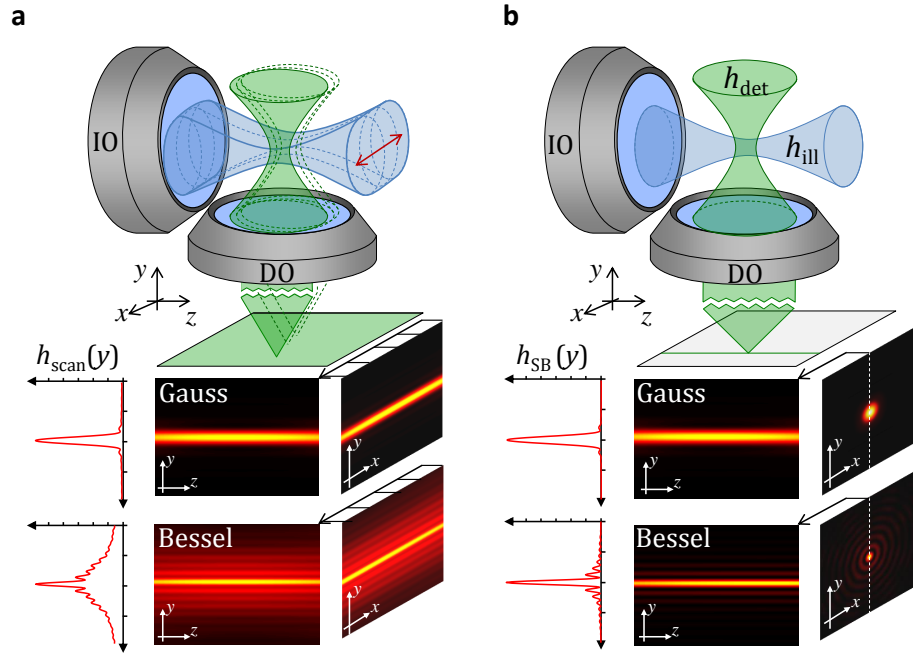


Figure 6.1: Schematic illustration of the wide-field and confocal-line detections modes. Conventional light-sheet microscopy with scanned beams is shown in (a), confocal-line detection light-sheet microscopy in (b). The illumination beam focused by an objective lens (IO) is scanned in the focal plane of the detection lens (DO). For conventional microscopy, a 2D image is recorded during the movement of the beam. Confocal-line detection records the image only line-wise at the position of the beam. For wide-field detection, the irradiance corresponds to the projection of the beam along the scan axis, whereas it is given by the static beam for confocal-line detection. Slices through the irradiance of the illumination, $h(y, z)$ and $h(x, y)$, and axial profiles $h(y)$ shown below the sketch for Gaussian beams (top) and Bessel-beams (bottom) illustrate the reduced width along the detection axis in the case of the static beam (h_{SB} , right) in comparison to the scanned beam (h_{scan} , left).

6.2 DESCRIPTION OF IMAGE FORMATION

The idea of confocal-line detection is not to scan the beam in order to avoid the associated loss in contrast. Instead, the image is recorded line by line at the position $\mathbf{b}_x = (b_x, 0, 0)$ of the static beam. The image

$$p_{SB}(\mathbf{r}, b_x, b_y) = (h_{SB}(\mathbf{r} - \mathbf{b}_x) \cdot c(\mathbf{r} - \mathbf{b}_y)) * h_{det}(\mathbf{r}), \quad (6.1)$$

of an object displaced vertically by $\mathbf{b}_y = (0, b_y, 0)$ is recorded by a line-sensor at a position equivalent to the beam position b_x in the focal plane $y_0 = 0$ of the detection objective. The line image reads

$$p_{CL}(\mathbf{r}; b_x, b_y) = (h_{SB}(\mathbf{r} - \mathbf{b}_x) \cdot c(\mathbf{r} - \mathbf{b}_y)) * h_{det}(\mathbf{r}) \Big|_{x=b_x, y=0}. \quad (6.2)$$

A three-dimensional volume image can then be obtained by subsequent reassembly of the line images at their respective positions b_x, b_y . Further insight is gained if the above formula is analyzed more closely. It can also be written as

$$p_{\text{CL}}(b_x, b_y, z)|_{b_x,0} = \iiint \left[\iiint c(\mathbf{r}' - \mathbf{b}_y) \cdot h_{\text{SB}}(\mathbf{r}' - \mathbf{b}_x) \cdot h_{\text{det}}(\mathbf{r} - \mathbf{r}') d^3\mathbf{r}' \right] \delta(x - b_x) \delta(y - 0) dx dy. \quad (6.3)$$

Because the δ -functions only affect h_{det} the integral reduces to

$$p_{\text{CL}}(b_x, b_y, z)|_{b_x,0} = \iiint c(x', y' - b_y, z') \cdot h_{\text{SB}}(x' - b_x, y', z') \cdot h_{\text{det}}(b_x - x', -y', z - z') dx' dy' dz'. \quad (6.4)$$

A convolution of illumination and detection PSF is carried out only along the sensor-axis. Along the x -axis, the image is given by the multiplication of the illumination and the detection PSF. Note that for the computation of the image of a single plane (corresponding to the position of the image sensor) no convolution along the y -axis is carried out but a simple integration. However, convolutions have to be carried out along x and z . In comparison, for a point-scanning system the signal recorded by a point-detector is given by the integral over the product $c(\mathbf{r}_0) \cdot h_{\text{SB}}(\mathbf{r}) \cdot h_{\text{det}}(\mathbf{r})$ for each position. The reduction in background is cannot be simply explained by this change of the mathematics that describe the image formation. It is also due to the possibility of reading out the static illumination beam only along its axis, which means that the illumination is given by h_{SB} instead of h_{scan} . Note that the formation of the image recorded by a line-sensor is correctly described by eq. 6.4 regardless of the irradiance of the illumination.

For a point source, e.g. a fluorescent sphere with $c(r) = c_0 \cdot \delta(\mathbf{r} - \mathbf{r}_i)$ positioned at the origin $\mathbf{r}_i = (0, 0, 0)$ eq. 6.4, delivers the system point-spread function $h_{\text{sys,CL}}(\mathbf{r})$ for confocal-line detection:

$$h_{\text{sys,CL}}(x, y, z) = h_{\text{SB}}(x, y, 0) \cdot h_{\text{det}}(x, y, z). \quad (6.5)$$

In contrast the PSF of a conventional wide-field line-scanned light-sheet microscope (DSLMS / MISERB) is

$$h_{\text{sys,LS}}(x, y, z) = h_{\text{scan}}(0, y, 0) \cdot h_{\text{det}}(x, y, z) \quad (6.6)$$

The derivation is shown in section 2.2.1. The product in equations 6.5 & 6.6 describes the overlap between the illumination and detection PSF which is crucial to image quality. As pointed out before, the difference in the illumination, described by $h_{\text{SB}}(x, y, 0)$ and $h_{\text{scan}}(0, y, 0)$, has a strong effect on image quality, especially for the Bessel beam that has a non-monotonously decaying radial intensity profile (see Figure 6.1). This aspect will be quantified using simulation data in the next section.

In confocal-line detection light-sheet microscopy with an infinitely thin line detector, the irradiance of a static beam h_{SB} is multiplied with the detection probability h_{det} to obtain the system-PSF h_{sys} . The illumination h_{SB} can be

assumed to be independent of z -position along the beam's depth of field. In this region, the line image can be described by

$$p_L(z) = (h_{\text{sys,CL}}(\mathbf{r}) * c(\mathbf{r})) \Big|_{x=x_L, y=y_L} \quad (6.7)$$

where x_L is the lateral position corresponding to the line detector and y_L the axial position. The width $2s$ of the line-sensor can be accounted for by integrating the image over an area equivalent to the pixel size in the image plane.

$$h_{\text{sys,CL}}(x, y, z; s) = \int_{-s < x_0 < s} h_{\text{SB}}(x, y, z) \cdot h_{\text{det}}(x - x_0, y, z) dx_0 \quad (6.8)$$

where $s = s_{\text{pix}}/M$ with the magnification of the detection objective lens M .

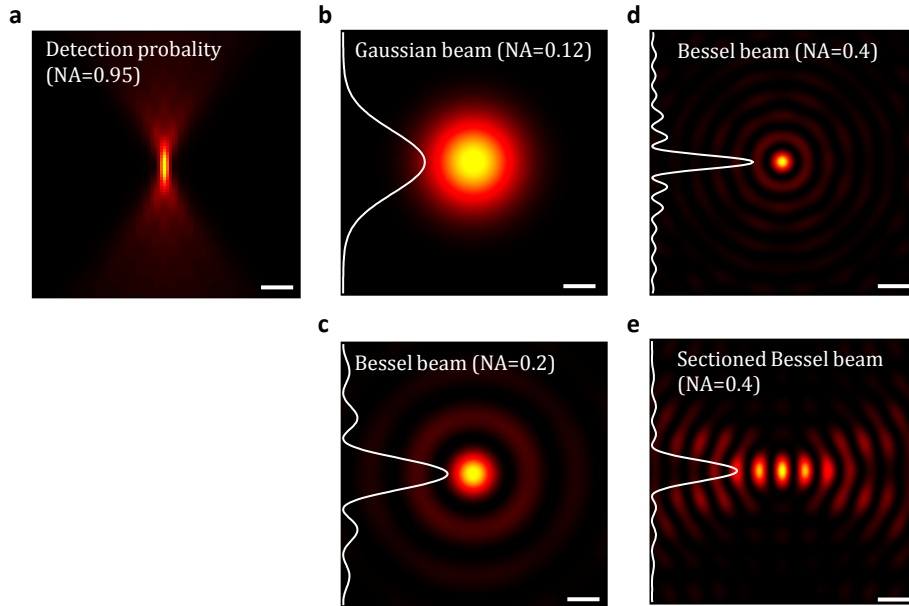


Figure 6.2: Illumination and detection point-spread functions.

The projection of the detection probability function along z , $\int h_{\text{det}}(x, y, z) dz$ is shown for $\text{NA}_{\text{det}} = 0.95$ in (a). Slices through the irradiance $h_{\text{ill}}(x, y, z = 0)$ are shown for a Gaussian beam with $\text{NA} = 0.12$ (b), a Bessel beam with low numerical aperture, $\text{NA} = 0.2, \epsilon = 0.72$ in (c), a Bessel beam with high $\text{NA} = 0.4$ and $\epsilon = 0.94$ in (d) and for a sectioned Bessel beam with $\text{NA} = 0.4, \epsilon = 0.94$ and $\beta = 88^\circ$ in (d). Axial profiles $h_{\text{ill}}(y)$ for $x = z = 0$ are shown as insets.

6.3 AXIAL RESOLUTION AND OPTICAL SECTIONING PERFORMANCE

As outlined before in Section 2.2.1, the system point-spread-function $h_{\text{sys}}(\mathbf{r}) = h_{\text{ill}}(\mathbf{r}) \cdot h_{\text{det}}(\mathbf{r})$ is well-suited to assess resolution and optical sectioning. In the following, the axial resolution and optical sectioning performance of the light-sheet microscopy for confocal-line detection will be assessed using simulated system point-spread functions that were obtained by the propagator approach. The illumination-PSF $h_{\text{ill}}(\mathbf{r})$ was computed in cubic arrays with $1024 \times 1024 \times 1024$ voxels and an isotropic discretization of $\delta r = \lambda/16 = 23\text{nm}$.

6.3.1 Resolution

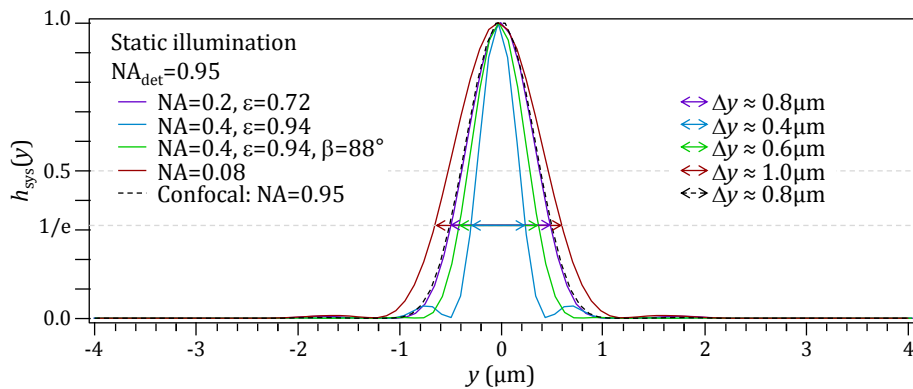


Figure 6.3: Axial resolution in a light-sheet microscope with confocal-line detection.

Using the measure introduced in Section 2.2.2, it is possible to assess the resolution offered by the illumination beams and the detection PSF presented in Figure 6.2. The axial resolution can be derived from the width of $h_{\text{sys}}(0, y, 0)$ at $1/e \approx 37\%$ of the maximum value (see Figure 6.3). The best resolution of $\Delta y \approx 400\text{nm}$ is provided by illumination with a high-NA Bessel beam. For the sectioned Bessel beam, the axial resolution $\Delta y \approx 600\text{nm}$ is slightly inferior. The low-NA Bessel beam offers the same axial resolution $\Delta y \approx 800\text{nm}$ as the point-scanning confocal microscope. Confocal-line detection light-sheet microscopy with Gaussian beam illumination delivers the worst axial resolution $\Delta y_{\text{DSLML}} \approx 1\mu\text{m}$.

6.3.2 Optical Sectioning

However, as mentioned before, resolution only measures the ability to separate two points in close proximity. The ability to suppress background from layers other than the focal plane of the detection lens can be quantified by the optical sectioning measure introduced in Section 2.2.3. From the four illumination beams and the detection probability shown in Figure 6.2 the system point-spread function was generated for confocal-line detection and for a point-scanning confocal microscope. To assess the optical sectioning $G(y)$ according to eqn 2.20 was computed. The graph shown in Figure 6.4 can be interpreted in two interesting ways. First, one can look at the slope of the curve around $y = 0\mu\text{m}$. A large slope at position y means that a high relative amount of fluorescence $F(y)$ (see eqn 2.19) is collected in the respective plane. Second, one can look at the range along y out of which a majority (63%) of the signal is collected. This quantity is measured by the dy_{OS} as defined by eqn 2.21.

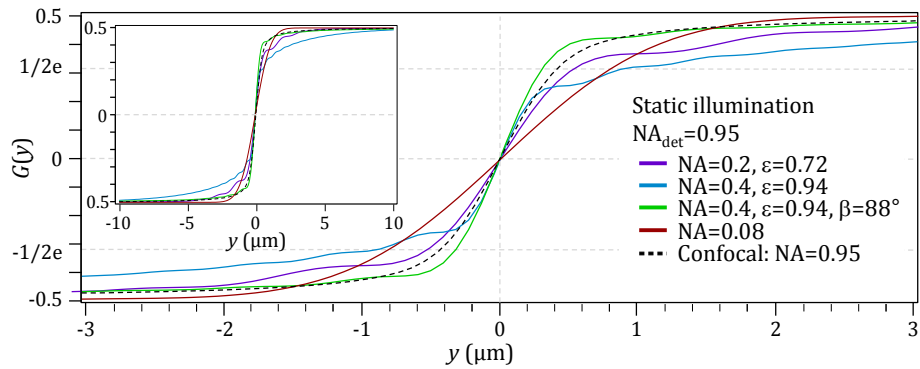


Figure 6.4: Optical sectioning in a light-sheet microscope with confocal-line detection.

The largest amount of relative fluorescence from a thin layer around the focal plane of the detection lens is obtained for illumination by a sectioned Bessel beam which essentially illuminates the detected line from the side. The excellent performance with respect to the optical sectioning in a light-sheet microscopy with confocal-line detection makes this class of beam especially interesting. Therefore, the beam is discussed in more detail in Section 6.8. The high-NA Bessel beam also yields a large relative amount of signal from a very thin volume, but the beam also illuminates planes far away from the focal plane more strongly than all other techniques compared here. About 20% of the total signal originate from layers that are more than $3\mu\text{m}$ away from the focal plane. From the inset in Figure 6.4 it can be seen, that 100% of the fluorescence is collected from a volume

with a thickness of $\approx 20\mu\text{m}$. A Bessel beam with a low $\text{NA} = 0.2$ and ring factor $\epsilon = 0.72$ is much better in this regard. Performance with this beam is similar to point-scanning confocal microscopy but a larger amount of fluorescence is detected from layers with $|y| > 1\mu\text{m}$. Gaussian beam illumination is ideal in the way that almost 100% of the signal is collected from a range of $|y| < 2\mu\text{m}$. However, of all methods, the Gaussian beam exhibits the lowest slope in the range of $|y| < 0.6\mu\text{m}$. There are visible effects in the images that arise from the different performance concerning this property. For example in Figures 6.18 and 6.18, more small-scale details of objects in the focal plane are visible in the images for Bessel beam illumination than for Gaussian illumination even though the relative background is higher for Bessel beam illumination.

In conclusion, confocal-line detection greatly improves the performance for Bessel beam illumination, especially with respect to resolution and the detection of a large relative amount of signal from planes nearby the detection objective's focal plane. But the optical sectioning for low-NA and especially the high-NA Bessel beam is still inferior to that of a point-scanning confocal microscope.

6.4 CONFOCAL-LINE DETECTION WITH A CONVENTIONAL LIGHT-SHEET MICROSCOPE

The straight-forward way to acquire line images $p_L(z)$ would be to use a line sensor. But confocal-line detection (CL-MISERB) can also be implemented without changes to the hardware in conventional light-sheet microscopes that allow beam scanning. The camera is then used to record 2D-images for each lateral position $b_i = i \cdot dx$ of the illumination beam. The line images

$$p_i(x, z) = p_{SB}(x, y, z, b_i, b_y) \quad (6.9)$$

for $b_y = y$, are extracted from the static beam images (eqn 6.1) by multiplication with a smooth mask

$$m_i(x, z) = \exp \left\{ -(x - x_i)^2 / w^2 \right\} \quad (6.10)$$

The lateral position of the mask x_i must coincide with that of the beam b_i . Therefore, a calibration step is necessary, which is described below in Section 6.4.2. The width of the mask w typically corresponds to a few pixels on the chip and is determined by the beam's width, so that $2w \approx \lambda / NA_{ill}$ for both Bessel and Gaussian beams – with the important difference that Bessel beams are created at higher NAs for an equal depth of field. The final image

$$p_{CL}(x, z) = \sum_i p_i(x, z) \cdot m_i(x, z) \quad (6.11)$$

is obtained by simple addition of the line images. For comparison, images that correspond to those obtained by a scanned illumination beam (MISERB / DSLM) can be obtained from the assembly of non-confocal images $p_{LS}(x, z) = \sum_i p_i(x, z)$ that result from using masks with $w \rightarrow \infty$. The equivalency is also mathematically shown by eqn A.6 in Appendix A. A small constant offset due to electronic noise introduced by the detection sensor can be subtracted to allow comparison of signal-to-background.

6.4.1 Beam Multiplexing

When using a 2D-image sensor to record line images it is beneficial to use beam multiplexing, i.e. to position N illumination beams in the sample volume at the same time to record N line images in parallel. The final image obtained by beam multiplexing is

$$p_{MCL}(x, z) = \sum_i \left(\sum_j p_{SB}(x, b_y, z, b_x = (i \cdot N + j) \cdot dx,) \right) \cdot \sum_j m_j(x, z). \quad (6.12)$$

where i is the index of the multiplexed images, $j = 1 \dots N$ is the beam position index within each image and $N \cdot dx$ the distance of the multiplexed beams in each image. The increase in acquisition speed mainly results from the fact that the camera has to be read out only once for N beam positions. Further increase in image speed is only possible if the total exposure time for all beam positions can

be reduced. Therefore, the power of the illumination beam needs to be increased. The optimum value would be a factor of N for N -fold beam multiplexing. When employing beam multiplexing care has to be taken to choose the distance $N \cdot dx$ between the beams to be larger than the diameter of the beam. Furthermore, the beam broadening due to scattering by the sample has to be taken into account. If the distance is chosen to small, the beams mutually increase background at the positions of the other beams.

6.4.2 Calibration

Confocal-line detection microscopy demands precise knowledge of the lateral beam position b_x in the image plane (xz -plane). The first step is therefore to establish a relationship between the signal applied to the scanning mirror and the lateral beam position. Therefore, a set of n images $p_i(x, z)$ is taken. The beam position in image p_i is given by

$$b_x = i \cdot dx + x_{\text{off}}. \quad (6.13)$$

The calibration procedure consists in determining the lateral offset position of the beam x_{off} in the first image and the lateral displacement dx between to images. The position of the beam b_x can be inferred from the z -projection of the recorded image intensity. Either maximum selection

$$F_{z,\text{max}}(x, i) = \max_z(p_i(x, z)) \quad (6.14)$$

or z -integration

$$F_{z,\text{int}}(x, i) = \int p_i(x, z) dz \quad (6.15)$$

can be used.

Both methods exhibit advantages and disadvantages in different situations. For homogeneous, extended objects (like drosophila egg chambers), $F_{z,\text{int}}$ is preferable. Because $F_{z,\text{int}}$ depends also on the number of fluorescent objects along z for a certain x -position of the beam care must be take when this measure is applied. It is most helpful when fluorescence homogeneously distributed. $F_{z,\text{max}}$ is more robust to sparse, irregular distributions of fluorophores like small, isolated objects (e.g. micro-spheres). In this case, the density of $c(\mathbf{r})$ has only to be high enough that particles are lying close to the beam axis for each position. These will necessarily be brighter than those lying further away from the beam position thus allowing to precisely infer the beam position. In contrast to $F_{z,\text{max}}$, $F_{z,\text{int}}$ is susceptible to misaligned beams. For example, the trained user can readily identify if the beam is tilted in the image xz -plane by looking at $F_{z,\text{int}}$. The recognition of misaligned beams is in general not possible with $F_{z,\text{max}}$.

Images obtained according to equations 6.14 and 6.15, respectively, are shown in Figure 6.5 for image data $p_i(x, z)$ corresponding to the image of the drosophila egg chamber shown below in Figure 6.10. The parameters dx and x_{off} are obtained by fitting a linear function to the x -positions with maximum intensity extracted from F_z for the n images (marked by dashed lines in Fig. 6.5).

The calibration procedure is substantially facilitated by the knowledge of the proportionality a between the difference of the lateral beam position dx and the

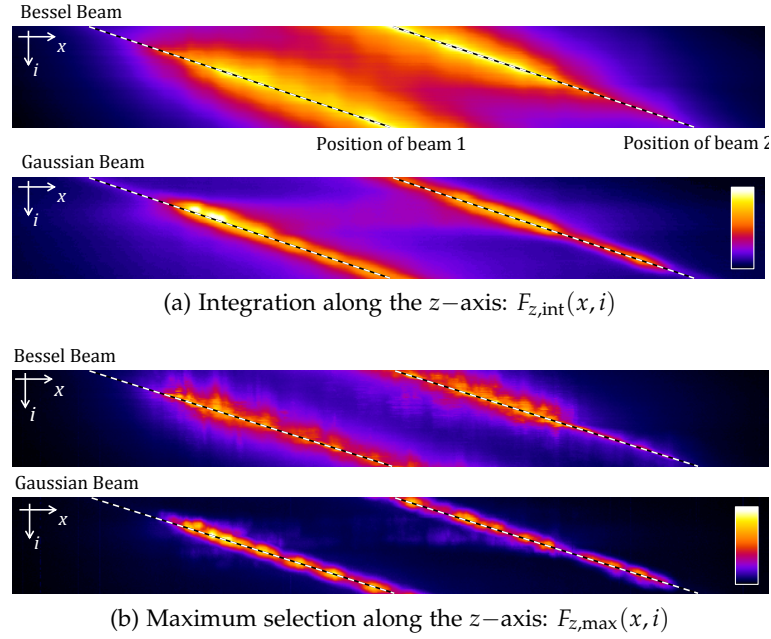


Figure 6.5: Calibration of the line-confocal detection method.

Sum projection (a) and maximum selection (b) of the images i along the illumination axis y for each beam position x_j . The top images show Bessel beam, the bottom images a Gaussian beam. The beams are two-fold multiplexed. The extracted beam positions are indicated by dashed lines.

difference of the (voltage) signal dU applied to the scan mirror, i.e. the change of the angle of the scan mirror

$$dx = a \cdot dU$$

Different to x_{off} , the parameter $a = dx/dU$ is very robust against drift and it is therefore sufficient to determine a only once for the setup. Thus, with dx known, the fitting procedure only needs to provide x_{off} .

6.5 PERFORMANCE ANALYSIS USING IMAGES OF STRONGLY SCATTERING BEADS

The first sample investigated consists of fluorescent polystyrene spheres (PS) with a diameter of $d = 0.75\mu\text{m}$. (Fluoresbrite YG, Polysciences) fixed in an agarose gel cylinder at a high concentration of $c = 8 \cdot 10^9/\text{ml}$. The data shown in this section was published in [Fahrbach and Rohrbach, 2012]. PS-spheres are strong scatterers due to their high refractive index of $n = 1.6$ and sufficiently small to allow measurements of PSF_{LS} and PSF_{CL} .

A volume $s_x \cdot s_y \cdot s_z = 40\mu\text{m} \cdot 10\mu\text{m} \cdot 220\mu\text{m}$ was imaged using the detection lens with the highest NA and magnification that was available (W Achroplan 63x/0.95, Zeiss). The sampling along the detection optical axis was $dy = 0.5\mu\text{m}$. In total, $N = s_x/dx = 100$ images $p_i(x, z)$ for static illumination beams with a sampling of the lateral position of $dx = 0.4\mu\text{m}$ were recorded for illumination by Gaussian and Bessel beams with equal depth of field. From these images, confocal images p_{LC} for a width of the line-mask $2w = 0.7\mu\text{m}$ were computed using eqn 6.11. Images corresponding to scanned illumination beams were also computed by addition of all images (compare Appendix A).

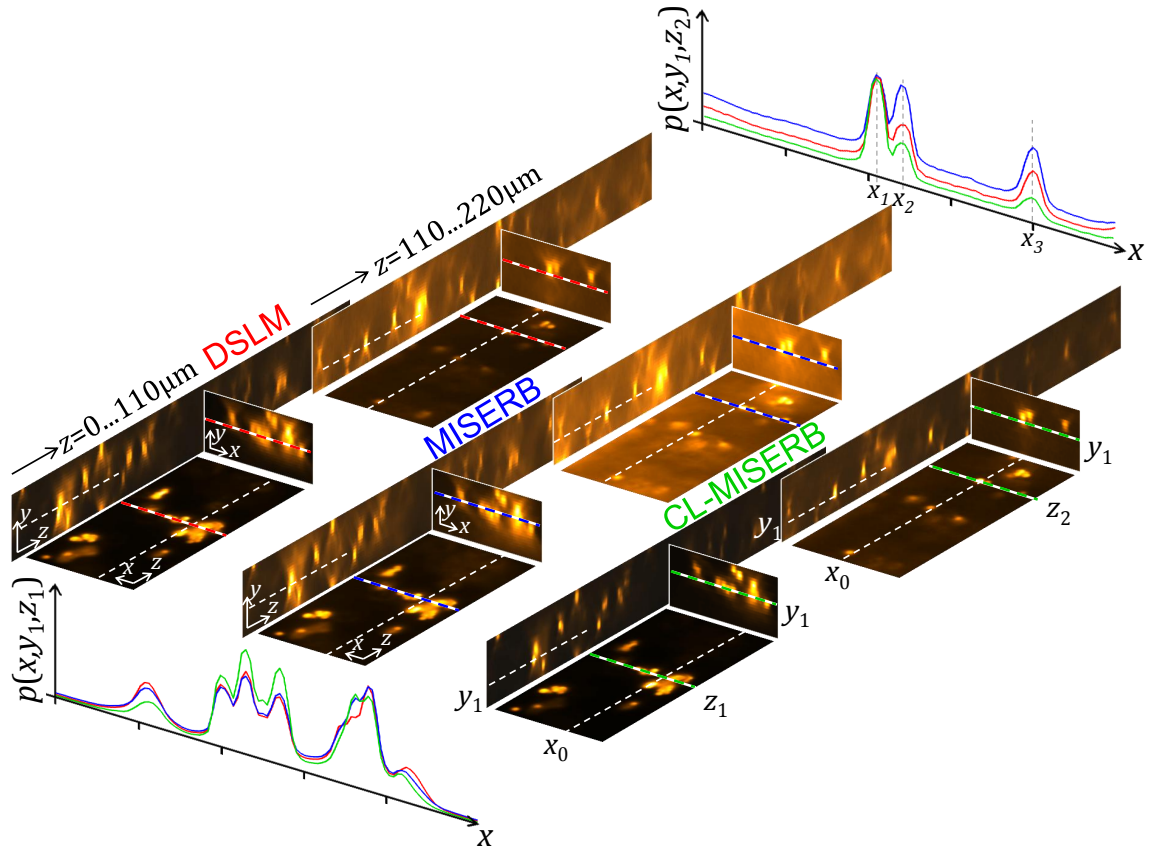


Figure 6.6: Images resulting from illumination with a scanned Gaussian beam (DSL), a Bessel beam (MISERB) and line-confocal detection for Bessel beam illumination (CL-MISERB). All white dashed lines indicate the positions where the images slices intersect, the coordinate is marked for the images of CL-MISERB. Vertical slices $p(x, y_1, z)$ in the plane spanned by the illumination z -axis and detection optical y -axis are shown standing upright. The slices are split into two parts with separately adjusted dynamic range. One for the range $z = 0 \dots 110 \mu\text{m}$ and one for $z = 110 \dots 220 \mu\text{m}$. The white dashed lines ($y_1 = 6 \mu\text{m}$) indicate the intersections with slices $p(x, y_1, z)$ corresponding to the regular image plane. These are images from sections with $z = 0 \dots 35 \mu\text{m}$ and $z = 110 \dots 145 \mu\text{m}$. Images slices $p(x, y, z_1)$ and $p(x, y, z_2)$ are shown standing behind the corresponding slices. Additionally profiles $p(x, y_1, z)$ for $z = z_1 = 18.4 \mu\text{m}$ and $z = z_2 = 136.2 \mu\text{m}$ are shown for positions that are indicated by colored dashed lines in the corresponding images with colors as following: red stands for DSLM, blue for MISERB and green for CL-MISERB.

Slices through the image volumes $p(x, y, z)$ are shown in Figure 6.6. The colored dashed lines in the $p(x, y)$ and $p(x, z)$ -slices denote the positions of the lateral 1D-intensity profiles $p(x, y = y_1, z = z_1)$ and $p(x, y = y_1, z = z_2)$ that are plotted at the bottom and on top of the figure, respectively. The profiles are normalized to have equal maximum values. The images and 1D-profiles allow the following conclusions: As expected, the image slices $p(x, z)$ reveal that scanned Bessel beam illumination (MISERB) provides inferior contrast. The contrast improvement for CL-MISERB relative to MISERB is especially striking in the back part of the volume. Even though the images convey the impression that scanned Gaussian beams (DSLMS) and confocal-line detection Bessel beams (CL-MISERB) offer similar contrast, the $p(x, y)$ and the $p(y, z)$ -slices clearly show that the extent of the images of the spheres along the detection y -axis is much more confined for CL-MISERB. This property will be analyzed in more detail below.

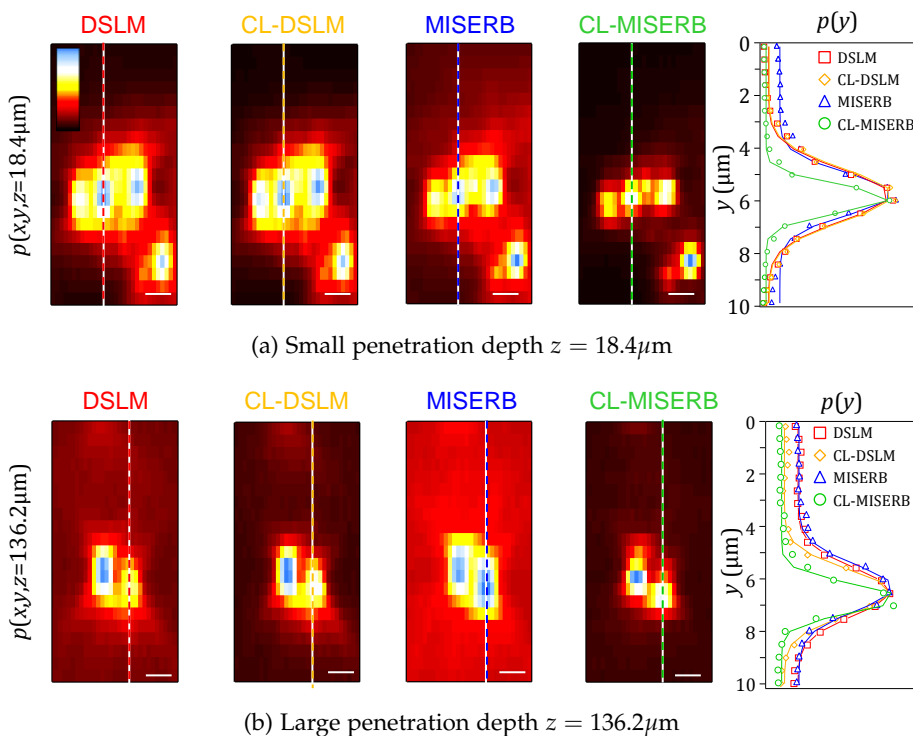


Figure 6.7: Image slices through fluorescent spheres with profile along the detection axis.

Image slices through single spheres revealing the axial resolution. (a) For all imaging modes, slices $p(x, y)$ for low penetration depth of the illumination beam $z = z_1 = 18.4\mu\text{m}$ and for large $z = z_2 = 136.2\mu\text{m}$ are shown. The dashed lines indicate the positions of the axial profiles $p(y)$ through one fluorescent polystyrene sphere ($d = 0.75\mu\text{m}$) that are shown right-hand. The Gaussian fit function from which the axial resolution is derived is included as continuous line (DSLMS is shown in red, CL-DSLMS in orange, MISERB in blue, CL-MISERB in green). The scale bar corresponds to $1\mu\text{m}$.

The line profiles $p(x)$ are hard to interpret without further knowledge. The difficulty lies in the fact that the parameter to be assessed is three-dimensional. The profile $p(x, z_1)$ looks similar for all imaging modes, but CL-MISERB offers the largest values of $p(x, z)$ in the center and lowest magnitude for the lobe on the left side. From the profile $p(x, z_2)$ the strong suppression of background offered by confocal-line detection is immediately recognizable. While all imaging modes

image the bead at x_1 best, the signal at x_2 and x_3 is weakest for CL-MISERB, while it is highest for MISERB. The 1D-profile offers no possibility to explain the origin of this discrepancy. The objects have to be located in 3D to make it possible to draw conclusions from the magnitude of their image. Analysis of the $p(y, x)$ -image (Figure 6.7) reveals the origin of the different fluorescence intensities, which is the different y -position of the spheres located at x_1 , x_2 and x_3 . The spheres at x_2 and x_3 are not located in the imaged plane. Because CL-MISERB offers best axial resolution Δy , the images reveal the smallest extent of the object's images along the y -axis. Therefore, the signal magnitude at x_2 and x_3 in the $p(x, y = y_0, z_1)$ -profile is weaker. Unlike for the assessment of lateral resolution, looking directly at line-profiles in xz -images may be misleading because less signal is neither per se better or worse. A solution to this problem, that consists in a more detailed analysis will be presented in the next section.

6.5.1 Determination of Resolution and Signal-to-background

The image of small fluorescent spheres enables the measurement of the point-spread-function to a good approximation. To obtain representative results, we analyzed the images of $n = 119$ spheres along the beam propagation distance $z = 0 \dots 220 \mu\text{m}$. The center positions (x_i, z_i) of the solitary spheres were identified manually for $i = 1 \dots n$ from a maximum projection image along the y -axis $p_{\max}(x, z)$. The profile along the detection axis at the position of the spheres $p(x_i, y, z_i)$ is evaluated for each of the four different imaging types by fitting a Gaussian function

$$p_i = p_{\text{BG},i} \cdot \left(1 + R_i \cdot \exp \left\{ - (y - y_i)^2 / w_i^2 \right\} \right) \quad (6.16)$$

and extracting two parameters relevant for image quality:

1. The focal width (FWHM) $\Delta y = 2w\sqrt{\lg 2}$ as a measure for the axial resolution.
2. The signal-to-background ratio $R = p_S / p_{\text{BG}}$.

Both parameters, Δy_i and R_i are then analyzed in dependence of the position of the sphere along the illumination axis z_i . The axial resolution of the imaging

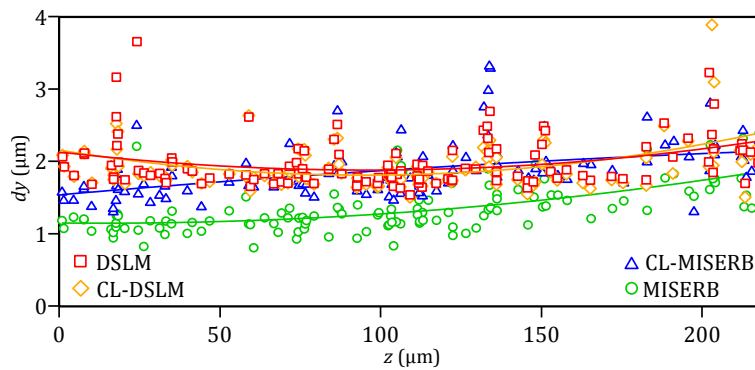


Figure 6.8: Axial resolution in Line Confocal detection microscopy.

The FWHM-value value $dy(z_i)$ for the line-profiles through spheres $i = 1 \dots 119$ plotted against the z -coordinate z_i of the sphere it was measured for.

method can be inferred from the extent of the point-spread function, as it is a

direct measure for the minimum resolvable distance between two adjacent points. The focal widths Δy_i plotted against the coordinate of the sphere z_i for which the profile $p(x_{c,i}, y, z_{c,i})$ was taken is shown in Figure 6.8. Least-squares parabolic fits $\Delta y(z) = a + bz + cz^2$ are shown for better comparability. Whereas the resolution Δy is similar for scanned Gaussian (DSLML) and scanned Bessel beams (MISERB), confocal-line detection offers a substantial improvement by a factor of 1.7 for small distances z and a factor of 1.3 for large z for illumination by Bessel-beams (CL-MISERB). No improvement is visible for confocal-line detection of Gaussian beams (CL-DSLML, blue slope) relative to DSLML (red slope).

The static illumination by a Bessel beam effectively leads to a strongly suppressed detection of the fluorescence excited by the ring-system around the confined main lobe. The Gaussian beam is broader and has a monotonously decreasing intensity profile which is hardly affected by the removal of intensity from outer regions.

For Gaussian beam illumination Δy is smallest around $z \approx 110\mu m$, where the waist of the beam lies. The focusing by $NA_{\text{ill}} \approx 0.07$ results in a waist size $dy \approx 0.5\lambda/NA_{\text{ill}} \approx 3.5\mu m$. In contrast, Bessel beams exhibit a stable transverse extent of the main peak along their propagation-invariant depth of field in homogeneous space. The width of the bead images increases only slightly with z due to scattering and broadening of the thin central lobe. The broadening effect of the Gaussian beam due to scattering is less visible, since local beam distortions due to scattering are mostly within the beam's natural width, which is always larger than $3.5\mu m$. Nevertheless, energy is continuously taken out of the beam, which results in a reduction of the amplitude of $p(y)$, but hardly in the width. As outlined before, a major goal of confocal-line detection microscopy

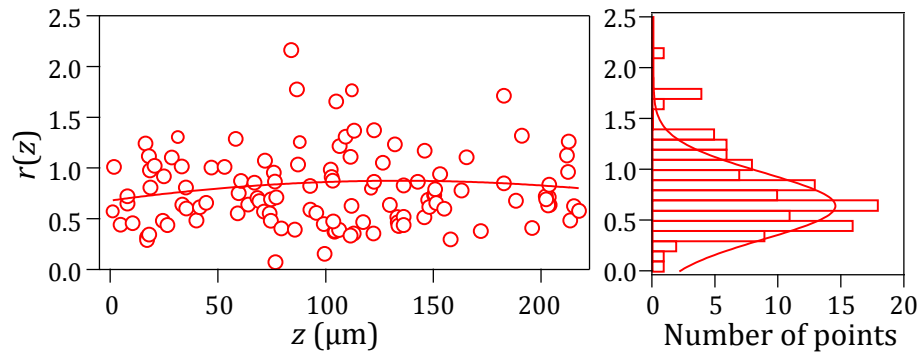


Figure 6.9: Signal-to-background in confocal-line detection microscopy.

Signal-to-background provided confocal-line detection microscopy with Bessel beam illumination (CL-MISERB) is compared to wide-field detection for illumination by scanned Gaussian beams (DSLML). The distance-dependent quotient $r(z) = R_{\text{DSLML}}/R_{\text{CL-MISERB}}$ of the signal-to-background ratios $R(z) = p_S(z)/p_{\text{BG}}(z)$ for DSLML and CL-MISERB is shown with a parabolic fit on the left. Values $r(z) < 1$ indicate positions where better signal-to-background is provided by CL-MISERB. The histogram of all quotients $r(z)$ together with a fit Gaussian function is shown on the right. The histogram shows a maximum at $r = 0.6$.

is to reduce the background in order to increase the signal-to-background ratio R . The background is produced mainly by the images of spheres far away from the focal plane of the detection lens. This background is already strongly suppressed by light-sheet microscopy but even more by confocal-line detection. Computation of the quotient $r = R_{\text{DSLML}}/R_{\text{CL-MISERB}}$ facilitates the comparison

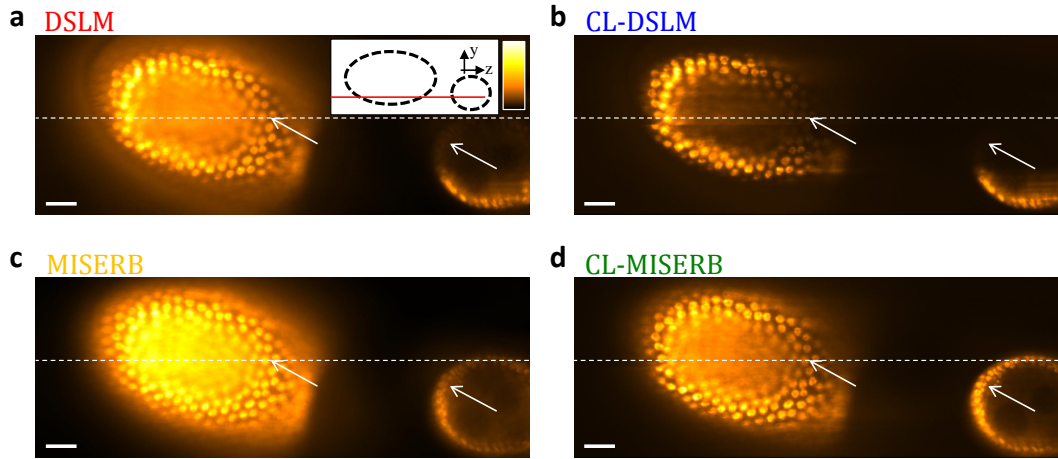


Figure 6.10: Images of drosophila egg-chambers with wide-field and confocal-line detection. Fluorescence images of drosophila egg chambers for illumination by Gaussian beams (a, c) and Bessel beams (b, d). Images for wide-field detection are shown in a, b. Images for confocal-line detection are shown in (c, d). The size of the images shown is $\Delta x \cdot \Delta z = 80\mu\text{m} \cdot 220\mu\text{m}$. All illumination beams propagate along the z-axis from the left to the right.

of DSLM relative to CL-MISERB. By plotting r_i against z_i , as shown in Figure 6.9, the following conclusions can be drawn: For a large majority of the imaged spheres, the signal-to-background is better for CL-MISERB, as indicated by a large number of spheres with $r_i < 1$. However, it is hard to judge from this graph alone. Therefore, a histogram of the $n = 119$ values of r_i is shown in Figure 6.9. The mean quotient is $r_0 = 0.64$ which means that, on average, the signal-to-background ratio of CL-MISERB is better than for DSLM by a factor $1/r_0 \approx 1.5$.

It is striking that the quotient r_i varies strongly even for two spheres with a small mutual distance Δz_i along the propagation axis. There are two possible explanations for this fact. One is the different propagation behavior of the Gaussian and the Bessel through the scattering medium. As outlined already in Chapter 3 the beams feature different angular spectra and are therefore scattered differently. The Gaussian beam is affected more strongly by on-axis-scatterers than the Bessel beam, whereas the opposite is the case for off-axis-scatterers. Moreover, background suppression by confocal-line detection was employed for the Bessel beam but not for the Gaussian beam. The effect of background-rejection by confocal-line detection is position dependent in a scattering medium and can therefore also be an explanation for the large variance of r_i .

6.6 IMAGING PERFORMANCE IN DROSOPHILA EGG-CHAMBERS

The suitability of confocal-line detection for imaging biological samples was tested on fluorescence-labeled egg chambers from the drosophila fly with br antibody staining of dad coupled to follicle cells. These results were published in [Fahrback and Rohrbach, 2012]. The images obtained for Gaussian and Bessel beam illumination with wide-field or confocal-line detection are shown in Figure 6.10. The lateral beam sampling was $dx = 0.5\mu\text{m}$ and for confocal-line detection the mask width was $2w = dx$. $N = 80$ full-frame images were recorded and two-fold beam multiplexing with a beam distance of $N \cdot dx \approx 40\mu\text{m}$ was

employed. The two drosophila egg chambers shown are located behind each other (relative to the illumination direction). By taking images in different layers it was determined that the egg-chambers are also slightly displaced to each other along the detection optical axis. This is indicated by the schematic inset, where the red line indicates the image plane. The shape of the egg-chambers is ellipsoidal. The stained cells are situated on the surface only. As the staining of the cells was very weak, long exposure times ($T = 2\text{ s}$ per position) were necessary. The interior of the egg-chamber also reveals a fluorescence signal. This might be auto-fluorescence. Another possibility is that some of the dye unintentionally stained the interior region.

The image quality of the egg-chamber on the left side of the image is discussed first: DSLM offers satisfactory contrast. The cells can be resolved individually to a large fraction. However, the egg-chamber is surrounded by a halo that is even stronger than in the MISERB images. As expected, MISERB delivers modest contrast as many cells of the egg chamber located below and above the focal plane are illuminated. Relative to the cells in the front, the cells at the back side (marked by an arrow) of the egg-chamber are brighter. This is also indicated by the axial line profile that is shown in Fig. 6.11. CL-MISERB offers very good contrast all over the egg chamber. The decline in signal across the egg-chamber is comparable to DSLM, but the contrast is much better. Confocal-line detection for Gaussian beam illumination (CL-DSLM) fails to properly image the egg-chamber. While it offers best contrast at the front of the egg-chamber, the signal is strongly reduced for larger penetration depth and the back side of the egg-chamber is hardly visible. This strong decline in signal can also be recognized in the axial profile (Fig. 6.11). Obviously, the Gaussian beam is spread and/or deviated due to scattering. The irradiance along the straight line that is read out by confocal-line detection is very low already at modest penetration depths.

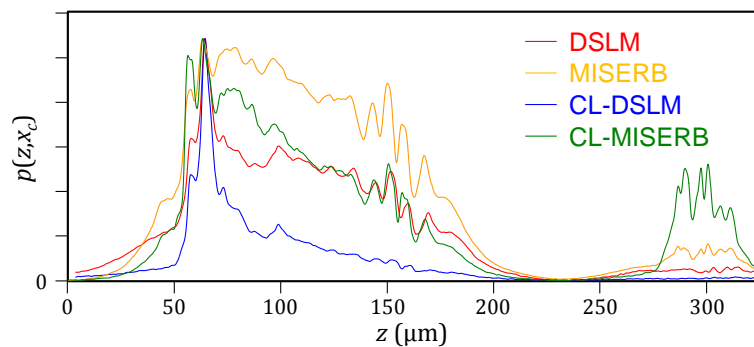


Figure 6.11: Axial line profile through images of drosophila egg-chambers

The image quality of the egg-chamber on the right side is very different for the four imaging modes. It is hardly visible for illumination by a Gaussian beam (DSLM). The impression is that the first egg-chamber casts a shadow on the second one. This effect is even more pronounced for confocal-line detection (CL-DSLM). The Gaussian illumination beam must be spread and scattered out of the image plane by the first egg chamber, so that the irradiance at the position of second egg-chamber is very weak. In the confocal-line detection case, the deviation of the beam is even more critical than for wide-field detection. For Bessel beam illumination, however, the second egg-chamber is fully visible. Single cells can be resolved and even some fine structure at the interior is observable. The Bessel beam seems to propagate essentially unperturbed through

the first egg-chamber delivering high irradiance to the second egg-chamber. The good penetration cannot be explained by the self-reconstruction of Bessel beams behind an isolated obstruction [Bouchal et al. \[1998\]](#). Although scattered by the first egg chamber to a large fraction, the Bessel beam self-reconstructs by constructive interference without significant irradiance drop-off along the predicted z -line, which the confocal-line detection principle selects for the final image.

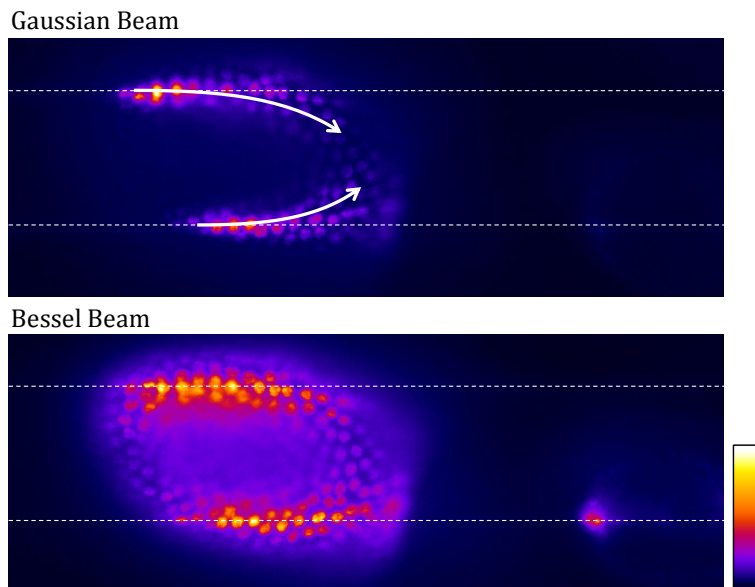


Figure 6.12: Propagation of Gaussian and Bessel beams through drosophila egg-chambers.

The images show Gaussian beams in the top image and Bessel beams in the bottom image. The beams illuminate the sample at two lateral positions separated by $\approx 40\mu\text{m}$. The beam axes are marked by dashed lines. The Gaussian beam is bent inwards and spread so that the irradiance at the second egg-chamber is too low to generate noticeable signal. In contrast the Bessel beam illuminates the second egg-chamber directly on the initial propagation axis.

In summary, confocal-line detection increases contrast and additionally utilizes the directional propagation stability of the Bessel beams. Therefore, the image quality for illumination by Gaussian beams that are easily deflected is inferior to that offered by Bessel beams. Using confocal-line detection is therefore less useful with Gaussian beams than with Bessel beams. Hardly any light is collected if the beam is scattered or deflected from the propagation axis. Evidence for the strong spreading of the Gaussian illumination beams and the bending along strong refractive index changes as e.g. the edge of the egg chamber is given in [Figure 6.12](#).

6.7 QUANTITATIVE CONTRAST ANALYSIS IN IMAGES OF MULTICELLULAR SPHEROIDS

Spheroidal clusters of cancerous cells are an ideal model system for studying the development of cancer. A low light-dose and high imaging speed, but even more the necessity to study three-dimensional samples in a natural environment being key factors, light-sheet microscopy is the tool of choice for the investigation of these aggregates of cells. However, the focus of the investigations in the context

of this thesis lay on the comparison of the image quality that can be obtained by the different techniques. Therefore, the spatial frequency analysis presented in section 2.2.4 is utilized.

6.7.1 Image Decomposition

The goal of the analysis in this chapter is the comparison of the relative image contrast resulting from different illumination beams. Therefore, the relation between high and low spatial frequencies in the images is computed as a measure for the signal-to-background ratio. The method is described in detail in Section 2.2.4. The absolute values strongly depend on the cut-off frequency k_F between low and high spatial frequencies. The relative comparison that is performed here is not sensitive to k_F . The values could therefore be chosen based on visual inspection of the high- and low-pass-filtered images as illustrated in Figure 6.13. A value of $k_F = 0.6/\mu\text{m}$ leads to a separation of the relevant image information in the high-pass filtered image p_{HSF} , where the stained cell walls are clearly visible on a uniform background. The low-pass filtered image p_{LSF} contains no relevant image information but the background that allows to roughly identify the shape of the cluster and of some cells. The next step lies in the validation of the method.

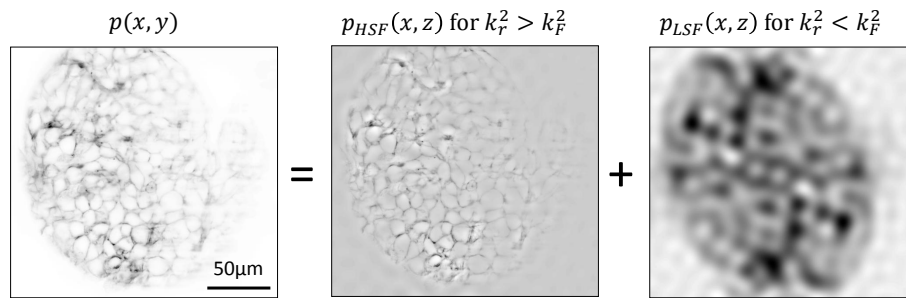


Figure 6.13: Spatial frequency image decomposition.

Example for image decomposition into low-frequency background and high-frequency information for a cut-off frequency of $k_F = 0.6/\mu\text{m}$.

6.7.2 Image Contrast Dependency on the Confocal Line Width

It is well known that image contrast in confocal point-scanning microscopy strongly depends on the size of the pinhole. This dependency also holds for confocal-line detection microscopy. An infinite diameter of the pinhole corresponds to a wide-field image and analogous an infinite slit width w corresponds to the case of full-frame detection for scanned illumination beams. The visual perception that image contrast increases when the slit-width is decreased is supported by the analysis using the spatial frequency decomposition. In Figure 6.14 the fraction $\text{SBR} = \text{HSF}/\text{LSF}$ of high (HSF) and low spatial frequencies (LSF) is shown for 4 different slit-widths. 15 images of a spheroidal cell cluster taken in different y -planes were analyzed in order to be able to judge the variability of the obtained values. Apart from a slight increase in SBR with the image plane index i the values show only very small deviations for adjacent planes which means that the measure is not susceptible to specific features in the images. The increase of SBR for larger i can be easily explained: the image plane y_0 lies deeper within the cell cluster and therefore the blur in the image due to

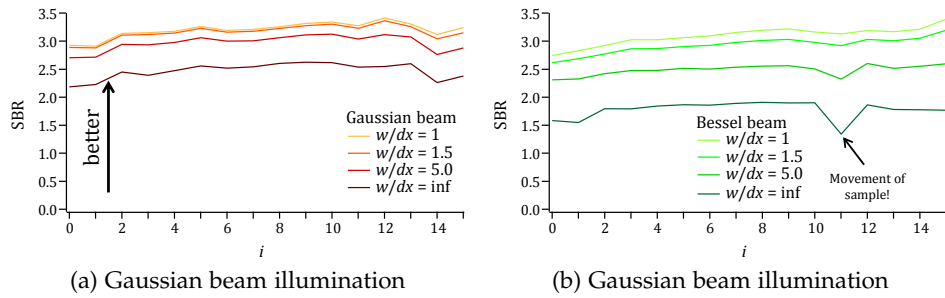


Figure 6.14: Relative Information Content dependency on the confocal-line width

scattering of detected fluorescence is larger. Note that movement of the sample during the image acquisition leads to a significant drop in the image quality factor SBR for image $i = 11$ with Bessel beam illumination. Most importantly, the SBR increases for thinner confocal-line detection slit masks. The measure accurately reproduces the predicted and perceived improvement in the relative content of image information, i.e. the image contrast achievable by confocal-line detection.

6.7.3 Image Contrast Comparison

Using the method that was validated in the previous section it is now possible to analyze the relative information content, i.e. the contrast, for different imaging modes. In this section, wide-field and confocal-line detection images of tumor multicellular spheroids illuminated by Gaussian and Bessel beams are compared.

To generate the final image, $N = 100$ raw images were recorded where the illumination beam was four-fold multiplexed at a distance of $N \cdot dx = 50\mu\text{m}$. The beams were displaced in discrete steps of $dx = 0.5\mu\text{m}$ for each raw image. Post-processing was performed according to the description given in Section 6.4. A mask width of $w = \infty$ was used to obtain the wide-field images (DSLML, MISERB) and confocal-line detection images (CL-DSLML, CL-MISERB) were generated using $w = dx = 0.5\mu\text{m}$. For both illumination beams, a stack of 41 images was recorded. The first image of the stack ($i = 0$) is taken approximately in the center of the spheroid. For the next images the spheroid is moved away from the detection objective in steps of $dy = 2\mu\text{m}$.

Gray-scale images from a plane in the center of the cell cluster ($i = 3$) are shown in Figure 6.15, and for a plane closer to the surface ($i = 39$) in Figure 6.16. The reproduction shown here allow only a rough judgment of overall image contrast. The images taken in the center of the cluster reveal less details and give the impression of overall lower contrast than those taken for a shorter path of the detection light through the sample (Fig. 6.16). Confocal-line detection is generally capable to deliver strongly improved image contrast. The scanned Gaussian beam (DSLML) delivers similar image quality as CL-MISERB at first glance but the decay along the illumination axis is stronger. The image obtained from Gaussian beam illumination with confocal-line detection has the highest contrast but also exhibits strong artifacts, mainly in the form of stripes along the illumination axis.

These visual impressions are supported by the signal-to-background analysis as shown in Figure 6.17. Similar to the results shown in the previous section,

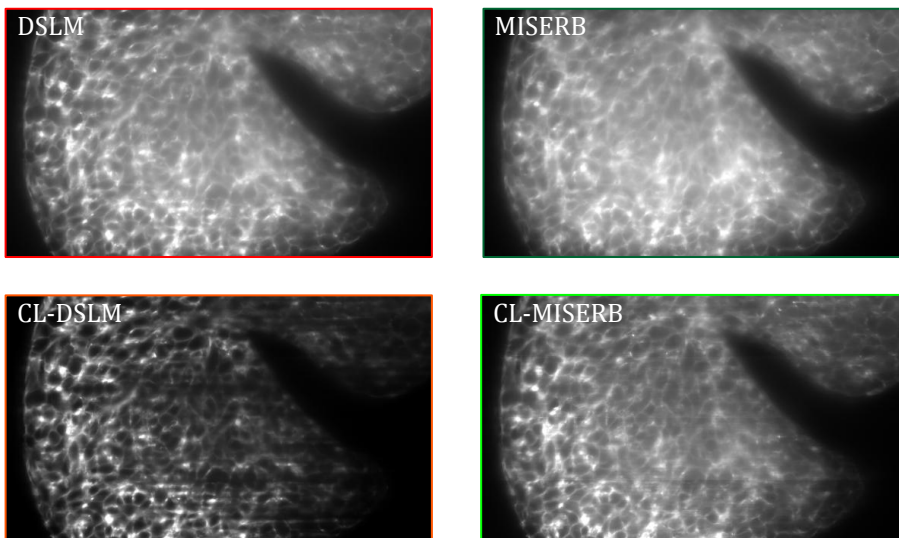


Figure 6.15: Images of a layer in the center of a tumor cell cluster. The images show plane y_3 of the tumor cell cluster which is close to the center of the spheroidal cell cluster. The images show an area of $325\mu\text{m} \times 200\mu\text{m}$.

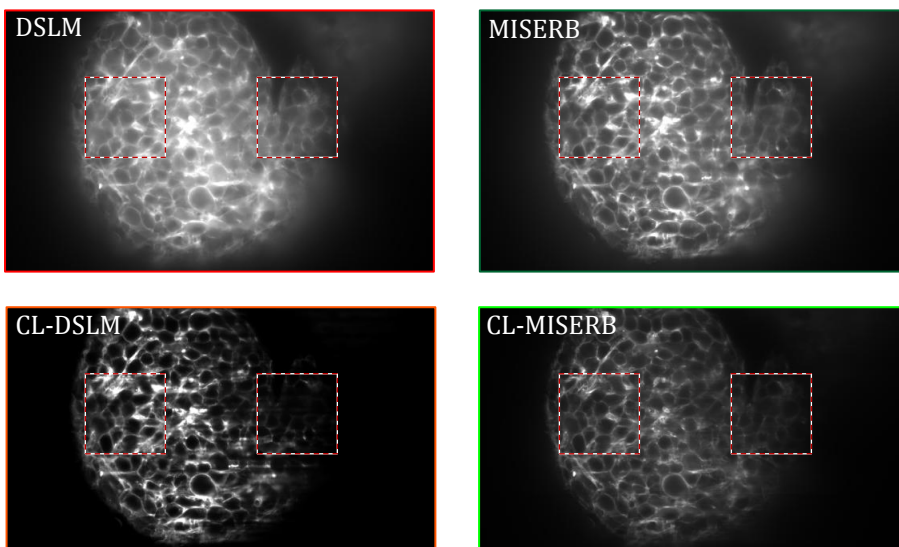


Figure 6.16: Images of a layer close to the surface of a tumor cell cluster. The images show plane y_{39} of the tumor cell cluster which is close to the surface. The images show an area of $325\mu\text{m} \times 200\mu\text{m}$. Magnified images of the regions marked by the dashed squares are shown in Figure 6.18.

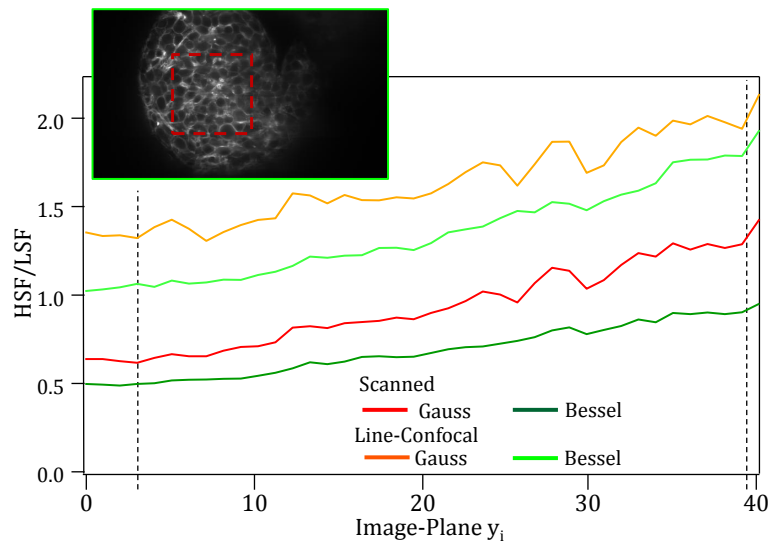
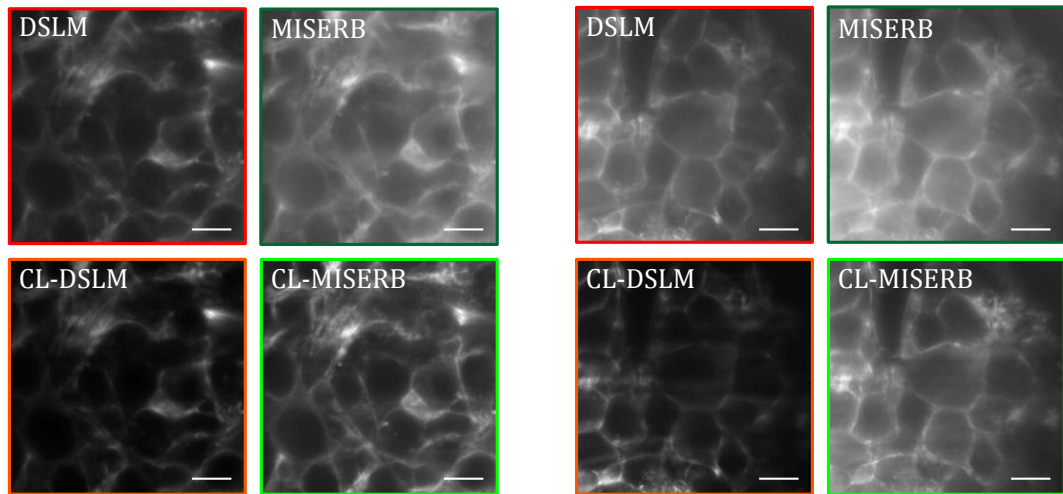


Figure 6.17: Image contrast analysis of an image stack of a tumor cell cluster. The inset shows the region where the signal-to-background (SBG=HSF/LSF) was evaluated. The dashed lines indicate the y -position of the images shown in Figure 6.15 and 6.16, respectively.

the image contrast increases with the index i , thus for planes closer to the detection objective lens. While, as expected, lowest signal-to-background (SBR) is delivered by scanned Bessel beams, confocal-line detection with Bessel beam illumination leads to higher values of SBR than conventional illumination by scanned Gaussian beams. The highest values, however, are delivered by confocal-line detection in combination with Gaussian beam illumination. However, when looking at the magnified image details, shown in Figure 6.18, one can see that CL-DSLM does not deliver good images, especially at large penetration depths. This result reveals a shortcoming of the SBR-measure: Good and bad (artifacts) contrast cannot be separated. SBR yields good values when signal (HSF) decay is accompanied by background (LSF) decay, as it is the case in confocal-line detection when the beams are scattered within the image plane and away from the detected confocal line. Therefore, even though signal-to-background is highest for CL-DSLM, the best overall image quality, i.e. the most useful images with the highest information content are certainly delivered by CL-MISERB. The amount of small-scaled image details for those images is exceptionally high, as can be seen in Fig. 6.18.



(a) Image details at low penetration depth. The position is marked by the left square in (a)

(b) Image details at high penetration depth. The position is marked by the right square in (a).

Figure 6.18: Enlarged image details for low and high penetration depth of the illumination beams.

The details are taken from the images shown in Figure 6.16 and show a plane at the surface of a tumor cell cluster. The enlarged details are taken for low (a) and high (b) penetration depth of the illumination beams. The size of the enlarged details is $60 \times 60 \mu\text{m}^2$.

6.8 IMPROVED OPTICAL SECTIONING BY SECTIONED BESSEL BEAMS

Sectioned Bessel beams feature an asymmetric profile where the central lobe of the beam is mainly fed from two opposite sides. These beams were introduced in Section 3.2.2. Their directional propagation stability was investigated numerically in Section 4.2. The resolution and optical sectioning was compared to other illumination beams in Section 6.3. These beams can be used to illuminate a thin line from the sides. If fluorescence is detected along the line using the confocal-line detection scheme it is expected that significantly less background will be recorded. This interesting potential application to a new variant of the Bessel beam is investigated in detail in the following section.

6.8.1 The Optimum Section Angle

The optical sectioning performance depends on the overlap of the illumination and detection point-spread functions. The ring system of sectioned Bessel beam is suppressed in two opposite sectors. Therefore these beams can be used to illuminate a line from two opposing sides. The idea of using sectioned Bessel beams together with confocal-line detection is the following: If the region sparsely illuminated by the sectioned Bessel beam is adapted to the collection volume of the detection objective lens, the detection of background fluorescence should be strongly reduced.

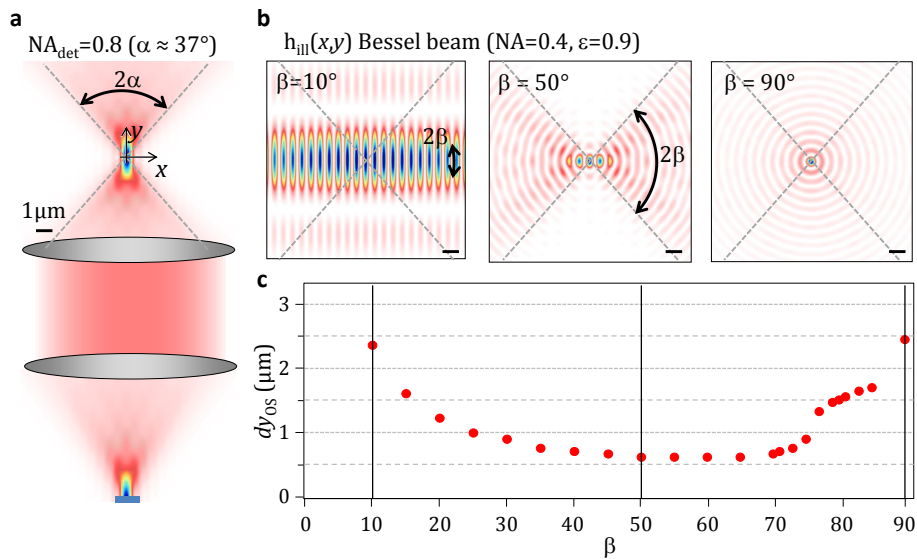


Figure 6.19: Dependence of the Optical Sectioning on the Angle of the sectioned Bessel beam.

The detection path is shown in (a) using a projection of h_{det} along the z -axis. Irradiance cross-sections for three different angles β are shown in (b). The optical sectioning performance in dependence of the section angle β is shown in (c).

The detection objective lens collects light from a region that can be roughly approximated as double cone with opening angle $2\alpha = 2\arcsin(\text{NA}_{\text{det}}/n)$. A projection along the z -axis of the detection probability distribution is shown in Figure 6.19a.

Sectioned Bessel beams with a section angle of β are formed by interference of plane waves that travel with a maximum angle β against the x -axis. The

ring system is largely suppressed in the complementary sector with central angle $180^\circ - 2\beta$. Sectioned Bessel beams for three angles β are shown in Figure 6.19b. To find the value of β that provides best optical sectioning a simulation was performed using a discretization of 47nm in a cube with a side length of 1024pixels ($\approx 50\mu\text{m}$). The wavelength $\lambda_0 = 500\text{nm}$ then corresponds to 8 pixels in a medium with $n = 1.33$. For sectioned Bessel beams with $\beta = 10^\circ$ to $\beta = 90^\circ$ in steps of 5° , the optical sectioning was computed using the fluorescence-sea method introduced in Section 2.2.3. dy_{OS} shown in Figure 6.19c gives the range along the detection y -axis where $63\% = 1 - 1/e$ of the total signal is detected. The graph indicates best optical sectioning for angles β in the range of 40° to 60° . While smaller values of β result in a grating-like structure that is only poorly confined along y (compare $h_{\text{ill}}(x, y)$ for $\beta = 10^\circ$ in Fig. 6.19b), the sectioned Bessel beam increasingly resembles a conventional Bessel beam for larger angles β (compare $h_{\text{ill}}(x, y)$ for $\beta = 90^\circ$ in Fig. 6.19b).

The optical sectioning is improved by a factor of ≈ 4 from $dy_{\text{OS}} = 3\mu\text{m}$ to $dy_{\text{OS}} = 0.8\mu\text{m}$ relative to a conventional Bessel beam. Surprisingly, the dependence of the optimum value of β on the detection Numerical Aperture NA_{det} is very small and no significant difference could be observed for other values.

6.8.2 Analysis of Optical Sectioning Dependency on the Depth of Field

The asymmetry of the sectioned Bessel beam cannot only be exploited to improve the optical sectioning, but to obtain optical sectioning that is independent on the illumination beam's depth of field, i.e. the size of the field of view along the illumination axis. This ability of the sectioned Bessel beam separates this beam from all other illumination beams like Gaussian and Bessel beams, where the symmetrical cross-section extends when the depth of field is increased. In Figure 6.20 the optical sectioning for confocal-line detection is plotted against the illumination beam's depth-of-field for Gaussian, Bessel and sectioned Bessel beams. For the Gaussian beam a nonlinear dependency can be observed. This is in agreement with theory predicting a quadratic interdependence between the Gaussian beam's depth of field and its waist diameter (see Section 3.1). Optical sectioning provided by a Bessel beam increases in a more linear fashion which is superposed by steps. Those arise from the Bessel beams rings. The linear interdependency can be understood if one looks at the cross-section of the volume where the Bessel beam is shaped which has the shape of a rhombus (Figure 3.10). In contrast, optical sectioning for the sectioned Bessel beams is independent on the depth of field. Due to the asymmetrical shape of the sectioned Bessel the cross-section of the beam mainly increases along the x -axis where no light is detected. There is no additional overlap with the detection PSF h_{det} for a larger depth-of-field.

Note that the origin of the steps in the $dy_{\text{OS}}(dz)$ curve for the Bessel beam can be understood by looking at Figure 6.4. The slope of the curve changes very strongly at a certain value of y . When $dy_{\text{OS}}/2$ reaches this value the proportionality between dz and dy_{OS} is changed and leads to a jump in dy_{OS} .

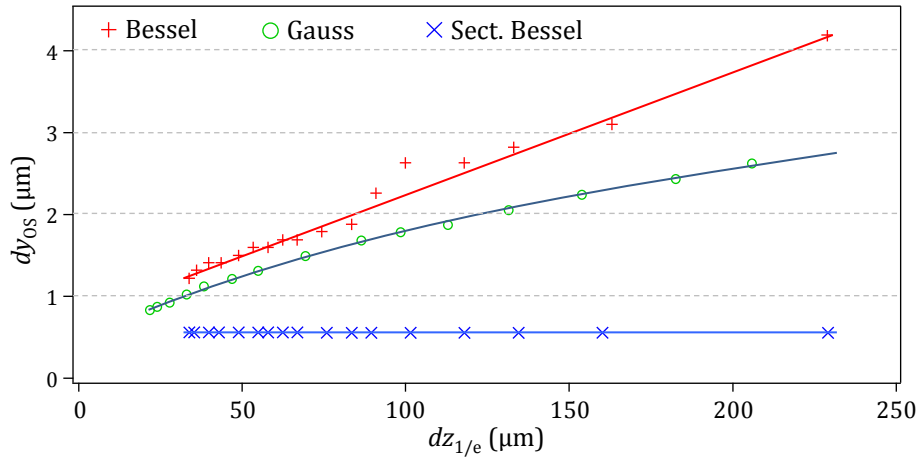


Figure 6.20: Dependence of the optical sectioning on the depth of field.

6.8.3 Analysis of the Quality of Images of Tumor Multicellular Spheroids

To test the performance of sectioned Bessel beams, Tumor Multicellular Spheroids were imaged. This section contains a detailed analysis and the comparison of the image quality resulting from 4 different imaging modes: In addition to Confocal-Line Detection for illumination by Gaussian, Bessel and sectioned Bessel beams, wide-field detection for Gaussian beam illumination is included as it represents the most commonly used technique. For each beam, a stack of 15 images was recorded and the wide-field and confocal-line detection images were generated as described in Section 6.4. The images are shown in Figure 6.21a-d. The signal-to-background analysis was performed as in the previous section. Figure 6.21e shows that confocal-line detection with sectioned Bessel beams offers a very good signal-to-background SBR. The sectioned Bessel beam yields the approximately the same SBR as the Gaussian beam, but looking at the images reveal more details at larger penetration depth into the sample. The penetration depth into the strongly scattering cell cluster was also quantitatively evaluated. This can be simply achieved by a profile $p_{\text{avg}}(z)$ that averages the signal across the width of the image. The results are shown in Figure 6.21f. The Bessel beam and the sectioned Bessel beam show significantly larger signal strength for large penetration depths $z > 100\mu\text{m}$. This quantitative finding is in agreement with the images shown in Figure 6.21a-d, where the confocal-line detection image for Gaussian beam illumination exhibits a strong decrease in signal at the right side of the spheroid, where the illumination beam has to travel the longest distance through the cell cluster.

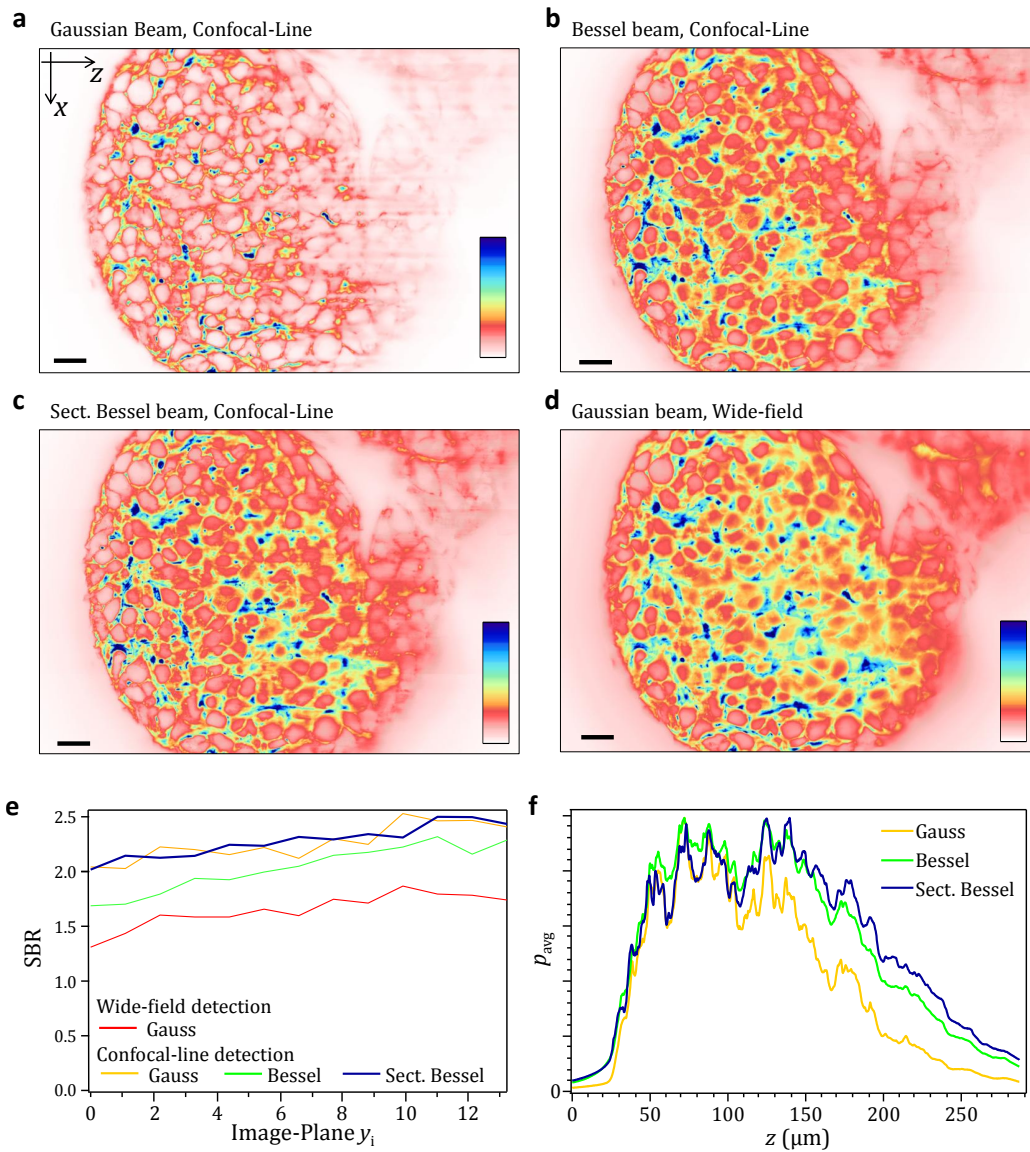


Figure 6.21: Image quality comparison for confocal-line detection with sectioned Bessel beam illumination.

Images obtained for illumination by sectioned Bessel beams for confocal-line detection can be compared to other imaging modes (a-d). All images show the same plane of a tumor multicellular spheroid. All beams propagate along z . The size of the scale bar is $20\mu\text{m}$. The contrast of the tumor multicellular spheroid images measured by the spatial frequency analysis is shown in (e). The average signal in dependence of the beams penetration depth into the sample is shown in (f).

6.9 DISCUSSION

Altogether, the results shown in this chapter show that confocal-line detection light-sheet microscopy greatly improves image contrast, i.e. optical sectioning, for all tested illumination beams. When a line-sensor is used for image acquisition, confocal-line detection is able to reduce background without post-processing. Bessel beams offer inferior optical sectioning in the region around their propagation axis because the ring system does not illuminate the detection focal plane more strongly than the layers around it. However, the Bessel beam's main lobe that is well localized is able to provide superior resolution and very good optical sectioning. This potential cannot be used for wide-field detection but with confocal-line detection.

Measurements on fluorescent spheres (§ 6.5) enabled a precise measurement of the axial resolution in a strongly scattering medium which showed that Bessel beams offer a strong improvement in resolution along the detection optical axis relative to Gaussian beams. Images of biological samples such as *Drosophila* egg-chambers (§ 6.6) and Tumor Multicellular Spheroids (§ 6.6) revealed that Bessel beams yield images with drastically improved information content in the presence of strong beam perturbation by the sample. This advantage is due to the directional propagation stability (§ 4.1.1). Another possibility offered by the line-detection is the use of so-called sectioned Bessel beams (§ 3.2.2) that offer the best optical sectioning of all beams. Moreover, these beams offer optical sectioning that is in principle independent of the field of view, i.e. the depth of field of the beam need to fully illuminate the sample (§ 6.8).

However, there also exist **drawbacks to confocal-line detection**. First, in the present realization, the technique is very slow. However, this problem can be resolved in multiple ways which are discussed in detail in section 6.9.1. Second, the sample is exposed to a higher light-dose. This aspect is quantitatively analyzed in section 6.9.2.

There exist **other interesting techniques to increase image contrast** by background rejection in a post-processing step, most notably structured illumination and HiLo. An in-depth comparison to these techniques is given in section 6.9.3. An alternative method to improve the information content of images and reject background lies in deconvolution. This post-processing is commonly applied to modern light-sheet microscopy images but has not been tried in combination with Bessel beams. It is especially interesting especially if it includes statistical approaches because of the potential to deal with the Poisson noise inherent to the recorded signal [Richardson, 1972, Lucy, 1974]. However, deconvolution has some drawbacks: First, it is computationally costly and therefore will always be more time-consuming than optical hardware solutions. Second, deconvolution requires the system-PSF h_{sys} to be known at every position. Therefore, it is best if h_{sys} is position-invariant. Directional propagation stability renders Bessel beams interesting candidates for deconvolution approaches to further increase the image quality.

A **potential application** of confocal-line detection microscopy might be fluorescence correlation spectroscopy (FCS). The technique requires a precise knowledge of the system PSF and might therefore benefit from illumination by self-reconstructing beams. Moreover, as FCS requires high frame-rates to be able to measure high-frequency components of the diffusion, measurements are performed on small sub-regions. Confocal-line detection light-sheet microscopy in

combination with a high-speed line-camera would enable FCS along lines inside large organisms.

6.9.1 Speed

The present realization of confocal-line detection requires a full-frame image to be taken for each beam position. For Bessel beams created at $NA \approx 0.4$ the requirement on the sampling along the scan direction is $\delta x \leq 0.5\mu\text{m}$.

First, the number of full-frame raw images that has to be recorded can be significantly reduced by beam multiplexing. This technique, where one camera image is taken for the sample illuminated along several lines can be realized in two ways. On the one hand, provided that the scanning mirror is sufficiently fast, the illumination beam can be steered to multiple positions within the field of view during a single camera exposure. On the other hand, if the laser power available is sufficiently high, the illumination beam can be multiplexed (e.g. holographically) so that several beams illuminate the sample side by side at the same time. The minimum spacing of the beams required depends on their diameter, i.e. their depth of field. For a sample size of $300\mu\text{m}$ along the illumination axis a spacing of $\Delta x = 50\mu\text{m}$ is necessary for Bessel beam illumination with $NA \approx 0.3$ meaning that $N = \Delta x / \delta x = 100$ images have to be taken for $\delta x = 0.5\mu\text{m}$. When the signal recorded by the image sensor, i.e. the sample fluorescence, is strong, the rate at which final images can be acquired is limited only by the transfer rate of the camera and is therefore approximately $N = \Delta x / \delta x$ times slower for confocal-line detection. The increase in speed by multiplexing is then given by the number of beams. However, if sample fluorescence is weak (either intrinsically or due to weak lasers) the limiting factor is the time needed to collect a sufficient number of photons. However, the most important aspect of beam-multiplexing, is the reduction in overhead data that the camera has to transfer to the computer.

Second, the rolling shutter of a full frame camera can be synchronized to the position of the scanned illumination beam. This approach has been demonstrated only recently [Baumgart and Kubitscheck, 2012]. The speed of this technique is the same as for conventional scanned beam wide-field light-sheet microscopy. However, the width of the active area depends on the clock of AD converter in the camera and the exposure time. Therefore, the effective confocal slit width increases for longer exposure times. Unless the AD-clock can be tuned, the frame-rate cannot be chosen freely for a given confocal slit width. Modern CMOS cameras do not yet allow the necessary changes to the hardware. More quantitatively, if the sensor possesses n_z pixels along the illumination axis and a digitization frequency of f_{AD} , then the exposure time for a confocal slit width of m_x pixels is $t_{\text{exp}} = 1 / f_{AD} \cdot n_z \cdot m_x$. The full-frame exposure-time is $T_{\text{exp}} = n_x \cdot t_{\text{ext}}$. Typical values of $f_{AD} = 80\text{MHz}$, $n_x = n_z = 2000$ and $m_x = 4$ result in $t_{\text{exp}} = 10\mu\text{s}$ and $T_{\text{exp}} = 20\text{ms}$.

Third, a second scanning mirror can be introduced in the detection optical path that is synchronized to the scanning mirror in the illumination path in a way that the illuminated line within the sample is always imaged on the same position on the camera. The camera can then either be replaced by a line-sensor, or operated with a region-of-interest that corresponds to a thin line with a width of a few pixels. With a realistic frame-rate of 25kHz that can be achieved for such ROIs, full frames can be acquired at a rate of $\approx 30\text{..}60\text{fps}$ depending on the

width of the field of view. Using a second scanning mirror in the detection path and standard camera, a frame rate of 10fps was recently demonstrated [Silvestri et al., 2012].

6.9.2 Sample Exposure to Light

In this section the sample exposure to light is quantitatively analyzed in order to estimate the amount of photo-damage and bleaching that the sample is exposed to. The analysis is based on the extraction of the relationship between signal strength and the total energy brought into the sample. These considerations were published in [Fahrbach and Rohrbach, 2012].

6.9.2.1 Experimental Data

This section addresses the question how the signal amplitude p_S and the total excitation energy E can be extracted from the experimental data. p_S is the signal amplitude, i.e. the *usable signal* which sits on top of the background level. The analysis is based on the measurements on fluorescent polystyrene spheres shown in section 6.5. One can obtain p_S from the experimental data by evaluating axial profiles through the sphere images $p(y)$ and by performing least-square-fits using the Gaussian function

$$p_{\text{fit}}(y) = p_{\text{BG}} + p_S \cdot e^{-(y-y_0)^2/w_y^2} \quad (6.17)$$

As an estimate of the total beam power E incident on the sample we use the total detected fluorescence F of the sample. We assume the image $p_{\text{LS}}(x, y_0, z)$ recorded by the camera at position y_0 to be proportional to the fluorescence, which itself is proportional to the excitation intensity from a laterally scanned beam with irradiance $h_{\text{scan}}(x, y, z)$. With extinction cross-section μ_{ext} , fluorophore quantum yield Q , fluorophore concentration C_F and detection point-spread function h_{det} we write

$$\begin{aligned} F &= q \cdot \iint p_{\text{LS}}(x, y_0, z) dx dz \\ &= 1/\delta t \cdot \iint [(h_{\text{scan}}(\mathbf{r}) \cdot \mu_{\text{ext}}(\mathbf{r}) \cdot Q(\mathbf{r}) \cdot C_F(\mathbf{r})) * h_{\text{det}}(\mathbf{r})]_{y=y_0} dx dz \end{aligned}$$

Here it is assumed that the imaging process effectively leads to an integration in y -direction:

$$\begin{aligned} F &= \iiint (h_{\text{scan}}(\mathbf{r}) \cdot \mu_{\text{ext}}(\mathbf{r}) \cdot Q(\mathbf{r}) \cdot C_F(\mathbf{r})) dx dy dz \\ &= \mu_{\text{ext}} \cdot Q \cdot C_F \iiint h_{\text{scan}}(\mathbf{r}) dx dy dz \\ &= \mu_{\text{ext}} \cdot Q \cdot C_F \cdot E/\delta t \end{aligned} \quad (6.18)$$

For a high enough density of fluorophores C_F (e.g. distribution of beads), all with similar μ_{ext} and Q , we assume these values to be independent from the position \mathbf{r} . The above equation means that the detected fluorescence is proportional to the total excitation energy of the illumination light sheet. Assuming the same amount of absorption for both Bessel and Gaussian beams, the excitation energy

can be expressed by the integral over the intensity cross-section A of the scanned beam

$$E/\delta t \approx 1/A \cdot \iint h_{\text{scan}}(x, y) dx dy \quad (6.19)$$

E does not provide any information on the image contrast, but can be regarded as an indication on the amount of bleaching (and photo-damage) that the sample is exposed to. The computation of F gives a better indication on the amount of bleaching than the incident beam power would give. Finally, we obtain

$$\eta = \frac{p_S}{E} = \frac{p_S}{\iint p_{\text{LS}}(x, y_0, z) dx dz}. \quad (6.20)$$

This efficiency is computed for the technique providing best image quality, confocal-line detection with Bessel beam (CL-MISERB) and the technique that makes most efficient use of illumination light, wide-field detection with Gaussian beam (DSLML) illumination. The overall energy E that the sample (§ 6.5) was exposed to is measured by the detected fluorescence signal for all 100 positions x_i of the beam in the sample $\sum_i F_z(x_i)$ is 1.5 times stronger for illumination by a Bessel beam than for a Gaussian beam, such that $E_B = 1.5E_G$. This means that 50% more energy has been deposited into the sample by the Bessel beam. The average ratio of usable signals p_S which is extracted from profiles $p(y)$ is 3.9 times stronger in the DSLM-images than in the CL-MISERB images, such that $p_{S, \text{DSLML}} = 3.9 \cdot p_{S, \text{CL-MISERB}}$. Thus the total efficiency ratio is

$$\frac{\eta_{\text{DSLML}}}{\eta_{\text{CL-MISERB}}} = \frac{p_{S, \text{DSLML}}}{p_{S, \text{CL-MISERB}}} \cdot \frac{E_B}{E_G} = 3.9 \cdot 1.5 = 5.8. \quad (6.21)$$

In summary, to obtain equal usable signal amplitudes in the images, the Bessel beam in the confocal-line detection mode deposits 5.8 times more energy into the sample. This is the cost for an increase in signal-to-background and axial resolution in a strongly scattering bead cluster. The signal-to-background ratio is increased by 30% and resolution by up to 100% in combination with a significantly improved robustness to beam perturbations.

The ratio $\eta_{\text{DSLML}}/\eta_{\text{CL-MISERB}}$ is influenced by the scattering and absorption within the sample. It is therefore sensible to further analyze the η in dependence of the penetration depth z . Therefore, the signal in the front part and the back part of the object was analyzed separately. In the front ($z = 0\mu\text{m}$ to $z = 70\mu\text{m}$) of the image, where absorption and scattering of the beam out of the field of view does only play a minor role, the average signal is stronger for Bessel beam illumination by a factor of $p_{S, \text{DSLML}}/p_{S, \text{CL-MISERB}} \approx 1.29$. In the back part ($z = 150\mu\text{m}$ to $z = 215\mu\text{m}$) of the image, the ratio is $p_{S, \text{DSLML}}/p_{S, \text{CL-MISERB}} \approx 1.64$. When normalized to equal signal strength of both DSLM and CL-MISERB for low penetration depth, the signal deep inside the scattering medium detected for CL-MISERB is stronger by a factor of $1.64/1.29=1.27$ compared to DSLM. As described above, the ratio of detected fluorescence signal between illumination by Gaussian beam and Bessel beam depends on the penetration depth into scattering media. As the ratio of detected fluorescence in the back part of the image is 1.64, to obtain equal signal magnitude there, the Bessel beam needs only to deliver $3.9/1.27=3.1$ times more energy into the sample, a further indication of the superior penetration strength of the Bessel beam.

6.9.2.2 Estimation based on numerical data

In addition to the investigation of experimental data, an analysis using numerical simulation results is insightful to answer the following question: How large is the beam's power that is used to provide image signal in relation to the part of the beam that contributes to the background. The analysis is based on the assumption that the beam power is linearly proportional to the number of excited fluorophores. The light generates a usable signal (information on the structure) with an efficiency is given by the relationship between the power in the vicinity of the focal plane of the detection objective E_S and the total power of the beam $P = \iint h_{\text{ill}}(x, y) dx dy$. Usable signal can only be generated by that part of the beam's power that is close to the focal plane y_0 of the detection objective lens within a distance determined by its focal depth dy . For the scanned beam the useful part of the beam's power is computed by the integration of the irradiance in x -direction over the full lateral extent of the beam and in y -direction over the thickness of the plane out of which a usable signal may be obtained which yields $P_{S, \text{scan}} = \iint h_{\text{ill}}(x, |y - y_0| < dy)$. The area is marked

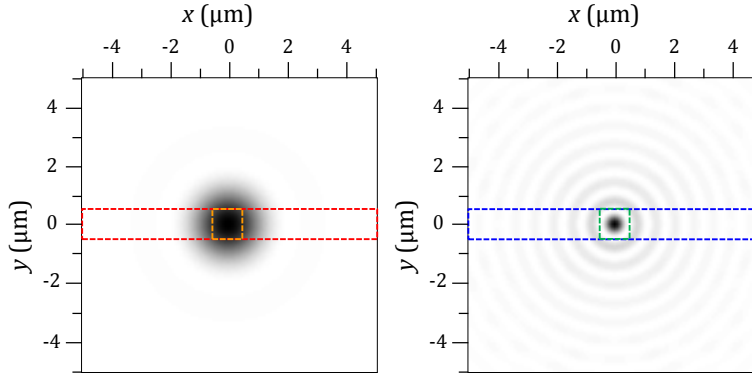


Figure 6.22: Usable signal generation by Gaussian and Bessel beams. The figure shows the transverse intensity profiles of a Gaussian beam with $\text{NA}=0.15$ (a) and a Bessel beam with $\text{NA}=0.3$, $\varepsilon = 0.8$ (b). The beams exhibit equal depth of field $dz \approx 100 \mu\text{m}$. Assuming a focal depth of the detection objective lens of $dy = 2 \mu\text{m}$, the red and blue dashed lines indicate regions that generate usable signal for scanned illumination Gaussian and Bessel beams, respectively. In the case of confocal-line detection the signal is obtained from the area surrounded by the dashed orange and green boxes for Gaussian and Bessel beams, respectively, when the confocal slit width is $w_x = 2 \mu\text{m}$.

by rectangles in Figure 6.22 for $dy = 2 \mu\text{m}$. For confocal-line detection only the (fluorescence signal excited by the) main lobe has to be considered so that $P_{S, \text{CL}} = \iint_{|x-x_0| < w_x, |y-y_0| < dy} h_{\text{ill}}(x, y) dx dy$. The relevant area is marked for $dy = 2 \mu\text{m}$ in Figure 6.22 by squares. The efficiency is

$$\eta_{\text{scan}} = \frac{\int \int_{|y-y_0| < dy} h_{\text{ill}}(x, y) dx dy}{\iint h_{\text{ill}}(x, y) dx dy} \quad (6.22)$$

for wide-field detection and

$$\eta_{\text{CL}} = \frac{\int_{|x-x_0| < w_x} \int_{|y-y_0| < dy} h_{\text{ill}}(x, y) dx dy}{\iint h_{\text{ill}}(x, y) dx dy}. \quad (6.23)$$

for confocal-line detection. The values for the efficiencies resulting from different illumination and detection are shown in Table 2. Accordingly CL-MISERB

delivers about $\eta_{\text{DSLM}}/\eta_{\text{CL-MISERB}} = 5.8$ times more energy to the sample than DSLM for the same signal strength, provided the depth of field of the detection objective is $dy = 2\mu\text{m}$, which corresponds to $\text{NA} \approx 1.0$. This result is in good agreement to the experimental data, which reveals $\eta_{\text{DSLM}}/\eta_{\text{CL-MISERB}} = 5.7$. For $dy = 1\mu\text{m}$ the ratio $\eta_{\text{DSLM}}/\eta_{\text{CL-MISERB}} = 4.6$ as the Bessel beam's main lobe confines more power on a smaller cross section. Note that in most experimental data shown previously in this chapter the slit width was $w_x \approx 0.5$ to block as much scattered background as possible. In this case the Bessel beam exhibits an even more favorable efficiency.

Efficiency	Gaussian beam (NA=0.15)	Bessel beam (NA=0.3, $\epsilon=0.8$)
η_{scan} for $dy = w = 1\mu\text{m}$	34%	14%
η_{CL} for $dy = w = 1\mu\text{m}$	12.5%	7.4%
η_{scan} for $dy = w = 2\mu\text{m}$	58%	21%
η_{CL} for $dy = w = 2\mu\text{m}$	36.2%	10.1%

Table 2: Efficiencies for different illumination beams and detection focal depths dy detection

However, it has to be mentioned that all quantitative analysis on photo-bleaching and photo-toxicity is extremely complex because a large number of parameters like the wavelength, irradiance and also the duration of the illumination play an important role that has yet to be rigorously analyzed in detail. The results presented here can therefore only be regarded as rough estimates.

6.9.3 Confocal-line detection vs. Structured Illumination

Another contrast-enhancement techniques is structured illumination (SI) [Breuninger et al., 2007, Keller et al., 2010, Planchon et al., 2011]. For SI, initially developed to provide optical sectioning in wide-field microscopes by Neil et al. [1997], the sample is illuminated with a periodic sinusoidal pattern. Three images are taken with the pattern shifted by a third of its period each time. The final image is then obtained by a post-processing step. Therefore, while the technique requires no hardware changes to a line-scanning light-sheet microscope, it is slower and, as a rule of thumb, exposes the sample to 1.5 times more light than conventional light-sheet microscopy. However, this rule is only true when the same maximum laser power is used in both imaging modes. When the goal of the user is to obtain a certain signal above background/noise, the illumination light needed strongly depends on the sample. The contrast improvement might enable the use of less illumination light. However, for low signal strength the noise amplification by a factor of $\approx \sqrt{3}$ according to Hagen et al. [2012] in the post-processing step might make the use of stronger sample irradiance necessary. In practice, another problem to the technique is the introduction of artifacts in the images which arise from slight imperfections in the periodicity of the grating illumination [Schröter et al., 2012]. This problem is greatly reduced by employing a technique called HiLo [Mertz and Kim, 2011]. HiLo-images are generated by combining a high-pass filtered image obtained from regular, i.e.

homogeneous sample illumination and a low-pass filtered image of the sample illuminated by a periodic grating.

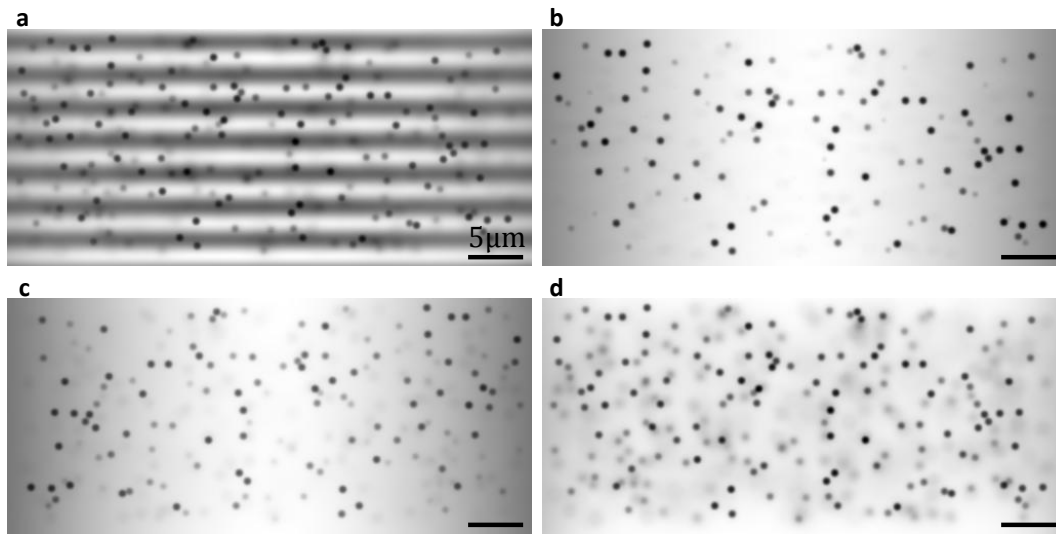


Figure 6.23: Image comparison: Line-confocal detection vs Structured illumination in homogenous media

Simulated image data for non-fluorescent spheres ($d = 0.75\mu\text{m}$) in fluorescent environment. Here, the spheres have the same refractive index as the environment ($n = 1.33$) and the illumination beam is therefore unperturbed. The wavelength is $\lambda_0 = 500\text{nm}$. The figure shows an image slice obtained for scanned Bessel-beam illumination (a), for Bessel beam illumination with line-confocal detection mode ($w = 1.5\lambda$) (b) and for structured illumination (SI_3) (c). One phase for structured illumination ($p = 3\mu\text{m}$) is shown in (d). Bessel beams propagate from left to right and are scanned from the top of the images to the bottom.

While both techniques offer advantages when used with Gaussian illumination beams in weakly scattering media a serious drawback arises from the use of SI or HiLo in scattering media or with Bessel beams. First, in contrast to confocal-line detection, the techniques record images with a large background which is removed only in post-processing. This means that poor use is made of the camera's dynamic range. Moreover, a strong component of Poisson shot-noise arising only from the background superimposes the structural information in the image. Therefore, images have to be recorded for stronger sample illumination to achieve similar signal-to-background as with confocal-line detection. Second, scattering of the illumination beam might result in destruction of image information by the post-processing step. This effect is discussed in detail below. In short, as the final image in structured illumination arises from the modulation of the illumination, information is lost when the modulation is blurred due to beam spreading.

In the following, confocal-line detection and structured illumination are compared using simulated data. This method is advantageous since it allows the assessment of the effect of scattering and beam broadening on the image contrast enhancement. The realistic illumination where scattering is accounted for can be compared to an ideal illumination of the same object where scattering is disregarded. The simulation volume with dimensions $24 \times 24 \times 48\mu\text{m}^3$ contains ≈ 2500 spheres with a diameter of $d = 0.75\mu\text{m}$. The fluorescence distribution of the non-fluorescent spheres embedded in a fluorescent medium ($n_{\text{bg}} = 1.33$) is described by $c(\mathbf{r})$.

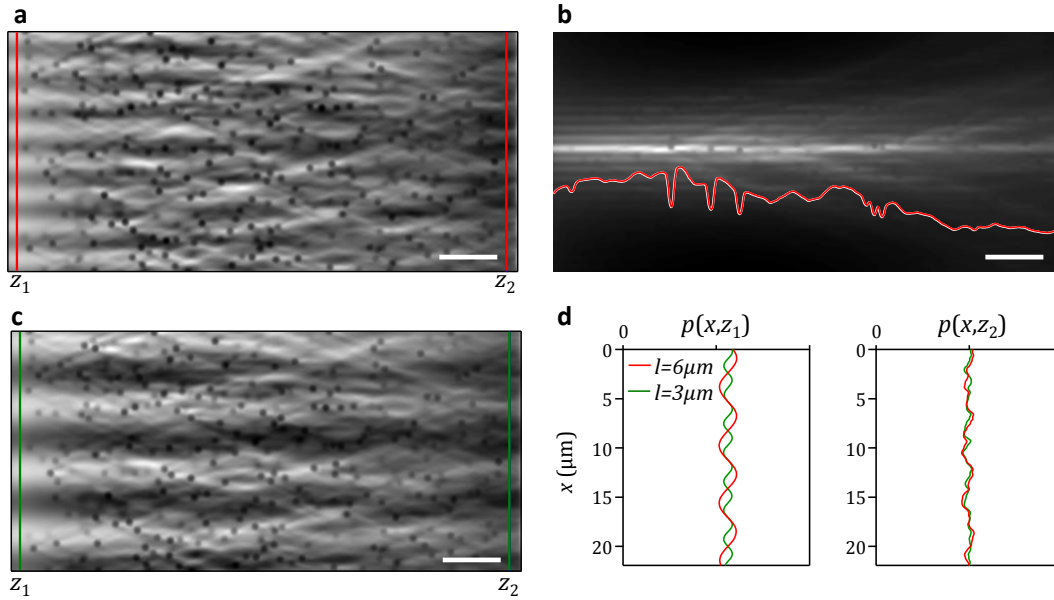


Figure 6.24: Modulation depth for structured illumination of scattering media.

The loss in modulation contrast for deep penetration into scattering media is illustrated by means of a BPM-simulation. The simulation data shows the propagation of the Bessel beam through non-fluorescent silica spheres ($d = 0.75\mu\text{m}$, $n = 1.41$) in fluorescent environment ($n = 1.33$). The images result from the modulation with a period of $p = 6\mu\text{m}$ (a) and $p = 3\mu\text{m}$ (b). Line-scans for small and large penetration into the sample are shown in figure (c) and (d), respectively. A single Bessel beam with on-axis intensity profile is shown in (e). Beams propagate from left to right and are scanned from top to bottom.

Illumination patterns for a single plane are obtained by

$$h_{\text{plane}}(x, y, z) = \sum_i A_i \cdot h_{\text{ill},i}(x, y, z) \quad (6.24)$$

where $h_{\text{ill},i}$ is the beam's power distribution obtained for propagation through the sample at discrete positions x_i and A_i is a position dependent amplitude. In the case of line-scanning light-sheet microscopy the amplitude $A_i = 1$ is position-independent. For structure illumination the amplitude is modulated sinusoidally and reads $A_i = \sin(2\pi \cdot i \cdot dx/l)$ where l is the period of the illumination grating. To obtain images, the sample's fluorescence distribution $c(\mathbf{r})$ is multiplied with the illumination pattern $h_{\text{plane}}(\mathbf{r})$ and convolved with the orthogonal detection PSF $h_{\text{det}}(\mathbf{r})$ (see eqn 2.1)

Images obtained by scanning the non-scattered beam (Figure 6.23a) exhibit a strong background, which is reduced by structured illumination in Figure 6.23b or confocal-line detection (Figure 6.23c). The images clearly show that the structured illumination by Bessel beams with a lateral grid distance $3\mu\text{m}$ (an image obtained for illumination by a grating is shown in Figure 6.23d) and subsequent reconstruction reduces the background even better.

However, the situation changes when scattering is taken into account such that beam-spreading occurs. The propagation of Bessel beams through the same distribution of spheres was computed with the refractive index of the spheres now set from n_{bg} to $n = 1.41$. The beam propagation method (BPM) which is described in Appendix B in detail was used to account for the perturbation of the beam by the spheres. The use of the same sample allows a direct comparison

of the resulting images and thus judge the effect of the perturbation. The images shown in Figure 6.24a, c show the grid patterns resulting from scattered illumination beams that are modulated during the lateral scans with periods of $3\mu\text{m}$ and $6\mu\text{m}$, respectively. The modulation strength of the illumination grid becomes even smaller in the back of the scattering sample than in the front, which is clearly visible in the images and further manifested by the profile for a low penetration depth $p(x, z = 1\mu\text{m})$ and at the back of the sample $p(x, z = 40\mu\text{m})$ shown in Figure 6.24d. This effect can be accredited to the perturbation of the beam that is spread while propagating into the scattering sample, as can be seen in Figure 6.24b.

Images obtained for confocal-line detection and structured illumination (SI₃) with two grid periods and sample illumination by an ideal non-scattered light-sheet are shown in Figure 6.25a. The reconstructed images for structured illumination reveal a stronger decline in signal along z as the in-focus image information has been subtracted by the post-processing due to decreased modulation contrast, which is a result of the scattering (see Figure 6.25c and d). In the line-confocal case a loss in intensity from left to right due to scattering is also visible (see Figure 6.25b), but the light-sheet remains smoother while still offering good sectioning at higher signal strength as can be seen in the 1D-linescans taken for a short and after a longer propagation distance (Figure 6.25g, h, where scattering artifacts are especially strong in the images resulting from SI).

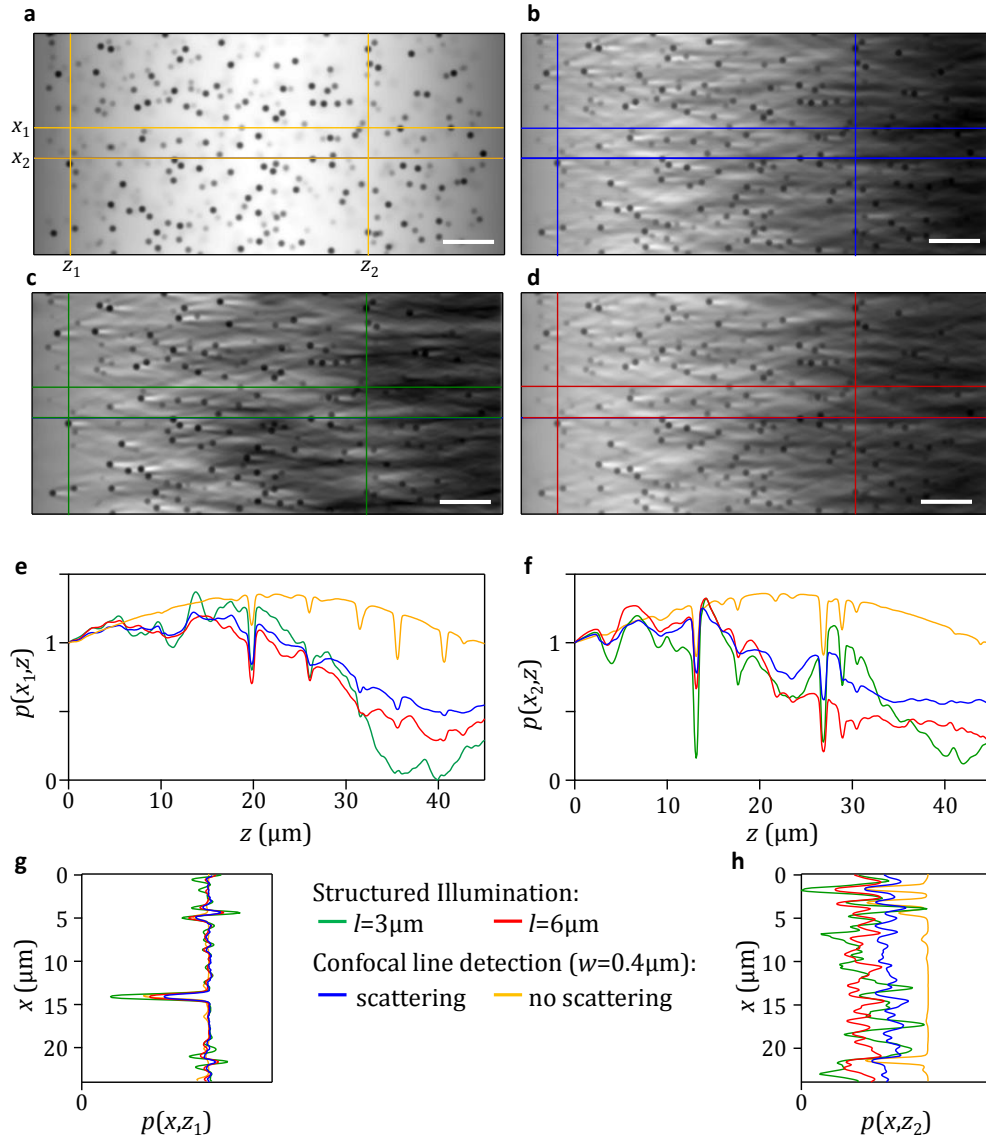


Figure 6.25: Line-confocal and structured illumination images of a scattering sample.

A line-confocal detection image ($w = 0.4\mu\text{m}$) is shown in (a). Reconstructed structured illumination images (SI₃ mode) using a $3.0\mu\text{m}$ period and $6.0\mu\text{m}$ period are shown in (b) and (c), respectively. An image with confocal-line detection for ideal illumination by a non-scattered Bessel beam is shown in (d). Lateral intensity profiles $p(x)$ for low (e) and deep (f) penetration into the scattering medium allow to compare the image contrast. Profiles $p(z)$ for two different lateral positions (g, h) show the decay in signal along the beam's propagation axis.

The decline of $p(z)$ can also be seen in the profiles $p(z)$ that are shown in Figure 6.25e,f. For confocal-line detection the image contrast occupies a much larger range of the detection sensor because the beam is not scanned across the field of view during a single camera exposure (see also the illustration of $h_{\text{scan}}(y)$ in Figure 6.1).

TWO-PHOTON FLUORESCENCE EXCITATION

This chapter deals with two-photon fluorescence excitation (TPE) by Bessel beams in light-sheet microscopy. The chapter starts with a short motivation (§ 7.1) followed by a description of the principles and theoretical foundations of the non-linear fluorescence excitation (§ 7.2). Simulations were carried out to estimate the potential gain by 2p excitation (§ 7.5). The experimental setup that was built is described in Section 7.4. A number of experiments on artificial samples consisting of small fluorescent spheres (§ 7.6) and on biological samples, i.e. tumor multicellular spheroids (§ 7.7) were carried out to test the performance. The chapter closes with a detailed discussion of the findings (§ 7.8).

7.1 MOTIVATION

The process underlying two-photon fluorescence excitation (TPE) was first described theoretically by Goepfert-Mayer in 1931. The effect is interesting for applications in biomedical imaging for a number of reasons. Two photons can excite a molecule to a state with an energy equivalent to the sum of the energy of both photons if they hit the molecule within a very short time period. The photon density necessary to trigger this process is very high so that the experimental demonstration for application in microscopy was only realized in 1990 [Denk et al., 1990]. The TPE signal is proportional to the square of the photon density at the position of the molecule, i.e. the square of the irradiance. For illumination by Bessel beams this dependency means a lower fluorescence excitation by the ring system relative to the central lobe which is advantageous since it offers the possibility to generate thin Bessel-beam light-sheets that are not broadened by the ring system. The principle is illustrated in Figure 7.1. More

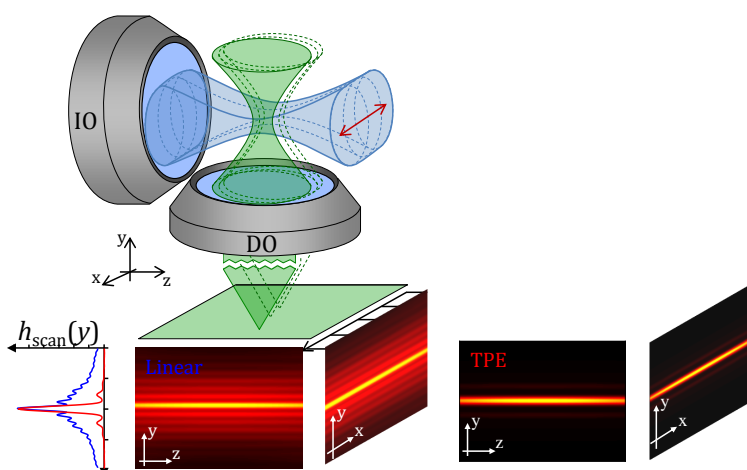


Figure 7.1: Schematic comparison of linear and two-photon Bessel beam light sheet microscopy.

details are given in Section 7.2.5. Another potential improvement may arise from the suppression of fluorescence excited by scattered light if the corresponding magnitude is small, i.e. the intensity of the scattered light is low. As each photon

has to deliver only half the energy necessary for the transition, two-photon excitation of the same fluorophore is possible at wavelengths twice as long. Several practical advantages arise from this fact [So et al., 2000, Helmchen and Denk, 2005]. First, photons that carry half the energy are less likely to cause damage to the sample by photo-toxic effects. Second, the large spectral distance between the illumination and fluorescence light enables a very good separation of the two colors. Third, because red light is scattered less than blue light by small particles, two-photon excitation can be used to image deep in scattering media with point-scanning microscopes [Beaurepaire et al., 2001]. If this advantage can be transferred to light-sheet microscopy, penetration depth for illumination with self-reconstructing beams could be enhanced even further to obtain a higher image quality within larger samples.

7.2 PRINCIPLE AND BACKGROUND

The following section deals with the foundations of two-photon absorption and fluorescence emission. Thereafter, the consequences of scattering of the illumination beam for the signal strength are described. The dimensions of the volume of non-linear fluorescence excitation by Bessel beams are discussed, before the potential resolution and optical sectioning capability is computed using simulated data. The section closes by an analysis of the system-PSF for misaligned systems.

7.2.1 Two-photon Absorption and Fluorescence Emission

The power emitted by a single molecule excited by two-photon fluorescence (TPE) is

$$F_{2p}(\mathbf{r}) = \sigma_{\text{TPE}} \cdot I_i(\mathbf{r})^2 \quad (7.1)$$

where I_i is the illumination irradiance at the position of the fluorophore and σ_{TPE} is its two-photon absorption cross-section. [Albota et al., 1998] contains more detailed information on σ_{TPE} for a number of fluorescent markers. Special care must be taken regarding the units due to a mixture of present-day notation with the historical notation as introduced by Goeppert-Mayer when she first examined the two-step excitation processes. While the unit of σ_{TPE} as used in the above equation is m^4/W , the TPE cross-section σ_2 is often given in GM, where $1\text{GM} = 10^{-50}\text{cm}^4\text{s}/\text{photons}$. In this context, photons stands for the energy of a single photon so that $\sigma_{\text{TPE}} = \frac{10^{-58}}{h\nu} \cdot \sigma_2$ where h is the Planck constant, ν is the frequency of the light and σ_2 is the TPE absorption coefficient in m^4s [Mertz, 2010a]. It follows that $\sigma_{\text{TPE}} = 5 \cdot 10^{-34}\text{J}^{-1} \cdot \text{m}^{-1} \cdot \lambda \cdot \sigma_2$. For a typical value of $\sigma_2 = 1\text{GM} = 10^{-8}\text{m}^4\text{s}$ at a wavelength of $\lambda = 800\text{nm}$ the TPE cross-section is $\sigma_{\text{TPE}} = 4.0 \cdot 10^{-40}\text{m}^4/\text{W}$ in SI-Units. When a power of 1mW is focused onto an area of $A = 1\mu\text{m}^2$, the power of the two-photon fluorescence is $F_{\text{TPE}} \cdot A = 4 \cdot 10^{-22}\text{W}$. For pulsed lasers, a term describing the pulse-shape has to be introduced in eqn 7.1 that relates the time-averaged ($\langle \dots \rangle_t$) irradiance to the median of the irradiance according to $\langle I^2 \rangle_t = g_2 \cdot \langle I \rangle_t^2$ so that

$$F_{\text{TPE}}(\mathbf{r}) = \sigma_{\text{TPE}} \cdot g_2 \cdot \langle I(\mathbf{r}) \rangle_t^2. \quad (7.2)$$

For pulsed light, where τ_i is the time interval between two pulses with duration τ_p , the amplification factor is $g_2 = \tau_i / \tau_p$. Values of $g_2 \approx 10^5$ can be achieved to greatly enhance the strength of the fluorescence signal [Mertz, 2010b]. Note that the fluorescence F depends linearly on the pulse length τ_p and not quadratically. Thus, effects that broaden the pulse, such as dispersion in the optical path, or inside scattering media are less important than a high overall efficiency (transmission) of the illumination path as well as a tight high-quality focus, which directly affect the irradiance. The fluorescence from a volume V_{TPE} ,

$$F_{\text{TPE}}(\mathbf{r}) = c \cdot \gamma_\psi \cdot V_{\text{TPE}} \cdot \sigma_{\text{TPE}} \cdot g_2 \cdot \langle I(\mathbf{r}) \rangle_t^2. \quad (7.3)$$

is obtained by multiplication of F_{TPE} with the fluorophore concentration $c(\mathbf{r})$, the two-photon volume contrast γ_ψ Mertz [2010c]. An important implication of this result is the following: When the focal volume V_{TPE} can be approximated by the product of the beam's cross-section and its focal depth so that $V_{\text{TPE}} = A \cdot dz$ it follows that $F \propto V_{\text{TPE}} \cdot I^2 = A \cdot dz \cdot P^2 / A^2 = P^2 \cdot dz / A$. For Gaussian beams, where $A \propto \lambda^2 / \text{NA}^2$ and $dz \propto \lambda / \text{NA}^2$ for a small NA, the total fluorescence yield is independent of the focusing NA.

7.2.2 Fluorescence Signal in Scattering Media

Linear and non-linear fluorescence excitation obey different differential equations. Here, a sample with a single-photon absorption cross section of the molecules σ_{lin} , a two-photon absorption cross-section σ_{TPE} and a scattering cross section σ_{scat} is used to describe the evolution of the irradiance and fluorescence signal along the illumination axis. Using the coefficients $\mu_{\text{lin}} = \rho_{\text{lin}} \sigma_{\text{lin}}$ and $\mu_{\text{scat}} = \rho_{\text{scat}} \sigma_{\text{scat}}$, where ρ is the density of the absorbers and scatterers, respectively, the change in irradiance along the propagation axis z is

$$dI/dz = -\mu_{\text{lin}} \cdot I(z) - \mu_{\text{scat}} I(z) \quad (7.4)$$

so that

$$I(z) = I_0 \cdot \exp\{-(\mu_{\text{lin}} + \mu_{\text{scat}})z\}. \quad (7.5)$$

The decay of the irradiance and the fluorescence $F_{\text{lin}}(z) = \sigma_{\text{lin}} \cdot I(z)$ is exponential. The result is very different in the nonlinear case, where

$$dI/dz = -\mu_{\text{TPE}} \cdot I^2(z) - \mu_{\text{scat}} I(z) \quad (7.6)$$

holds. $\mu_{\text{TPE}} = \rho_{\text{TPE}} \sigma_{\text{TPE}}$ is the two-photon absorption coefficient. It follows that

$$I(z) = \frac{I_0}{(1 + \mu_{\text{TPE}} I_0 / \mu_{\text{scat}}) e^{\mu_{\text{scat}} z} - \mu_{\text{TPE}} I_0 / \mu_{\text{scat}}}.$$

The fluorescence signal depends quadratically on the irradiance, so that $F(z) = \sigma_{\text{TPE}} \cdot I^2(z)$. When absorption is the dominant effect ($\mu_{\text{scat}} \rightarrow 0$), then the irradiance $I(z)$ is described by $I(z) = I_0 / (1 + I_0 \mu_{\text{TPE}} z)$ which is a Lorentz-function - an important difference to the case of linear absorption where the irradiance decays exponentially.

However, in sparsely stained but strongly scattering media

$$dI/dz = \mu_{\text{scat}} \cdot I(z) \quad (7.7)$$

holds. The two-photon signal for such media that are characterized by $\mu_{\text{scat}} \gg \sigma_{\text{TPE}} \cdot I^2(z)$ is

$$F_{\text{TPE}}(z) = \sigma_{\text{TPE}} \cdot I^2(z) = \sigma_{\text{TPE}} \cdot e^{-2 \cdot \mu_{\text{scat}} \cdot z}. \quad (7.8)$$

For equal μ_{scat} , the fluorescence decays twice as fast for TPE than for the linear case. The penetration depth is only half as large. However, the scattering coefficient is generally wavelength-dependent. In order to perform better in turbid media

$$\mu_{\text{scat}}(\lambda_{\text{exc,TPE}}) < 0.5 \mu_{\text{scat}}(\lambda_{\text{exc,lin}}) \quad (7.9)$$

has to be fulfilled for $\lambda_{\text{exc,lin}} \approx 0.5 \lambda_{\text{exc,TPE}}$. As $\mu_{\text{scat}}(\lambda) = \rho_{\text{scat}} \sigma_{\text{scat}}(\lambda)$ where, ρ_{scat} is wavelength-independent, the scattering cross-section $\sigma_{\text{scat}}(\lambda)$ must be smaller at a longer wavelength. For small particles, where Rayleigh-scattering dominates, the cross-section scales with λ^{-4} . These particles exhibit a 16-fold smaller value of the scattering cross-section at the double wavelength. The scattering by larger objects such as whole cells can be described by Mie-Theory, which predicts a λ^{-2} dependency of the cross-section on the size. This relation would mean a four times smaller scattering cross section at the two-photon excitation wavelength. Altogether, if one considers the stronger decay for two-photon-fluorescence as described in eqn 7.8 and the larger Stokes shift for two-photon excitation which means that for GFP, for example, $\lambda_{\text{exc,TPE}}/\lambda_{\text{exc,lin}} \approx 920/488 = 1.9$, the penetration depth for two-photon fluorescence excitation into scattering material can be roughly expected to be a factor of 1.8 to 5 times better than for linear fluorescence excitation. Note that for better clarity, the reduced scattering coefficient, which is given by multiplication with the scattering anisotropy factor g , was not employed in the above consideration. The difference due to the factor $(1 - g)$ for polystyrene spheres with $d = 0.75 \mu\text{m}$ is only 4% (compare Table 3).

7.2.3 Dimensions of the Two-Photon Bessel Beams

This section presents the relationship between the beam dimensions and the parameters NA and ϵ for two-photon fluorescence excitation. For homogeneous (annular or circular) illumination of the back-focal plane, the axial profile for linear fluorescence excitation is

$$F_{\text{lin}}(z) = \sigma_{\text{lin}} I(z) = \sigma_{\text{lin}} I_0 \cdot \text{sinc}(dk_z \cdot z/2)^2 \quad (7.10)$$

and the two-photon fluorescence excitation profile is

$$F_{\text{TPE}}(z) = \sigma_{\text{TPE}} I(z)^2 = \sigma_{\text{TPE}} I_0^2 \cdot \text{sinc}(dk_z \cdot z/2)^4 \quad (7.11)$$

Due to $\text{sinc}(\tilde{\zeta})^4 = 1/2$ for $\tilde{\zeta} = 1.0$, the full-width of the beam at half of the maximum irradiance (FWHM) is obtained by $\Delta z_{\text{TPE}} = 4.0/dk_z$. The 1/e-DOF is

given by $\Delta z_{\text{TPE}} = 4.78/dk_z$ since $\text{sinc}(\xi)^4 = 1/e$ for $\xi = 1.19$. Analogous to eqn 3.21 for Bessel beams, the FWHM focal depth of the fluorescence signal $F(z)$ is

$$\Delta z_{\text{TPE}} = \frac{0.64\lambda_0}{\left(\sqrt{n^2 - \epsilon\text{NA}^2} - \sqrt{n^2 - \text{NA}^2}\right)} \quad (7.12)$$

$$\approx \frac{1.28 n \lambda_0}{\text{NA}^2 (1 - \epsilon)} \quad (7.13)$$

where the expansion for small values of ϵ could be used because $\epsilon < 1$ by definition. Note, that the depth of field (FWHM) of the on-axis irradiance of the Bessel beam is larger by a factor of $\Delta dz/\Delta z_{\text{TPE}} = 1.39$ since $\text{sinc}(\xi)^2 = 1/2$ holds for $\xi = 1.39$. To excite the same dye by linear and two-photon processes, different wavelengths are used, so that $\Delta z/\Delta z_{\text{TPE}} = 1.39 \cdot \lambda_{\text{TPE}}/\lambda$. To obtain two-photon and linear fluorescence excitation profiles $F(z)$ with equal depth of field the NA and/or ϵ can be adapted. An equal depth of field $\Delta z = \Delta z_{\text{TPE}}$ requires

$$\frac{1.76 \cdot \lambda_0}{\text{NA}^2 (1 - \epsilon)} = \frac{1.28\lambda_{2p}}{\text{NA}_{\text{TPE}}^2 (1 - \epsilon_{\text{TPE}})}. \quad (7.14)$$

The ring thickness parameter has to be adapted according to

$$\epsilon_{\text{TPE}} = 1 + 0.73 \cdot (\epsilon - 1) \cdot \frac{\lambda_{\text{TPE}}}{\lambda_0} \cdot \frac{\text{NA}^2}{\text{NA}_{\text{TPE}}^2}. \quad (7.15)$$

For two-photon excitation, where $\lambda_{\text{TPE}} \approx 2\lambda_0$, the equation can be approximated by

$$\epsilon_{\text{TPE}} \approx -0.45 + 1.45\epsilon. \quad (7.16)$$

when $\text{NA}_{\text{TPE}} = \text{NA}$. This result means, that for two-photon excitation smaller values of ϵ have to be used, because the focus is longer for focusing by equal NA due to the longer wavelength. Equal depth of field can only be achieved when the linear beam is elongated by choosing $\epsilon > 0.45/1.45 = 0.3$. A smaller value of $\epsilon_{\text{TPE}} < \epsilon$ for equal depth of focus also means that the beam that excites two-photon fluorescence carries a smaller amount of energy in the rings. Using eqn 3.34 for $\epsilon > 0.6$, the ratio between beam power in the main lobe and the rings $P^{\text{rel}} = P_m/P_0 \approx 0.83 \cdot (1 - \epsilon)$ is $P_{\text{TPE}}^{\text{rel}}/P_{\text{lin}}^{\text{rel}} \approx 1.5$ which means that for equal depth of field at the same NA the two-photon Bessel beam carries 50% more of the total power in the central lobe.

Note that the central lobe is also larger for two-photon Bessel beams. According to eqn 3.26 the diameter scales linearly with the wavelength. For an equivalent diameter of the central lobe, the focusing NA has to obey $\text{NA}_{\text{TPE}} = \text{NA} \cdot \lambda_{\text{TPE}}/\lambda$. In this case the ring thickness parameter is $\epsilon_{2p} = 1 + 0.723 \cdot (\epsilon - 1) \cdot \lambda/\lambda_{2p}$ and $P_{\text{TPE}}^{\text{rel}}/P_{\text{lin}}^{\text{rel}} = 0.723 \cdot \lambda/\lambda_{2p}$ which means that $P_{\text{TPE}}^{\text{rel}}/P_{\text{lin}}^{\text{rel}} \approx 0.36$ for $\lambda_{2p} \approx 2\lambda$. The two-photon Bessel beam therefore carries 64% less of the total power in the main lobe. The much larger ring width parameter $\epsilon_{\text{TPE}} = 0.64 + 0.36\epsilon$ is necessary to achieve the equivalent depth of field at an NA that provides the same size of the main lobe at $\lambda_{\text{TPE}} \approx 2\lambda$.

7.2.4 Dependence of the Fluorescence on the Beam's Depth-of-Field

This section contains an analysis of the dependence of the relative fluorescence generated by the beam's main lobe on the depth of field of the illumination beam. As the fluorescence depends nonlinearly on the beam's irradiance, no exact analytical expression could be found that describes the ratio of fluorescence excited by the main lobe and by the ring system. However, some interesting conclusions can be obtained by carefully using approximations introduced in Section 3.2.1.

In 2p-DSLM similar signal rates can be achieved as in point-scanning confocal microscopy even though the numerical aperture of the illumination is much smaller in the case of the light-sheet microscope. For a conventional focused flat-top the mean irradiance in the focus is $I \propto P/w_0^2$ with the beam diameter $w_0 \propto \lambda/\text{NA}$. The fluorescence is therefore $F \propto P^2/w_0^4$. Consequently, the fluorescence excitation probability in the focus scales with NA^4 . But the focal volume is proportional to NA^{-4} . The total excitation integrated of the focal volume $V \cdot F$ is therefore independent of the NA (see also [Truong et al., 2011]). Conventional two-photon point-scanning confocal microscopy generates a higher signal but over a shorter period of time as each point is scanned separately. In the scanned beam light-sheet microscope, each point is illuminated by a lower irradiance over a much longer timescale.

For Bessel beams, the situation is slightly different. Efficient two-photon fluorescence excitation is limited to the Bessel beam's main lobe. The volume of the central lobe is given by, $V = \pi \cdot r_0^2 \cdot \Delta z_{2p}$, where Δz_{2p} is the beam's depth of field and r_0 the main lobe's radius. As can be seen in equation 7.12, $\Delta z_{\text{TPE}} \propto (1 - \epsilon)^{-1} \text{NA}^{-2}$. The radius can be inferred the position of the first minimum $r_0 \approx 0.76 \cdot \lambda / ((\sqrt{\epsilon} + 1) \cdot \text{NA})$. The volume of the main lobe is therefore $V \propto (\sqrt{\epsilon} + 1)^{-2} (1 - \epsilon)^{-1} \text{NA}^{-4}$. The relative amount of power $P^{\text{rel}} \propto (1 - \epsilon) / (1 + \sqrt{\epsilon})^2$ in the main lobe is independent of the NA. But the irradiance is $I \propto P_0 \cdot P^{\text{rel}} / r_0^2$, so that the fluorescence excitation can be approximated by $F \propto I^2 \propto P_0^2 \cdot (\epsilon - 1)^2 \cdot \text{NA}^4$. The total fluorescence generated by the entire main lobe is $F \cdot V \propto P_0^2 \cdot (1 - \epsilon) / (1 + \sqrt{\epsilon})^2$, which, as in the linear case, approaches 0 for $\epsilon \rightarrow 1$ when a large amount of power is located in the ring system. The total fluorescence $F \cdot V$ is therefore independent of NA. The power in the beam needs to be increased only when the depth of field is adapted by raising the ring parameter. However, if only the numerical aperture is changed, the overall fluorescence excited by the main lobe remains constant.

7.2.5 Optical Sectioning

This section investigates the potential increase in optical sectioning that arises from non-linear fluorescence excitation with Gaussian and Bessel beams using simulated data. Figure 7.2a cross-sections $F(x, y)$ are shown for linear ($F \propto I$) and two-photon ($F \propto I^2$) fluorescence excitation by static Gaussian and Bessel beams. To the side, the line-profiles through the beam axis $F(0, y, 0)$ are plotted. All beams exhibit equal FWHM-length of the fluorescence excitation profile $F(0, 0, z)$ along the beam axis. The Bessel beam's main lobe is much thinner than the Gaussian beam. The ring system of the Bessel beam is strongly suppressed due to the nonlinear excitation. However, as two-photon excitation uses light

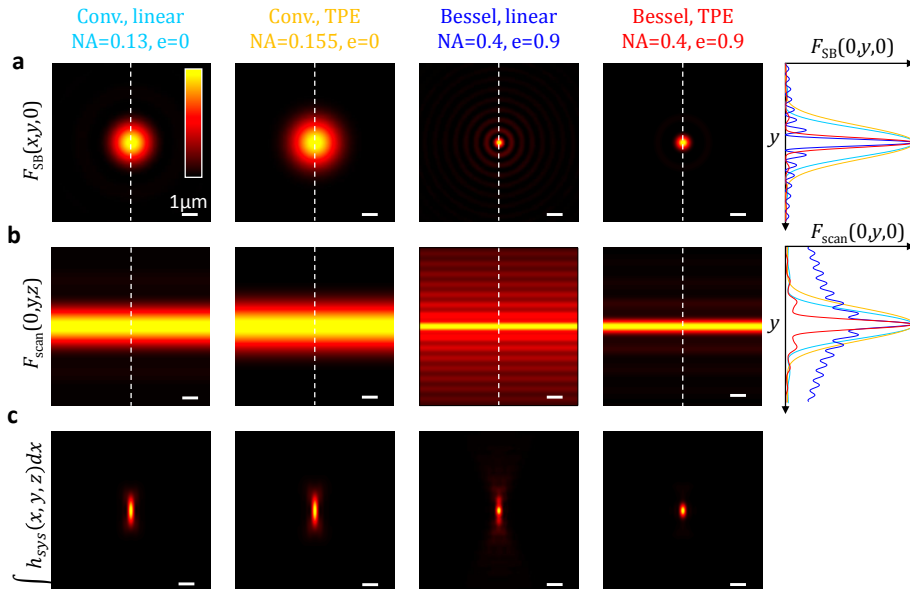


Figure 7.2: Cross-sections through static illumination beams and light-sheets for linear and two-photon-excitation by Gaussian and Bessel beams.

Lateral cross-sections through static beams (a) demonstrate the strong suppression of the ring system for TPE. The thinnest light-sheet (b) can be created by a TPE with a Bessel beam. For this case, the system-PSF (c) is confined to the smallest volume.

at the double wavelength, the central lobe is more extended than that of a linear Bessel beam. Figure 7.2b shows cross-sections $F_{scan}(0, y, z)$ through the light-sheet generated by scanned illumination beams. Due to the very weak two-photon fluorescence excitation by ring system, Bessel beams are able to generate very thin light-sheets. As can be seen from the profile $F_{scan}(0, y, 0)$, the contribution of the first ring is very small and further rings are barely noticeable. In contrast, the light-sheet created by a Gaussian beam is slightly thicker for 2p excitation. A projection of the system PSF along the scan axis (Fig. 7.2c) reveals the strong confinement of the collected fluorescence to a small volume. Note that the total fluorescence collected from each layer, $F(y) = \iint h_{sys} dx dz$ (compare 2.2.3) exhibits the same shape as $F_{scan}(0, y, 0)$ shown in Figure 7.2b because the detection lens collects all fluorescence generated (see also eqn 5.3 in §5.1.2).

The optical sectioning dependence of the depth of field of the illumination beam was investigated using the *fluorescence sea* method introduced in section 2.2.3. dy_{OS} shown in Figure 7.3 gives the width of the layer along the detection axis out of which 63% of the total detected fluorescence signal originates. The Bessel beams for linear and TPE were generated at the same numerical aperture of $NA=0.4$. It can be clearly seen that Bessel beams provide better optical sectioning for TPE than for linear fluorescence excitation. The difference is especially striking for wide-field detection. But also when confocal-line detection is applied in the linear case, dy_{OS} is still close to 50% better for small samples ($\approx 50\mu m$). The relative improvement is less significant for larger samples that require a longer depth-of-field. The fluorescence excitation by the rings close to the main lobe is enhanced more strongly when the ring parameter ϵ is increased to increase the depth of field for non-linear fluorescence excitation than in the linear case. For a beam with a large depth of field, the confinement of the

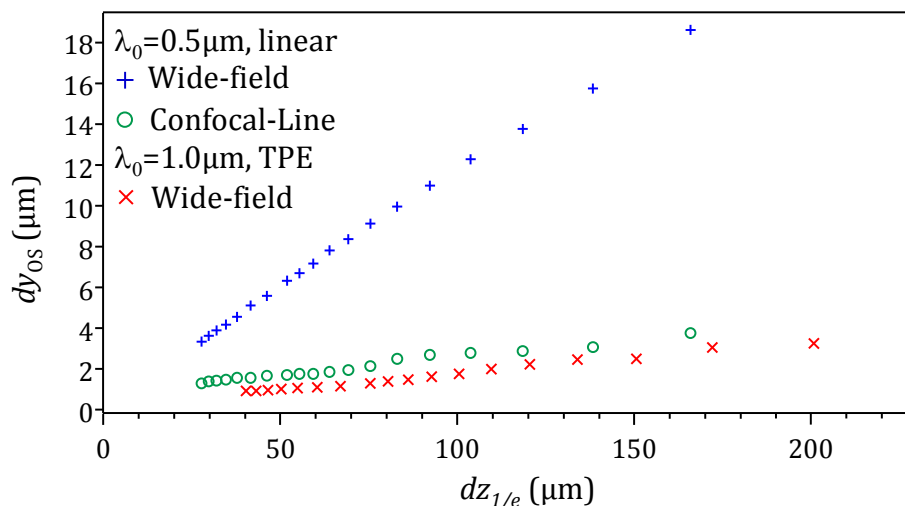


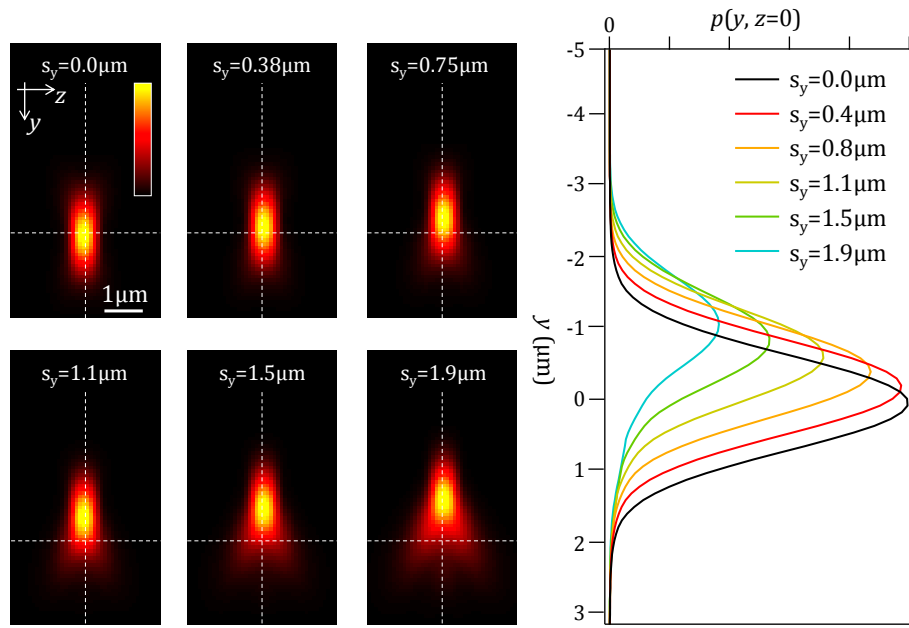
Figure 7.3: Two-Photon Bessel beam light sheet microscopy: Optical sectioning
The optical sectioning in dependence of the Bessel beam's depth-of-field was computed using simulated data.

detected fluorescence to the focal plane by confocal-line detection works more efficiently than TPE.

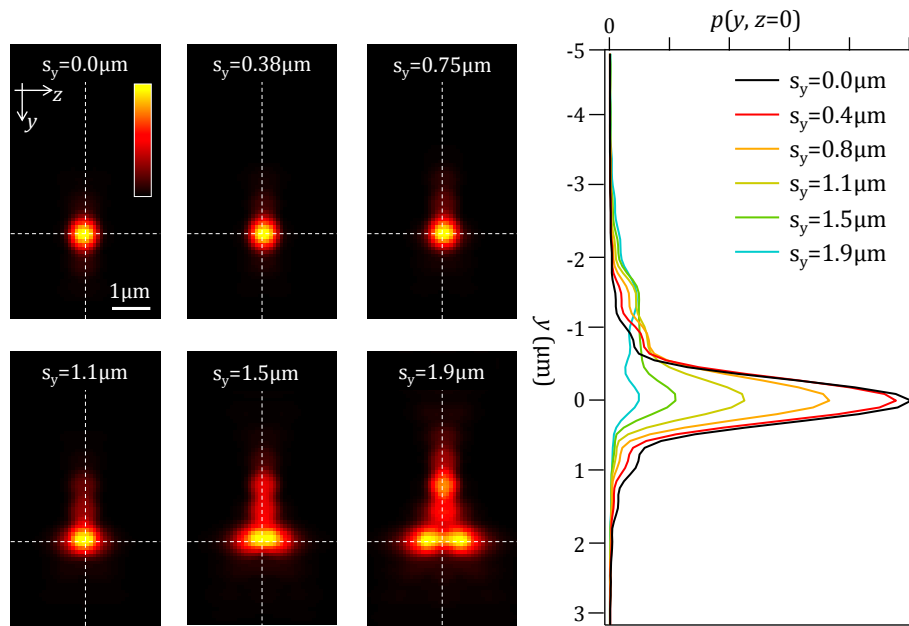
7.2.6 Importance of Precise Alignment of the Illumination Beam

The precise adjustment of the illumination beam with respect to the focal plane of the detection lens is of paramount importance for high-resolution microscopy. The size of the main lobe of a non-linear Bessel beam is only about twice the wavelength (for weak focusing by $\text{NA}=0.4$, see eqn 3.26). Even slight deviations of the illumination beam lead to a non-confocality, i.e. the illumination beam and the detection point-spread-function do not overlap. Small misalignments are clearly manifested in the images of small spheres. When these are used to quantify resolution and contrast (e.g. Figure 6.7), even slight misalignments would lead to wrong conclusions. Using data from simulations, Figure 7.4 illustrates this effect. An illumination beam is misaligned along the detection optical axis by s_y with respect to the detection focal plane. The figure shows the images of a small fluorescent sphere with $d = 750\text{nm}$ that is located in the focal plane of the detection objective lens. It can be seen that misalignment has a small effect for Gaussian beam illumination. There is only a decrease in signal strength even for strong misalignments. The axial resolution is practically unaltered. In contrast, the effect is dramatic for Bessel beam illumination. There is a drastic decrease in signal strength alongside a strong change in the shape of the image of the sphere.

The simulation results allow to infer the alignment tolerance for light-sheet microscopy. Misaligned Gaussian beams produce only a slight change in the shape of the image where it seems as if spherical aberrations were present, even for a misalignment of $s_y = 1.9\mu\text{m}$. For Bessel beam illumination, problems arise from $s_y = 0.8\mu\text{m}$. The alignment is of great importance to enable reliable imaging of small structures. The requirement on the temporal stability, i.e. regarding drift of the setup over time, are especially high because light-sheet microscopy is a technique with strong emphasis on long-term observation of samples. Precise



(a) Gaussian beam



(b) Bessel beam

Figure 7.4: Image of a sphere ($d = 750\text{nm}$) for a misaligned light-sheet microscope for linear fluorescence excitation of a sphere by a Gaussian beam and for two-photon excitation by a Bessel beam.

alignment of the illumination beam is feasible using the alignment procedure described in Section 3.4.4.

7.3 SIMULATION OF THE IMAGING PERFORMANCE

In this section, the imaging performance of scattering media for TPE by Bessel beam illumination is analyzed and compared to Gaussian beam illumination for both linear and TP excitation. Simulations were performed to provide a rough idea of the magnitude of the two major effects on the image quality that arise from nonlinear fluorescence excitation:

- the fluorescence excited by the ideal illumination beam is affected more strongly by perturbation due to $F \propto I^2$.
- the fluorescence excited by weak scattered light is suppressed due to $F \propto I^2$.

The simulation of the beam propagation through the inhomogeneous medium was performed using the beam propagation method (BPM, see Appendix B for details). The transverse size of the computed array was 1024×1024 pixels or $48\mu\text{m} \times 48\mu\text{m}$ which corresponds to a discretization of $\delta = 47\text{nm}$. Spheres with a diameter $d = 1\mu\text{m}$, refractive index of $n = 1.41$ and volume density $\rho = 0.08$ were distributed in the central part of the volume with a cross section of $256 \times 256 \text{pixel} = 12 \times 12 \mu\text{m}^2$. The illumination beam was scanned across the cluster in discrete steps of $\delta x_{\text{step}} = 4 \text{pixel} = 199 \text{nm}$. Image volumes were obtained by convolution of the central volume with a detection point-spread-function for $\text{NA}_{\text{det}} = 0.8$. The simulation was carried out for linear and two-photon fluorescence excitation by a Gaussian and a Bessel beam, respectively. The parameters were: $\text{NA}_{\text{Gauss}}^{\text{lin}} = 0.06$ or $\text{NA}_{\text{Gauss}}^{2p} = 0.069$ for the Gaussian beam and $\text{NA}_{\text{Bessel}}^{\text{lin}} = 0.4$, $\epsilon^{\text{lin}} = 0.94$ or $\text{NA}_{\text{Bessel}}^{2p} = 0.4$, $\epsilon^{2p} = 0.914$ for the Bessel beam. The FWHM of the (linear or nonlinear) fluorescence excitation along the illumination axis is $\Delta z \approx 110\mu\text{m}$ in all four cases. The wavelengths were $\lambda_{\text{lin}} = 0.5\mu\text{m} = 8 \text{pixel}$ and $\lambda_{2p} = 1.0\mu\text{m} = 16 \text{pixel}$ for linear and two-photon fluorescence excitation, respectively. As in the experiments for linear fluorescence excitation (see Sections 5.3 & 5.4), the fluorescence distribution was chosen to visualize the beam's irradiance: Non-fluorescent spheres are embedded in a fluorescent environment.

The simulation results are shown in Figure 7.5. All images are shown in auto-scaled false-colors, thereby allowing to assess the relative strength of the contrast of the objects (the spheres) and of the artifacts (the deviations from a homogenous background around the spheres). But as the images are shown with auto-scaled LUTs they do not reveal the absolute image contrast, i.e. the dynamic range. The contrast was analyzed separately. Results are shown below.

The ideal image (Figure 7.5e), where the sample is illuminated by a very thin unscattered light-sheet, sets the benchmark. As expected, Gaussian beam illumination (Figure 7.5a) leads to a very inhomogeneous sample illumination and strong stripe-shaped artifacts behind the scattering spheres. In the Bessel beam image (Figure 7.5b), the artifacts are much less visible in comparison to the spheres. Most spheres can be clearly identified, their shape can be recognized and their location identified. Surprisingly, two-photon-excitation does not necessarily lead to better image quality. TPE for Gaussian beam illumination shows very heavy artifacts that dominate the image. The strength largely inhibits the

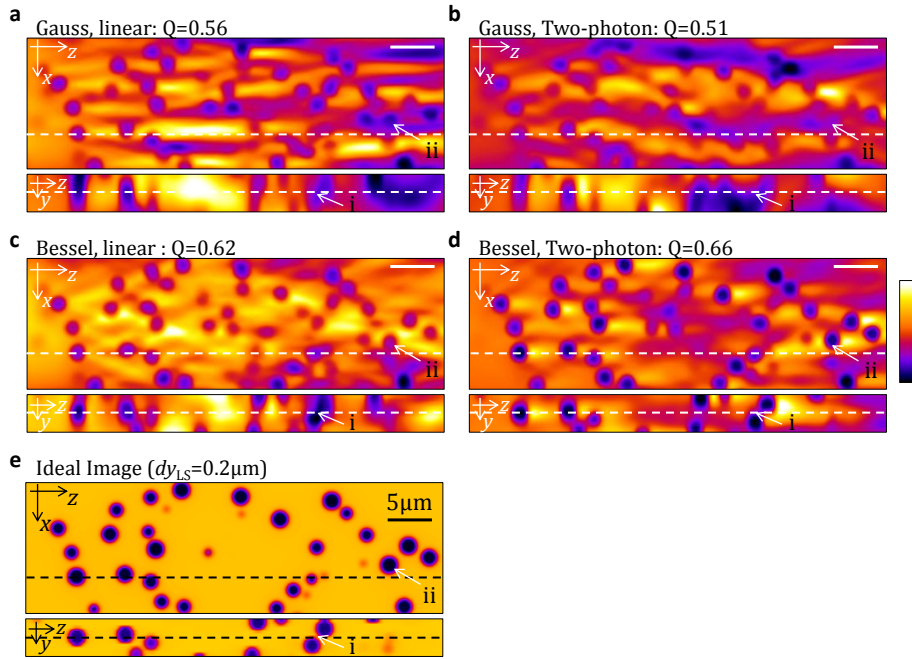


Figure 7.5: Simulation of imaging of beads with linear and two-photon fluorescence excitation by Gaussian and Bessel beams.

The axis of intersection of the xz and yz -slices is indicated by dashed lines in the images. The images are all auto-scaled except the ideal image.

determination of the structure of the imaged sample. This dominance of the artifacts is ascribed to the quadratic dependency of the fluorescence on the beam's irradiance, which leads to a larger drop in signal when scatterers redistribute the beam's energy out of the focal region. In contrast, the two-photon Bessel-beam illumination image clearly shows the best image quality. On the one hand, scattering artifacts are very weak. On the other hand the spheres are imaged with very high and even contrast, i.e. the resemblance to the ideal image is very high. Especially on the right side of the image (for large penetration depth of the illumination beam), the image's contrast and similarity to the ideal image is far superior to the two-photon Gaussian beam image. These findings are supported by the yz -slices shown beneath each image. For TPE by a Bessel beam, the images of the spheres are well constrained along the detection y -axis and the background shows relatively low spatial deviations.

Analysis based on image decomposition into ideal and ghost images (see Section 2.2.5) enables a more precise quantification of the image contrast. The images are decomposed into p_{ideal} and p_{ghost} as for the experimental data shown in Figure 2.6. The lateral standard deviation of the images, normalized to the average value of the real image \bar{p} (see eqn 2.34) is shown in Figure 7.6. The Q -values (see eqn 2.33) for the different imaging modes are equal to the ratios of the mean values of \hat{s}_{ideal} and \hat{s}_{ghost} . The Q -values for Bessel beam illumination are higher than for Gaussian beam illumination in both the linear and the non-linear case. The lowest value $Q_{\text{Gauss},2p} = 0.51$ is obtained for TPE by a Gaussian beam. Linear fluorescence excitation is only slightly better with $Q_{\text{Gauss},\text{lin}} = 0.56$. The Bessel beam images yield values of $Q_{\text{Bessel},2p} = 0.66$ and $Q_{\text{Bessel},\text{lin}} = 0.62$ that are better by 20% than the corresponding images for illumination by Gaussian beams in both the linear and the non-linear case. Note that the absolute dynamic range of the image for linear fluorescence excitation by Bessel beams is small due

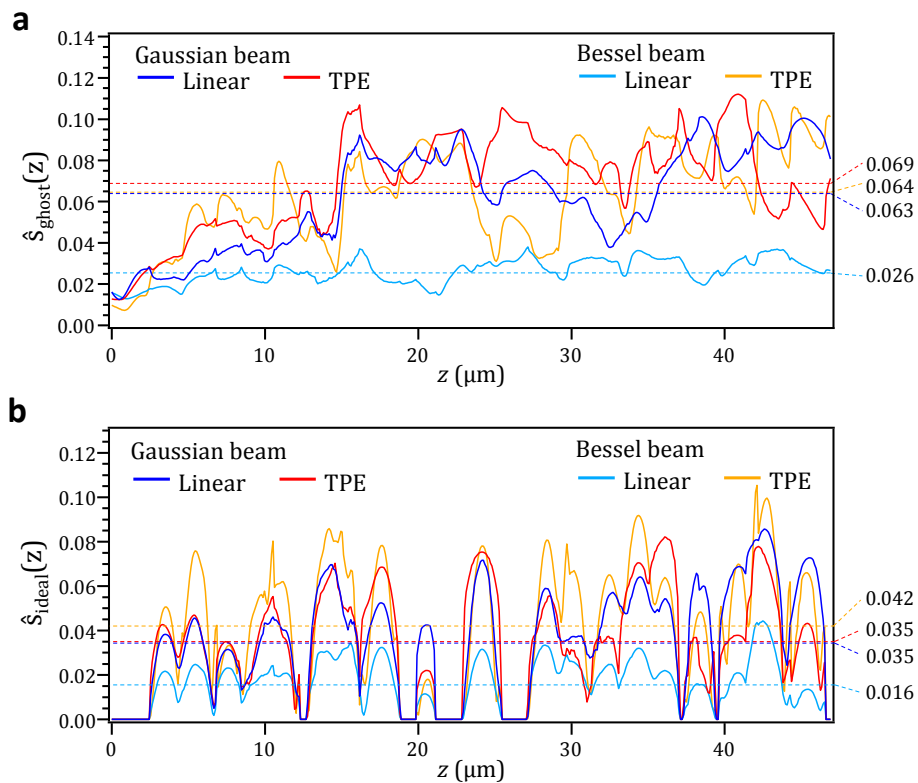


Figure 7.6: Ideal and ghost image contrast for simulated light-sheet microscopy images. The graph shows the ideal and the ghost image contrast for the images shown in Figure 7.5 above. The mean values are included as dashed lines in matching colors. The increase in ghost image contrast along the propagation axis z is apparent.

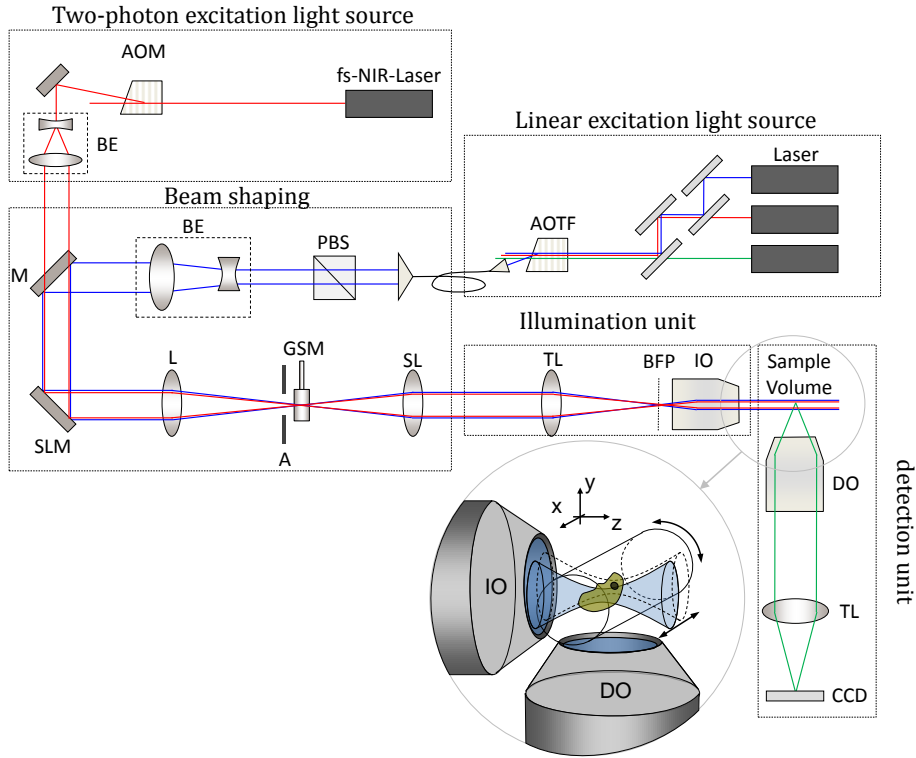


Figure 7.7: Sketch of the light-sheet microscope with added two-photon illumination beam path.

the background created by the ring structure of the beam. This fact is manifested in the small values of \hat{s}_{ideal} and \hat{s}_{ghost} . Altogether, this quantitative analysis confirms the visual impression that was described above.

The simulation does not account for the pulsed nature of the light necessary to achieve two-photon fluorescence excitation. The image quality may therefore be overestimated. However, Wang et al. [2009] showed that a 200fs pulse does not significantly spread in time even after propagation skin or a compound of skin and fat over a distance of more than 20mm.

7.4 EXPERIMENTAL SETUP

A strong light source had to be added to the existing setup to allow the direct comparison of linear and two-photon fluorescence excitation. A sketch of the modified setup is shown in Figure 7.7. A pulsed laser (Chameleon, Coherent) that is very well suited for two-photon excitation in microscopy applications was integrated. The laser is tunable over a wide range ($\lambda = 760\text{...}940\text{nm}$) and provides ultra-short pulses $\tau = 150\text{fs}$ with a repetition rate of 80MHz at high average powers $P = 800\text{...}1600\text{mW}$. The pulsed NIR laser is coupled into the existing beam path directly after being expanded to fully illuminate the spatial light modulator (SLM).

Both beams illuminate the same SLM (Pluto NIR-2, Holoeye) that has a special broad-band coating and adapted firmware to allow the phase modulation over a wide spectral range from 405nm to 1064nm. This ability is extremely helpful for the comparative experiments carried out for this thesis. The spatial light modulator is steered by the PC using a graphics card. The hologram is transferred as an 8bit gray-scale image $h_{\text{img}}(x, y)$ to the SLM. The device translates this signal

into a corresponding voltage that induces a change in the orientation of the birefringent liquid crystal and hence a phase delay $h(x, y)$ on the incoming wave-front (see section 3.4 for details). A look-up table q translates the values of $h_{\text{img}}(x, y)$ nonlinearly into appropriate voltages. Due to dispersion in the SLM's LCoS display, the same voltage (and therefore hologram image $h_{\text{img}}(x, y)$) leads to a larger phase shift for red-shifted light. Therefore, a different look-up table has to be used to achieve a full phase shift of 2π for the maximum value in the hologram image (which is $2^8 = 256$) at two wavelengths $\lambda_{\text{lin}} = 488\text{nm}$ and $\lambda_{2p} = 800\text{--}920\text{nm}$. This change of the LUT can only be carried out in a time-consuming manual step that consists in overwriting the SLMs memory. Hence, another method was employed here. For all colors, the same LUT is used. This LUT allows a maximum phase delay of $d\phi = 2\pi$ at $\lambda_{2p, \text{max}}$. The use of this LUT for shorter wavelength causes additional effective phase wrapping if the phase-shift by the SLM is larger than 2π . This wrapping reduces the diffraction efficiency into the first order that is used for sample illumination. As the full dynamic range of 2^8 steps is not needed for the axicon and lens holograms, the gray-scale hologram image for shorter wavelengths is scaled to smaller maximum values. For example, for $\lambda = 488\text{nm}$, the image hologram value that achieves a phase shift of 2π is 100, which means that the hologram can still feature 100 distinct phase shifts, which is sufficient to achieve high diffraction efficiencies.

While there are no indications that the SLM's performance is affected by the high powers of the pulsed NIR-laser, the deposition of heat might cause deformations that lead to a phase shift that superimposes with the hologram. In the short time available, no effects could directly be accredited to heating of the SLM by laser light. Using a pulse auto-correlator, the pulse width of the light diffracted by the hologram was measured. No change in pulse shape and duration was found. This finding agrees with [Bock et al. \[2009\]](#), who also state that the effect of LCoS devices becomes critical only below a pulse duration of $\tau = 6\text{fs}$.

The illumination optics consist of achromatic lenses with a broadband anti-reflection coating for the visible spectral range. While these components are not especially designed for the near-infrared (NIR) spectral range, the transmission was found to be sufficient. Most importantly, there are no significant reflections that would create artifacts in the optical path or especially in the sample chamber. The illumination objective lens transmits $\approx 85\%$ around $\lambda = 800\text{nm}$. The mirrors employed in the setup are silver coated and reflect NIR light to a very large fraction of $R > 98\%$. This situation is extremely helpful as it means that the same illumination optical path can be used for both spectral ranges.

A very precise overlap of the two laser beams is of paramount importance to illuminate the sample in a controlled way and produce comparable results. To be able to generate precisely overlapping beams in the sample volume it would be best if both laser beams were aligned co-axially already in front of the SLM. The required precision is extremely high (see Section 7.2.6). The task was rendered even more difficult because both the NIR and the VIS laser beam are expanded to diameters of several millimeters to fully illuminate the SLM. The required precision could not be achieved by manual alignment. However, the position and angle of the beams in the sample chamber can be steered by the position of the hologram on the SLM and the addition of a prism phase, respectively. The procedure that was developed to achieve a sufficiently good overlap is described

in Section 3.4.4. The position can be steered to a precision of 165nm, which is determined by the pixel size of 8 μ m and the magnification of the illumination optical path $M_{\text{III}} = 8.25/400 \approx 1/50$. The angular alignment precision is in practice not limited by the SLM but by the capability to measure the tilt of the beam against the DO's focal plane.

7.5 BEAM IMAGES MEASURED IN HOMOGENEOUS FLUORESCENCE

The first experiment was performed to illustrate the ability of nonlinear fluorescence excitation to successfully suppress the Bessel beam's rings system. Figure 7.8a and b show the linear and non-linear fluorescence excitation by Bessel beams, respectively. The beams have equal depth of field of $dz \approx 300\mu\text{m}$. The width of the main lobe is very similar, but the fluorescence detected at the position of the ring system is strongly reduced by TPE. Lateral profiles taken at three different positions along the beam axis are shown below in Figure 7.8c and further demonstrate the efficient suppression of the ring system.

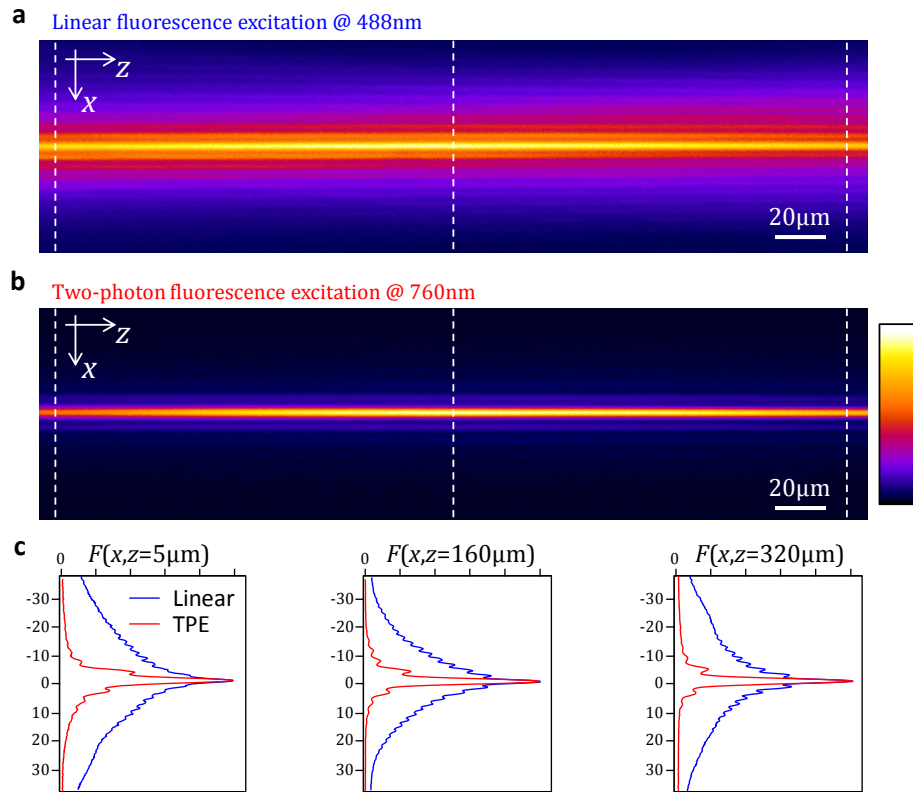


Figure 7.8: Linear & Two-Photon fluorescence excitation by Bessel beams.

The two beams are produced at $NA \approx 0.2$ and have equal depth of field $dz \approx 300\mu\text{m}$. Fluorescence is excited at $\lambda = 488\text{nm}$ and by two-photon absorption at $\lambda = 760\text{nm}$ in Rhodamine solution.

7.6 RESOLUTION AND CONTRAST MEASURED USING SCATTERING FLUORESCENT SPHERES

To measure resolution and background with well-defined objects, fluorescent spheres ($d = 0.75\mu\text{m}$) were fixed in an agarose gel cylinder at a concentration $c \approx 3 \cdot 10^7/\text{ml}$. The images were recorded using a lens (W-Achroplan 40x/0.8, Zeiss) with a theoretical lateral resolution of $dx_{1/e} = 0.8\mu\text{m}$ and axial resolution of $dy_{1/e} = 2.0\mu\text{m}$. The sampling of the CCD camera was $\delta x = 0.25\mu\text{m}$. The sample was displaced in steps $\delta y = 0.25\mu\text{m}$ along the detection axis to acquire a stack of 160 images with isotropic sampling. Maximum projections of the stack of images along the detection axis y are shown in Figure 7.9a & b for two-photon and linear excitation, respectively.

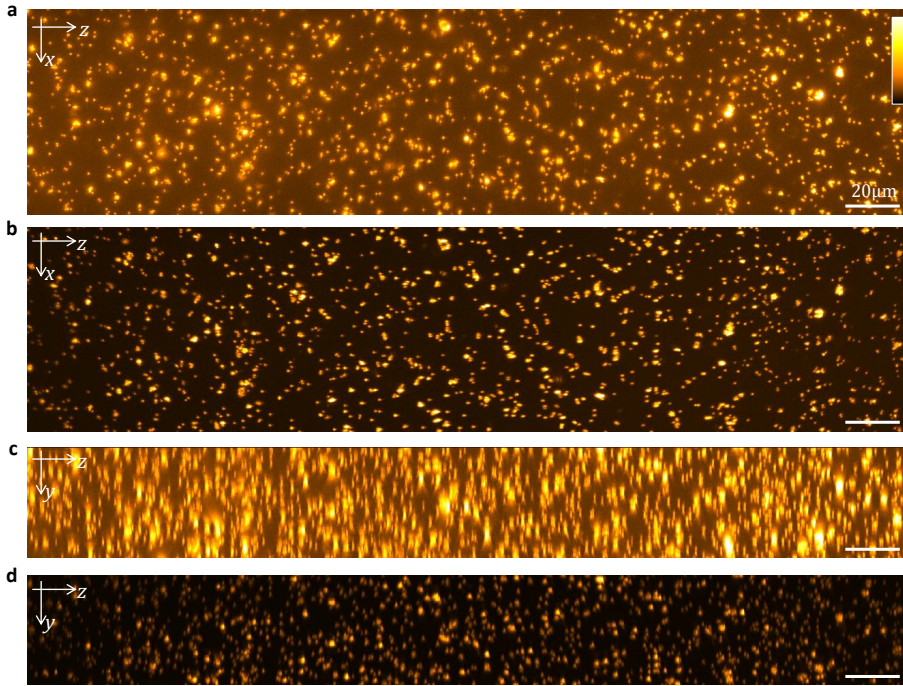


Figure 7.9: Images of fluorescent spheres for linear and two-photon fluorescence excitation by scanned Bessel beams.

Images of a volume with dimensions $s_x \cdot s_y \cdot s_z = 75\mu\text{m} \cdot 40\mu\text{m} \cdot 325\mu\text{m}$ were recorded for linear for two-photon excitation by scanned Bessel beams. Maximum projections along the detection optical axis are shown in (a) for linear excitation and (b) for TPE. Projections along the scan axis are shown in (c) for linear excitation and (d) for TPE.

The maximum projections of the image stack along the scan-axis x shown in Figure 7.9c & d reveal directly that the two-photon Bessel beam light-sheet strongly reduces the size of the point-spread function that is measured at the position of each fluorescent sphere. This reduction corresponds to an increase in resolution. y -profiles through the spheres allow a more quantitative analysis. The locations (x_i, z_i) of ≈ 1200 sphere were determined from a maximum projection image along the detection optical axis. The y -position, axial resolution and signal-to-background were obtained from fitting a Gaussian function to the $p(y)$ -profiles analogous to Section 6.5.

The powers of the beams were adjusted in a way to achieve equal average signal amplitudes for both linear and non-linear excitation (see Figure 7.8). However, the large width of the sheet in the linear case causes a higher background in the images, as can be seen in the graph 7.10a. Figure 7.10b, where $dy_{1/e}$ is plotted against the z -position of the measurement reveals that resolution is independent of the penetration depth of the illumination beam into the sample. The axial resolution for two-photon fluorescence excitation is $dy \approx 2\mu\text{m}$. On average, $dy_{1/e}$ is approximately half as large for two-photon excitation.

A slight increase in signal-to-background along the propagation axis can be noticed for the linear Bessel beam. It seems that this is due to drift during the measurement. The system was perfectly aligned for both the beam at $\lambda = 488\text{nm}$ and the beam at $\lambda = 800\text{nm}$ at the beginning. The measurements at $\lambda = 800\text{nm}$ were performed first. At the time of the measurement at $\lambda = 488\text{nm}$, the system must have been slightly misaligned already resulting in a slightly better resolution and signal-to-background for linear Bessel beam at large depths z . A

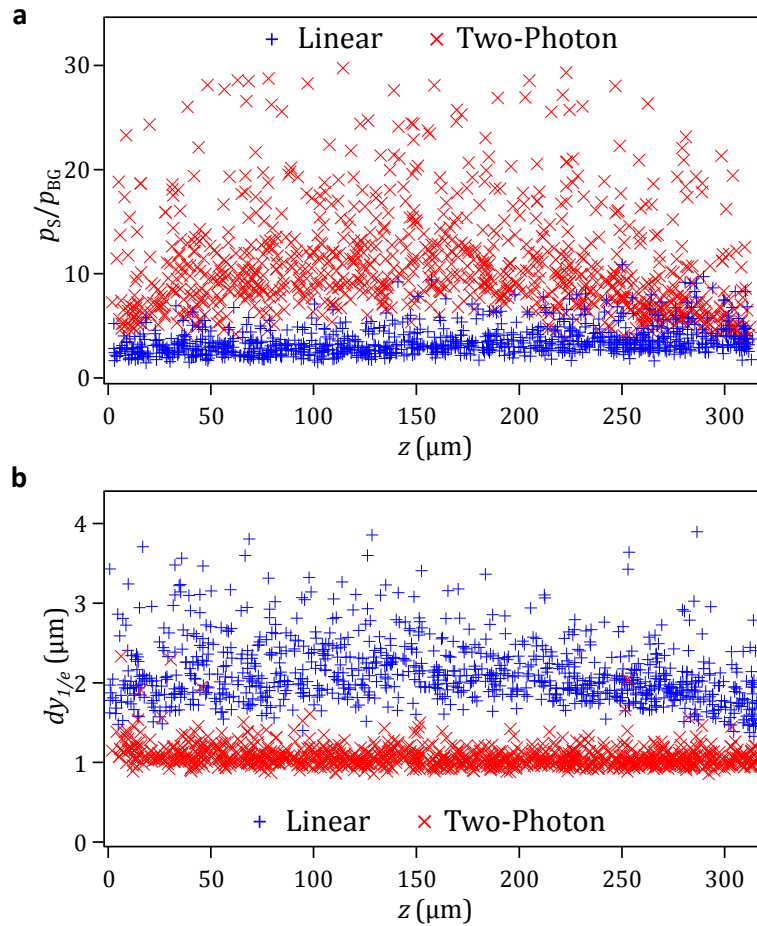


Figure 7.10: Quantitative measurements of linear and two-photon imaging performance. From the images shown in Figure 7.9, the signal-to-background (a) and resolution (b) was extracted from fits to $p(y)$ -profiles through ≈ 2400 polystyrene spheres. The values are shown as a function of the z -positions of the spheres in (a).

possible explanation for the drift is the heating of the SLM due to the strong irradiance by the pulsed NIR-laser. However, these effects are very small. The signal amplitude along the illumination axis remains constant, even though the resolution increases, which indicates better alignment for large z . Probably, the signal would be stronger in the front if the beam was perfectly aligned. Nevertheless, the different imaging performance of the different illumination techniques in the presence of scattering is demonstrated by these measurements. In summary, TPE by scanned Bessel beams increases signal-to-background by a factor of ≈ 4 and resolution by a factor of ≈ 2 relative to linear fluorescence excitation.

7.7 IMAGING PERFORMANCE MEASURED IN MULTICELLULAR SPHEROIDS

To assess the imaging performance of two-photon fluorescence excitation by Bessel beams relative to other techniques in a biological medium, tumor multicellular spheroids were imaged. For TPE at $\lambda = 920\text{nm}$, the low fluorescence signal required long exposure times of several seconds (2s - 4s) per plane with 2×2 pixel binning.

7.7.1 Analysis of Image Artifacts

Figure 7.11a shows an image acquired for linear fluorescence excitation by Bessel beams and confocal-line detection. The image (Fig. 7.11b) obtained by two-photon fluorescence excitation and wide-field detection reveals two sides. On the one hand, the image appears to have superior contrast. On the other hand, artifacts in the form of uneven signal strength across the spheroid can be clearly recognized.

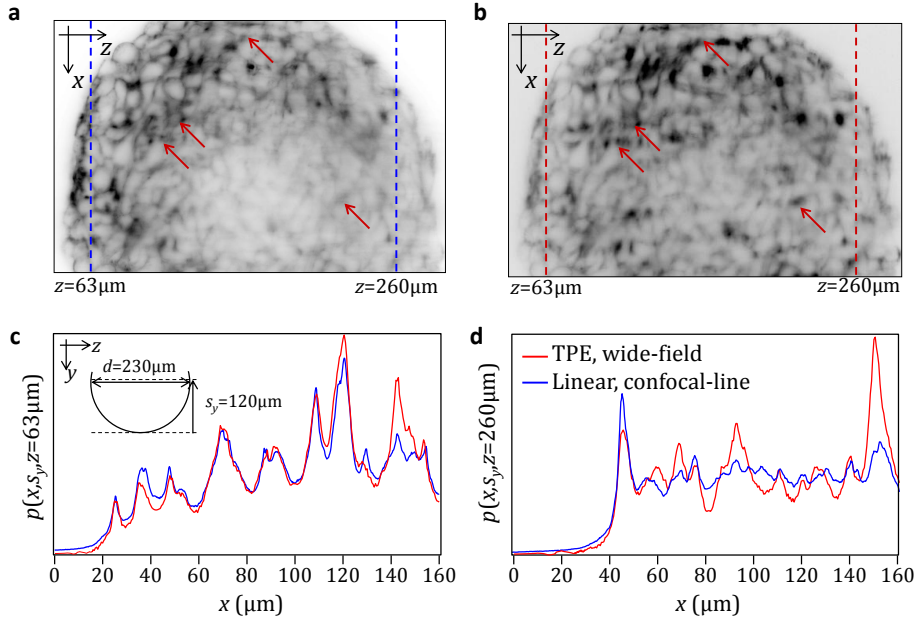


Figure 7.11: Imaging performance in tumor multicellular spheroids.

A plane $120\mu\text{m}$ inside a tumor multicellular spheroid with a diameter of $d \approx 230\mu\text{m}$ (see sketch in (c)) was imaged by confocal-line detection with linear fluorescence excitation by Bessel beams (a) and two-photon fluorescence excitation by Bessel beams with wide-field detection (b). Line-scans for low and high penetration depth are shown in (c) and (d), respectively. The positions are indicated by dashed lines in (a) and (b). TPE leads to a less regular illumination of the spheroid with strong deviations at the positions marked by arrows in (a) and (b).

At first, the image contrast is assessed. Line-profiles taken at the left side ($z = 63\mu\text{m}$) of the cell spheroid are shown in Figure 7.11c. Confocal-line detection for linear fluorescence excitation provides essentially the same contrast as wide-field detection does for two-photon excitation by scanned Bessel beams. The numerical investigation of the optical sectioning performance presented in Section 7.2.5 revealed that a strong relative improvement of contrast by the nonlinear fluorescence excitation with respect to confocal-line detection can only be expected for a short depth of field of the illumination beam. The cell clusters have a diameter of approximately $240\mu\text{m}$ and the focal depth of the illumination beam is chosen accordingly. It is therefore not surprising that the contrast at $z = 63\mu\text{m}$ is similar.

However, at the back-side of the sample, the modulation in the line-profile of the TPE image is much stronger (Fig. 7.11d). Due to the complex and unknown structure of the sample it is not possible to decompose the image into ideal and ghost images to assess their respective contrast which makes the interpretation of this line-profile difficult. It seems that contrast offered by two-photon excitation

is higher. However the impression given by the graph can also be misleading since the strong outliers can also originate from inhomogeneous illumination. The signal generated by the two imaging methods is similar except from the two outliers at $x \approx 45\mu\text{m}$ and $x = 155\mu\text{m}$ and in the region $x = 80 \dots 100\mu\text{m}$ where the combination of low and high signal could be explained by a redistribution of light due to scattering by the sample. Is TPE by Bessel beams more susceptible to artifacts? This question is studied in more detail in the following.

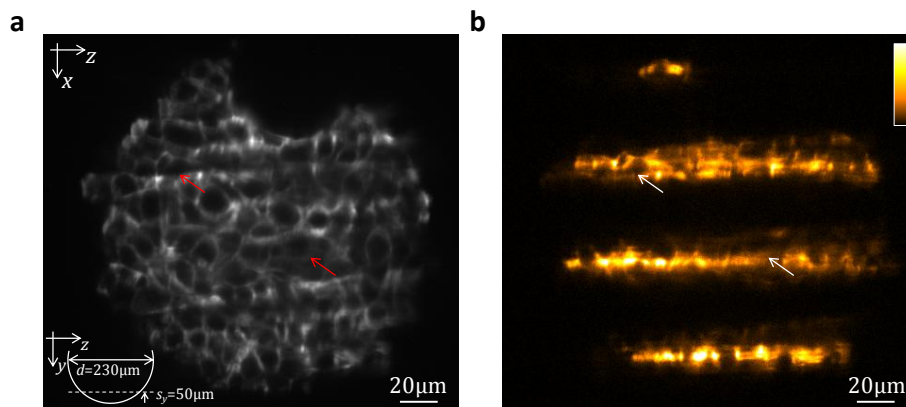


Figure 7.12: Image artifacts in NL-MISERB.

Image of a cell cluster obtained by two-photon fluorescence excitation with Bessel beam illumination (a). The TPE for the illumination beam at four positions in the cluster (b) reveals strong perturbations and off-axis fluorescence excitation. The deviation of the beam leads to uneven TPE. The arrows mark areas with stronger (left) and weaker (right) signal.

While scattering seems to affect the near-infrared light much less while it propagates through the sample, the image obtained by non-linear fluorescence excitation also reveals stronger artifacts. Similar to images obtained from Gaussian beam illumination, the signal is uneven across the sample. It seems that light is redirected and strongly deflected. Stripes within the sample exhibit a strong signal while neighboring areas remain dark (see arrows in Figure 7.11). The redistribution of light in the sample is visualized by Figure 7.12. A plane that is situated approximately $70\mu\text{m}$ below the center of the spheroid was imaged. The result (Fig 7.12a) reveals strong stripe-shaped artifacts. Figure 7.12b shows the illumination beam propagating through the sample at four equidistant lateral positions. Especially the two central positions illustrate that the fluorescence is excited not only along the central lobe of the Bessel beam, but over a larger area. It is a surprising result of this measurement that the self-reconstructing Bessel beam, shows such strong susceptibility to the sample, especially as the near-infrared light is supposed to be much less affected by small scattering components of the sample. A close look at the image offers a possible explanation. It seems that the artifacts are caused by very large obstructions. The perturbation by large obstructions with a size of $\approx 10\mu\text{m}$ can be seen the following way. The light is not scattered into a large solid angle, but deflected at the surface of by the change in refractive index. If the surface is slightly curved, as it is the case for large cells, the light is not only deflected but also focused. In this case, the non-linear dependence of the fluorescence from the irradiance can even lead to stronger, more localized artifacts than for linear fluorescence excitation. However, it has to be noted, that artifacts are more visible for TPE due to the high overall contrast offered by the method.

7.7.2 Contrast Improvement by Confocal-line Detection

Confocal-line detection can also improve the image quality for two-photon fluorescence excitation by Bessel beams. Similar to confocal-line detection for Gaussian beams, the slit detection mainly acts to reject background fluorescence due to scattering. However, it can also be helpful on the detection side. Confocal-

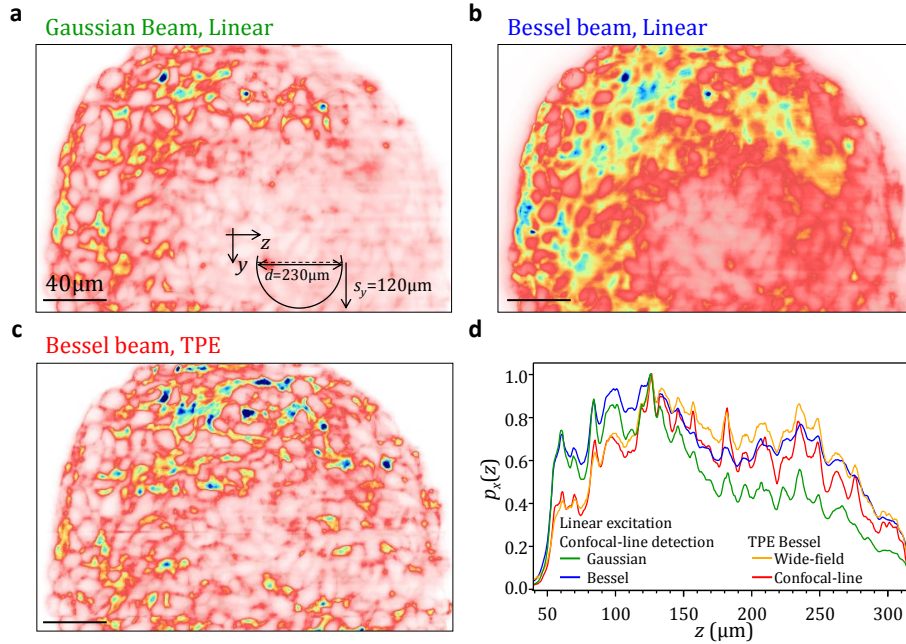


Figure 7.13: Contrast improvement by confocal-line detection for TPE by Bessel beam illumination.

Images of a multicellular spheroid for two-photon fluorescence excitation by a Bessel beam. (a) and (c) were obtained for scanned illumination, (b) and (d) for confocal-line detection. (a), (b) show a plane in the center of the spheroid ($s_y = -5\mu\text{m}$) where the fluorescence light has to travel a long distance through the through the sample to reach the detection lens. This distance is smaller for the images (c) and (d) where $s_y = 75\mu\text{m}$.

line detection images were acquired using the method presented in Section 6.4. The illumination beam was four-fold multiplexed and scanned across the sample in 100 steps of $0.4\mu\text{m}$. Figure 7.13 shows images obtained for two-photon Bessel beam illumination for wide-field and for confocal-line detection, respectively. The increase in contrast by confocal-line detection in Figure 7.13b which shows a plane close to the center of the cell cluster ($s_y \approx -5\mu\text{m}$) is obvious. The improvement by confocal-line detection for the images of a plane closer to the surface ($s_y \approx 75\mu\text{m}$). Measurements of the contrast using the spatial frequency metric introduced in Section 2.2.4 shown in Figure 7.14 support the finding that the enhancement of image contrast by confocal-line detection is especially strong in layers deep within the sample. The ratio is $c_{\text{CL}}/c_{\text{WF}} = 1.8$ for $s_y \approx -5\mu\text{m}$, whereas $c_{\text{CL}}/c_{\text{WF}} = 1.3$ for an image at $s_y \approx 75\mu\text{m}$ close to the surface of the cell cluster facing the detection objective lens.

7.7.3 Measurement of Penetration Depth

To measure the penetration depth into scattering samples, the fluorescence signal within a small area around the propagation axis of the beam is evaluated.

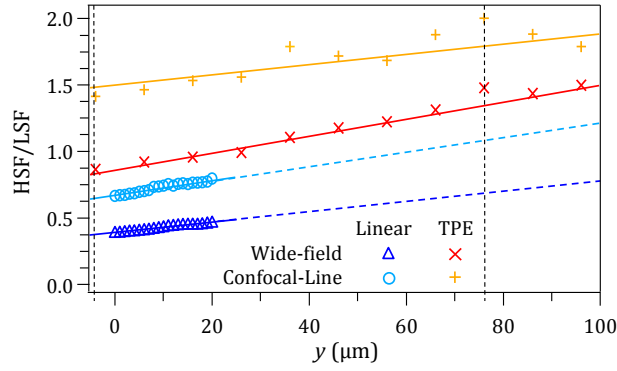


Figure 7.14: Measurement of contrast for TPE by Bessel beam illumination.

For comparison, the results obtained for linear fluorescence excitation obtained from a smaller volume at the center of the spheroid are included. The positions of the images shown in Figure 7.13, $s_y = -5\mu\text{m}$ and $s_y = 75\mu\text{m}$, are indicated by black vertical lines.

The on-axis fluorescence can also be obtained by multiplying the image of a static beam with a mask. As for confocal-line detection, the mask cuts off light scattered out of the beam's central lobe. Therefore, to measure the beam's fluorescence excitation ability at large depths the confocal-line detection image can be integrated along the scan axis x to obtain

$$p_x(z) = \frac{1}{dx} \int_{w_x} p(x, z) dx = \sum_i F_i(z). \quad (7.17)$$

To accurately measure the penetration depth, the shape of the spheroid has to be taken into account. The profile $F_i(z)$ is corrected for each position x so that z corresponds only to the propagation distance of the beam in the spheroid. Moreover, the final profile is normalized to the width of the spheroid for each z -position. An illustration is shown in Figure 7.15a. The profiles post-processed in this way (Fig 7.15b) reveal a significantly higher penetration depth for illumination by Bessel beams than for Gaussian beams. TPE by Bessel beam improves the penetration by a factor of 1.7 relative to linear excitation. The improvement relative to linear Gaussian beams by a factor of 3.7 is even more striking. It constitutes a further example for the Gaussian beam's inferior performance in scattering media.

Theoretical estimations (§ 7.2.2) predicted an increase by a factor of 1.8 to 5 depending on the size of the scatterers. The improvement found is on the lower end of this range. The small improvement in penetration depth over the Bessel beam at $\lambda = 488\mu\text{m}$ is probably due to structure of the spheroid that consists of large cells rather than small Rayleigh-scatterers. As outlined before (§ 7.7.1), the refractive index distribution in the multicellular spheroid perturbs pulsed near-infrared Bessel beams in a way that leads to strong artifacts. This finding also indicated that the perturbation in the cell cluster is mainly due to large scatterers.

7.8 DISCUSSION

In this chapter, two-photon fluorescence excitation (TPE) by self-reconstructing beams in a light-sheet microscope was studied. The motivation was manifold:

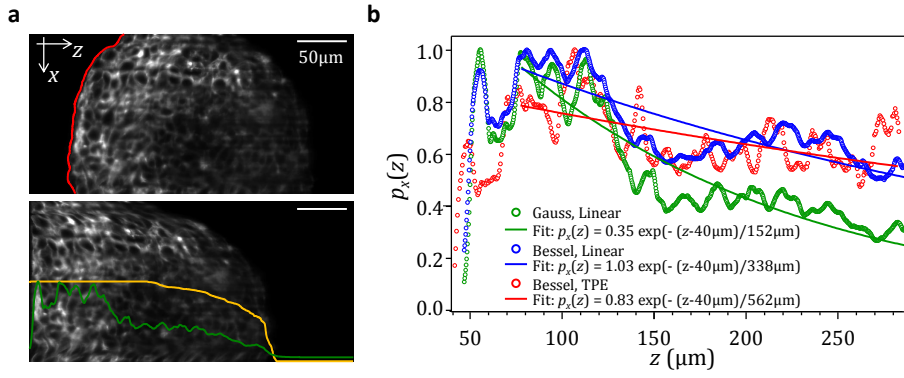


Figure 7.15: Penetration depth for nonlinear Bessel beam illumination.

The penetration depth into the scattering cell cluster is measured using corrected profiles. The red line in the top image of (a) illustrates the z -coordinate $z_{off}(x)$ where the illumination beam penetrates the spheroid. This offset is subtracted to obtain the image shown below in (a). The average signal along x , $p_{corr}(z)$ is indicated in green and the width of the spheroid $p_{mask}(z)$ in orange. The corrected, normalized profiles $p_x(z) = p_{corr}(z)/p_{mask}(z)$ are shown in (b) together with exponential fits for three different imaging modes: linear fluorescence excitation by Gaussian beam and Bessel beam illumination, respectively and TPE by Bessel beam illumination.

First, to increase contrast by suppression of the Bessel beam's rings. Second, to increase penetration depth into scattering samples due to the longer wavelength of the excitation beam. Overall, it can be said that while the first goal has been fully achieved, the improvement in the penetration depth was on the lower end of the expected range.

Simulation: Simulations were used to study the image quality for Gaussian and Bessel beam illumination with linear and two-photon excitation (§ 7.3). The simulation with the beam propagation method (see Appendix B) does not account for pulsed illumination. This neglect does not influence the results if the temporal structure of the excitation light is conserved along the propagation across the field-of-view. It was shown that typical scattering does not lead to strong temporal spreading of the beam and that as a result the ratio of fluorescence generated by scattered and unscattered photons at different locations is independent of the temporal structure of the beam by [Theer and Denk \[2006\]](#).

Resolution and Signal-to-background: Using fluorescent spheres as a first test sample, a drastic improvement in both resolution and signal-to-background was found. These results agree with the numerical analysis (§ 7.2.5). The possible improvement by two-photon Bessel beam illumination of small, weakly scattering samples (primarily for cell culture in dishes with diameters around $50\mu\text{m}$) has also been demonstrated by [Planchon et al. \[2011\]](#). However, large strongly scattering samples were investigated for the first time in the context of this thesis.

Artifacts: Concerning artifacts, the main question that was addressed here is whether the interplay between

- the quadratic dependence of the fluorescence on the irradiance, $F \propto I^2$
- the decreased scattering cross-section of small particles, $\sigma_{scat} \propto \lambda^{-\alpha}$ with $2 < \alpha < 4$

leads to a more even fluorescence excitation across the plane that is illuminated by the light-sheet. An important factor is the size and shape of the scattering particles. Large spherical particles focus the incident light and therefore lead to a stronger spatial redistribution of the fluorescence excitation for TPE than in the linear case.

The simulations presented in Section 7.3 indicate the strong susceptibility of TPE by Gaussian beams that leads to extreme artifacts in the images. For TPE by Bessel beams, the situation is improved significantly. This effect was quantitatively analyzed by decomposition of images of known structures into ideal and ghost images that was introduced in Section 2.2.5. For the small spheres ($d = 1\mu\text{m}$) used in the simulation, it was found the TPE with Bessel beams is the best choice to obtain high-contrast images and at the same time avoid artifacts.

However, in the images of the cell spheroids, stripe-shaped artifacts are visible for TPE by Bessel beams. The increased visibility of scattering artifacts is of course partly due to the considerably better optical sectioning performance of the TPE Bessel beam light-sheet microscope. It has to be investigated in more detail whether only the visibility of the artifacts increases or the absolute strength. The decomposition into ideal and ghost image contrast is unfortunately not possible in this case due to the unknown structure of the sample and the therefore unknown ideal image.

Penetration depth: The primary advantage of two-photon fluorescence excitation in standard confocal microscopy is that the nonlinear dependence suppresses out-of-focus fluorescence sufficiently so that no pinhole in the detection path is needed. Therefore, a larger amount of scattered fluorescence photons can be collected. The increased penetration depth into scattering samples is largely attributed to this difference [Theer and Denk, 2006]. This advantage does not transfer to the perpendicular geometry of the light-sheet microscope.

However, due to the strongly reduced scattering cross section for Mie- and Rayleigh-scatterers by factors of 4 to 16, respectively, an increase in penetration depth of the light-sheet by a factor of 1.6 to 5 was expected. For experiments performed on cell clusters an improvement by 1.6 was found for Bessel beams (Figure 7.15). Two-photon excitation by Gaussian beams in a light-sheet microscope was investigated by Truong et al. [2011]. The authors state that while penetration into drosophila embryos could not be improved significantly, the advantage of two-photon fluorescence excitation lies in the suppression of fluorescence excitation by the scattered light in the back of the sample. Therefore, the two-sided illumination can be used in parallel in order to increase image acquisition speed. In the case of linear excitation this option is not favorable as the scattered light at the back of the sample yields a very blurry image which superimposes with the good image created by the unscattered light sheet penetrating the sample from the opposite direction.

Comparison to point-scanning two-photon microscopy: A major problem in two-photon point-scanning confocal microscopy of strongly scattering samples is the out-of-focus fluorescence. Because the detection axis is anti-parallel to the illumination axis, no separation is possible and for large depths strong background is recorded. Using a perpendicular arrangement similar to a light-sheet microscope the propagation of a static beam into a scattering samples was observed from the side by Ying et al. [1999]. They showed that the power in the focus gets weak in comparison to the fluorescence created by light before

it reaches the focus. While the perpendicular arrangement of illumination and detection allows for a separation, the scattering of the fluorescence on the detection path is more problematic in the light-sheet microscope, because of the wide-field detection. [Truong et al. \[2011\]](#) state that for imaging drosophila embryos, TPE-DSLM images contain more background than those obtained by TPE point-scanning confocal microscopy but less than conventional linear excitation DSLM images.

This property also represents the main advantage: because of parallelized illumination and detection and the efficient use of illumination light, two-photon light-sheet microscopy is faster and less invasive in terms of photo-damage and bleaching. When two-photon light-sheet microscopy is employed for these reasons, the question remains which illumination beam should be used. Due to hardware limitations, no experimental data could be measured for Gaussian beams. Simulation results (§ 7.3) indicate that Bessel beams are highly advantageous compared to Gaussian beams. For TPE by Bessel beams, the light-sheet is thinner (Fig. 7.2), the optical sectioning better (Fig. 7.3) and the strength of artifacts is much weaker (Fig. 7.6).

Limitations of the setup: Experimental data could not be obtained for a number of samples (e.g. Sytox stained zebra-fish) due to a very low overall fluorescence signal strength or strong auto-fluorescence. There are several possible reasons for this. First, the staining of the sample could not have been suited for two-photon illumination. While this issue could not be ruled out, the marking in both the zebra-fish and the cell spheroids was aimed at two-photon imaging. The imaging speed in the spheroid was at least comparable to that of a point-scanning TPE-LSM. Second, the low signal is due to the low light efficiency of the optical path. The power delivered to the sample is not high enough for sufficiently strong signals. There are losses due to fact that all optics in the illumination path are optimized for light in the visible spectral range and not for the near infrared. Also, the effective diffraction efficiency of the spatial light modulator is smaller than 50%. SLMs with better performance are available. These devices do not have the extreme broadband-capability of the SLM that was employed for the investigations presented here. These were primarily aimed at a comparison of linear and two-photon Bessel beams and therefore necessarily relied on the specific SLM used. However, most of the illumination power is lost because the SLM had to be over-illuminated. This waste of laser power is necessary to achieve homogeneous illumination of the SLM, which is needed to create Bessel beams with sufficient depth of field at high NAs. The power measured in the back-focal plane was $P_{\text{BFP}} \approx 200\text{mW}$, which is far less than the 600mW at similar pulse length used by [Theer and Denk \[2006\]](#) for point-scanning two-photon microscopy in scattering media. However, it is close to the power used by [Planchon et al. \[2011\]](#) where a much smaller ring width parameter $\epsilon \approx 0.84$ was employed. In conclusion, two-photon excitation by Bessel beam illumination in a light-sheet microscope requires very large powers. The limitations on sample size and imaging speed have to be further investigated using more suitable hardware.

Outlook: What are the next steps? First, an experimental investigation of the performance of TPE for Gaussian beams to verify the findings of the simulation results would be interesting. Therefore, the illumination path would have to be slightly altered to make more efficient use of the beam power. Only recently, a setup has been proposed to compare linear and TPE by Gaussian and Bessel

beam [Olarte et al. \[2012\]](#). However, the beams are not shaped by holographic devices but by a lens or an axicon that is mechanically introduced into the illumination beam path to create Gaussian or Bessel beams, respectively. The study does not investigate the performance of beams with equal depth of field and the performance is assessed using weakly scattering samples, i.e. *c. elegans* worms. The second step that should be undertaken is to study the bleaching and photo-toxicity for TPE by Bessel beams in living samples. For TPE, the power transported in the ring system of the Bessel beam is substantial even though a limited amount of non-linear fluorescence is created. It remains to be seen what kind of live-imaging experiments will be possible at this level of sample exposure.

SUMMARY, CONCLUSION & OUTLOOK

In the following, the primary results of this thesis are summarized together with concluding remarks. Thereafter, a final discussion follows that also gives an outlook onto interesting future developments to light-sheet microscopy with self-reconstructing beams.

8.1 SUMMARY & CONCLUSION

Altogether, the work on microscopy with self-reconstructing beams as presented in this thesis brings together three areas of research where important advances have been reported in recent years. First, the use of spatial light modulators that allow flexible and precise shaping of beams with high spatial and temporal resolution. Second, light-sheet microscopy as an important tool designed to investigate large biological samples at higher speed and lower photo-damage than with all other light microscopy techniques. Third and most importantly, the phenomenon of self-reconstructing beams.

The **use of spatial light modulators for shaping of the illumination beam in a light-sheet microscope** was introduced here for the first time. The flexible beam shaping device enabled the precise control over the beam dimensions as well as axial and lateral beam profile. To enable the efficient use of the available laser power for both Gaussian and Bessel beam generation, the SLM was used to create virtual beams that were imaged into the sample volume. Intelligent superposition of phase holograms was developed to suppress the influence of parasitic higher orders that arise from the pixelated device [Fahrbach and Rohrbach, 2010]. Moreover, phase-shape holography [Roichman and Grier, 2006] was employed to enable amplitude modulation by a phase-only device. This capability was used to precisely tailor the illumination beams, to avoid axial variations of the Bessel beam profile, and even to create a new class of beams, the so-called sectioned Bessel beams [Fahrbach and Rohrbach, a].

Improved light-sheet microscopy of scattering samples by self reconstructing beams: Since the first paper by Huisken et al. [2004] demonstrated the potential of light-sheet based microscopy in modern cell and developmental biology a great number of potential applications in other fields from cell culture to neurology have been demonstrated. One of the few weaknesses of the technique is the degradation of image quality by scattering of the illumination light. The use of self-reconstructing beams for sample illumination in light-sheet microscopy addresses the following three factors that limit the image quality in LSFM. First, due to light's natural beam spreading, there is a tradeoff between the illumination beam's depth of field and its beam waist. Second, as the illumination light path lies in the plane to be imaged, scattering and absorption result in strongly visible artifacts in the images such as dark and bright stripes behind scatterers (ghost images). Third, scattering causes additional non-uniform spreading of the illumination beam along the propagation into the sample. The perturbations lead to a limited penetration depth of conventional beams, i.e.

a decrease in image quality and signal strength within the images along the illumination axis .

As has been shown by many results in this thesis, **illumination by Bessel beams enables important improvements of the image quality** in all of the three above-mentioned categories. First, in contrast to conventional beams, due to its propagation invariance the Bessel beam offers homogeneous axial resolution within its depth of field (Fig. 1.4). Second, the strength of artifacts is significantly reduced. Third, the penetration depth into scattering material is increased. These aspects constitute primary results of this thesis [Fahrbach et al., 2010]. Simulations (§ 4.2) and experiments (§ 4.3) indicate the superior directional stability and stronger robustness of Bessel beams propagating into scattering material. Moreover, an increase in penetration depth in scattering media was also measured (§ 4.3.2). The increased performance inside scattering samples allows the observation of details at a depth within samples that has not been accessible so far (§ 4.3.3). Further experiments demonstrated increased image quality in inhomogeneous media because of weaker ghost images, i.e. image artifacts (§ 5.4) as predicted by numerical simulation by Rohrbach [2009].

The development of **confocal-line detection to suppress fluorescence created by the Bessel beam's ring system** was another key achievement of this thesis. The method consists in acquiring the image line-wise only at the position of the beam. The resulting images exhibit significantly more contrast than conventional wide-field detection light-sheet microscopy images for both illumination by Bessel beams and (conventional) Gaussian beams. An increase in axial resolution can be achieved only for Bessel beam illumination [Fahrbach and Rohrbach, 2012]. The improvement in contrast has been quantitatively analyzed using two independent methods. First, by analyzing the dimensions of the images of small fluorescent spheres (§ 6.5) Second, by measuring the signal-to-background in images of tumor multicellular spheroids (§ 6.7) using the spatial-frequency analysis (§ 2.2.4). This measure was derived in order to quantify the contrast in irregular samples with an unknown structure. It is given by the relation of high and low spatial frequencies in an image and based on the measure for *useful contrast* by Truong et al. [2011].

Confocal-line detection in combination with illumination by **sectioned Bessel beams** is especially interesting [Fahrbach and Rohrbach, a]. These asymmetrical beams yield the best optical sectioning of all illumination beams and furthermore provide the same optical sectioning performance for large objects as for small ones (§ 6.8). Furthermore their directional propagation stability is almost identical to conventional Bessel beams (§ 4.2, § 6.8.3).

Light-sheet microscopy with two-photon fluorescence excitation by Bessel beam illumination delivers images with significantly higher contrast than for linear fluorescence excitation [Fahrbach and Rohrbach, b]. As expected, the fluorescence excitation of the ring system is suppressed (§ 7.5). By measuring the dimensions of the images of small fluorescent spheres, the increase in contrast and axial resolution could be quantitatively analyzed (§ 7.6). It was also found that perturbations by the sample are more pronounced for TPE. Due to the higher contrast of the images, the visibility of artifacts in images of tumor multicellular spheroids was found to be larger for TPE than for linear fluorescence excitation (§ 7.7). A significant increase in penetration depth of TPE by Bessel beams over linear excitation was found. However, the improvement by a factor of 1.6 measured in in tumor multicellular spheroids was on the lower end of the

theoretically expected range. Contrast could be significantly increased especially inside the cluster for confocal-line detection which indicates the capability of the method to additionally improve image quality by rejecting scattered fluorescence.

8.2 FINAL DISCUSSION AND OUTLOOK

Self-reconstructing illumination beams are ideal for light-sheet microscopy because the improvement in image quality comes without compromising the potentially very high image acquisition speed that represents one of the major advantages of light-sheet microscopy. Many processes in biology occur on time-scales that require an imaging technique capable of delivering tens of frames per second over a large field of view. Light-sheet microscopy is unique in its ability to capture fast processes over large volumes such as the beating of a zebra-fish heart [Arrenberg et al., 2010], cell division [Planchon et al., 2011] or the migration of cells in a developing embryo [Keller et al., 2008]. Therefore, it seems not suitably to combine this fast method with a slow approach to increase image quality and penetration depth. For example, structured illumination can increase image contrast but requires the acquisition of several images. The penetration into scattering media can be increased by adaptive optics. But these techniques are still very slow even though great advances have been achieved in recent times [Mosk et al., 2012].

The methods to increase image quality that have been successfully integrated in light-sheet microscopy try to limit the reduction in acquisition speed. The stripe-shaped artifacts have been made less visible by fast tilting of the light-sheet in the image plane [Huisken and Stainier, 2007]. However, this method does not reduce scattering but only the visibility of the artifacts. Moreover the tilting speed has to be much faster than the image acquisition speed of the camera to work effectively, but is limited by the scanning mirror. Multi-view image fusion requires imaging of the sample from multiple sides with a rotation of the sample in-between [Verveer et al., 2007, Swoger et al., 2007]. To avoid this time consuming step, expensive multi-view setups with several cameras and lenses have been built [Krzic et al., 2012, Tomer et al., 2012]. Bessel-beam illumination is compatible to these high-speed imaging techniques and could be used to further improve the results.

Two interesting properties of self-reconstructing Bessel beams still remain **open questions**: First, the **performance is especially good for large obstructions**. The experimental data, where the beams are scattered by two large spheres (§ 4.3.1, and § 5.2), egg chambers (§ 6.6) or the cells in a spheroidal cell cluster (§ 6.7) underline this finding. Bessel beams do not show such a significant improvement in penetration depth for small spheres (§ 6.5). It is assumed that in the case of large, mainly forward scattering spheres, less light is removed from the Bessel beam's central lobe than for isotropic scattering which effectively redistributes the photons in all directions so that fewer will be able to interfere constructively at the position of the Bessel beam's central lobe.

Second, **the performance depends of self-reconstruction on the numerical aperture of the beam**. It was found the high-NA Bessel beams are able penetrate deeper (§ 4.1.1). This ability cannot be due to the larger beam cross-section, as sectioned Bessel beams perform equally well as conventional Bessel beams even though their cross-section is smaller. Key factors to self-reconstruction seem to be the large radial component of the wave-vector and the beam formation by

radially counter-propagating plane waves. Due to the radial transport, localized scattering obstacles affect the central lobe of a Bessel beam only over a very short distance along the propagation axis.

Light-sheet microscopy allows imaging of large samples at high frame rates and with low damage due to exposure to the fluorescence excitation by laser light. It therefore closes the gap between slower and less flexible techniques with **resolution** in the nanometer range and macroscopic techniques [Ntziachristos, 2010]. At present, large scattering samples are mainly investigated by acoustic imaging (at ultrasound frequencies), magnetic resonance tomography (MRT) or slow tomographic techniques like optical coherence tomography [Huang et al., 1991] or optical projection tomography [Sharpe et al., 2002]. While these methods are suitable for large specimens they offer distinctively lower temporal and spatial resolution. Higher resolution in optical microscopy can be obtained by shifting the limit imposed by diffraction. This goal can be achieved either by going to shorter wavelengths or by applying special super-resolution techniques. Extremely short wavelengths of x-rays are used by computer tomography or PET. These techniques are not suitable for long-term imaging due to the damage caused by the high-energy gamma rays. Shorter wavelengths in the visible spectral range are more susceptible to scattering. All current super-resolution techniques are slow and limited to thin, homogeneous samples. It remains to be seen how these techniques can be improved in the future. A possible improvement may arise from the implementation of super-resolution techniques into light-sheet microscopes. A first step has been undertaken when PALM was integrated in a SPIM [Cella Zanacchi et al., 2011], albeit at a significant loss of image acquisition speed in comparison to conventional light-sheet microscopy. However, in large inhomogeneous samples, resolution is not limited by diffraction as the scattered illumination beam is broadened considerably due to scattering.

Nonetheless, approaches to **super-resolution by structured illumination** (SIM) in a light-sheet microscope are an interesting option. The illumination pattern that is necessary to increase resolution is usually a regular grating that is shifted in phase in order to obtain homogenous sample illumination [Gustafsson, 2000]. In common bright-field SIM, the whole sample has to be illuminated by a grating for each plane that is imaged. The sample is therefore exposed to much more light than necessary (similar to confocal microscopy). In light-sheet microscopy it would be possible to launch the grating side-wise into the sample. Thereby, the light-dose could be strongly reduced. There are some problems that have to be overcome: First, the increase in resolution is dependent on the period of the grating. In order to achieve a significant increase in resolution a grating has to be formed by two plane waves that travel at large angles relative to each other. For example one could use a sectioned Bessel beam with a small section angle β (§ 6.8.1). However, an illumination lens with a high numerical aperture is necessary. Such lenses are large and feature small working distances so that mounting perpendicular to the detection lens might not be possible due to insufficient space. Alternatively, in a setup with two opposed illumination lenses, the grating could be created by two counter-propagating beams. However, SIM in strongly scattering media is challenging because the phase and amplitude of the grid structure quickly degrades due to sample-induced phase perturbations. In this case the approach to reconstruct a super-resolved image from sample illumination with unknown speckle patterns can be helpful [Mudry et al., 2012].

Light-sheet microscopy makes very **efficient use of light**. In comparison to point-scanning confocal microscopy only the part of the object is illuminated that is also imaged. However, on the detection side, there is still room for improvement, as in most cases, objective lenses with low numerical apertures ($NA \approx 0.5$) are used. A low numerical aperture offers the advantage of very simple light-sheet adjustment. Moreover, there are indications that the image quality deep inside scattering samples is more strongly degraded for detection lenses with higher NAs. However, this issue has not yet been investigated systematically. Water immersion objective lenses that combine a high NA with a long working distance are very complex and therefore still very rare and expensive. The complicated optics leads to inferior transmission values. For example the W Plan Apochromat 20x/1.0 by Zeiss transmits only $\approx 85\%$ of the fluorescence. In comparison, simpler objectives commonly transmit more than 95%. Detection lenses with high numerical aperture and accordingly low depth of focus cause unnecessary difficulties in the alignment of the light-sheet. In Section 7.2.6 the strong impact of misalignment, especially for Bessel beam illumination, is pointed out. As the axial resolution is mainly given by the thickness of the light-sheet, a high NA_{det} is not needed for good axial resolution. Moreover, as light-sheet microscopes are particularly well suited for long-term imaging, the requirements on the mechanical stability are extremely demanding. In conclusion, a high NA_{det} offers high fluorescence detection efficiency but imposes very high requirements on the alignment and mechanical stability of the system. A possible option that combines a high NA_{det} with good robustness consists in the artificial increase in the depth of field of a high-NA detection lens. Engineering of the point-spread function of the detection lens can be achieved by insertion of a phase element in the detection path. Radially symmetrical phase plates that increase the depth of field with minimal effect on image quality can be generated using the Toraldo principle [Martinez-Corral et al., 2002]. However, special care must be taken regarding two factors. First, the increase in depth of field should not come at the price of image artifacts. Second, the phase masks have to be efficient so that the gain in collection efficiency by the higher NA is not lost, for example by diffraction into higher orders for periodic phase masks or a ring system for axicons.

Improvement in data analysis: At present, light-sheet microscopes with fast cameras can acquire more image data at higher speed ($\approx 1\text{GB/s}$) than standard computer systems can handle. A major task beyond the further development of optical aspects like the image quality in strongly scattering media therefore lies in the development of concepts for data processing. Computational image analysis and automated information extraction from the recorded images are of paramount importance to the further development of light-sheet microscopy. There are already first approaches to on-line processing of the recorded data, for example the segmentation and localization of the positions of individual cells in whole organisms over time [Tomer et al., 2012, Krzic et al., 2012]. But the aspect of data analysis, compression and storage will become especially important in the context of an increased resolution for light-sheet microscopes that is enabled by Bessel beam illumination. So far, light-sheet microscopes that use Bessel beams and thereby offer isotropic resolution in the order of a few hundred nanometers are only used for small volumes of $< 50\mu\text{m}^3$ [Planchon et al., 2011]. The amount of data for high-resolution images of extended samples will be much larger. For neurology, imaging whole brains at high resolution is

of especially high importance due to the fact that the scale at which information is relevant for understanding the function span from single neurons to the whole neuronal network, i.e. brain. To gain appropriate image data, the current challenges are to overcome the limited penetration depth of light into brain tissue and the processing of the large amounts of data that are recorded. Current state-of-the-art methods [Li et al., 2010] are slow so that data processing does not represent the bottleneck. But light-sheet microscopy with illumination by self-reconstructing beams can play an important role in this field by increasing the image acquisition speed. At this point methods to quickly process the large amounts of data will have to be developed.

8.2.1 Penetration & Image Artifacts

To further improve the penetration depth into scattering media, adaptive optics may be necessary. There has been impressive progress in recent years in this field. The availability of flexible beam shaping by spatial light modulators together with increasing computational power make this technique very interesting for the future. At the moment, adaptive optics approaches are still too slow to be useful in wide-field live imaging. However, this combination could be used to improve image quality in small sub-regions with particular image details of interest. Automated computerized image analysis could be used to assess image contrast and information content on-line in parallel to the acquisition process. In specific regions, the beam perturbation could then be analyzed in more detail and optimized. To this end, existing approaches could be used that are based on the analysis of light that is coherently back-scattered into the illumination objective [Aubry et al., 2007, Aubry and Derode, 2009] or the light transmitted through the sample [Vellekoop and Mosk, 2007, Čižmár et al., 2010, Conkey et al., 2012]. Moreover, adaptive optics approaches can be increased in speed by taking the additional structural information provided by the detected fluorescence into account using intelligent algorithms. Especially interesting in the context of light-sheet microscopy with phase-shaped self-reconstructing beams is the possibility to further improve adaptive optics algorithms and adapt these to Bessel beams.

For Bessel beams, each radial position on the axicon generates the central lobe at a specific position along the beam axis. There is a linear correlation between the irradiance by the main lobe and the complex field at the axicon for a certain radius, i.e. $I_{\text{Bessel}}(0,0,z) \propto E_{\text{Axicon}}(r)$ with $z = r/\tan\alpha$ where $\alpha = \arcsin(\text{NA}/n)$. Therefore, one can directly access the axial profile of the Bessel beam by manipulation of the amplitude and phase of the axicon. This potentially powerful approach to adaptive optics has not yet been undertaken. The correction may be facilitated by detection of light transmitted through the object with another lens opposed to the illumination objective. Another camera could record the irradiance in the back-focal plane of this lens. The irradiance at a certain radius r can then also be traced to obstacles affecting the plane wave that contributes to the main lobe at a certain position $z = r/\tan\alpha$.

8.2.2 Confocal-Line Detection: Outlook

A particular strength of light-sheet microscopy is the **high-speed performance**. The total exposure time to achieve equal signal strength p_S is equal for the case of wide-field detection of the full image plane and for all line images taken with the confocal-line detection principle. Therefore, there is no physical reason that the imaging speed should be limited. However, there exist practical ones which make the high-speed implementation of confocal-line detection demanding and time-consuming.

Using **beam multiplexing**, a distance of about $40\mu\text{m}$ (for sample sizes around $300\mu\text{m}$) between adjacent beam positions is sufficient to avoid cross-talk, i.e. that adjacent beams mutually create background at the position of the other beam. Provided that the scanning mirror is fast enough and the available laser power sufficiently high, approximately 100 full-frame images have to be recorded per image plane. This method is therefore only an option when speed is not important, but image quality.

Another possible approach consists in using a **rolling shutter camera** in a way that the shutter acts as an effective slit-aperture [Baumgart and Kubitscheck, 2012]. However, in this case, for a given “slit” width, the exposure time is fixed by the camera's AD clock. Moreover, the fastest camera available at the moment (Orca Flash 4.0, Hamamatsu) features a rolling shutter that does not allow to use the full camera for confocal-line detection. The camera does not work with a single rolling shutter that runs from one side of the camera to the other, but with two separate shutters that start in the center of the camera and run towards the two sides of the sensor. Therefore, only half of the sensor could be used - at a speed of 100fps.

However, the practical method to maximize image acquisition speed with the confocal line-detection scheme has yet to be investigated. The most direct way seems to be to include a **line-sensor** in the detection path together with an additional scanning mirror that images the illuminated line onto the sensor and is coupled to the other scanning mirror in the illumination path. This method implies a very thin slit width given by the pixel size of the line-sensor and the magnification of the detection lens. In the confocal-line detection experiments performed so far, the width of the virtual pinhole was equal to more than one pixel line. While a thinner confocal-line leads to better background rejection and higher contrast (Figure 6.14), it also leads to lower signal strength. The effect is especially strong at larger beam penetration depth z for Gaussian beam illumination.

Another advantage of confocal-line detection lies in the **different limitation of the field-of-view**. In light-sheet microscopy, the image quality degrades along the illumination axis. Therefore, a rectangular field of view (where the long axis is the scan axis x) is more adapted to the properties of light-sheet microscopy images, whereas most image sensors have an aspect ratio that is close to 4:3. By using a line-sensor and a scanning mirror, one can record images as wide as the field of view of the detection lens allows, but only as long as the illumination beam is able to provide homogeneous image quality. For example using state-of-the-art line sensors (AViVA EM4, e2v) it could be possible to record images with dimensions 512×2048 at 85fps.

Confocal-line detection offers an additional degree of freedom as the detected line can be illuminated from the sides. This circumstance enables **innovative**

illumination schemes. One potential application is presented in Section 6.8, where sectioned Bessel beams are used for illumination to greatly improve optical sectioning and moreover make the axial resolution independent of the field-of-view. One could further improve the performance in the back of the sample by shaping the axial profile of the illumination beam [Čižmár and Dholakia, 2009]. One goal could be to compensate for the loss in on-axis-power of the beam by providing more power at larger penetration depths. In the scanned mode, the additional power forming the Bessel beams central lobe at large penetration depth z would create additional background at low z . For Gaussian beams the shape of the angular spectrum and the tight spatial confinement of the beam render such engineering of the axial beam profile impossible.

Alternatively to confocal-line detection, where the image is taken line-wise along x , one could employ a conventional camera and make use of a stripe that is very thin along the propagation axis of the illumination beam z but broad along x . This stripe can be illuminated by scanning a very short beam laterally to obtain an image that is wide along the scan axis x but short along the propagation axis of the illumination beam z . The complete image is obtained subsequently by taking several image slices along the z axis and subsequent fusion of these stripes. A similar approach has been presented by [Schacht et al., 2010, Buytaert and Dirckx, 2007] for Gaussian beam illumination. The advantage of using short Bessel beams lies in their self-reconstruction ability. Short Bessel beams feature a smaller relative amount of power in the ring system than longer ones but share equal self-reconstruction capabilities. The dependency of the susceptibility to scatterers on the NA has not been investigated for Gaussian beams yet, but it is likely that in contrast to Bessel beams, Gaussian beams at higher NA are more susceptible to scattering.

One of the most promising direct potential applications for confocal-line detection with Bessel-beam illumination, however, is to **fluorescence correlation spectroscopy (FCS)** [Magde et al., 1972]. This technique allows to locally probe molecular parameters inside a physiological three-dimensional environment by temporal auto-correlation of the signal recorded for a single point in the object. The technique strongly relies on a precise knowledge of the effective focal volume, i.e. the system point-spread function h_{sys} . It has recently been successfully implemented in a light-sheet microscope [Wohland et al., 2010], where it benefits from the good light efficiency and - in contrast to FCS with a confocal microscope - the possibility to probe more than one position in parallel. In SPIM-FCS each pixel of the camera acts as a pinhole and allows to measure the diffusion of a particle through effective the focal volume h_{sys} corresponding to that pixel. Based on the results of this thesis that showed that h_{sys} is more robust and position invariant for illumination with self-reconstructing beams, it is very probable that FCS might be improved by the combination. For example the range of samples that light-sheet-based FCS can be applied to might be increased. Moreover, FCS could be performed at positions deep within large samples that have been inaccessible so far. To obtain good temporal information on the diffusion of the molecules through the focal volume, light-sheet based FCS is usually performed on a very small field of view probing at maximum 4000 positions in parallel to be able to run the camera at maximum speed. A potential new setup would therefore be based on a line-confocal detection setup with a line-sensor that allows probing around 2000 positions along a line at a speed of 100kHz (in contrast to 500Hz at present) and would open up completely

new temporal resolution ranges to FCS. Comparable speeds have been achieved only very recently by using a special custom made detector array [Buchholz et al., 2012] that features only 1000 detectors.

8.2.3 *Two-Photon Excitation by Bessel beams: Outlook*

This thesis demonstrates that the image contrast for light-sheet microscopy with Bessel-beam illumination of strongly scattering media can also be increased by two-photon fluorescence excitation. Due to the quadratic dependency of the fluorescence on the beam's irradiance the Bessel ring system excites a lower relative amount of fluorescence.

The irradiance needed for sufficient strength of the TPE fluorescence signal is orders of magnitude higher than for linear excitation. Photo-toxicity and photo-damage caused by the strong irradiance have yet to be investigated in practice. While the analytical and numerical results obtained suggest that the absolute light dose is increased by a factor between 6 and 10 for Bessel beam illumination relative to conventional illumination it remains to be seen how non-linear effects affect the results in living samples for TPE.

In scattering media two-photon fluorescence excitation is especially susceptible as it relies on ultra-short pulses in the range of $\approx 150\text{fs}$. Scattering does not only deteriorate the spatial redistribution of light but also the temporal. It has yet to be investigated to which degree the nonlinear-fluorescence excitation by Bessel beams offers an improvement in the presence of strong dispersion of the pulsed illumination light [Johnson et al., 2003, Bruce et al., 1995]. Adaptive optics may also be able to improve the spatiotemporal shape of Bessel beams in scattering media. [Aulbach et al., 2011, McCabe et al., 2011, Katz et al., 2011].

On the other side, pulsed illumination may also offer interesting new possibility like time-gating, where scattered photons that necessarily travel a longer distance to reach the same point as ballistic photons can be filtered out temporally. Moreover, by illuminating the sample from different sides so that two pulses only overlap in a certain region might offer new potential ways to improve image quality. A special method is two-color-two-photon excitation (TCTPE) which was presented for confocal microscopy [Wang et al., 2008] and confocal theta microscopy [Cambaliza and Saloma, 2000]. In TCTPE, pulsed light at two different wavelengths, λ_1 and λ_2 , is used to generate TPE only in the region, where the foci of the two wavelengths overlap. The advantage of this approach lies in the fact that one can choose the wavelengths $\lambda_1 < \lambda_{\text{lin}}/2$ below and $\lambda_2 > \lambda_{\text{lin}}/2$ above half the linear excitation wavelength λ_{lin} . In this case, light of neither wavelength alone is able to excite TPE. Therefore, higher out-of-focus irradiance is possible without significant fluorescence generation as fluorescence is excited only the region of overlap. One could imagine the combination of different self-reconstructing beams to further increase resolution or even the robustness to perturbation [Blanca and Saloma, 2001].

COMPARISON OF LINE WISE DETECTION AGAINST
PLANE-WISE DETECTION

The image is given by

$$p(\mathbf{r}) = (c(\mathbf{r}) \cdot h_{\text{LS}}(\mathbf{r})) * h_{\text{det}}(\mathbf{r}). \quad (\text{A.1})$$

If the light-sheet

$$h_{\text{scan}}(\mathbf{r}) = \frac{1}{T} \int_0^T h_{\text{SB}}(\mathbf{r} - \mathbf{b}(t)) dt. \quad (\text{A.2})$$

is generated by continuous sweeping of the beam and wide-field detection, the image is

$$p(\mathbf{r}) = \left(c(\mathbf{r}) \cdot \frac{1}{T} \int_0^T h_{\text{SB}}(\mathbf{r} - \mathbf{b}(t)) dt \right) * h_{\text{det}}(\mathbf{r}) \quad (\text{A.3})$$

$$= \frac{1}{T} \int_0^T [(c(\mathbf{r}) \cdot h_{\text{SB}}(\mathbf{r} - \mathbf{b}(t))) * h_{\text{det}}(\mathbf{r})] dt \quad (\text{A.4})$$

where usually $b(t) = (v_c \cdot t, 0, 0)$. Discretization of the illumination beam sweep

$$\begin{aligned} h_{\text{LS}}(\mathbf{r}) &= \frac{1}{T} \int_0^T h_{\text{SB}}(x - v_c \cdot t, y, z) dt \\ &\approx \frac{1}{T} \sum_{i=0}^N h_{\text{SB}}(x - v_c \cdot \Delta t \cdot i, y, z) \Delta t \end{aligned} \quad (\text{A.5})$$

with $\mathbf{b}(t_i) = (v_c \cdot \Delta t \cdot i, 0, 0)$ means

$$\begin{aligned} p(\mathbf{r}) &= \left(c(\mathbf{r}) \cdot \frac{1}{T} \sum_{i=0}^N h_{\text{SB}}(\mathbf{r} - \mathbf{b}(t_i)) \Delta t \right) * h_{\text{det}}(\mathbf{r}) \\ &= \frac{1}{T} \sum_{i=0}^N [(c(\mathbf{r}) \cdot h_{\text{SB}}(\mathbf{r} - \mathbf{b}(t_i))) * h_{\text{det}}(\mathbf{r})] \Delta t \\ &= \sum_{i=0}^N p_i(\mathbf{r}) \end{aligned} \quad (\text{A.6})$$

where $p_i(\mathbf{r}) = (c(\mathbf{r}) \cdot h_{\text{ill}}(\mathbf{r} - \mathbf{b}(t_i))) * h_{\text{det}}(\mathbf{r})$ is the image of the beam at every position. The final image can therefore easily be generated from the single images recorded for confocal-line detection. Discretization of the illumination beam sweep is also employed for computational approaches to image formation (§§ 6.9.3, 7.3).

THE BEAM-PROPAGATION METHOD

B.1 THEORETICAL BACKGROUND

In this section, the beam-propagation method (Feit et al. [1976], Feit and Fleck Jr. [1978]) which was used for the simulations is explained. A derivation is presented and the limitation of the method are discussed. The field of the beam $E(x, y)$ computed in discrete steps along the propagation axis z . The field distribution $E_i(x, y)$ is propagated along a slice with thickness δz which is characterized by a refractive index distribution $n_i(x, y)$. The beam's field distribution in the next layer is therefore

$$E_{i+1}(x, y) = E_i(x, y) \cdot P_i(x, y, k_x, k_y) \quad (\text{B.1})$$

with the full propagator

$$P_i(x, y, k_x, k_y) = \exp \left\{ i\delta z \sqrt{n_i(x, y)^2 \cdot k_0^2 - k_r^2} \right\} \quad (\text{B.2})$$

which depends on the spatial coordinates x, y as well as the spatial frequencies k_x, k_y with $k_r = \sqrt{k_x^2 + k_y^2}$ being the radial component of the wave-vector $\mathbf{k} = n\mathbf{k}_0$. If the refractive index is independent of x, y there remains only the dependency on k_r and P can simply be multiplied with the spectrum of the field

$$\tilde{E}_i(k_x, k_y) = \iint E_i(x, y) e^{-i(k_x x + k_y y)} dx dy \quad (\text{B.3})$$

that is simply obtained by 2D-Fourier transformation. The field in the next plane $i + 1$ is then

$$E_{i+1}(x, y) = \tilde{E}_i(k_x, k_y) \cdot P_i(k_x, k_y). \quad (\text{B.4})$$

This *propagator approach* can be used to compute the beam profiles in homogeneous environments, for example in Chapter 3.

The idea behind the beam propagation method is to decompose the refractive index distribution $n_i(x, y)$ into an average value \bar{n} and a (small) position dependent differences $\delta n_i(x, y)$. The propagator then becomes

$$P_i(x, y, k_x, k_y) = \exp \left\{ i\delta z \sqrt{(\bar{n} + \delta n(x, y))^2 \cdot k_0^2 - k_r^2} \right\}. \quad (\text{B.5})$$

It is possible to separate P_i into a term that depends only on spatial coordinates x, y and one that depends only on spatial frequencies k_x, k_y by using two assumptions:

1. Small local deviations in the refractive index $\delta n_i(x, y)$ from the mean value \bar{n} .
2. Paraxiality: $k_r^2 \ll k_z^2$

so that

$$P_i^{\text{BPM}}(x, y, k_x, k_y) \approx \exp \{i\delta z \cdot \delta n(x, y) \cdot k_0\} \cdot \exp \left\{ i\delta z \cdot \sqrt{(\bar{n} \cdot k_0)^2 - k_r^2} \right\}. \quad (\text{B.6})$$

where the dependency on spatial coordinates and spatial frequencies are separated. It is now possible to compute the beam propagation through inhomogeneous media by

$$E_{i+1}(x, y) = \exp \{i\delta z \cdot \delta n_i(x, y) \cdot k_0\} \cdot \mathcal{FT} \left\{ \tilde{E}_i(k_x, k_y) \cdot \exp \left\{ i\delta z \cdot \sqrt{(\bar{n} \cdot k_0)^2 - k_r^2} \right\} \right\}. \quad (\text{B.7})$$

Because only 2-dimensional arrays are used that are transformable into each other by Fourier transforms, a process that is highly optimized, the computational cost is greatly minimized by the assumptions made. Higher precision without these approximations can be achieved by the (Vector) Wave Propagation Method developed by [Brenner and Singer \[1993\]](#) and [Fertig and Brenner \[2010\]](#).

B.2 ESTIMATION OF THE ERRORS ARISING FROM APPROXIMATIONS

How large are the deviations arising from the assumptions that lead to eqn B.6? The transition from eqn B.5 to B.6 possible due to

$$k_{z,\text{acc}} \rightarrow k_{z,\text{approx}} \quad (\text{B.8})$$

The relative error in the computation of the phase made by the approximation is

$$\phi_{\text{approx}}/\phi_{\text{acc}} = \frac{\delta n(x, y)k_0 + \sqrt{(\bar{n} \cdot k_0)^2 - k_r^2}}{\sqrt{(\bar{n} \cdot k_0)^2 + (\delta n(x, y)k_0)^2 - k_r^2}}. \quad (\text{B.9})$$

For a given set of change in refractive index, average refractive index, and wavelength, the error is dependent on the radial component k_r of the wave-vector so that the different components of the angular spectrum run out of phase due to the approximation. An example is shown in Figure B.1. It can be seen that the phase $\phi_{\text{acc}} = k_z \cdot \delta z$ is always underestimated by the approximation. For $\delta n \leq 0.3$ which corresponds approximately to the refractive index difference of water ($n = 1.33$) and polystyrene ($n = 1.61$) the error is smaller than $1/0.98=2\%$ for values of k_r corresponding to NAs smaller than 0.5. A considerable field strength $\tilde{E}(k_r > k_0 NA)$ may build up nevertheless along the propagation through the medium because scattering of the beam leads to a redistribution of the spectral field $\tilde{E}(k_r)$ to higher k_r .

The main deficiencies of the beam propagation method for the purpose of simulating the propagation of light through scattering samples are therefore different from those that arise purely from the approximation itself. The most important ones are:

First, backward scattering of light is not taken into account, which is a fundamental problem which is discussed in Section B.3.

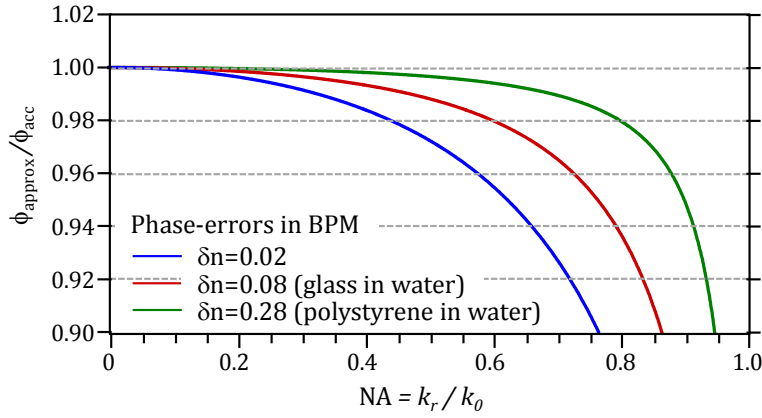


Figure B.1: Relative error of the phase computed by the BPM.

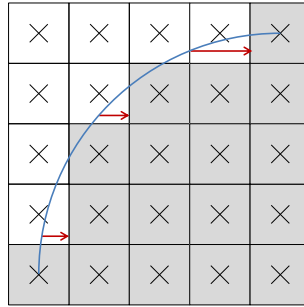


Figure B.2: Sketch of the error arising from the discretization of a sphere.

The second problem is purely technical and lies in the discretization of the simulated volume. If the simulation is used to understand the propagation through large volumes while at the same time scattering by relatively small particles is of interest, the discretization of the typically spherical particles might lead to larger errors than the method itself. The error arising from discretization can be estimated to be

$$s_\phi \approx \delta n \cdot k_0 \cdot 0.5 \text{pixel} \quad (\text{B.10})$$

on average (compare Fig. B.2). Consider for example the situation where the wavelength $\lambda_0 = 0.5\mu\text{m}$ in water corresponds to 4 pixels ($\delta = 94\text{nm}$) and is scattered by spheres with a radius of 4 pixels and a refractive index difference of $\delta n = 0.28$. This results in $s_\phi = 0.16$ for a maximum phase shift by the sphere corresponding to $\delta\phi = \delta n \cdot k_0 \cdot 8 \cdot \delta = 2.65$. However, due to the low computational effort required by BPM-simulations a finer discretization can be chosen which reduces the problems that arise from discretization.

B.3 ERRORS ARISING FROM NEGLIGENCE OF BACKWARD SCATTERING

As derived in detail in [Bohren and Huffman](#) using Mie-Theory, the scattering cross-section of a sphere is

$$C_{\text{sca}} = \frac{2\pi}{k^2} \sum_{n=1}^{\infty} (2n+1) \left(|a_n|^2 + |b_n|^2 \right), \quad (\text{B.11})$$

and the back scattering efficiency is

$$C_{\text{back}} = \frac{\pi^2}{k^2} \left| \sum_n (2n+1) (-1)^n (a_n - b_n) \right|^2. \quad (\text{B.12})$$

The coefficients are

$$a_n = \frac{m\psi_n(mx)\psi'_n(x) - \psi_n(x)\psi'_n(mx)}{m\psi_n(mx)\xi'_n(x) - \xi_n(x)\psi'_n(mx)} \quad (\text{B.13})$$

$$b_n = \frac{\psi_n(mx)\psi'_n(x) - \psi_n(x)\psi'_n(mx)}{\psi_n(mx)\xi'_n(x) - \xi_n(x)\psi'_n(mx)} \quad (\text{B.14})$$

where $x = k \cdot a$ with a being the radius of the particle with relative refractive index $m = n_{\text{scat}}/n_{\text{BG}}$. The Riccati-Bessel functions $\psi_n(\rho) = \rho j_n(\rho)$ and $\xi_n(\rho) = \rho h_n^{(1)}(\rho)$ with the spherical Bessel function $j_n^{(1)}$ and the spherical Hankel function $h_n^{(1)}$ are used.

The scattering anisotropy parameter is given by the average cosine of the scattering angle, $g = \langle \cos \theta \rangle$, or by

$$g = \frac{\pi}{k^2} \frac{1}{C_{\text{sca}}} \int_{-\pi}^{\pi} |S_1|^2 + |S_2|^2 \cos \theta d\theta. \quad (\text{B.15})$$

S_1 and S_2 are the matrix elements that define the amplitudes of the horizontally and vertically polarized scattered field, respectively. They are computed by

$$S_1 = \sum_n \frac{2n+1}{n(n+1)} (a_n \tau_n + b_n \pi_n) \quad (\text{B.16})$$

$$S_2 = \sum_n \frac{2n+1}{n(n+1)} (a_n \tau_n - b_n \pi_n) \quad (\text{B.17})$$

with the functions $\pi_n = P_n^l / \sin \theta$ and $\tau_n = dP_n^l / d\theta$ where P_n^l is the associated Legendre function.

For the numerical simulations that were used to quantify the directional propagation stability in Section 4.2, glass spheres with a refractive index of $n = 1.41$ and diameters of $d = 2\mu\text{m}$ and $d = 4\mu\text{m}$ were used. As shown in Table 3, the back-scattering cross-section of the spheres is very small in absolute terms and also in comparison to the total scattering cross-section C_{sca} . As mentioned before, the beam-propagation method cannot account for back-scattering, but at the sizes of the spheres that were used, this shortcoming should have very limited impact on the results that were obtained.

$d = 2\mu\text{m}$	$\lambda_0 = 488\text{nm}$	$\lambda_0 = 800\text{nm}$
n_{scat}	1.41	1.41
$x = k \cdot a$	17.1	10.4
C_{sca}	$5.51\mu\text{m}^2$	$2.35\mu\text{m}^2$
C_{back}	$2.1 \cdot 10^{-3}\mu\text{m}^2$	$18 \cdot 10^{-3}\mu\text{m}^2$
$C_{\text{back}}/C_{\text{sca}}$	0.039%	0.78%
g	0.985	0.970

(a) Diameter $d = 2\mu\text{m}$

$d = 4\mu\text{m}$	$\lambda_0 = 488\text{nm}$	$\lambda_0 = 800\text{nm}$
n_{scat}	1.41	1.41
$x = k \cdot a$	34.2	20.9
C_{sca}	$42.1\mu\text{m}^2$	$29.2\mu\text{m}^2$
C_{back}	$33 \cdot 10^{-3}\mu\text{m}^2$	$13.6 \cdot 10^{-3}\mu\text{m}^2$
$C_{\text{back}}/C_{\text{sca}}$	0.08%	0.05%
g	0.990	0.988

(b) Diameter $d = 4\mu\text{m}$

Table 3: Scattering properties of silica spheres of different sizes in water.

BIBLIOGRAPHY

- A. Abbott. Biology's new dimension. *Nature*, 424, 2003. (Cited on page 1.)
- M. Agour, E. Kolenovic, C. Falldorf, and C. von Kopylow. Suppression of higher diffraction orders and intensity improvement of optically reconstructed holograms from a spatial light modulator. *J. Opt. A*, 11(10):105405, 2009. (Cited on page 59.)
- M. A. Albota, C. Xu, and W. W. Webb. Two-Photon Fluorescence Excitation Cross Sections of Biomolecular Probes from 690 to 960 nm. *Appl. Opt.*, 37(31):7352–6, 1998. (Cited on page 132.)
- M. Anguiano-Morales, A. Martínez, M. Iturbe-Castillo, S. Chávez-Cerda, and N. Alcalá-Ochoa. Self-healing property of a caustic optical beam. *Appl. Opt.*, 46(34):8284–90, 2007a. (Cited on pages 14 and 73.)
- M. Anguiano-Morales, M. M. Méndez-Otero, M. D. Iturbe-Castillo, and S. Chávez-Cerda. Conical dynamics of Bessel beams. *Opt. Eng.*, 46(7):078001, 2007b. (Cited on pages 14 and 73.)
- A. Arrenberg, D. Y. R. Stainier, H. Baier, and J. Huisken. Optogenetic Control of Cardiac Function. *Science*, 330(11):971, 2010. (Cited on pages 11 and 159.)
- A. Aubry and A. Derode. Random matrix theory applied to acoustic backscattering and imaging in complex media. *Phys. Rev. Lett.*, 102:084301, Feb 2009. (Cited on page 162.)
- A. Aubry, A. Derode, P. Roux, and A. Tourin. Coherent backscattering and far-field beamforming in acoustics. *J. Ac. Soc. Am.*, 121(1):70–77, 2007. (Cited on page 162.)
- J. Aulbach, B. Gjonaj, P. Johnson, A. P. Mosk, and A. Lagendijk. Control of Light Transmission through Opaque Scattering Media in Space and Time. *Phys. Rev. Lett.*, 106(10):5–8, 2011. (Cited on page 165.)
- E. Baumgart and U. Kubitschek. Scanned light sheet microscopy with confocal slit detection. *Opt. Express*, 20(19):21805, 2012. (Cited on pages 122 and 163.)
- Y. Baykal. Log-amplitude and phase fluctuations of higher-order annular laser beams in a turbulent medium. *J. Opt. Soc. Am. A*, 22(4):672–9, 2005. (Cited on page 73.)
- E. Beaurepaire, M. Oheim, and J. Mertz. Ultra-deep two-photon fluorescence excitation in turbid media. *Opt. Commun.*, 188:25–29, 2001. (Cited on page 132.)
- T. Bernas, M. Zarebski, R. R. Cook, J. W. Dobrucki, and P. R. Cook. Minimizing photobleaching during confocal microscopy of fluorescent probes bound to chromatin: role of anoxia and photon flux. *J. Microsc.*, 215(Pt 3):281–96, 2004. (Cited on page 10.)
- E. Betzig, G. H. Patterson, R. Sougrat, O. W. Lindwasser, S. Olenych, J. S. Bonifacino, M. W. Davidson, J. Lippincott-Schwartz, and H. F. Hess. Imaging intracellular fluorescent proteins at nanometer resolution. *Science*, 313(5793):1642–5, 2006. (Cited on page 7.)
- C. M. Blanca and C. Saloma. Two-color excitation fluorescence microscopy through highly scattering media. *Appl. Opt.*, 40(16):2722–9, 2001. (Cited on page 165.)
- M. Bock, S. K. Das, and R. Grunwald. Programmable ultrashort-pulsed flying images. *Opt. Express*, 17(9):7465–78, Apr 2009. (Cited on page 144.)
- C. F. Bohren and D. R. Huffman. *Absorption and Scattering of Light by Small Particles*. WILEY VCH, Weinheim. (Cited on page 171.)

- M. J. Booth and T. Wilson. Strategies for the compensation of specimen-induced spherical aberration in confocal microscopy of skin. *J. Microsc.*, 200(1):68–74, 2000. (Cited on page 76.)
- M. J. Booth, M. A. A. Neil, and T. Wilson. Aberration correction for confocal imaging in refractive-index-mismatched media. *J. Microsc.*, 192(2):90–98, 1998. (Cited on page 76.)
- M. J. Booth, M. A. A. Neil, R. Juskaitis, and T. Wilson. Adaptive aberration correction in a confocal microscope. *Proc. Natl. Acad. Sci. USA*, 99(9):5788–92, 2002. (Cited on pages 8 and 76.)
- M. Born and E. Wolf. *Principles of Optics*. Press, Cambridge University, 7th ed. edition, 1999. (Cited on page 41.)
- E. Botcherby, R. Juskaitis, and T. Wilson. Scanning two photon fluorescence microscopy with extended depth of field. *Opt. Commun.*, 268(2):253–260, 2006. (Cited on page 14.)
- E. Botcherby, M. J. Booth, R. Juskaitis, and T. Wilson. Real-time extended depth of field microscopy. *Opt. Express*, 16(26):21843–8, 2008. (Cited on page 14.)
- Z. Bouchal. Resistance of nondiffracting vortex beam against amplitude and phase perturbations. *Opt. Commun.*, 210(3-6):155–164, 2002. (Cited on pages 14 and 74.)
- Z. Bouchal, J. Wagner, and M. Chlup. Self-reconstruction of a distorted nondiffracting beam. *Opt. Commun.*, 151(4-6):207–11, 1998. (Cited on pages 14, 43, 73, 74, and 111.)
- S. Bradburn, W. T. Cathey, and E. R. Dowski. Realizations of focus invariance in optical-digital systems with wave-front coding. *Appl. Opt.*, 36(35):9157–66, 1997. (Cited on page 15.)
- G. J. Brakenhoff, G. W. H. Wurpel, K. Jalink, L. Oomen, L. Brocks, and J. M. Zwier. Characterization of sectioning fluorescence microscopy with thin uniform fluorescent layers: Sectioned Imaging Property or SIPcharts. *J. Microsc.*, 219(3):122–32, 2005. (Cited on page 7.)
- K.-H. Brenner and W. Singer. Light propagation through microlenses: a new simulation method. *Appl. Opt.*, 32(26):4984–4988, 1993. (Cited on pages 75 and 170.)
- T. Breuninger, K. Greger, and E. H. K. Stelzer. Lateral modulation boosts image quality in single plane illumination fluorescence microscopy. *Opt. Lett.*, 32(13):1938–40, 2007. (Cited on pages 13 and 126.)
- J. Broky, G. A. Siviloglou, A. Dogariu, and D. N. Christodoulides. Self-healing properties of optical Airy beams. *Opt. Express*, 16(17):12880–91, 2008. (Cited on pages 15, 73, and 74.)
- N. C. Bruce, F. E. Schmidt, J. C. Dainty, N. P. Barry, S. C. Hyde, and P. M. French. Investigation of the temporal spread of an ultrashort light pulse on transmission through a highly scattering medium. *App. Opt.*, 34(25):5823–8, 1995. (Cited on page 165.)
- J. Buchholz, J. W. Krieger, G. Mocsár, B. Kreith, E. Charbon, G. Vámosi, U. Keschull, and J. Langowski. Fpga implementation of a 32x32 autocorrelator array for analysis of fast image series. *Opt. Express*, 20(16):17767–82, 2012. (Cited on page 165.)
- J. A. N. Buytaert and J. J. J. Dirckx. Design and quantitative resolution measurements of an optical virtual sectioning three-dimensional imaging technique for biomedical specimens, featuring two-micrometer slicing resolution. *J. Biomed. Opt.*, 12(1):014039, 2007. (Cited on pages 12, 39, 42, and 164.)

- M. O. Cambaliza and C. Saloma. Advantages of two-color excitation fluorescence microscopy with two confocal excitation beams. *Opt. Commun.*, 184:25–35, 2000. (Cited on page 165.)
- F. Cella Zanacchi, Z. Lavagnino, M. P. Donnorso, A. Del Bue, L. Furia, M. Faretta, and A. Diaspro. Live-cell 3D super-resolution imaging in thick biological samples. *Nature Meth.*, 8(12):1047–1050, 2011. (Cited on page 160.)
- A. Chong, W. H. Renninger, D. N. Christodoulides, and F. W. Wise. Airy-Bessel wave packets as versatile linear light bullets. *Nature Photon.*, 4:103–6, 2010. (Cited on page 14.)
- J. A. Conchello and J. W. Lichtman. Optical sectioning microscopy. *Nature Meth.*, 2(12):920–931, 2005. (Cited on page 7.)
- D. B. Conkey, A. Caravaca-Aguirre, and R. Piestun. High-speed scattering medium characterization with application to focusing light through turbid media. *Opt. Express*, 20(2):1733–40, 2012. (Cited on page 162.)
- J. A. Davis, G. Jarod, and D. Cottrell. Diffraction-free beams generated with programmable spatial light modulators. *Appl. Opt.*, 23(31):698, 1993. (Cited on page 14.)
- W. Denk, J. H. Strickler, and W. W. Webb. Two-photon laser scanning fluorescence microscopy. *Science*, 248:73–76, 1990. (Cited on pages 7 and 131.)
- J. A. Dijkstra, F. Rietz, K. A. Lorincz, M. van Hecke, and W. Losert. Refractive index matched scanning of dense granular materials. *Rev. Sci. Inst.*, 83(1):011301, 2012. (Cited on page 92.)
- H.-U. Dodt, U. Leischner, A. Schierloh, N. Jährling, C. P. Mauch, K. Deininger, J. M. Deussing, M. Eder, W. Zieglgänsberger, and K. Becker. Ultramicroscopy: three-dimensional visualization of neuronal networks in the whole mouse brain. *Nature Meth.*, 4(4):331–6, 2007. (Cited on pages 11, 12, 13, 39, 42, 84, and 93.)
- G. Donnert, C. Eggeling, and S. W. Hell. Major signal increase in fluorescence microscopy through dark-state relaxation. *Nature Meth.*, 4(1):81–86, 2007. (Cited on page 93.)
- E. R. Dowski and W. T. Cathey. Extended depth of field through wave-front coding. *Appl. Opt.*, 34(11):1859–66, 1995. (Cited on page 74.)
- A. Dubietis, E. Kucinskas, G. Tamosauskas, E. Gaizauskas, M. A. Porras, and P. Di Trapani. Self-reconstruction of light filaments. *Opt. Lett.*, 29(24):2893–5, 2004. (Cited on page 14.)
- J. Durnin, J. J. M. jr, and J. H. Eberly. Diffraction-Free Beams. *Phys. Rev. Lett.*, 58(15):1499–1501, 1987. (Cited on pages 14 and 43.)
- C. J. Engelbrecht and E. H. K. Stelzer. Resolution enhancement in a light-sheet-based microscope (SPIM). *Opt. Lett.*, 31(10):1477–9, 2006. (Cited on page 21.)
- T. Ersoy, B. Yalizay, and S. Akturk. Self-reconstruction of diffraction-free and accelerating laser beams in scattering media. *J. Quant. Spec. Rad. Trans.* (Cited on pages 73 and 74.)
- F. O. Fahrbach and A. Rohrbach. Light-sheet microscopy with field-of-view independent optical sectioning using Sectioned Bessel beams. *to be published*, a. (Cited on pages 157 and 158.)
- F. O. Fahrbach and A. Rohrbach. Light-sheet microscopy in thick scattering media using scanned Bessel beams and two-photon fluorescence excitation. *to be published*, b. (Cited on page 158.)

- F. O. Fahrbach and A. Rohrbach. A line scanned light-sheet microscope with phase shaped self-reconstructing beams. *Opt. Express*, 18(23):24229–24244, 2010. (Cited on page 157.)
- F. O. Fahrbach and A. Rohrbach. Propagation stability of self-reconstructing Bessel beams enables contrast-enhanced imaging in thick media. *Nature Commun.*, 3:632, 2012. (Cited on pages 104, 109, 123, and 158.)
- F. O. Fahrbach, P. Simon, and A. Rohrbach. Microscopy with self-reconstructing beams. *Nature Photon.*, 4:780–785, 2010. (Cited on pages 26, 69, 71, and 158.)
- M. D. Feit and J. A. Fleck Jr. Light propagation in graded-index optical fibers. *Appl. Opt.*, 17(24):3990–8, Dec 1978. (Cited on pages 75 and 169.)
- M. D. Feit, J. Morris, and J. A. Fleck Jr. Time-dependent propagation of high energy laser beams through the atmosphere. *Appl. Phys.*, 10:129–160, 1976. (Cited on pages 75 and 169.)
- M. Fertig and K.-H. Brenner. Vector wave propagation method. *J. Opt. Soc. Am. A*, 27(4):709–717, Apr 2010. (Cited on page 170.)
- C. H. Foyer, M. Leiardais, and K. J. Kunert. Special review Photooxidative stress in plants. *Physiologia Plantarum*, (Asada), 1994. (Cited on page 9.)
- E. Fuchs, J. Jaffe, R. Long, and F. Azam. Thin laser light sheet microscope for microbial oceanography. *Opt. Express*, 10(2):145–154, 2002. (Cited on pages 11, 42, and 84.)
- S. Fujiwara. Optical Properties of Conic Surfaces. I. Reflecting Cones. *J. Opt. Soc. Am.*, 575(3):287–92, 1962. (Cited on page 14.)
- V. Garcés-Chávez, D. McGloin, H. Melville, W. Sibbett, and K. Dholakia. Simultaneous micromanipulation in multiple planes using a self-reconstructing light beam. *Nature*, 419(6903):145–7, 2002. (Cited on pages 15, 73, and 74.)
- J. García-Márquez, V. López, A. González-Vega, and E. Noé. Flicker minimization in an LCoS spatial light modulator. *Opt. Express*, 20(8):8011–16, 2012. (Cited on page 31.)
- J. M. Girkin, S. Poland, and A. J. Wright. Adaptive optics for deeper imaging of biological samples. *Curr. Opin. Biotech.*, 20(1):106–10, 2009. (Cited on page 8.)
- K. Greger, J. Swoger, and E. H. K. Stelzer. Basic building units and properties of a fluorescence single plane illumination microscope. *J. Mod. Opt.*, 78(2):023705, 2007. (Cited on page 33.)
- M. Gu and C. J. R. Sheppard. Three-dimensional Imaging in Confocal Fluorescent Microscopy with Annular Lenses. *J. Mod. Opt.*, 38(11):2247–2263, 1991. (Cited on page 14.)
- M. Gu and C. J. R. Sheppard. Effects of Annular Pupils on Confocal Fluorescent Imaging. *J. Mod. Opt.*, 39(9):1883–1896, 1992. (Cited on page 14.)
- M. Gu, T. Tannous, and C. J. R. Sheppard. Effect of an annular pupil on confocal imaging through highly scattering media. *Opt. Lett.*, 21(5):312–4, 1996. (Cited on page 14.)
- M. G. Gustafsson. Surpassing the lateral resolution limit by a factor of two using structured illumination microscopy. *J. Microsc.*, 198(2):82–7, 2000. (Cited on pages 7 and 160.)
- M. G. Gustafsson. Nonlinear structured-illumination microscopy: wide-field fluorescence imaging with theoretically unlimited resolution. *Proc. Natl Acad. Sci. USA*, 102(37):13081–6, 2005. (Cited on page 7.)

- J. C. Gutiérrez-Vega, M. D. Iturbe-Castillo, and S. Chávez-Cerda. Alternative formulation for invariant optical fields: Mathieu beams. *Opt. Lett.*, 25(20):1493–5, 2000. (Cited on page 45.)
- J. C. Gutiérrez-Vega, M. D. Iturbe-Castillo, G. A. Ramirez, E. Tepichín, R. M. Rodríguez-Dagnino, S. Chávez-Cerda, and G. H. C. New. Experimental demonstration of optical Mathieu beams. *Opt. Commun.*, 195(8):35–40, 2001. (Cited on page 45.)
- J. C. Gutiérrez-Vega, R. M. Rodríguez-Dagnino, M. A. Meneses-Nava, and S. Chávez-Cerda. Mathieu functions, a visual approach. *Am. J. Phys.*, 71(3):233, 2003. (Cited on page 45.)
- N. Hagen, L. Gao, and T. S. Tkaczyk. Quantitative sectioning and noise analysis for structured illumination microscopy. *Opt. Express*, 20(1):403–413, Jan 2012. (Cited on page 126.)
- R. D. L. Hanes, M. C. Jenkins, and S. U. Egelhaaf. Combined holographic-mechanical optical tweezers: construction, optimization, and calibration. *Rev. Sci. Instr.*, 80(8):083703, 2009. (Cited on page 31.)
- S. W. Hell and J. Wichmann. Breaking the diffraction resolution limit by stimulated emission: stimulated-emission-depletion fluorescence microscopy. *Opt. Lett.*, 19(11):780–2, 1994. (Cited on page 7.)
- S. W. Hell, P. E. Hänninen, A. Kuusisto, M. Schrader, and E. Soini. Annular aperture two-photon excitation microscopy. *Opt. Commun.*, 117:20–24, 1995. (Cited on page 14.)
- F. Helmchen and W. Denk. Deep tissue two-photon microscopy. *Nature Meth.*, 2(12):932–940, 2005. (Cited on page 132.)
- S. T. Hess, T. P. K. Girirajan, and M. D. Mason. Ultra-high resolution imaging by fluorescence photoactivation localization microscopy. *Biophys. J.*, 91(11):4258–72, 2006. (Cited on page 7.)
- T. E. Holekamp, D. Turaga, and T. E. Holy. Fast three-dimensional fluorescence imaging of activity in neural populations by objective-coupled planar illumination microscopy. *Neuron*, 57(5):661–72, 2008. (Cited on pages 11 and 84.)
- C.-L. Hsieh, Y. Pu, R. Grange, G. Laporte, and D. Psaltis. Imaging through turbid layers by scanning the phase conjugated second harmonic radiation from a nanoparticle. *Opt. Express*, 18(20):20723–31, 2010. (Cited on page 76.)
- D. Huang, E. A. Swanson, C. P. Lin, J. S. Schuman, W. G. Stinson, W. Chang, M. R. Hee, T. Flotte, K. Gregory, C. A. Puliafito, and J. G. Fujimoto. Optical coherence tomography. *Science*, 254(5035):1178–1181, 1991. (Cited on pages 8 and 160.)
- J. Huisken and D. Y. R. Stainier. Even fluorescence excitation by multidirectional selective plane illumination microscopy (mSPIM). *Opt. Lett.*, 32(17):2608–10, 2007. (Cited on pages 13, 42, 93, and 159.)
- J. Huisken and D. Y. R. Stainier. Selective plane illumination microscopy techniques in developmental biology. *Development*, 136(12):1963–75, 2009. (Cited on page 11.)
- J. Huisken, J. Swoger, F. D. Bene, J. Wittbrodt, and E. H. K. Stelzer. Live Embryos by Selective Plane Illumination Microscopy. *Science*, 305:1007–9, 2004. (Cited on pages 11, 33, 39, 42, 84, and 157.)
- A. Jesacher, C. Maurer, A. Schwaighofer, S. Bernet, and M. Ritsch-Marte. Near-perfect hologram reconstruction with a spatial light modulator. *Opt. Express*, 16(4):2597–603, 2008. (Cited on page 58.)

- N. Ji, D. E. Milkie, and E. Betzig. Adaptive optics via pupil segmentation for high-resolution imaging in biological tissues. *Nature Meth.*, 7(2):141–7, 2010. (Cited on page 76.)
- P. Johnson, A. Imhof, B. Bret, J. Rivas, and A. Lagendijk. Time-resolved pulse propagation in a strongly scattering material. *Phys. Rev. E*, 68(1):1–9, 2003. (Cited on page 165.)
- M.-J. Jou, S.-B. Jou, H.-M. Chen, C.-H. Lin, and T.-I. Peng. Critical Role of Mitochondrial Reactive Oxygen Species Formation in Visible Laser Irradiation-Induced Apoptosis in Rat Brain. *J. Biomed. Science*, 3283016(9):507–516, 2002. (Cited on page 9.)
- S. Kalchmair, N. Jährling, K. Becker, and H.-U. Dodt. Image contrast enhancement in confocal ultramicroscopy. *Opt. Lett.*, 35(1):79–81, 2010. (Cited on page 13.)
- O. Katz, E. Small, Y. Bromberg, and Y. Silberberg. Focusing and compression of ultrashort pulses through scattering media. *Nature Photon.*, 5(6):372–7, 2011. (Cited on page 165.)
- A. Kaufmann, M. Mickoleit, M. Weber, and J. Huisken. Multilayer mounting enables long-term imaging of zebrafish development in a light sheet microscope. *Development*, 139(17):3242–7, 2012. (Cited on pages 10 and 36.)
- P. J. Keller, F. Pampaloni, and E. H. K. Stelzer. Life sciences require the third dimension. *Curr. Opin. Cell Biol.*, 18(1):117–24, 2006. (Cited on page 10.)
- P. J. Keller, A. D. Schmidt, J. Wittbrodt, and E. H. K. Stelzer. Reconstruction of Zebrafish Early Embryonic Development by Scanned Light Sheet Microscopy. *Science*, 322:1065–1069, 2008. (Cited on pages 11, 39, 84, and 159.)
- P. J. Keller, A. D. Schmidt, A. Santella, K. Khairy, Z. Bao, J. Wittbrodt, and E. H. K. Stelzer. Fast, high-contrast imaging of animal development with scanned light sheet-based structured-illumination microscopy. *Nature Meth.*, 7(8):637–42, 2010. (Cited on pages 9, 13, and 126.)
- D. H. Kelly. Jo Stimulus Patterns for Visual Research. *J. Opt. Soc. Am.*, 50(11):1115–1116, 1960. (Cited on page 14.)
- U. Krzic, S. Gunther, T. E. Saunders, S. J. Streichan, and L. Hufnagel. Multiview light-sheet microscope for rapid in toto imaging. *Nature Meth.*, 9(7):xx, 2012. (Cited on pages 93, 159, and 161.)
- H. K. Lee, M. S. Uddin, S. Sankaran, S. Hariharan, and S. Ahmed. A field theoretical restoration method for images degraded by non-uniform light attenuation : an application for light microscopy. *Opt. Express*, 17(14):11294–308, 2009. (Cited on page 93.)
- U. Leischner, A. Schierloh, W. Ziegler, and H.-U. Dodt. Formalin-induced fluorescence reveals cell shape and morphology in biological tissue samples. *PLoS ONE*, 5(4):e10391, 04 2010. (Cited on page 93.)
- A. Li, H. Gong, B. Zhang, Q. Wang, C. Yan, J. Wu, Q. Liu, S. Zeng, and Q. Luo. Micro-optical sectioning tomography to obtain a high-resolution atlas of the mouse brain. *Science*, 330(6009):1404–8, 2010. (Cited on page 162.)
- J. W. Y. Lit and R. Tremblay. Focal depth of a transmitting axicon. *J. Opt. Soc. Am.*, 63(4):445, 1973. (Cited on page 14.)
- A. Lizana, I. Moreno, C. Jemmi, A. Márquez, J. Campos, and M. J. Yzuel. Time-resolved Mueller matrix analysis of a liquid crystal on silicon display. *Appl. Opt.*, 47(23):4267–74, 2008. (Cited on page 31.)

- A. W. Lohmann, R. G. Dorsch, D. Mendlovic, Z. Zalevsky, and C. Ferreira. Space-bandwidth product of optical signals and systems. *J. Opt. Soc. Am. A*, 13(3):470–3, Mar 1996. (Cited on page 11.)
- L. B. Lucy. An iterative technique for the rectification of observed distributions. *Astron. J.*, 79(6):745–754, 1974. (Cited on page 121.)
- R. P. MacDonald, S. A. Boothroyd, T. Okamoto, J. Chrostowski, and B. A. Syrett. Inter-board optical data distribution by Bessel beam shadowing. *Opt. Commun.*, 122:169–77, 1996. (Cited on page 74.)
- D. Magde, E. Elson, and W. W. Webb. Thermodynamic fluctuations in a reacting system: Measurement by fluorescence correlation spectroscopy. *Phys. Rev. Lett.*, 29:705–8, 1972. (Cited on page 164.)
- M. Martinez-Corral, M. Caballero, E. H. K. Stelzer, and J. Swoger. Tailoring the axial shape of the point spread function using the Toraldo concept. *Opt. Express*, 10(1):227–30, 2002. (Cited on page 161.)
- C. Maurer, A. Schwaighofer, A. Jesacher, S. Bernet, and M. Ritsch-Marte. Suppression of undesired diffraction orders of binary phase holograms. *Appl. Opt.*, 47(22):3994–8, 2008. (Cited on page 50.)
- D. J. McCabe, A. Tajalli, D. R. Austin, P. Bondareff, I. A. Walmsley, S. Gigan, and B. Chatel. Spatio-temporal focusing of an ultrafast pulse through a multiply scattering medium. *Nat. Commun.*, 2:447, 2011. (Cited on page 165.)
- C. W. McCutchen. Generalized Aperture and the Three-Dimensional Diffraction Image. *J. Opt. Soc. Am.*, 54(2):240–244, 1964. (Cited on pages 40 and 44.)
- J. H. McLeod. The Axicon: A New Type of Optical Element. *J. Opt. Soc. Am.*, 44(8):592–597, 1954. (Cited on page 14.)
- J. Mertz. *Introduction to Optical Microscopy*, pages 302–303. Roberts & Company Publishers, 2010a. (Cited on page 132.)
- J. Mertz. *Introduction to Optical Microscopy*, page 304. Roberts & Company Publishers, 2010b. (Cited on page 133.)
- J. Mertz. *Introduction to Optical Microscopy*, page 311. Roberts & Company Publishers, 2010c. (Cited on page 133.)
- J. Mertz and J. Kim. Scanning light-sheet microscopy in the whole mouse brain with HiLo background rejection. *J. Biomed. Opt.*, 15(1):016027, 2011. (Cited on pages 13 and 126.)
- A. P. Mosk, A. Lagendijk, G. Lerosey, and M. Fink. Controlling waves in space and time for imaging and focusing in complex media. *Nature Phot.*, 6(5):283–292, 2012. (Cited on page 159.)
- E. Mudry, K. Belkebir, J. Girard, J. Savatier, E. le Moal, C. Nicoletti, M. Allain, and A. Sentenac. Structured illumination microscopy using unknown speckle patterns. 6 (April):312–5, 2012. (Cited on page 160.)
- M. A. A. Neil, R. Juskaitis, and T. Wilson. Method of obtaining optical sectioning by using structured light in a conventional microscope. *Opt. Lett.*, 22(24):1905–7, 1997. (Cited on pages 7 and 126.)
- V. Ntziachristos. Going deeper than microscopy: the optical imaging frontier in biology. *Nature Meth.*, 7(8):603–14, 2010. (Cited on pages 8 and 160.)

- O. E. Olarte, J. Licea-Rodriguez, J. A. Palero, E. J. Gualda, D. Artigas, J. Mayer, J. Swoger, J. Sharpe, I. Rocha-Mendoza, R. Rangel-Rojo, and P. Loza-Alvarez. Image formation by linear and nonlinear digital scanned light-sheet fluorescence microscopy with gaussian and bessel beam profiles. *Biomed. Opt. Express*, 3(7):1492–1505, Jul 2012. (Cited on page 156.)
- F. Pampaloni, E. G. Reynaud, and E. H. K. Stelzer. The third dimension bridges the gap between cell culture and live tissue. *Nature Rev. Mol. Cell. Biol.*, 8(10):839–45, 2007. (Cited on pages 1, 10, and 33.)
- T. A. Planchon, L. Gao, D. E. Milkie, M. W. Davidson, J. A. Galbraith, C. G. Galbraith, and E. Betzig. Rapid three-dimensional isotropic imaging of living cells using Bessel beam plane illumination. *Nature Meth.*, 8(5):417–23, 2011. (Cited on pages 11, 33, 126, 153, 155, 159, and 161.)
- S. Popoff, G. Lerosey, M. Fink, A. C. Boccara, and S. Gigan. Image transmission through an opaque material. *Nature Commun.*, 1(81):6–10, 2010. (Cited on page 76.)
- E. G. Reynaud, U. Krzic, K. Greger, and E. H. K. Stelzer. Light sheet-based fluorescence microscopy: more dimensions, more photons, and less photodamage. *HFSP J.*, 2(5):266–75, 2008. (Cited on pages 11 and 33.)
- W. H. Richardson. Bayesian-Based Iterative Method of Image Restoration. *J. Opt. Soc. Am.*, 62(1):55–59, 1972. (Cited on page 121.)
- J. G. Ritter, R. Veith, J.-P. Siebrasse, and U. Kubitscheck. High-contrast single-particle tracking by selective focal plane illumination microscopy. *Opt. Express*, 16(10):7142–52, 2008. (Cited on page 43.)
- J. G. Ritter, J.-H. Spille, T. Kaminski, and U. Kubitscheck. A cylindrical zoom lens unit for adjustable optical sectioning in light sheet microscopy. *Opt. Express*, 2(1):185–193, 2011. (Cited on page 43.)
- J. M. Rodenburg, A. C. Hurst, and A. G. Cullis. Transmission microscopy without lenses for objects of unlimited size. 107:227–31, 2007. (Cited on page 76.)
- A. Rohrbach. Artifacts resulting from imaging in scattering media: a theoretical prediction. *Opt. Lett.*, 34(19):3041–3, 2009. (Cited on pages 7, 12, 26, 27, 91, 92, and 158.)
- Y. Roichman and D. G. Grier. Projecting extended optical traps with shape-phase holography. *Opt. Lett.*, 31(11):1675–77, 2006. (Cited on pages 58 and 157.)
- B. A. E. Saleh and M. C. Teich. *Fundamentals of Photonics*. Wiley, New York, 2nd ed. edition, 2007. (Cited on pages 41 and 42.)
- P. Schacht, S. B. Johnson, and P. A. Santi. Implementation of a continuous scanning procedure and a line scan camera for thin-sheet laser imaging microscopy. *Biomed. Opt. Express*, 1(2):598–609, 2010. (Cited on page 164.)
- M. Schrader, U. G. Hofmann, and S. W. Hell. Ultrathin fluorescent layers for monitoring the axial resolution in confocal and two-photon fluorescence microscopy. *J. Microsc.*, 191(2):135–140, 1998. (Cited on page 7.)
- T. J. Schröter, S. B. Johnson, K. John, and P. A. Santi. Scanning thin-sheet laser imaging microscopy (sTSLIM) with structured illumination and HiLo background rejection. *Biomed. Opt. Express*, 3(1):170–7, 2012. (Cited on page 126.)
- M. Schwertner, M. J. Booth, and T. Wilson. Characterizing specimen induced aberrations for high NA adaptive optical microscopy. *Opt. Express*, 12(26):6540–52, 2004. (Cited on page 8.)

- J. Sharpe, U. Ahlgren, P. Perry, B. Hill, A. Ross, J. Hecksher-Sorensen, R. Baldock, and D. Davidson. Optical projection tomography as a tool for 3d microscopy and gene expression studies. *Science*, 296(5567):541–5, 2002. (Cited on pages 8 and 160.)
- C. J. R. Sheppard and T. Wilson. Imaging properties of annular lenses. *Appl. Opt.*, 18(22):3764–9, 1979. (Cited on page 14.)
- H. Siedentopf and R. Zsigmondy. Über Sichtbarmachung und Größenbestimmung ultramikroskopischer Teilchen. *Ann. Phys.*, 4:1–39, 1903. (Cited on page 11.)
- L. Silvestri, A. Bria, L. Sacconi, G. Iannello, and F. Pavone. Confocal light sheet microscopy: micron-scale neuroanatomy of the entire mouse brain. *Opt. Express*, 20(18):20582, 2012. (Cited on page 123.)
- P. T. C. So, C. Y. Dong, B. R. Masters, and K. M. Berland. Two-photon Excitation Fluorescence Microscopy. *Annu. Rev. Biomed. Eng.*, 02:399–429, 2000. (Cited on page 132.)
- I. Solovei, M. Kreysing, C. Lanctôt, S. Kösem, L. Peichl, T. Cremer, J. Guck, and B. Joffe. Nuclear architecture of rod photoreceptor cells adapts to vision in mammalian evolution. *Cell*, 137(2):356–68, 2009. (Cited on page 75.)
- L. Song, E. J. Hennink, I. T. Young, and H. J. Tanke. Photobleaching kinetics of fluorescein in quantitative fluorescence microscopy. *Biophys. J.*, 68(6):2588–600, 1995. (Cited on page 10.)
- J. Swoger, P. Verveer, K. Greger, J. Huisken, and E. H. K. Stelzer. Multi-view image fusion improves resolution in three-dimensional microscopy. *Opt. Express*, 15(13):8029–42, 2007. (Cited on pages 93 and 159.)
- S. H. Tao and X. Yuan. Self-reconstruction property of fractional Bessel beams. *J. Opt. Soc. Am. A*, 21(7):1192–1197, 2004. (Cited on page 15.)
- M. Temerinac-Ott, O. Ronneberger, P. Ochs, W. Driever, T. Brox, and H. Burkhardt. Multiview deblurring for 3-d images from light sheet based fluorescence microscopy, 2012. (Cited on page 93.)
- P. Theer and W. Denk. On the fundamental imaging-depth limit in two-photon microscopy. *J. Opt. Soc. Am. A*, 23(12):3139–49, 2006. (Cited on pages 153, 154, and 155.)
- R. Tomer, K. Khairy, F. Amat, and P. J. Keller. Quantitative high-speed imaging of entire developing embryos with simultaneous multiview light-sheet microscopy. *Nature Meth.*, 9:755–763, 2012. (Cited on pages 93, 159, and 161.)
- T. V. Truong, W. Supatto, D. S. Koos, J. M. Choi, and S. E. Fraser. Deep and fast live imaging with two-photon scanned light-sheet microscopy. *Nature Meth.*, 8(9), 2011. (Cited on pages 9, 11, 25, 136, 154, 155, and 158.)
- E. G. van Putten, I. M. Vellekoop, and A. P. Mosk. Spatial amplitude and phase modulation using commercial twisted nematic LCDs. *Appl. Opt.*, 47(12):2076–81, 2008. (Cited on page 59.)
- A. Vasara, J. Turunen, and A. T. Friberg. Realization of general nondiffracting beams with computer-generated holograms. *J. Opt. Soc. Am. A*, 6(11):1748–54, 1989. (Cited on page 14.)
- T. Čižmár and K. Dholakia. Tunable Bessel light modes: engineering the axial propagation. *Opt. Express*, 17(18):12688–700, 2009. (Cited on page 164.)
- T. Čižmár, M. Mazilu, and K. Dholakia. In situ wavefront correction and its application to micromanipulation. *Nature Photon.*, 4(6):388–94, 2010. (Cited on pages 76 and 162.)

- I. M. Vellekoop and C. M. Aegerter. Scattered light fluorescence microscopy: imaging through turbid layers. *Opt. Lett.*, 35(8):1245–7, 2010. (Cited on page 76.)
- I. M. Vellekoop and A. P. Mosk. Focusing coherent light through opaque strongly scattering media. *Opt. Lett.*, 32(16):2309–11, 2007. (Cited on pages 76 and 162.)
- P. J. Verveer, J. Swoger, F. Pampaloni, K. Greger, M. Marcello, and E. H. K. Stelzer. High-resolution three-dimensional imaging of large specimens with light sheet-based microscopy. *Nature Meth.*, 4(4):311–313, 2007. (Cited on pages 33 and 159.)
- G. Vicidomini, M. Schneider, P. Bianchini, S. Krol, T. Szellas, and A. Diaspro. Characterization of uniform ultrathin layer for z-response measurements in three-dimensional section fluorescence microscopy. *J. Microsc.*, 225(1):88–95, 2007. (Cited on page 7.)
- A. H. Voie, D. Burns, and F. A. Spelman. Orthogonal-plane fluorescence optical sectioning: three-dimensional imaging of macroscopic biological specimens. *J. Microsc.*, 170(3):229–36, 1993. (Cited on pages 11, 39, 42, and 84.)
- C. Wang, L. Qiao, Z. Mao, Y. Cheng, and Z. Xu. Reduced deep-tissue image degradation in three-dimensional multiphoton microscopy with concentric two-color two-photon fluorescence excitation. *J. Opt. Soc. Am. B*, 25(6):976, 2008. (Cited on page 165.)
- X.-Q. Wang, J.-Y. Chen, L. Mi, and P.-N. Wang. A comparison of tissue penetrations between single and two-photon-excitations. *Appl. Phys. Lett.*, 65:143705, 2009. (Cited on page 143.)
- W. T. Welford. Use of Annular Apertures to Increase Focal Depth. *J. Opt. Soc. Am.*, 50(8):749–753, 1960. (Cited on page 14.)
- T. Wohland, X. Shi, J. Sankaran, and E. H. K. Stelzer. Single plane illumination fluorescence correlation spectroscopy (SPIM-FCS) probes inhomogeneous three-dimensional environments. *Opt. Express*, 18(10):10627–41, 2010. (Cited on page 164.)
- Y. Wu, A. Ghitani, R. Christensen, A. Santella, Z. Du, G. Rondeau, and Z. Bao. Inverted selective plane illumination microscopy (iSPIM) enables coupled cell identity lineaging and neurodevelopmental imaging in *Caenorhabditis elegans*. *Proc. Natl. Acad. Sci. USA*, 108(43):17708–13, 2011. (Cited on page 33.)
- A. N. Yaroslavsky, I. V. Y. P. C. Schulze, R. Schober, and H. S. F. Ulrich. Optical properties of selected native and coagulated human brain tissues in vitro in the visible and near infrared spectral range. *Physics in medicine and biology*, 47(12):2059–73, 2002. (Cited on page 91.)
- J. Ying, F. Liu, and R. R. Alfano. Spatial distribution of two-photon-excited fluorescence in scattering media. *App. Opt.*, 38(1):224–9, 1999. (Cited on page 154.)
- X. Zhuang. Nano-imaging with Storm. *Nature Phot.*, 3(7):365–7, 2009. (Cited on page 7.)

LIST OF FIGURES

Figure 1.1	Illustration of fundamental image quality parameters.	6
Figure 1.2	Schematic of a light-sheet microscope setup.	12
Figure 1.3	Illustration of limitations of light-sheet based microscopy.	13
Figure 1.4	Iso-surface plot of a Gaussian and a Bessel beam	14
Figure 2.1	Sketch of the light-sheet microscope	18
Figure 2.2	Images of fluorescent spheres for an epi-fluorescence and a light-sheet microscope.	18
Figure 2.3	The point-spread function of a light-sheet microscope with Bessel-beam illumination.	20
Figure 2.4	Comparison of the image formation for wide-field and confocal point detection.	22
Figure 2.5	Illustration of optical sectioning.	24
Figure 2.6	Image decomposition: Example	26
Figure 2.7	Photo of the setup	29
Figure 2.8	Sketch of the light-sheet illumination add-on.	30
Figure 2.9	Sample mounting and positioning in the sample chamber	33
Figure 2.10	Scheme of the image acquisition process.	35
Figure 3.1	Illustration of the variables used for the description of focusing by a lens.	39
Figure 3.2	Simulated irradiance of a focused flat-top beam.	40
Figure 3.3	Simulated irradiance of a Gaussian beam.	41
Figure 3.4	Simulated irradiance of a Bessel beam.	44
Figure 3.5	Simulated irradiance of a sectioned Bessel beam.	45
Figure 3.6	Radial irradiance and power for a focused flat-top beam and two Bessel beams with equal depth of field.	46
Figure 3.7	The relative power in the Bessel beam's main lobe.	49
Figure 3.8	Illustration of the spatial separation of the hologram's far-field-diffraction.	50
Figure 3.9	Image of a holographically shaped illumination beam in fluorescence with and without zeroth order.	51
Figure 3.10	Holographic control of the depth of field of Gaussian and Bessel beams.	52
Figure 3.11	The composition of holograms for beam shaping.	53
Figure 3.12	Exemplary holograms for the generation of Gaussian beams, Bessel beams and light-sheets.	54
Figure 3.13	Holographic control over the beam orientation.	55
Figure 3.14	Schematic explanation of the effect of low-pass filtering against axial oscillations of the on-axis beam irradiance.	56
Figure 3.15	Reduction of axial undulations of the on-axis irradiance of a Bessel beam by low-pass filtering of the hologram aperture.	58
Figure 3.16	Coherent imaging of illumination beams.	59
Figure 4.1	Illustration of directional propagation stability	62
Figure 4.2	Average on-axis power for different illumination beams propagating through scattering media.	64
Figure 4.3	Average normalized on-axis power for beams propagating through distributions of scattering spheres at different beam positions.	65
Figure 4.4	Irradiance cross-sections of a Gaussian and a Bessel beam propagating through a scattering medium.	66
Figure 4.5	Images of Gaussian and Bessel beams propagating at different distances to two large spheres.	67

Figure 4.6	Normalized standard deviations of the on-axis beam power.	68
Figure 4.7	Simulation of the irradiance of Gaussian and Bessel beams scattered by two spheres.	69
Figure 4.8	Measurement of beam propagation through a scattering medium.	70
Figure 4.9	Propagation of Gaussian and Bessel beams into human skin.	71
Figure 4.10	Maximum selection images of human skin.	72
Figure 5.1	Axial resolution for different scanned illumination beams.	78
Figure 5.2	Optical sectioning for different scanned illumination beams	79
Figure 5.3	Light-sheet microscopy of two non-fluorescent spheres.	81
Figure 5.4	Light-sheet microscopy behind a cluster of non-fluorescing spheres.	83
Figure 5.5	Comparison of light-sheet microscopy images of a cluster of spheres for different illumination beams.	85
Figure 5.6	Transverse intensity profiles of the images shown in Figure 5.5.	86
Figure 5.7	Contrast of the ghost image of a cluster of spheres for different illumination beams.	86
Figure 5.8	Comparison of real, ideal and ghost images for different illumination beams.	87
Figure 5.9	Decomposition of the image contrast for different illumination beams.	88
Figure 5.10	Light-sheet microscopy images of a drosophila.	90
Figure 6.1	Schematic illustration of the wide-field and confocal-line detection modes.	96
Figure 6.2	Illumination and detection point-spread functions.	99
Figure 6.3	Axial resolution in a light-sheet microscope with confocal-line detection.	99
Figure 6.4	Optical sectioning in a light-sheet microscope with confocal-line detection.	100
Figure 6.5	Calibration of the line-confocal detection method.	104
Figure 6.6	Images of fluorescent spheres obtained for confocal-line detection and scanned illumination	105
Figure 6.7	Image slices through fluorescent spheres with profile along the detection axis	106
Figure 6.8	Axial resolution in Line Confocal detection microscopy	107
Figure 6.9	Signal-to-background in confocal-line detection microscopy	108
Figure 6.10	Images of drosophila egg-chambers with wide-field and confocal-line detection.	109
Figure 6.11	Axial line profile through images of drosophila egg-chambers	110
Figure 6.12	Propagation of Gaussian and Bessel beams through drosophila egg-chambers	111
Figure 6.13	Spatial frequency image decomposition	112
Figure 6.14	Relative Information Content dependency on the confocal-line width	113
Figure 6.15	Images of a layer in the center of a tumor cell cluster.	114
Figure 6.16	Images of a layer close to the surface of a tumor cell cluster.	114
Figure 6.17	Image contrast analysis of an image stack of a tumor cell cluster.	115
Figure 6.18	Enlarged image details for low and high penetration depth of the illumination beams.	116
Figure 6.19	Dependence of the Optical Sectioning on the Angle of the sectioned Bessel beam.	117
Figure 6.20	Dependence of the optical sectioning on the depth of field.	119
Figure 6.21	Image quality comparison for confocal-line detection with sectioned Bessel beam illumination.	120
Figure 6.22	Usable signal generation by Gaussian and Bessel beams	125

Figure 6.23	Image comparison: Line-confocal detection vs Structured illumination in homogenous media	127
Figure 6.24	Modulation depth for structured illumination of scattering media	128
Figure 6.25	Line-confocal and structured illumination images of a scattering sample	130
Figure 7.1	Schematic comparison of linear and two-photon Bessel beam light sheet microscopy.	131
Figure 7.2	Cross-sections through static illumination beams and light-sheets for linear and two-photon-excitation by Gaussian and Bessel beams.	137
Figure 7.3	Two-Photon Bessel beam light sheet microscopy: Optical sectioning	138
Figure 7.4	Image of a sphere for a misaligned light-sheet microscope.	139
Figure 7.5	Simulation of imaging of beads with linear and two-photon fluorescence excitation.	141
Figure 7.6	Ideal and ghost image contrast for simulated light-sheet microscopy images.	142
Figure 7.7	Sketch of the light-sheet microscope with added two-photon illumination beam path.	143
Figure 7.8	Linear & Two-Photon fluorescence excitation by Bessel beams.	146
Figure 7.9	Images of scattering fluorescent spheres for linear and two-photon excitation by scanned Bessel beams.	147
Figure 7.10	Quantitative measurements of linear and two-photon imaging performance.	148
Figure 7.11	Imaging performance for in tumor multicellular spheroids.	149
Figure 7.12	Image artifacts in NL-MISERB	150
Figure 7.13	Contrast improvement by confocal-line detection for TPE by Bessel beam illumination.	151
Figure 7.14	Measurement of contrast for TPE by Bessel beam illumination.	152
Figure 7.15	Penetration depth for nonlinear Bessel beam illumination	153
Figure B.1	Relative error of the phase computed by the BPM.	171
Figure B.2	Sketch of the error arising from the discretization of a sphere.	171

LIST OF TABLES

Table 1	Image parameters for different detection objective lenses.	33
Table 2	Efficiencies for different illumination beams and detection focal depths d_y detection	126
Table 3	Scattering properties of silica spheres of different sizes in water.	173

